The Synthesis and Coordination Chemistry of Two Families of Polydentate Ligands - Exploring Their Potential for the Preparation of Molecule-Based Magnets

By

NILOOFAR ZARRABI

A Thesis Submitted to the Department of Chemistry in Partial Fulfillment of the Requirements for the Degree of

Master of Science

Supervised by

Professor Melanie Pilkington

Brock University

St.Catharines, Ontario, Canada

June 2011

THIS THESIS DEDICATED

TO

MY BELOVED FATHER

ABSTRACT

The synthesis and studies of two classes of polydentate ligands are presented as two projects. In project 1, four new carboxamide ligands have been synthesised via the condensation of 2,2',6,6'-tetrachloroformyl-4,4'-bipyridine or 2,6-dichloroformyl pyridine together with heterocyclic amines containing pyridine or pyrazole substituents. The coordination chemistry of these ligands has been investigated and studies have shown that with a Cu(II) salt, two carboxamide ligands $\mathbf{L_1}$ and $\mathbf{L_2}$ afford large clusters with stoichiometries $[Cu_8(L_1)_4Cl_{16}]\cdot CHCl_3\cdot 5H_2O\cdot 7CH_3OH$ **(I)** and $[Cu_9(L_2)_6Cl_6]\cdot CH_3OH\cdot 5H_2O\cdot (C_2H_5)_3N$ **(II)** respectively.

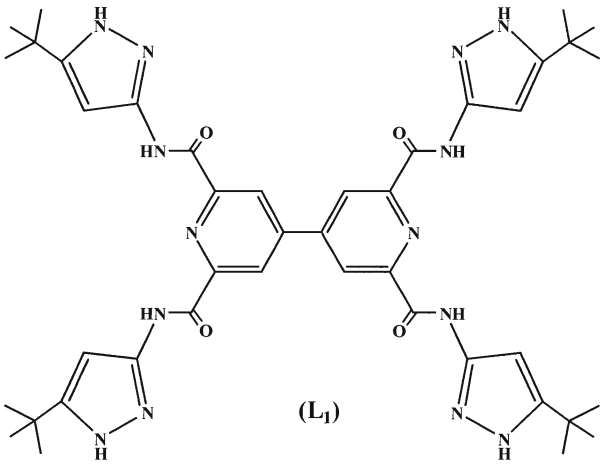

(L_1)

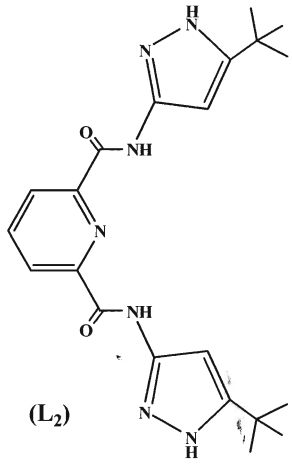

(L_2)

X-ray diffraction studies of cluster **(I)** reveal that it has approximate S_4 symmetry and is comprised of four ligands and eight copper (II) centers. Here, coordination takes place *via* amide O atoms, and pyrazole nitrogens. This complex is the first reported example of an octanuclear copper cluster with a saddle-shaped structure. The second cluster comprises nine copper ions that are arranged in a cyclic array. Each ligand coordinates three copper centers and each copper ion shares two ligands to connect six

ligands with nine copper ions. The amide nitrogens are completely deprotonated and both amide N and O atoms coordinate the metal centres. The cluster has three-fold symmetry. There are six chloride ions, three of which are bridging two neighbouring Cu(II) centres. Magnetic studies of **(I)** and **(II)** reveal that both clusters display weak antiferromagnetic interactions between neighbouring Cu(II) centers at low temperature.

In the second project, three complexes with stoichiometries $[Fe[N_3O_2](SCN)_2]_2$ **(III)**, R,R-$[Fe[N_3O_2](SCN)_2]$ **(IV)** and R,R-$[Fe[N_3O_2](CN)_2]$ **(V)** were prepared and characterized, where $[N_3O_2]$ is a pentadentate macrocycle. Complex **(III)** was prepared *via* the metal templated Schiff-base condensation of 2,2′,6,6′-tetraacetyl-4,4′-bipyridine together with 3,6-dioxaoctane-1,8-diamine and comprises of a dimeric macrocycle where the two Fe(II) centres are in a pentagonal-bipyramidal environment with the $[N_3O_2]$ ligands occupying the equatorial plane and two axial NCS ligands. Complexes **(IV)** and **(V)** were prepared via the condensation of 2,6-diacetylpyridine together with a chiral diamine in the presence of $FeCl_2$. The synthetic strategy for the preparation of the chiral diamine (4R,5R)-4,5-diphenyl-3,6-dioxa-1,8-octane-diamine was elucidated. The chirality of both macrocycles **(IV)** and **(V)** was probed by circular dichroism spectroscopy. The crystal structure of **(IV)** at 200 K contains two independent molecules in the unit cell, both of which contain a hepta-coordinated Fe(II) and axial NCS ligands. Variable temperature magnetic susceptibility and structural studies are consistent with a high spin Fe(II) complex and show no evidence of any spin crossover behaviour. In contrast, the *bis* cyanide derivative **(V)** crystallizes with two independent molecules in the unit cell, both of which have different coordination geometries consistent with different spin states for the two Fe(II) centres. At 250 K, the molecular structure of **(V)** shows the presence of both 7- and a 6-coordinate Fe(II) complexes in the crystal lattice. As the

temperature is lowered, the molecules undergo a structural change and at 100 K the structural data is consistent with a 6- and 5-coordinate Fe(II) complex in the unit cell. Magnetic studies confirm that this complex undergoes a gradual, thermal, spin crossover transition in the solid state. Photomagnetic measurements indicate this is the first chiral Fe(II) SCO complex to exhibit a LIESST.

TABLE OF CONTENTS

CHAPTER 5. Experimental

LIST OF FIGURES

LIST OF TABLES

LIST OF SCHEMES

LIST OF COMPOUNDS

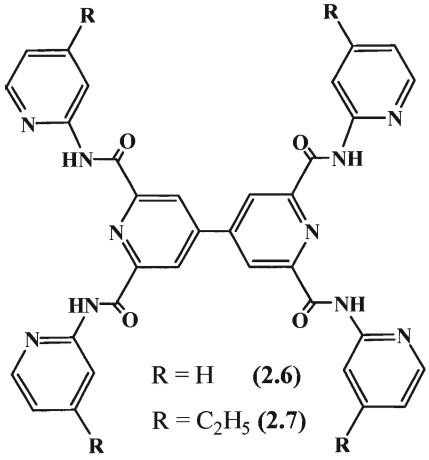

R = H (2.6)

R = C_2H_5 (2.7)

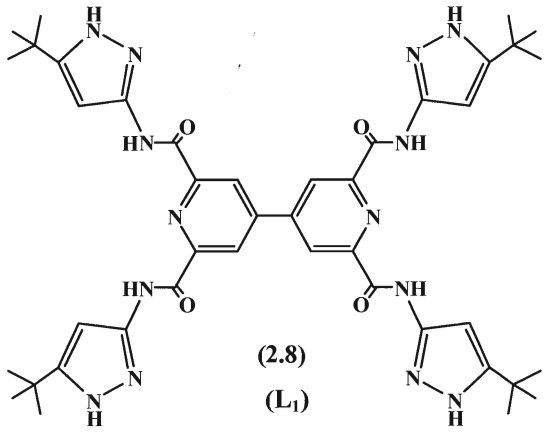

(2.8)

(L_1)

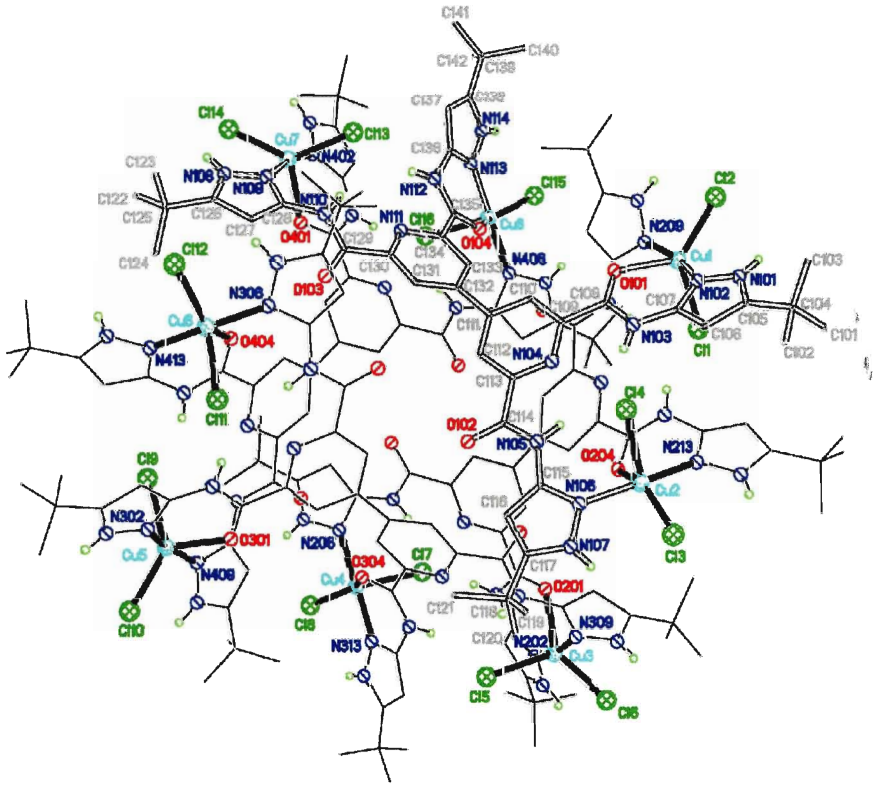

(2.17)

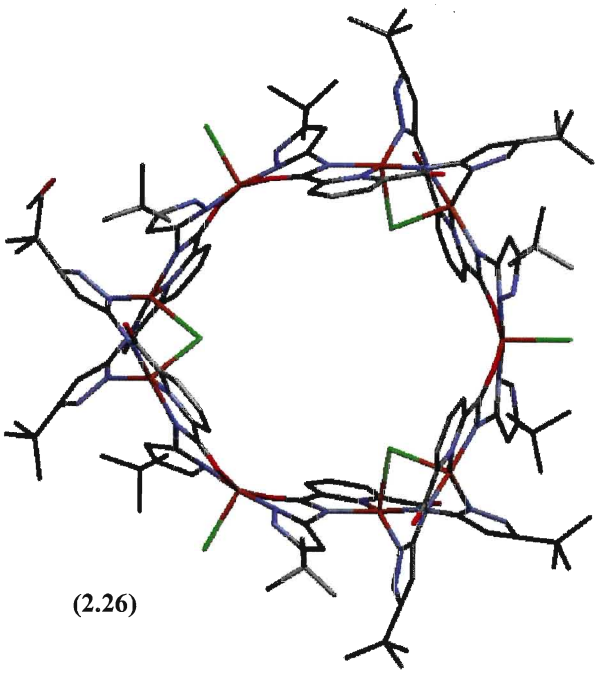

(2.26)

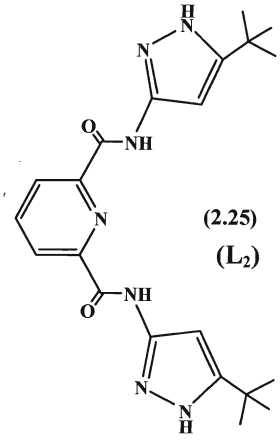

(2.25)
(L_2)

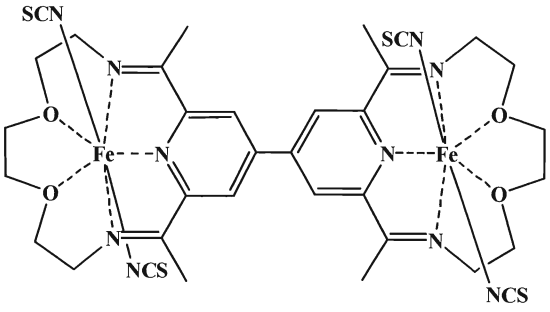

(4.3)

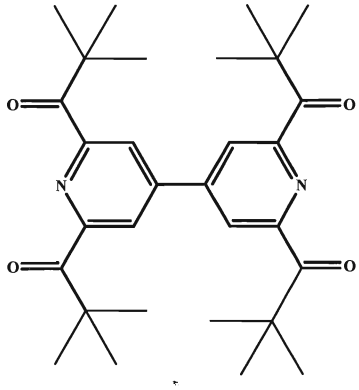

(4.5)

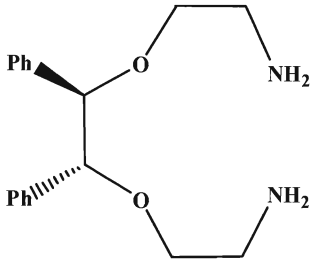

(4.11)

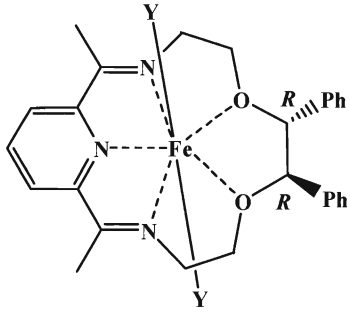

Y = NCS (4.12)
Y = CN (4.13)

LIST OF ABBREVIATIONS

0-D	zero-dimension
1-D	one-dimension
2-D	two-dimension
3-D	three-dimension
amu	atomic mass units, or Dalton (Da)
ACU	antiferromagnetic coupling
br	broad (IR and NMR peak descriptor)
calcd	calculated
°C	degree celsius
$CDCl_3$	deuterated chloroform
CD	circular dichroism
CH_3CN	acetonitrile
CN	cyanide
CW	continuous wave
d	doublet (NMR)
DMF	dimethyl formamide
DMSO	dimethyl sufoxide
EI	electron Impact ionization
emu	electromagnetic units (cm^3)
e	electron charge
Et	ethyl
Et_3N	triethylamine

Et_2O	diethyl ether
EtOH	ethanol
EPR	electron paramagnetic resonance
EXAFS	extended x-ray absorption fine structure
FAB	fast atom bombardment
fsa	2-hydroxy-3-carboxybenzylidene
FCU	ferromagnetic coupling unit
h	hour(s)
H_c	coercive field
H	spin hamiltonian
HS	high spin
Hcyd	cytidine
IR	infrared
J	coupling constant (NMR), magnetic exchange parameter
K	kelvin
KBr	potassium bromide
LS	low spin
LIESST	light-induced excited state spin trapping
m	multiplet (NMR)
Me	methyl
MeOH	methanol
$MgSO_4$	magnesium sulphate
mmol	mllimole
Mpt.	melting point

m_s	quantum number for the z-component of the electron spin
MeOH	methanol
MLCT	metal-ligand charge transfer
M_r	remnant magnetization
M_s	saturated magnetisation
MS	mass spectroscopy
m/z	mass/charge ratio
NaCl	sodium chloride
NaOH	sodium hydroxide
Na_2SO_4	sodium sulfate
NMR	nuclear magnetic resonance
NCS	thiocyanate
ORTEP	oak ridge thermal ellipsoid plot
OAc	acetate
ppm	parts per million
py	pyridine
P	pairing energy
R	agreement factor
RT	room temperature
s	singlet (NMR)
S	spin quantum number
sh	sharp(IR)
SQUID	superconducting quantum interference device
SCM	single chain magnets

SCO	spin crossover
SMM	single molecular magnets
ST	spin transition
t	triplet (NMR)
T	temperature
T_c	critical temperature
T_N	neel temperature
TLC	thin layer chromatography
triflate	trifluoromethanesulphonate
THF	tetrahydrofuran
UV- vis	ultraviolet visible
λ	wavelength
nm	nanometre
χ	magnetic suspetibility
χ_M	molar magnetic susceptibility
θ	weiss constant
μ_B	bohr magneton
μ_{eff}	magnetic moment
g	g-factor, proportionality constant
Δ_c	critical point
w	weak (IR)

ACKNOWLEDGEMENTS

Looking back, I am very grateful for all I have received throughout the years I spent at Brock. It has certainly shaped me as a person and has led me to where I am now. I want first to thank my supervisor Professor Melanie Pilkington for giving me the chance to study and research in Canada. I would like to thank her for generously providing the facility for my research projects and also for her support. Throughout my thesis-writing period, she provided me with great teaching, many good ideas and careful corrections.

I would like to thank Dr. Prashanth Poddutoori for helping me get through difficult times. I am grateful for all I learnt from him. His support, encouragement and positive attitude definitely helped me to be able to complete my thesis.

I am also indebted to Dr. Qiang Wang. His support, collaboration and contribution were very valuable in developing the synthetic strategy for the preparation of the chiral amine. I would like to thank all my labmates: Roland, Roger, Nick, Shari, Emma and Peter who made the lab. such a friendly environment.

My sincere thanks also go to Professor Martin Lemaire for the measuring magnetic properties of my samples as well as being so welcoming by offering great advice, suggestions and discussion whenever I needed it.

I wish to thank the Graduate Program Director, Professor Rothstein and my supervisory committee of Professor van der Est and Professor Nikonov. Their attitude definitely had a large impact on me. Their constructive criticism and support taught me how I could be a good teacher in future. I would like to thank chair of the chemistry department, Professor Heather Gordon for all of her support.

Many thanks to Tim Jones and Razvan Simionescu for Mass and NMR spectroscopy. Without their contribution, my projects would not have been possible.

My sincere thanks to Professor Clegg (University of Newcastle, UK) for help with refinement of the crystal data of my cluster, Professor Jerome Long and Professor Muralee Murugesu (University of Ottawa), Dr. Cédric Desplanches and Dr. Hongfeng Wang (Internal Bordeaux, France) for magnetic measurements. Many thanks to Professor J. M. Rawson (University of Windsor) for simulating the EPR spectra of my clusters.

I also want to thank the administrative assistants, Chris Skorski and Beulah Alexander for their help and assistance.

Finally, I am forever indebted to my parents for allowing me to leave them and follow my passion. They supported me, taught me, loved me and believed in me. The last sentence I heard from my father by phone before he passed away was "I am proud of you". That is enough for me to continue my research career. To him, I dedicate this thesis.

CHAPTER 1

Molecular Magnetism - Concepts and Ligand Design

1.1 Molecular magnetism

Traditional magnets comprised of metals (e.g. Fe, Cu, Ni) or metal oxides (e.g. CrO_2) are everywhere in our lives. They have found a wide range of applications in science, technology and domestic life, that include audio- and videotapes, door closures and magnetic stripes on credit cards. Molecular and macromolecular materials are also encountered broadly, and lend themselves to a different set of applications that include display technology, plastics and optics.

Molecule-based magnets are considered to be a class of molecular materials since the building blocks making up these materials are purely organic molecules, coordination compounds, or a mixture of both i.e. they are molecular in their nature. In contrast to traditional magnets where the unpaired electron spins reside only on metal atoms in d or f orbitals, in molecule-based magnets, the unpaired electrons may reside in d or f orbitals on isolated metal atoms, but may also reside in highly localised s and p orbitals on a purely organic species. Molecule-based magnets are also prepared by low temperature solution based methodologies rather than via the high temperature metallurgical processing or electroplating processes employed for the manufacture of traditional magnets. This facilitates the chemical tailoring of the molecular building blocks allowing chemists to tune their magnetic properties. This relatively new class of magnetic materials have expanded the materials properties typically associated with magnets to include low density, transparency, electrical insulation and low temperature fabrication, as well as the realization of dual property materials where magnetic ordering is combined with other

physical properties such as conductivity and/or optical properties.[1] Current research in this field is motivated by the need for a better understanding of the fundamental principles of magnetic behaviour in these systems, in particular when moving from isolated molecules to three-dimensional solids, as well as addressing the technological challenges associated with the realization of new materials.

The history of molecular magnetism began in 1951 with the study of a dinuclear complex, copper(II) acetate,[2] however it was not until the 1990s that the field became more widely recognized, following the discovery of the first molecule-based solids exhibiting spontaneous magnetization.[3] Over the past two decades, exciting new challenges have appeared on the horizon, including the use of a building block approach for the preparation of complex multifunctional magnetic materials, the invention of nanosized magnetic molecules, as well as the assembly and study of nanostructures that exhibit quantum effects. In all of these developments, coordination chemistry which was mapped out 150 years ago by Alfred Werner, plays a principal role. Prussian Blue, a mixed valent coordination compound of stiochemistry $Fe_4[Fe(CN)_6]_3 \cdot 14H_2O$, discovered in 1704 by the Berlin artist Diesbach is now recognized as being the first coordination compound and the first molecule-based magnetic solid,[4] it is noteworthy that, more than 300 years after its initial discovery, we are only now just realizing the potential applications of this and other families of magnetic coordination compounds.

1.1.1 History of magnetism

From the time that ancient Greek philosophers realized the value of the magnetic iron ore $FeO\text{-}Fe_2O_3$, numerous references to the material "Loadstone" can be found

worldwide, from the English philosopher William Gilbert and his work *De Magnete* [5] published in 1600, to the more modern approaches of Maxwell, Poisson and Faraday.[6] In 1907, Pierre Weiss assumed that interactions between magnetic molecules could be described by a molecular field.[7]At that time, the exact origin of the field was undetermined. It was not until 1931 that Paul Dirac proved mathematically the possibility of the existence of a monopole.[8] However, there is no evidence for the existence of a magnetic monopole experimentally. Dirac established the essential relationship between the elementary electric charge e and a proposed basic magnetic charge g, where n is an integer, n = 1,2,... The magnetic charge is $g = ng_D$; $g_D = \hbar c / 2e = 68.5e$ and is called the unit Dirac charge. In this regard, another useful equation is:

$$\vec{\mu} = -g_e \beta_e \vec{J} \qquad (1)$$

Where, $\vec{\mu}$, β_e and $\vec{J}$ are magnetic moment, Bohr magneton ($\beta_e = |e| \hbar/2m_e$) and angular momentum, respectively.

1.1.2 Magnetic phenomena

The essential part of any magnetic material is the presence of an unpaired electron or more accurately, the spin related with an unpaired electron. The motion of the electron about the nucleus produces a magnetic dipole moment, Figure 1.1. There is a fundamental difference between an electric dipole which does not require motion and magnetic dipoles that always require moving charges. If magnetic monopoles exist, they always appear in pairs and can not be separated.

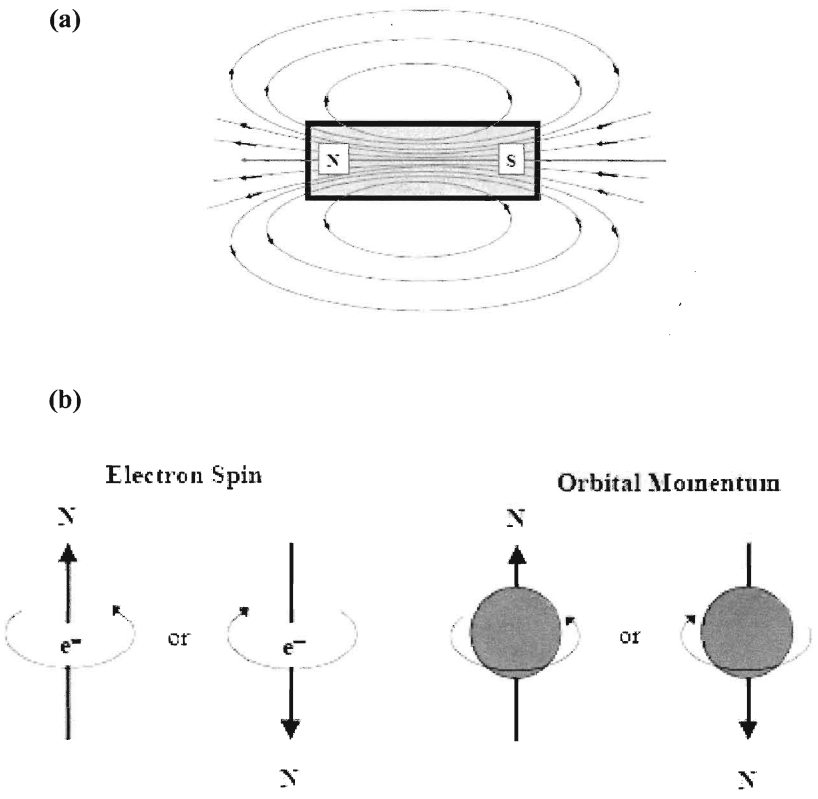

Figure 1.1. (a) A small bar magnet, it is now possible to imagine the magnetic dipole as consisting of two monopoles of opposite charge. (b) Origin of magnetic dipoles, the spin of the electron produces a magnetic field with a direction dependent on the quantum number m_s. Electrons orbiting around the nucleus create a magnetic field around the atom.[9] "Adapted from figure 1.3 of reference 9."

These spins, depicted in Figure 1.1 arrows (↑or ↓) and how they interact with each other determine the magnetic behavior of all magnets. Magnets are materials in which these spins are ordered.

In 1873, Maxwell presented a mathematical description for electromagnetic fields and their interactions with matter.[10] One of the most useful formulation of Maxwell's equations is:

$$B = H + 4\pi M \qquad (2)$$

The vector B is flux density or magnetic induction, H and M are the magnetic field and magnetization, respectively. Another important relationship used to describe the magnetic susceptibility χ of a material is given below equation (3). Here μ_o is the permeability of vacuum.

$$\chi = \mu_o M / B = M / H \qquad (3)$$

Magnetic susceptibility is the quantitative measure of the response of a material to an applied magnetic field. As magnetic interactions are typically characterized by their responses to variations in temperature and the applied magnetic field; magnetic susceptibility is therefore an important parameter to describe the general classes of magnetic interactions that arise due to order, structure and exchange.

1.1.3 Order, structure and exchange

In a magnetic material, unpaired electrons on atoms produce magnetic moments. The parallel or anti-parallel alignment of these moments or spins determines the type of magnetic structure that the material will possess. The exchange overlap integral and columbic integral of the electronic wave functions on neighbouring atoms are the most important parameter for determining the magnetic structure.[11] This overlap depends on neighbouring atomic distances, which are subject to size effects and or crystal lattice parameters. If the atoms are sufficiently near to each other then the potential to produce long range order exists. All materials are affected in some way by a magnetic field, and depending on this interaction they can be classified into four main classes: Para-, Ferro-, Antiferro- and Ferrimagnetisms, Figure 1.2.

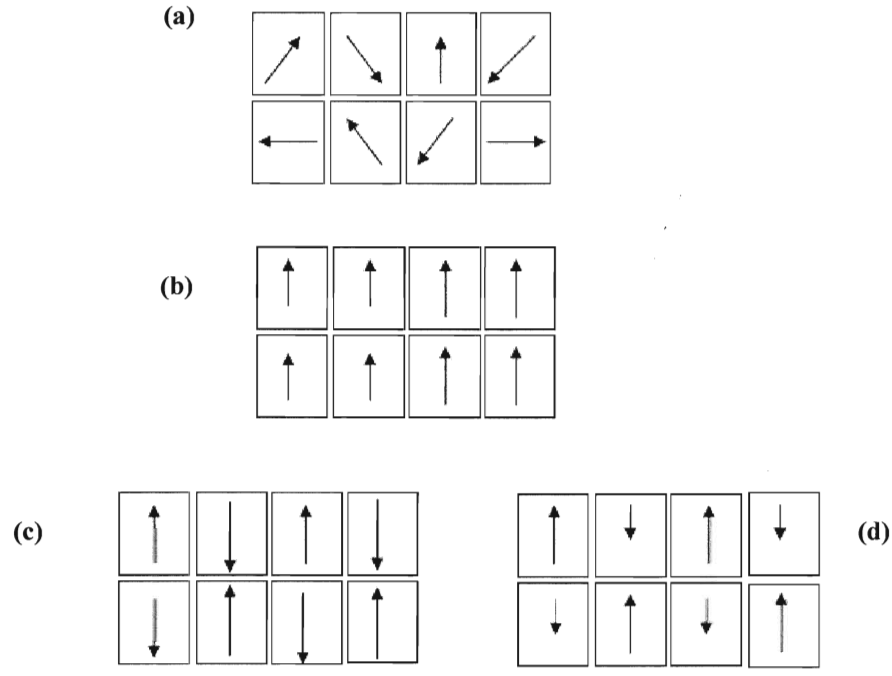

Figure 1.2. The alignment of magnetic moments at absolute zero for the four principle types of magnetism. (a) Paramagnetism random distribution of spins- independent spins that do not interact with each other; (b) Ferromagnets show parallel alignment of spins; (c) Antiferromagnets exhibit antiparallel alignment of spins; (d) Ferrimagnets consist of two magnetic spins of different strength.[12] "Adapted from figure 7.5 of reference 12."

All materials have some degree of diamagnetism. Diamagnetism occurs through a deformation of the electric charge distribution when a field is applied and it disappears when the field is removed. A diamagnetic material is further distinguished from all others due to the fact that its magnetic susceptibility (equation 3) is negative. The susceptibility is usually independent of both temperature and applied field strength for purely diamagnetic materials.

1.1.4 Paramagnetism

When the atomic, ionic, or molecular constituents have a non-zero magnetic moment, paramagnetism occurs allowing the applied field to align the moments and create a positive susceptibility. Each individual electron spin is independent of its neighbours. These spins, however, can be easily aligned with an applied magnetic field. Removal of the field will allow for a relaxation of the aligned states back to a random distribution of the moments. Typical paramagnets contain at least one unpaired electron resulting in an unbalanced angular momentum, orbital or spin. Temperature dependent behaviour is another important feature of paramagnets. The alignment of spins by an external magnetic field is hindered by random thermal interactions. Pierre Curie studied the thermal properties of magnetic materials, where he noted that the magnetic susceptibility (from equation 3) for a paramagnet is inversely dependent on temperature.[13]

$$\chi = \lim_{H \to 0} M/H = C/T \qquad (4)$$

Curie's constant C is characteristic of the atomic or molecular species, and temperature T starts at absolute zero. Equation 4 is known as the Curie Law.

1.1.5 Ferromagnetism

A fundamental phenomenon of condensed matter physics is the appearance of spontaneous order at low temperatures. Ferromagnets, antiferromagnets, liquid crystals and superconductors are all ordered phases. These ordered phases all share temperature dependence in such a way that some relevant physical property will exhibit a difference above and below a critical temperature T_C. For each phase one can define an ordering parameter which is zero for $T > T_C$ and non-zero for $T < T_C$. This parameter can now be

used to determine whether a system is ordered or not.[14] Ferromagnets are characterized by the parallel alignment of adjacent magnetic spins resulting in a large magnetic moment. Ferromagnets are rare because the alignment of adjacent magnetic spins can only occur if there is zero quantum mechanical overlap between the spin orbitals. Additionally, the long range ordering that occurs in ferromagnets is a function of domains that occur within a sample. Unlike paramagnets, ferromagnets exhibit a net magnetic moment in the absence of an applied magnetic field. The most common examples of ferromagnets include nickel, cobalt, iron and some of the rare earth metals such as gadolinium and dysprosium.

1.1.6 Antiferro- and ferrimagnetism

In an antiferromagnet, exchange coupling exists between neighboring moments resulting in an antiparallel alignment and thus a material with no net magnetic moment. At absolute zero, antiferromagnets behave like diamagnets when subjected to an applied field. However, as the temperature increases, the antiparallel alignment of the magnetic spins becomes weak as a consequence of thermal fluctuations. The susceptibility χ will increase until it reaches a temperature characteristic of the material where it will decline sharply. This abrupt change is indicative of a transformation from antiferromagnetism to paramagnetism, and is known as the Néel temperature (T_N). Below the Néel temperature, the system is ordered, Figure 1.3.

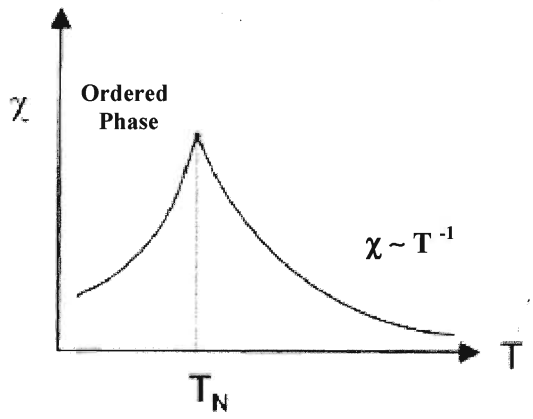

Figure 1.3. The susceptibility χ declines sharply as antiferromagnetism changes to a non-ordered paramagnetic state.[15] "Adapted from figure 3.8 of reference 15."

Antiferromagnets and ferrimagnets both use the superexchange mechanism to link two sublattices to create an antiparallel alignment of moments. However, ferrimagnets differ from antiferromagnets because the ions on the sublattices are not of equal magnitude and hence do not cancel. This difference in spin magnitude results in a net magnetic moment in the presence of an applied magnetic field.

1.1.7 Superparamagnetism and domain walls

Ferromagnetic materials exhibit a long-range ordering phenomenon at the atomic level that causes the unpaired electron spins to line up parallel to each other in a region called a domain, Figure 1.4. In 1906 Weiss proposed that these domains would align such that the total magnetic moment of the material was minimized.[16]

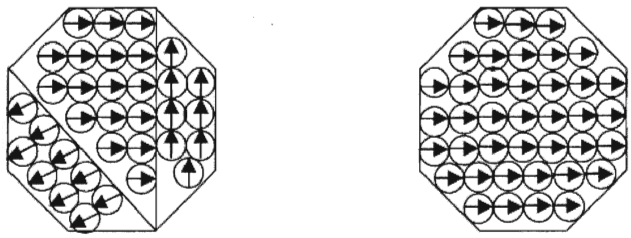

Figure 1.4. The random orientation of domains in a two dimensional ferromagnet is exhibited in (a), while (b) show the coherent orientation of spins in a single domain particle.[17] "Adapted from figure 13.35 of reference 17."

The result is that within ferromagnetic domains, the local magnetization for each domain reaches the saturation value. Between each domain is a boundary called the domain wall. These domain walls are classified by the angle of magnetization that will exists between them with the most common type of boundary being the Bloch wall. The Bloch wall consists of a 180° separation of the domain magnetization. The magnetization rotates in a plane parallel to the plane of the wall. The Néel wall consists of a 90° rotation perpendicular to the plane of the wall, Figure 1.5.

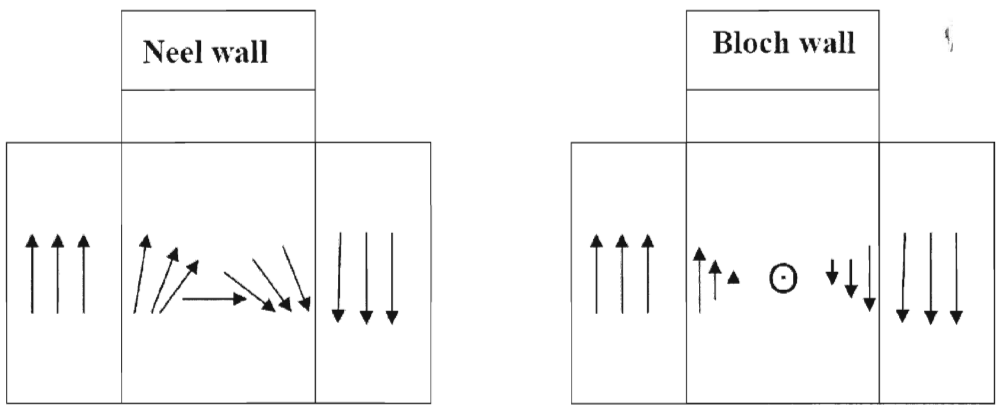

Figure 1.5. Bloch wall and Néel wall.[18] "Adapted from figures 9.2 and 9.5 of reference 18."

1.1.8 Magnetic characterization

The magnetic interactions described in the previous sections are quantified by measuring the magnetic response of the material to controlled changes in an applied magnetic field at a given temperature. Depending on how they respond, the specific magnetic properties and an overall magnetic strength can be identified and quantified. As described previously, all magnetic materials behave as paramagnets at high enough temperatures due simply to an great increase in the thermal energy that randomizes all of the spins. The critical temperature T_C is the start of magnetic ordering and is a function of the material. The Curie law (equation 4) describes temperature dependence in paramagnetic materials. Magnetic susceptibility quantitatively measures the response of a material to an applied field, Figure 1.6.

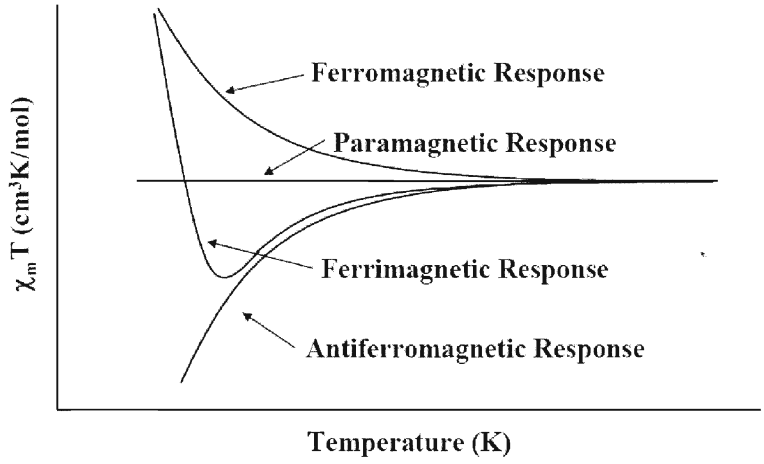

Figure 1.6. Magnetic susceptibility curves *vs* Temperature for paramagnet, ferromagnet, ferrimagnet and antiferromagnet upon long range order.[19] "Adapted from figures 1.15 and 6.16 of reference 19."

An ideal paramagnetic response of the $\chi_M T$ curve is temperature independent so that a straight line is obtained; ferromagnets have an increasing curve of $\chi_M T$ upon decreasing temperature; antiferromagnets have a downward curvature upon decreasing temperature.

Ferrimagnets display first a downward curvature and then an upward curvature. For a ferromagnetic material the temperature dependence deviates from the Curie law, and follows a slight modification known as the Curie-Weiss law, where θ is the Weiss constant.

$$\chi = C / (T-\theta) \qquad (5)$$

Figure 1.7 shows a plot of inverse susceptibility versus temperature for the three types of magnetic materials. An ideal paramagnet has a linear relationship that intersects zero as defined by the Curie-Weiss law (equation 5). The other types of materials exhibit cooperative magnetic effects. The ferro and antiferromagnetic materials exhibit opposite deviations.

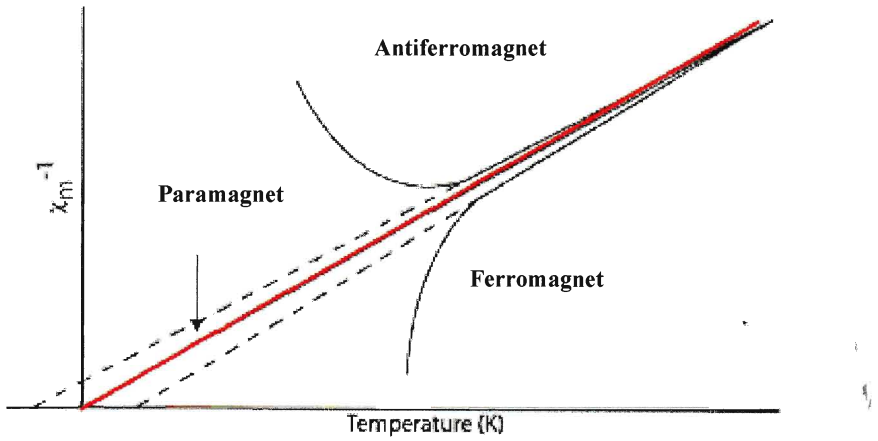

Figure 1.7. Plot of inverse susceptibility as a function of temperature for three main classes of magnetic materials.[20] "Adapted from figure 4.1 of reference 20."

At high enough temperatures all material behave linearly since the thermal energy can overcome any magnetic interactions. Positive Weiss constants indicate ferromagnetic interactions at sufficiently low temperatures, and are negative for antiferromagnets.

A distinguishing characteristic of ferromagnets and ferrimagnets is the presence of a hysteresis loop. The hysteresis loop can be obtained by plotting magnetization M of a ferromagnet versus the applied field H, Figure 1.8. That is, when applying a sufficiently large magnetic field, the magnetization becomes saturated at M_S; when the magnetic field is switched off, the magnetization does not vanish, but assumes a certain value referred to as the remnant magnetization, M_R. Zero magnetization can be achieved by applying a coercive field, H_c, in the opposite direction. It is the existence of this magnetic hysteresis loop that confers a memory effect on the material.

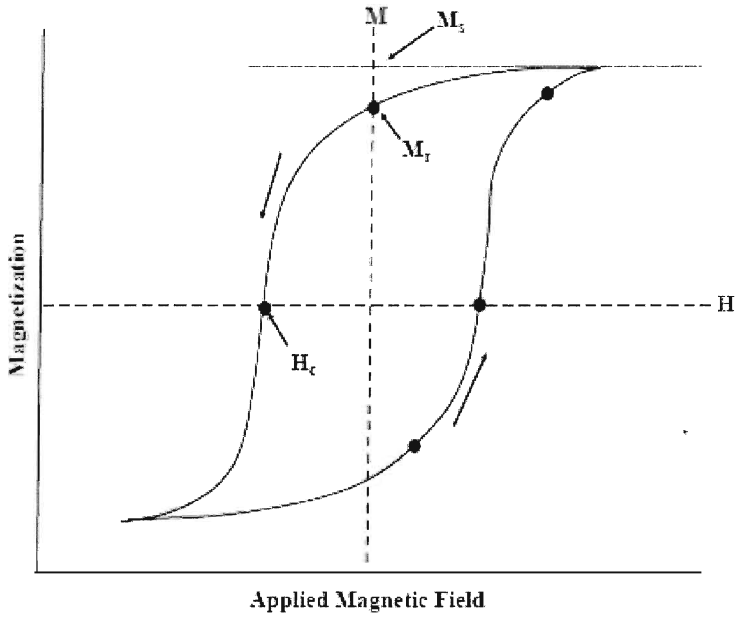

Figure 1.8. Hysteresis loop for a multidomain magnetic material. M_S is the magnetic saturation limit, M_r is the remnant magnetization at H = 0, H_C is the coercivity.[21] "Adapted from figure 7-1.1 of reference 21."

1.2 Ligand design for molecule-based magnets

Metallosupramolecular chemistry which refers to the use of metal ions in supramolecular chemistry, both as an assembly principle and for the introduction of specific properties, is an active field of research that is growing at a fast rate.[22] This can be attributed to the fact that synthetic routes to diverse families of ligands have been elucidated and are now more routinely employed.[22] As a consequence, the chemistry community has turned its attention to address the potential applications of these ligands and their coordination complexes. Over the past decade, a number of research groups have shifted the focus of their research to develop methodologies for introducing functionality into metallosupramolecular compounds.[23]

The chemical reactivity (redox or photochemical) and electronic, magnetic and/or optical properties of the metal ions together with the nature of the organic ligands, and the metal–ligand interactions give rise to unique properties for the resulting coordination complexes. Many of these materials with interesting physicochemical properties have been exploited in the area of molecular recognition and catalysis[24] as well as photo-, electro-, and magnetochemistry.[25] Magnetism is a very good example of a supramolecular property "since it results from the collective features of components bearing free spins and on their arrangements in organized assemblies".[26] The magnetic properties of polymetallic systems are therefore derived from the cooperative exchange interactions between paramagnetic metal ions. The nature and magnitude of the spin-exchange interactions between metal centers depends on a number of factors that includes: (i) the nature of the bridging ligand; (ii) the metal - to - metal ion distance(s); (iii) the bond angles subtended at the bridging ligands; (iv) the dihedral angle between the planes containing the metal ions, (v) the metal - to - ligand distances and (vi) the metal ion

stereochemistry.[27] In this respect, ligand design is crucial for both the organization of paramagnetic metal ions into a desired topology, as well as the efficient transmission of exchange interactions between the metal ions in a controlled manner. Metallosupramolecular compounds for which dimensionality can be tuned are currently being exploited for the "bottom-up" assembly of molecule-based magnetic materials.

In this respect, transition-metal oxalates and cyanometalate (distant cousins of the Prussian Blues) complexes have been successfully employed for the controlled self-assembly of magnetic materials with different lattice dimensionalities that include 0-D single-molecule magnets (SMMs), 1-D single chain magnets (SCMs), and 2- or 3-D molecule-based magnets.[28] In addition to smaller bridging ligands, the design and synthesis of larger polydentate ligands and their assembly into coordination complexes with predictable magnetic properties has interested inorganic chemists working in the field of magnetochemistry.[28]

One of the major goals is the controlled assembly of ferromagnetically coupled materials which can ultimately be exploited for memory storage devices that operate at or around room temperature. Of the theoretical strategies to achieve ferromagnetic spin alignment between two metal centres, those based on either orbital symmetry or spin polarization effects can be the most easily realized by synthetic chemists. If the metal-based magnetic orbitals are sufficiently close enough to overlap directly, then the sign of the magnetic interaction depends on their relative symmetry, as formalized by the Goodenough-Kanamori rules.[29] These rules have been exploited for the preparation of complexes with predictable magnetic properties. In this case, non-orthogonal spatially overlapping orbitals give rise to antiferromagnetic exchange and orthogonal, spatially overlapping orbitals afford ferromagnetic exchange. Two classical examples which show

the effect of magnetic orbital symmetry on the nature of metal to metal interactions are shown below for $[CuVO(fsa)_2en]\cdot CH_3OH$ **(1.1)** and $[Cu_2(fsa)_2en]\cdot CH_3OH$ **(1.2)**, Figure 1.9, where fsa = 2-hydroxy-3-carboxybenzylidene.

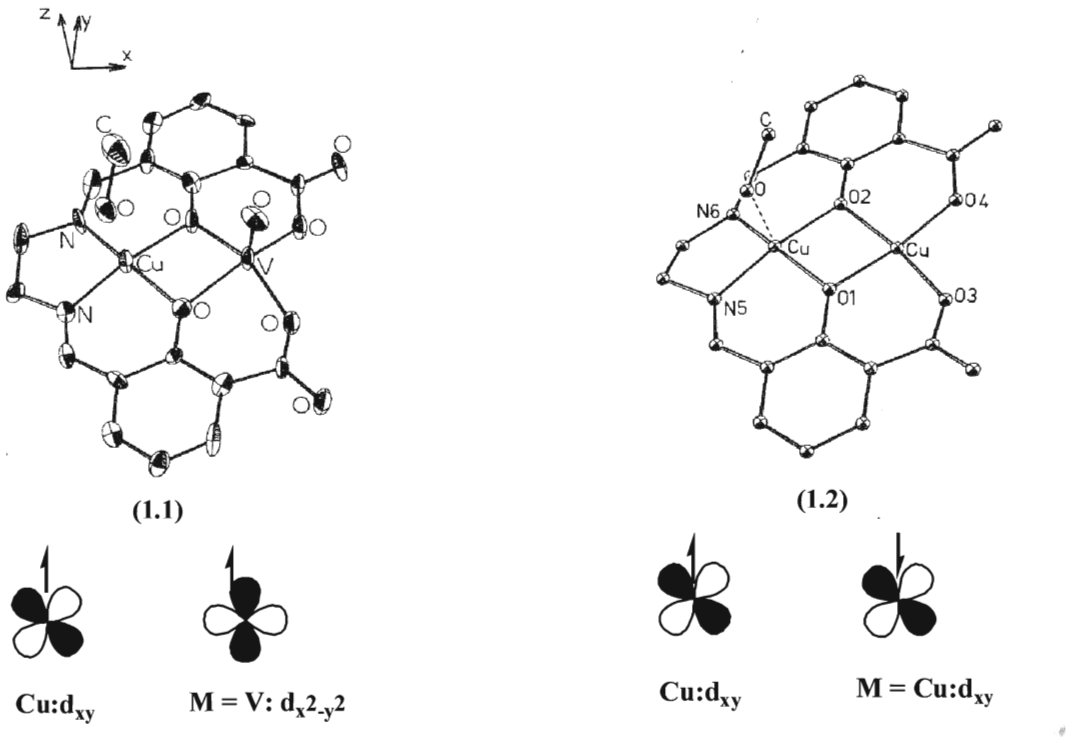

Figure 1.9. Molecular structures of $[CuVO(fsa)_2en]\cdot CH_3OH$ **(1.1)** and $[Cu_2(fsa)_2en]\cdot CH_3OH$ **(1.2)** and the effect of magnetic orbital symmetry on the nature of the exchange interaction, J.[30] "Reprinted with permission from reference 30b. Copyright {1982} American Chemical Society."

For both complexes, there is a pseudo mirror plane containing the metal ions, perpendicular to the plane of the ligand. In [CuVO] **(1.1)**, the magnetic orbital of the Cu(II) ion is constructed from a d_{xy} metallic orbital. This magnetic orbital is therefore

antisymmetric with regard to the CuOVO mirror plane. The magnetic orbital of the VO(II) is constructed from a d_{x2-y2} metallic orbital and is symmetric with respect to the same mirror plane. As a result there is zero overlap between these two magnetic orbitals and consequently the coupling is purely ferromagnetic. In the $[Cu_2(fsa)_2en]\cdot CH_3OH$ **(1.2)**, the two magnetic orbitals have the same symmetry and may overlap. It has been seen that antiferromagnetic contributions generally take precedence over ferromagnetic ones.[30] If the magnetic orbitals are too far apart to overlap directly, but require the participation of bridging ligand orbitals to mediate their interactions (superexchange process), then the properties of the bridging ligand also become important. This principle has received less systematic attention for metal complexes, when compared with the extensive work concerning the magnetic properties of organic polyradicals as a function of their molecular structures and topologies.[31] One of the major objectives of inorganic coordination chemists working in the area of molecular magnetism is to evaluate magnetic interactions between metal centers across a family of bridging ligands. In this respect, the effects of ligand size, conformation and topology can be studied.

A second (spin-polarisation) mechanism has been proposed by McCleverty and Ward to account for how the topology of a bridging ligand connecting two paramagnetic fragments can control the sign of the spin–spin exchange coupling for a series of coordination complexes.[30] For example, it has been experimentally determined that a *meta*-phenylene spacer separating two unpaired spins results in ferromagnetic exchange, whereas a *para*-phenylene spacer spin-pairing. Similarly, *meta*-substituted bridging ligands such as 1,3-dihydroxybenzene afford ferromagnetic coupling between two oxo-Mo(V) units, but *para*-substituted bridging ligands such as 1,4-dihydroxybenzene give rise to antiferromagnetic coupling. This can be rationalized using McCleverty and Wards

'spin-polarisation' mechanism that involves the alternation of the spin density around the ring of the connecting pathway, Figure 1.10. In this case, the unpaired electron on one Mo(V) center polarizes the spin of the electron cloud of the adjacent oxygen atom in the opposite sense; the next atoms in the sequence will be spin-polarized in the direction opposite to that of the oxygen atom, and so on, around the bridging ligand.[30] This principle has been applied to rationalize the exchange interactions for both linear and triangular trinuclear complexes.[30]

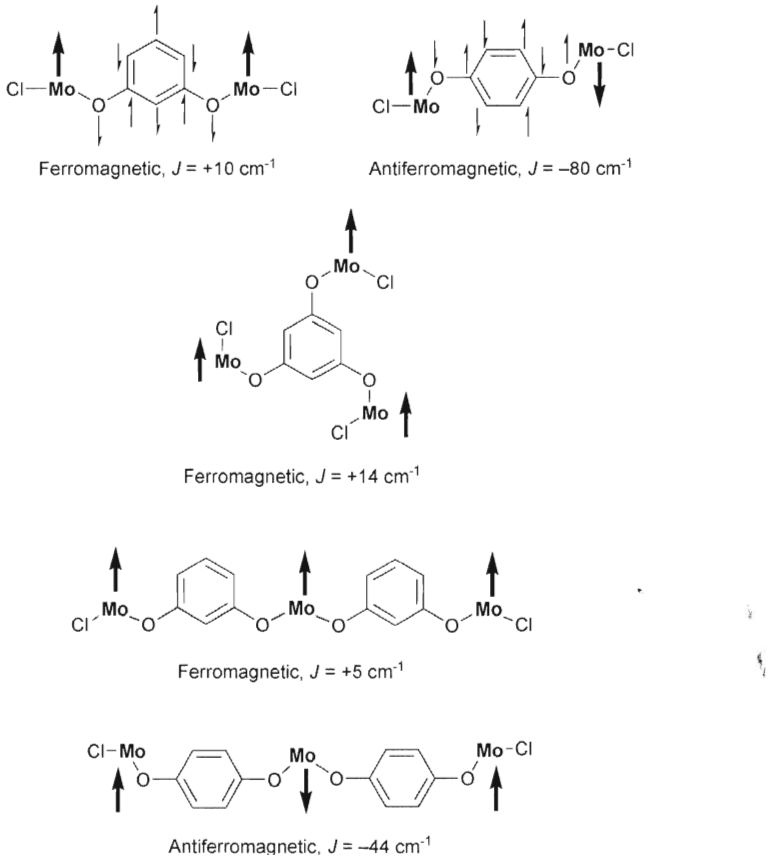

Figure 1.10. Control of magnetic exchange in dinuclear and trinuclear Mo(V) complexes according to the topology of the bridging ligand. The large arrows denote the unpaired electrons on the metal ions; the small arrows in the first two examples denote the spin density around the ring comprising the diamagnetic atoms of the bridging ligands.[32] "Reprinted with permission from reference 32. Copyright {1997} American Chemical Society."

This principle has also been extended to rationalize exchange interactions between metal centres in infinite lattices of complexes of stoichiometry $[CoL_2(NCS)_2]_\infty$ (where L = pyrimidine or pyrazine).[33] These complexes comprise parallel 2-D sheets in which a square grid of metal ions in the sheet are connected *via meta* pyrimidine or *para* pyrazine linkages with thiocyanate ligands in the axial positions, Figure 1.11. Applying the spin-polarisation rationale, the pyrimidine-bridged complex displays ferromagnetic coupling at low temperatures. This affords a material with a magnetically ordered state below 8 K which has the characteristics of a soft magnet.[33] In contrast, the pyrazine bridged complex displays antiferromagnetic coupling, with a magnetic susceptibility of zero at low temperature.[33]

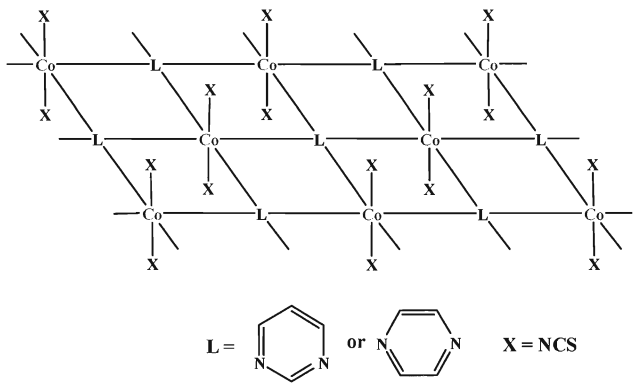

Figure 1.11. Infinite 2-D lattice of stiochiometry $[CoL_2(NCS)_2]_\infty$.[33] Reproduced with permission from reference 33. Copyright 1998 Wiley-VCH.

1.2.1 Oxamato ligands

The oxamato family of ligands have been particularly well investigated in the field of supramolecular magnetism, Figure 1.12.[34] This research has afforded diverse architectures that include discrete polynuclear coordination compounds and infinite multi-

dimensional coordination polymers that exhibit a range of interesting magnetic properties.[35]

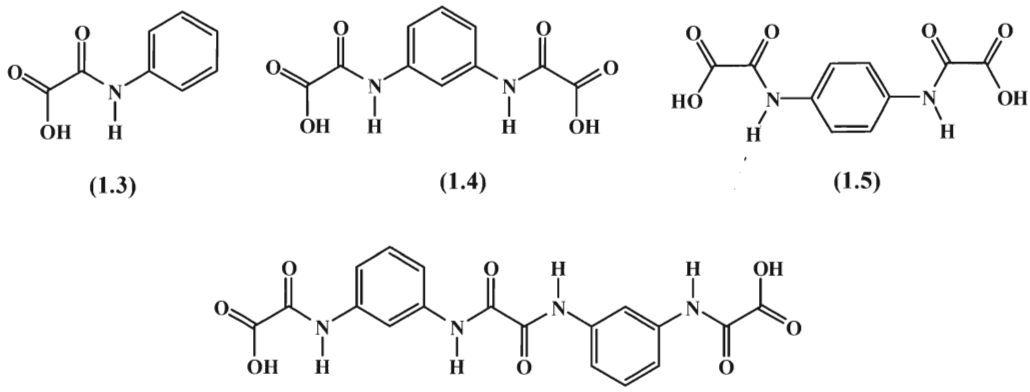

(1.3) (1.4) (1.5)

(1.6)

Figure 1.12. Oxamato ligands of different coordination modes: **a**) monodentate **(1.3)**, **b**) bidentate **(1.4)** and **(1.5)** and **c**) linear tridentate **(1.6)**.

The coordination chemistry of these ligands with selected divalent transition ions (M^{2+} = Cu, Ni, and Co) has been investigated.[35] It was found that oxamato ligands coordinate these metal ions through their amidate-nitrogen and carboxylate-oxygen donor atoms. For example, the coordination of ligands **(1.4)** and **(1.5)** with two equivalents of Cu(II) ions resulted in the formation of the two double-stranded $Cu(II)_2$ complexes **(1.7)** and **(1.8)** with S = 1 and S = 0 ground states respectively, Figures 1.13 (a) and (b).[37] Coordination of ligand **(1.6)** together with three equivalents of Cu(II) affords the linear trimetallic complex **(1.9)** with an S = 3/2 ground state, Figure 1.13c. These compounds demonstrate how spin control in metal complexes can be tuned via the topology of the bridging ligand. In this respect, the square-planar copper(II)-*bis*(oxalamide) moieties serve as spin-containing units, while the two meta-substituted phenylene spacers (in complexes **(1.7)** and **(1.9)**) act as a ferromagnetic coupling unit (FCU), Figure 1.13 (d).[37] This results in ferromagnetic exchange interactions between neighbouring metal centres

that propagate along the linear chain of metal ions where the intermetallic distances are in the range of 0.7–1.5 nm.[37]

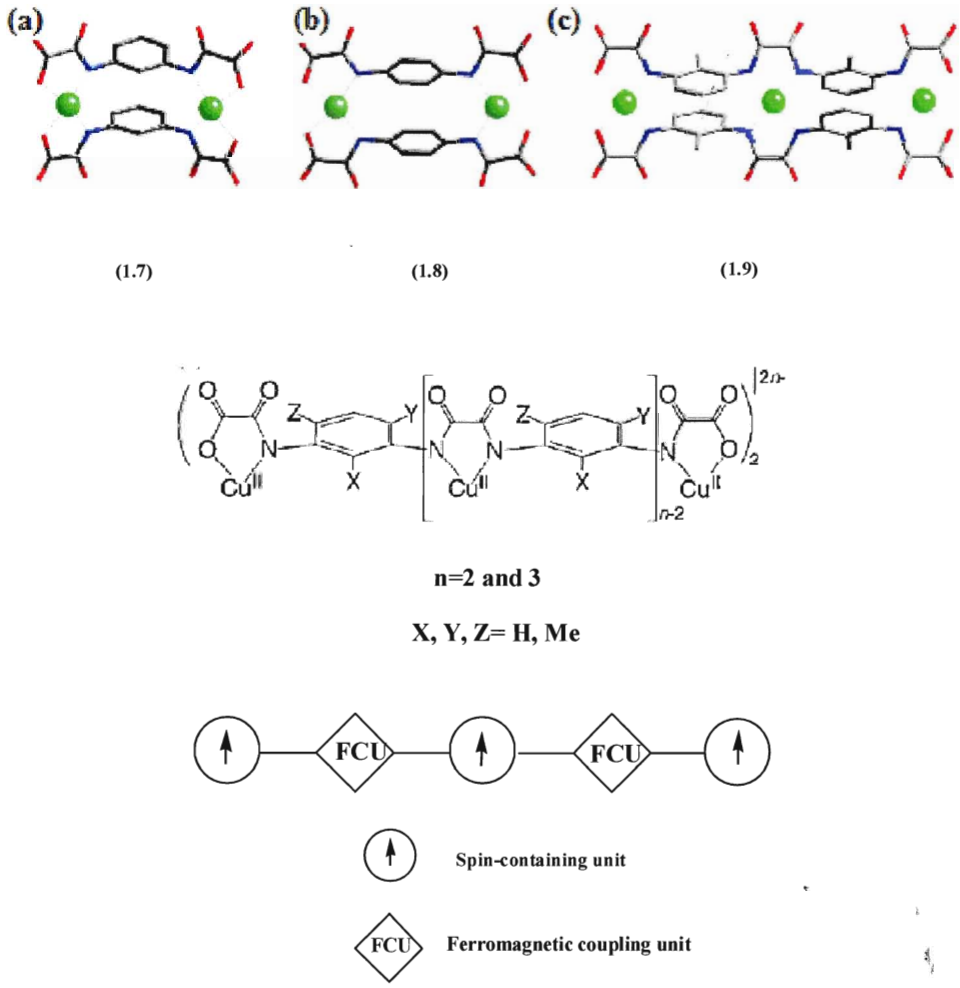

Figure 1.13. (a) Structure of the double-stranded $Cu(II)_2$ complex **(1.7)**. (b) Structure of the double-stranded $Cu(II)_2$ complex **(1.8)**. (c) Structure of the double-stranded $Cu(II)_3$ complex **(1.9)**. (d) Spin coupling model for the $Cu(II)_n$ oxamato complexes **(1.7)**, **(1.8)** and **(1.9)**, (n = 2, 3).[37] "Reprinted with permission from reference 37. Copyright {2007} American Chemical Society."

Oxamato-containing metal complexes can also coordinate a second metal ion via their two available *cis* carbonyl oxygen atoms. For example, coordination of the double-stranded $Cu(II)_2$ complexes **(1.7)** and **(1.8)** together with additional Cu(II) ions resulted in formation of complexes **(1.10)** and **(1.11)** respectively. These materials both exhibit "dimer-of-trimers" ladder-like structures, Figure 1.14. Here, the nature of the ground state spin can be interpreted based on the concept of antiferro- (ACU) and ferromagnetic coupling units (FCU) which was earlier used to control the spin state of organic polyradicals.[36] Thus, the $Cu(II)_2$ meta- and para- phenylene cores act as FCU and ACU, respectively, between the two $Cu(II)_3$ linear entities leading to either triplet or singlet ground states for the $Cu(II)_6$ molecules.[37]

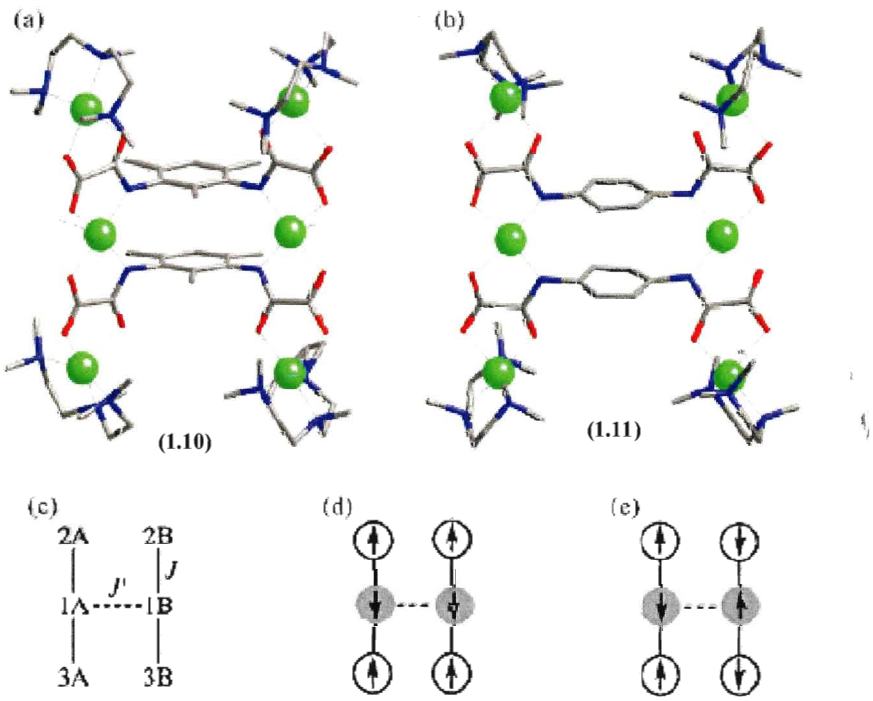

Figure 1.14. a) Dimer of trimer ladder like structures of **(1.10)** and (b) **(1.11)**. (c) Spin coupling scheme and spin topologies for the $Cu(II)_6$ complexes **(1.10)** and **(1.11)** with $J < 0$ and either (d) $J' > 0$ or (e) $J' < 0$.[38] "Reprinted with permission from reference 38. Copyright {2004} American Chemical Society."

1.2.2 Carboxamide ligands

Amide bonds or groups are most recognized as providing the linkage between amino acid residues in proteins. Carboxamide ligands are a class of amides with the general formula R-CO-NH_2 (where R = an aryl substituent such as Ph or pyridine), Figure 1.15. Carboxamides contain both O and N binding sites and as a result, possess different ligation modes. They can behave as neutral, mono- or dianionic ligands and have been pursued to-date for applications in asymmetric catalysis,[39] for the synthesis of dendrimers[40], as molecular receptors,[41] as well as for the preparation of platinum (II) complexes with antitumor properties.[42]

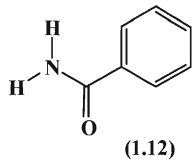

(1.12)

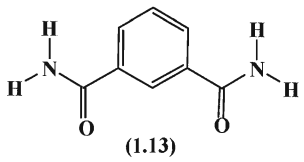

(1.13)

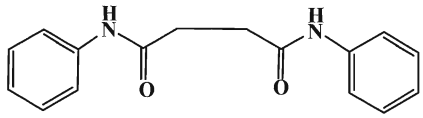

(1.14)

Figure 1.15. Three examples of carboxamide ligands.

Amides are formed via the condensation reaction of a carboxylic acid with an amine.[43] The ease of synthesis enables polydentate carboxamides with variable arrays of metal binding sites to be prepared. The neutral amide structure has two resonance forms, Figure 1.16. Due to the 40% double bond character of the carbon-nitrogen bond, rotation around this bond is restricted and the *trans* form is strongly favoured. The amide unit is therefore considered to be a planar and rigid structure. The C-N and C-O bonds possess comparable amounts of single and double bond character.[44]

Figure 1.16. Resonance forms of the amide group.

The coordinating properties of amides including carboxamides were thoroughly reviewed in 1981 by Sigel and Martin.[45] In the absence of metal ions the amide group is neutral. Complexation of a neutral amide generally occurs at the amide oxygen. Upon complexation of a neutral amide, the C-O bond becomes longer and weaker and the C-N bond becomes shorter and stronger. Both experimental and theoretical studies support increased double bond character in the C-N bond upon metalation at the amide oxygen.[45] In contrast to this, metalation of the neutral amide N weakens the C-N bond and reduces its barrier to rotation. The modes of binding in carboxamides can be controlled in some cases by the reaction conditions. In basic medium, the amide NH is deprotonated and metal ion coordination occurs through the amide anion.[45]If the conditions are slightly acidic, binding occurs through the carbonyl O atom.[46] First row transition metal ions facilitate the deprotonation of N bound amides in solution. The planarity of the amide functionality is maintained through deprotonation.[45] When compared to neutral amide groups, substitution of an amide proton by a metal ion disrupts the amide resonance, bond length changes are in the direction of more double bond character in the C-N bond and less double bond character in the C-O bond, i.e. going towards (II) in Figure 1.16. It should however be emphasized that both the C-O and C-N bonds still possess appreciable amounts of double bond character before and after substitution of a metal ion. These changes in bonding are well reviewed in the literature.[45] Important features of

carboxamide ligands include: (i) good σ-donor properties of the coordinated nitrogen (when deprotonated); (ii) ability of the ligands to stabilize metals in high formal oxidation states; (iii) low chemical reactivity of the amide bond and (iii) their ease of synthesis. From this class of ligands, pyridine carboxamides have been widely exploited as ligands in the field of metallosupramolecular chemistry, Figure 1.17.[45] This is due to their ability to participate in the self-assembly process forming molecular architectures that are stabilized via coordinate and hydrogen bonding interactions. In contrast to the previously discussed organic ligands, pyridine carboxamides have yet to be exploited by the molecular magnetism community.

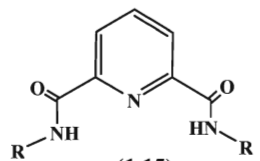

(1.15)

Figure 1.17. General structure of a pyridine carboxamide ligand (where R = H, alkyl, aryl).

The coordination complexes of pyridine carboxamide ligands **(1.16)** and **(1.17)** have been exploited as catalysts for the Beckmann rearrangement and the Lewis metal ion assisted Strecker reaction.[47]

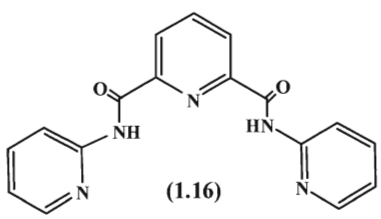

(1.16)

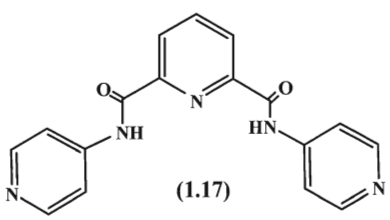

(1.17)

Figure 1.18. Molecular structure of ligands **(1.16)** and **(1.17)**.

Coordination of deprotonated **(1.16)** and **(1.17)** to Co (II) affords octahedral complexes **(1.18)** and **(1.19)** where the ligands chelate through their pyridine and amide N´s in a tridentate manner. The molecular structures of complexes **(1.18)** and **(1.19)** have been determined by X-ray crystallography, Figure 1.19.

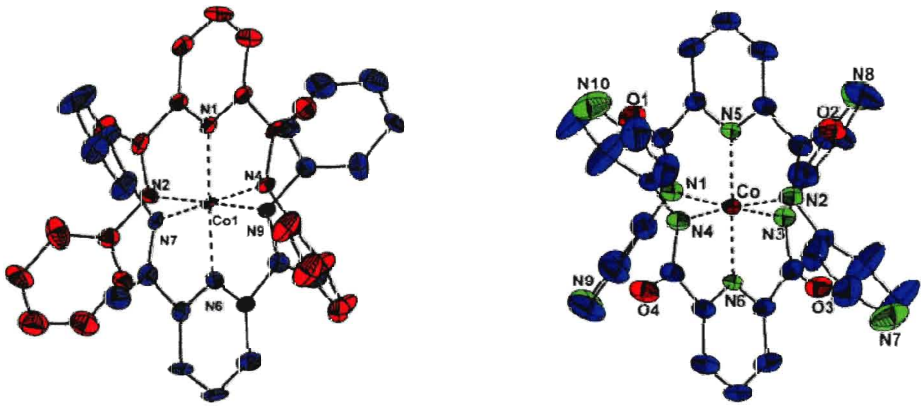

(1.18) **(1.19)**

Figure 1.19. Molecular structures of complexes **(1.18)** (left) and **(1.19)** (right).[47a] "Reprinted with permission from reference 47a. Copyright {2008} American Chemical Society."

Four of the pyridine rings of these ligands remain uncoordinated and so are available for coordination to a second metal ion. Following this strategy, reaction of **(1.18)** and **(1.19)** with Zn(II) affords the two heterometallic complexes **(1.20)** and **(1.21)**. The molecular structure of complex **(1.20)** reveals two Zn(II) ions coordinating to the hanging pyridine rings, Figure 1.20. Zn1 is coordinated further to two Cl^- anions, and Zn2 is coordinated to one Cl^- ion and to one DMA (dimethylacetamide) molecule affording a neutral complex.

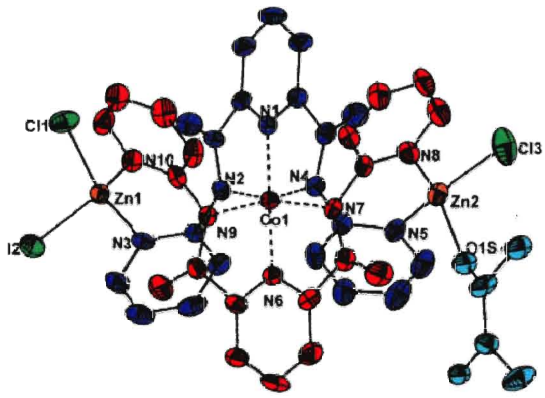

(1.20)

Figure 1.20. The molecular structure of the bimetallic complex **(1.20).** [47a] "Reprinted with permission from reference 47a. Copyright {2008} American Chemical Society."

In contrast, the coordination of complex **(1.19)** with Zn(II) resulted in the assembly of a 2-D network **(1.21)**, facilitated by the open nature of the pyridine arms, Figure 1.21.[47b] This network is comprised of six **(1.19)** building blocks which are connected *via* Zn^{2+} ions to form a hexagonal ring (Figure 1.21 (a), (b)) with two different geometrical environments for the Zn^{2+} ions. A honeycomb-shaped 2-D sheet interacts further with an adjacent 2-D sheet *via* H-bonding interactions between coordinated water molecules and the N(10) atom of the uncoordinated pyridine ring, affording a tubular structure running along the *c*-axis of the unit cell, Figure 1.2 (c). The interior of this tubular structure is filled with solvent water and nitrate anions.

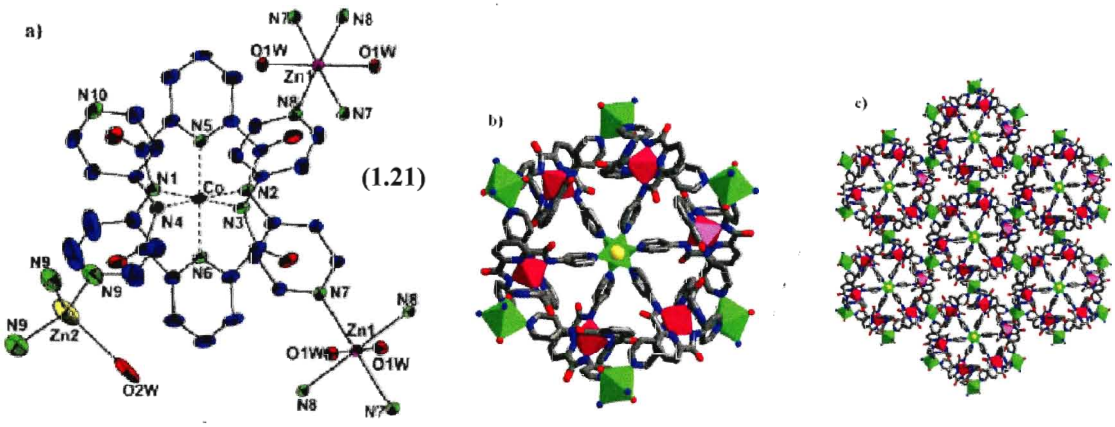

Figure 1.21. View of (a) molecular structure of **(1.21)** with partial numbering; thermal ellipsoids are drawn at 50% probability; (b) hexagonal structure resulting from the coordination of **(1.19)** building blocks to Zn^{2+} ions; (c) the assembled 2-D network, along the *c*-axis.[47b]- Reproduced by permission of the Royal Society of Chemistry (RSC).

Coordination of **(1.16)** with protonated pendant pyridine nitrogen atoms, together with Cu (II) ions affords a series of complexes whose formation is dictated by the reaction conditions. Reaction of **(1.16)** with one equivalent of $CuCl_2$ in the absence of base afforded the monomeric complex **(1.22)**. In this structure, both of the pyridyl nitrogen's are protonated. The molecular structure of this complex shows that the Cu(II) ion adopts a distorted trigonal bipyramidal geometry, Figure 1.22.

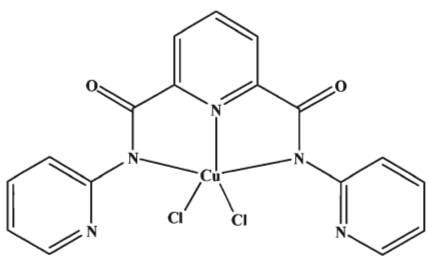

(1.22)

Figure 1.22. Molecular structure of complex **(1.22)**.[48] "Adapted from figure 5 of reference 48."

By changing the reaction conditions, using sodium hydride as the base and copper(II) tetrakis(pyridine) perchlorate as the metal salt, a second complex **(1.23)** was obtained, Figure 1.23.[49] The molecular structure of this complex reveals the formation of a dimer where two ligands are coordinated to two Cu(II) ions. The geometry around the Cu(II) ions is square pyramidal. Each Cu(II) is chelated to the nitrogen atoms of the central pyridine rings [N(10), N(10A)] and the deprotonated carboxamide groups [N(7), N(16), N(7A), N(16A)] of one **(1.16)** ligand, a pyridyl nitrogen atom [N(1A)] from the other **(1.16)** ligand in the dimer, and a water molecule, Figure 1.23. All four amide groups are planar. The C-O bond lengths range from 1.244 to 1.252 Å and the C-N bond lengths from 1.323 to 1.333 Å. The C-N bond lengths are 0.4 Å shorter in the complex when compared with the uncomplexed ligand whose structure has also been elucidated by X-ray crystallography. This is consistent with the view that upon chelation through the amide N, the amide resonance is disturbed and bond length changes are in the direction of more double bond character in the C-N bond and less double bond character in the C-O bond.[45]

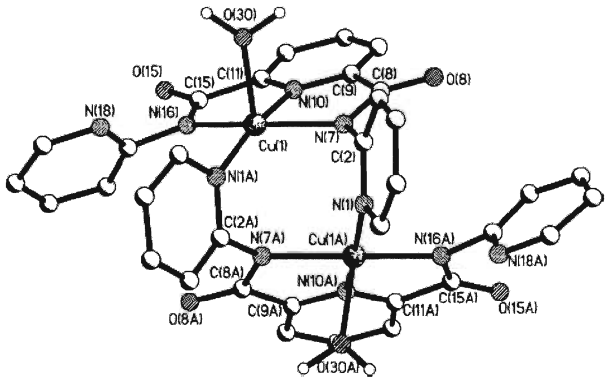

(1.23)

Figure 1.23. ORTEP plot of the molecular structure of **(1.23)**·$2H_2O$.[49]- Reproduced by permission of the Royal Society of Chemistry (RSC).

Bimetallic species of **(1.16)** with platinum(II) and palladium (II) have also been prepared and characterized, Figure 1.24.[50]

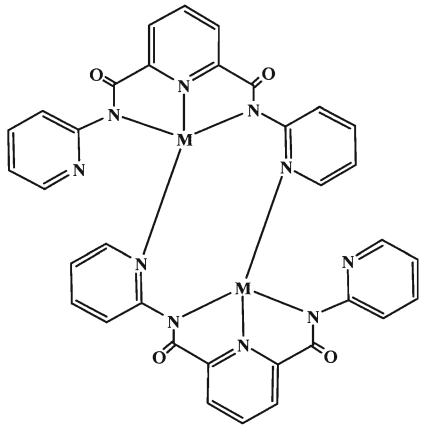

(1.24, 1.25)

Figure 1.24. Structure of dimeric complexes **(1.24)** M= Pt and **(1.25)** M=Pd. "Adapted from reference 50."

Mass spectroscopy showed a fragment consistent with the dimeric structures **(1.24)** and **(1.25)**, respectively. The IR spectrum contains two C=O stretching frequencies at 1644 and 1614 cm^{-1} for **(1.24)**, and 1642 and 1608 cm^{-1} for **(1.25)**. This is consistent with the complexes containing two non-equivalent amide groups. The molecular structure of the Pd complex determined by X-ray crystallography confirms the structural assignments of the mass and IR spectroscopic data.

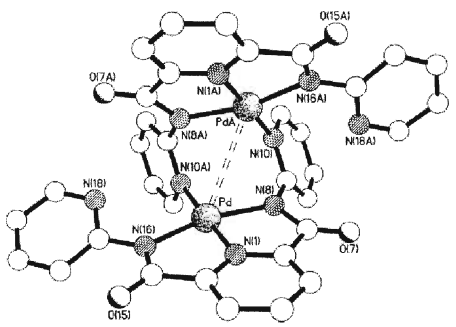

(1.25)

Figure 1.25. Molecular structure of compound **(1.25).**[50]- Reproduced by permission of the Royal Society of Chemistry (RSC).

The ligand coordinates in a binuclear bridging mode, Figure 1.25. The central 8-membered $C_2N_4Pd_2$ ring adopts a distorted boat-like conformation. The coordination geometry around the Pd(II) is distorted square planar.

Ligand **(1.17)** has been reported to form a second palladium complex **(1.26)** on coordination with Pd(dppm), where dppm = $PPh_2PCH_2PPh_2$. The molecular structure of complex **(1.26)** comprises an approximately square shaped 32-membered ring.[51] Two palladium ions chelate to the dppm ligands, Figure 1.26.

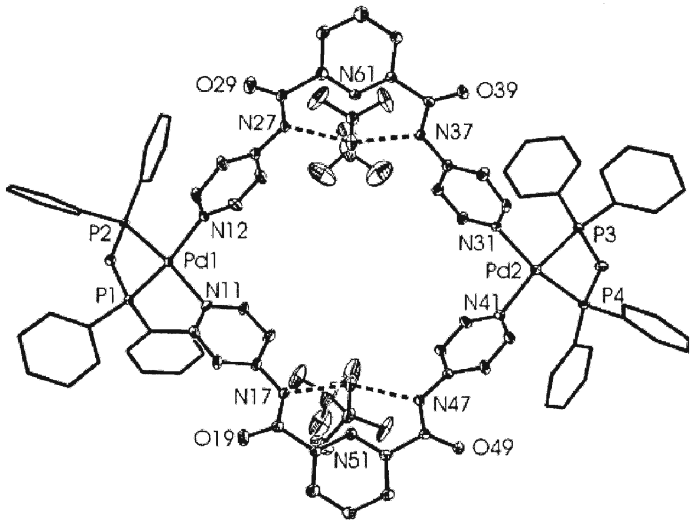

(1.26)

Figure 1.26. Top view of the "square" structure of the cationic complex **(1.26)**, with hydrogen bonding to two triflate anions.[51]"Reprinted with permission from reference 51. Copyright {2003} American Chemical Society."

In addition to monomeric and dimeric compounds, as well as networks, ligand **(1.17)** can also form clusters. Reaction of $AgNO_3$ with 0.5 equivalents of **(1.17)** in a (1:4:1) mixture of THF/DMF/H_2O, leads to the formation of cluster **(1.27)** containing four ligands and ten Ag^{2+} ions, Figure 1.27 (a). X-ray crystallography reveals that the main unit of this cluster has a crown-like architecture, Figure 1.27 (b).[52]

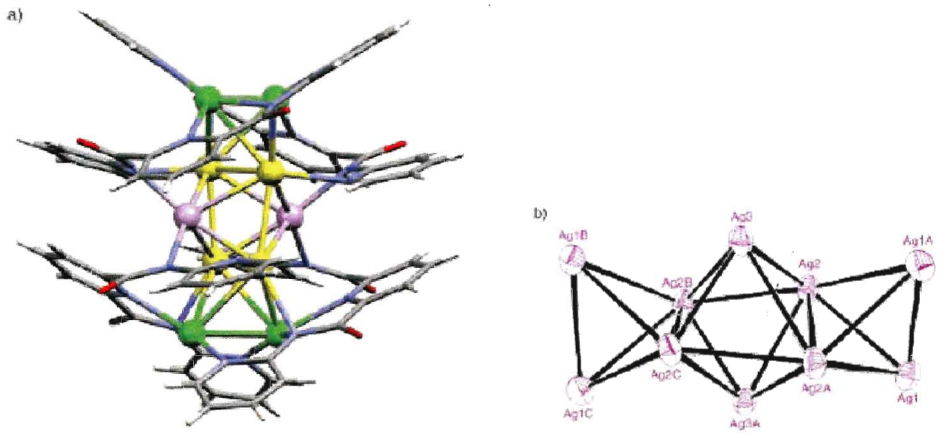

(1.27)

Figure 1.27. a) Molecular structure of **(1.27)**. b) Arrangement of the 10 silver atoms.[52] Reproduced with permission from reference 52. Copyright 2005 Wiley-VCH.

The tetra nuclear cluster **(1.28)** has also been prepared from ligand **(1.17)** together with $Zn(OAc)_2 \cdot 6H_2O$, Figure 1.28. This cluster comprises of three **(1.16)** ligands and four Zn(II) ions assembled around a central oxygen atom. Five N atoms of each ligand coordinate to three Zn ions.[52]

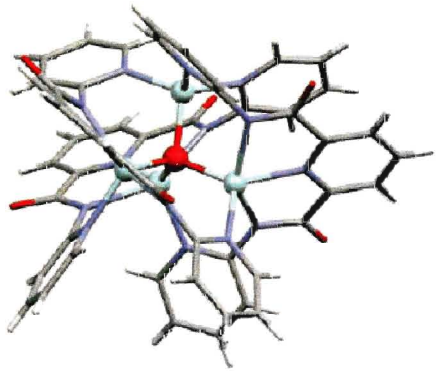

(1.28)

Figure 1.28. Molecular structure of **(1.28)**. [52] Reproduced with permission from reference 52. Copyright 2005 Wiley-VCH.

Finally, the tripyridyl tricarboxamide ligand **(1.29)**, Figure 1.29, affords a 2-D coordination polymer **(1.30)** with $AgPF_6$. The core unit of this polymer is shown in Figure 1.30 (a).[53]

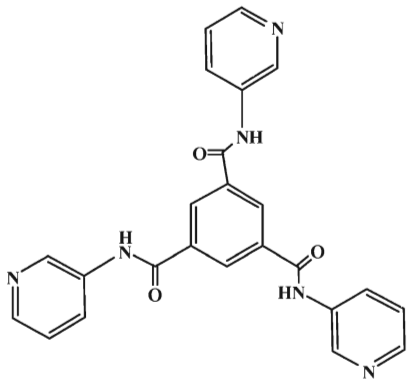

(1.29)

Figure 1.29. Molecular structure of tridentate bridging ligand **(1.29)**.[53] Reproduced by permission of the Royal Society of Chemistry (RSC).

48-Membered macrocycles are constructed from trigonal planar Ag(I) ions as connectors and three **(1.29)** ligands propagated into 2-D extended structures, Figure 1.30 (b). The Ag(I)···π interactions facilitate the formation of an inter-sheet dimeric structure, Figure 1.30 (c). PF_6^- anions and DMF solvent molecules occupy the interstices between the dimerized sheets.

(a)

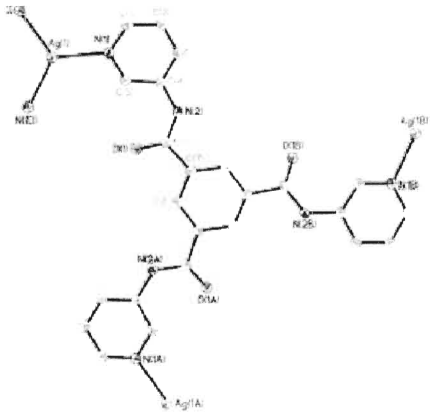

(1.30)

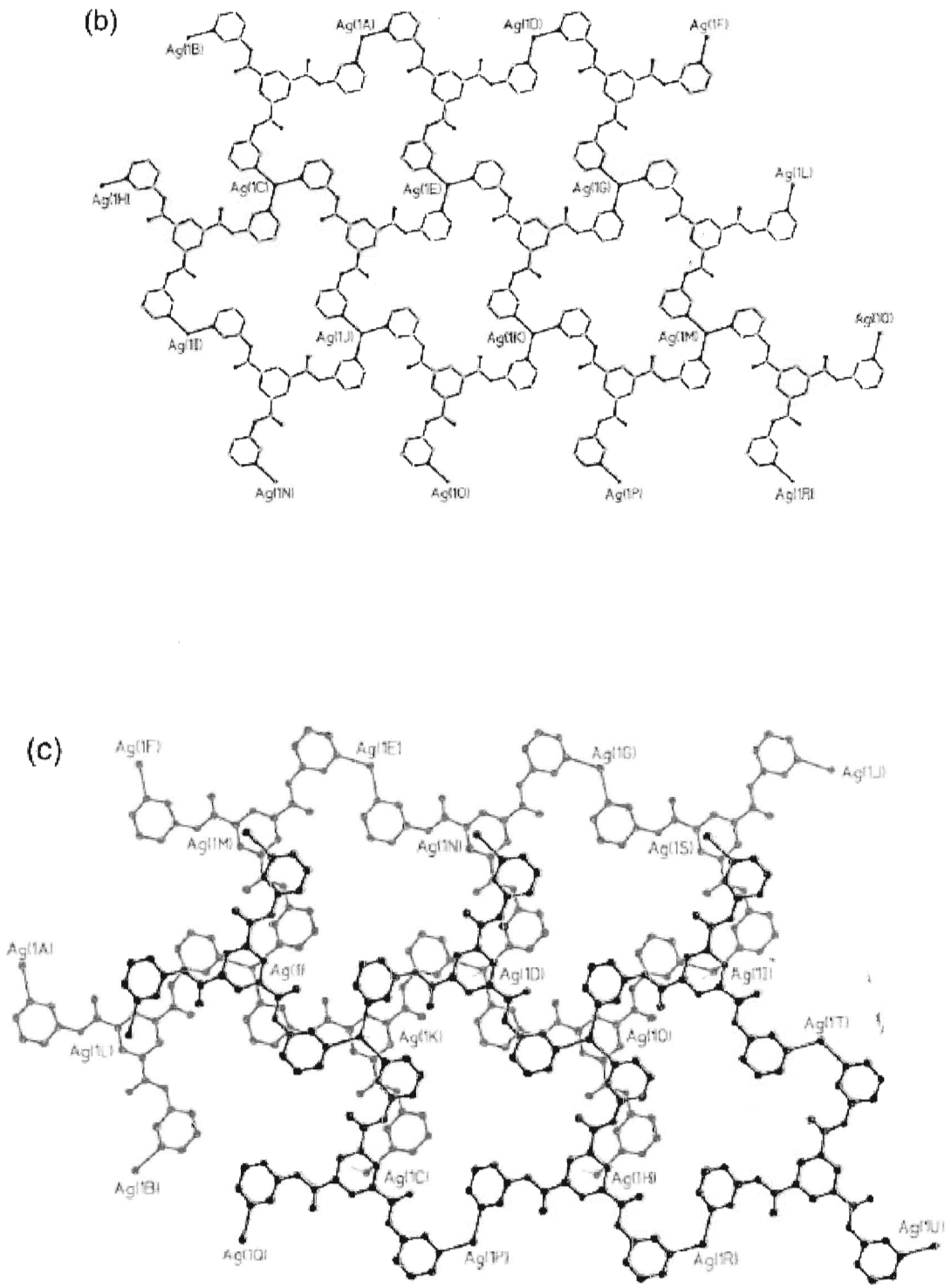

Figure 1.30. a) Molecular structure of the core of polymer **(1.30)**. b) The 2-dimensional extended framework, solvent molecules omitted for clarity (view down the *c*-axis). c) The inter-sheet dimeric structure.[53] Reproduced by permission of the Royal Society of Chemistry (RSC).

1.3 Conclusion

This review highlights how simple organic ligands have been exploited in the field of molecular magnetism and demonstrates the versatility of carboxamide ligands in the field of metallosupramolecular chemistry. It seems reasonable to expect that new families of polydentate carboxamide ligands together with appropriate transition metal ions will afford interesting architectures that could lend themselves to a number of applications that include the preparation of new molecular magnets.

CHAPTER 2

Preparation and Coordination Chemistry of a New Family of Bipyridine Carboxamide Ligands

Multitopic ligands with two or more discrete metal binding domains separated by spacers are key building blocks in synthetic chemistry and materials science.[22] The objectives of this project are the synthesis and characterization of novel multitopic carboxamide ligands for the assembly of multinuclear complexes for potential applications in the field of molecule-based magnetic materials. The versatility of pyridine carboxamide ligands for the preparation of a wide range of multinuclear complexes with various size has been reviewed in the previous chapter. The preparation of carboxamide ligands with 4,4'-bipyridine backbones or spacers and their coordination compounds have yet to be studied and evaluated with respect to their usefulness as building blocks for molecule-based magnets.

2.1 Design and Preparation of new carboxamide ligands

The short term objectives of this project were to functionalise 4,4′-bipyridine by adopting a ligand design strategy, introducing substituents into the *ortho* positions of the bipyridine rings. In this respect, 4,4'-bipyridine **(2.1)** was chosen as it has previously been successfully employed as an organic spacer in supramolecular chemistry, Figure 2.1.[49] In principle, the pyridine groups of the bipyridine can rotate along the central C-C bond, but as this rotation does not affect the mutual orientation of the two lone pairs, 4,4'-bipyridine is regarded as a "rigid bridging ligand" or "rigid scaffold".

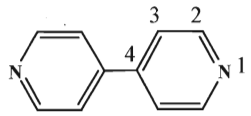

(2.1)

Figure 2.1. Molecular structure of 4,4′-bipyridine **(2.1)**.

The literature precedence for this work came from studies of the related pyridyl systems which were prepared and characterized in 2004 by Woollins *et al.* Scheme 2.1.[49]

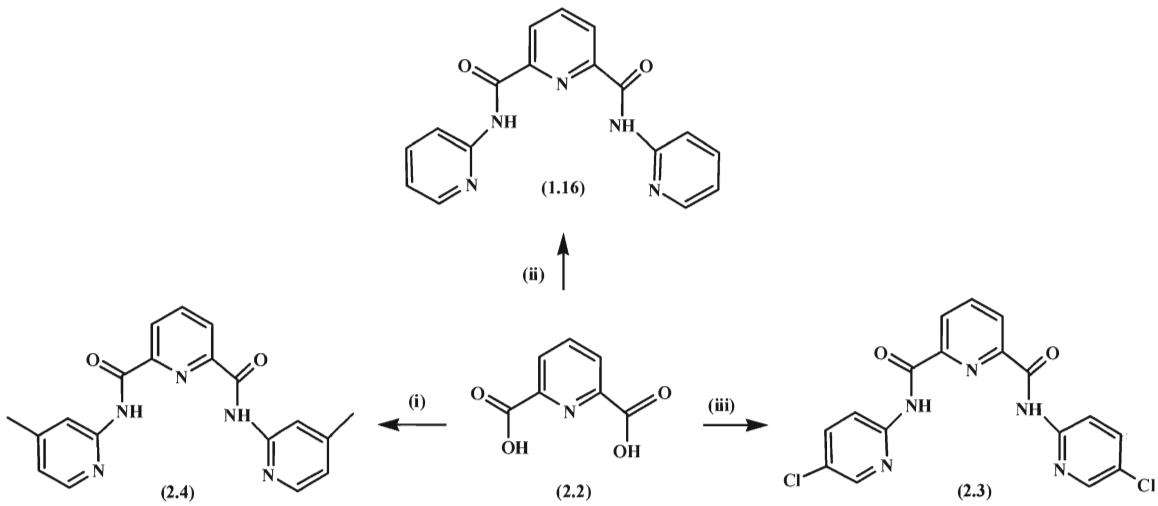

Scheme 2.1. Three examples of polydentate pyridine dicarboxamide ligands prepared via the condensation of pyridine-2,6-dicarboxylic acid with (i) 2-amino-4-methyl pyridine; (ii) 2-amino pyridine and (iii) 2-amino-5-chloropyridine.[49]

Since the pyridine systems afforded a number of new and interesting coordination compounds and structural information was available regarding the coordination preferences of their binding domains, we proposed to prepare the bipyridine derivatives which offer additional binding pockets for the chelation of transition metal ions. Following this strategy, three new polydentate 4,4′-bipyridine ligands **(2.6)** , **(2.7)** and **(2.8)** were prepared and characterized, Figure 2.2. Ligand **(2.6)** was problematic due to its

poor solubility in organic solvents. Ligands **(2.7)** and **(2.8)** had improved solubilites and the coordination chemistry of these ligands with first row transition metal ions was investigated. Our long term goal is to use ligand design to gain control over the distance and vectorial properties of the ligands. By introducing different substituents into the *ortho* positions of the 4,4′-bipyridine rings, we can change the coordination preferences of the binding domains which will in turn alter the solid state structures and physical properties of the complexes.

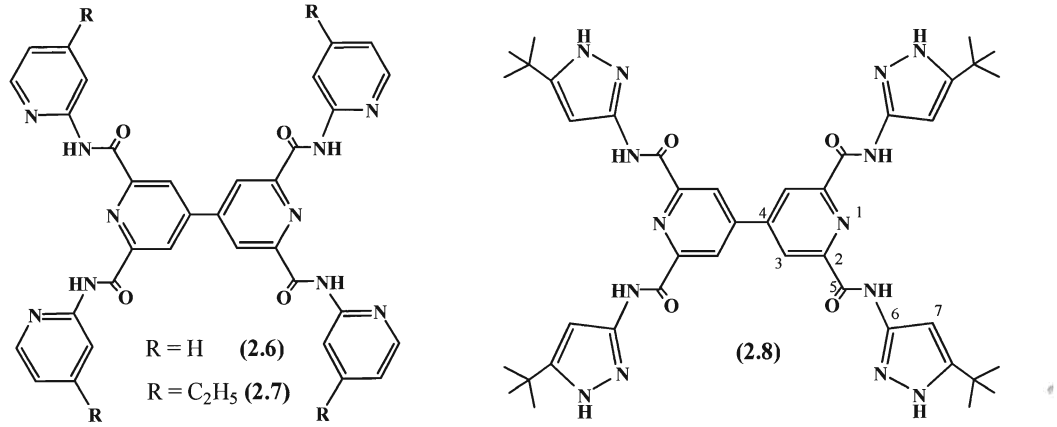

Figure 2.2. Molecular structures of ligands **(2.6-2.8)**.

All three carboxamide ligands were prepared via a modification of a literature procedure reported for the preparation of their pyridine analogues.[45] This general method involves refluxing 2,2',6,6'-tetra(chloroformyl)-4,4'-bipyridine **(2.5)** together with the appropriate amine overnight in toluene, Scheme 2.2.

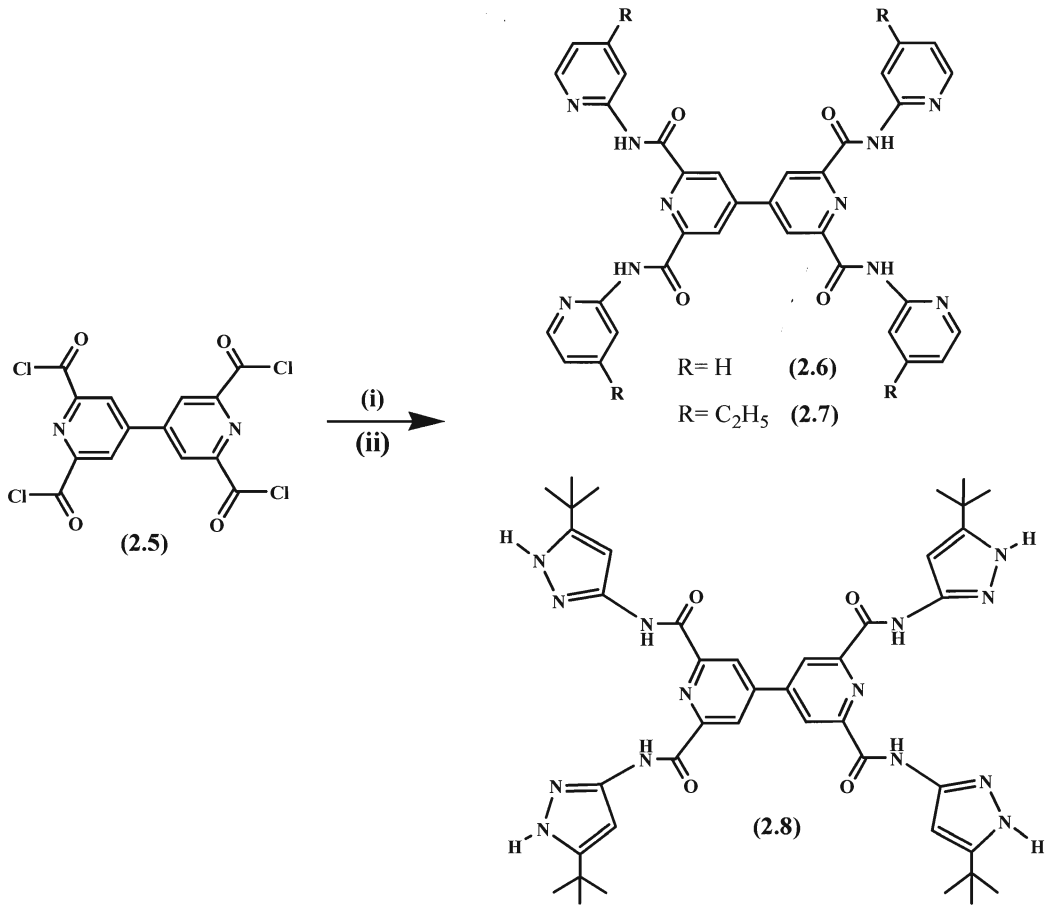

Scheme 2.2. Synthetic route for the preparation of carboxamide ligands **(2.6-2.8)**. **Reagents and conditions:** (i) 2- aminopyridine for ligand **(2.6)**, 4-ethyl-2-aminopyridine for ligand **(2.7)**, or 3-amino-5-tert-butyl pyrazole for ligand **(2.8)** (ii) reflux in toluene overnight.

The starting compound, 2,2',6,6'-tetrachloroformyl-4,4'-bipyridine **(2.5)** was prepared in four steps from commercially available 2,6-dimethylpyridine, **(2.9)**, Scheme 2.3.[54]

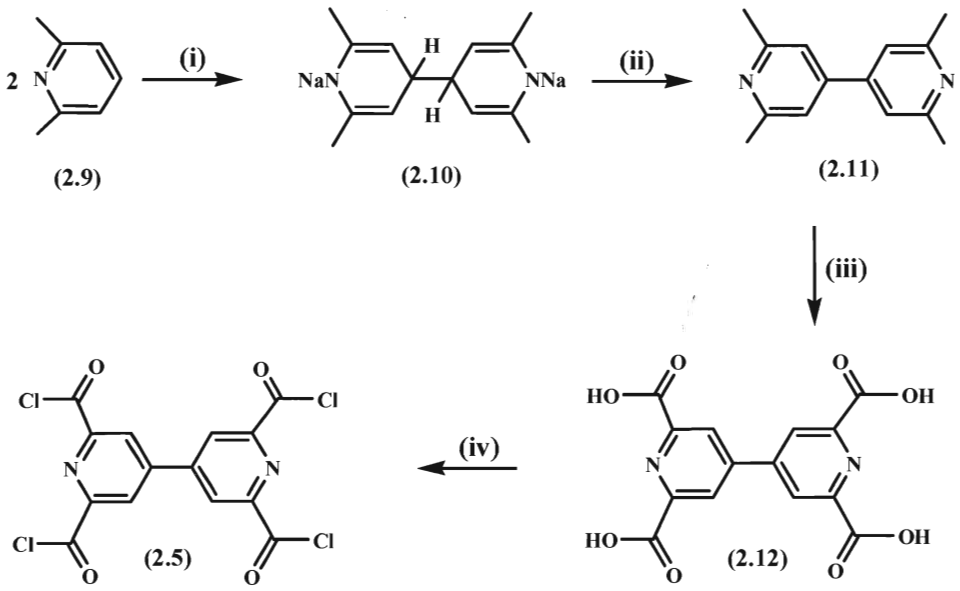

Scheme 2.3. Synthetic route for the preparation of 2,2',6,6'-tetrachloroformyl-4,4'-bipyridine **(2.5)**.[54]

Reagents and conditions: (i) Na/THF (ii) SO_2 (iii) CrO_3/conc. H_2SO_4 (iv) $SOCl_2$, DMF, reflux, 4 h.

During the course of this project, it has became apparent that the tridentate O-N-O binding mode of the tetra-acid **(2.12)** is now being exploited by research groups for the self-assembly of metal organic frameworks.[55] These materials have been shown to reversibly and selectively absorb small organic molecules such as H_2 and methane into the pores of their frameworks.[55]

2.2 Preparation and characterization of ligand (2.6)

Following the strategy presented in Scheme 2.2, ligand **(2.6)** was isolated as a pale yellow crystalline solid in 63% yield. The ^1H NMR spectrum of **(2.6)** is shown in Figure 2.3 and provides strong support for the successful synthesis of this compound. The amide NH proton is observed as a broad singlet downfield at 11.36 ppm. Taking into consideration the symmetry of the molecule, the singlet at 8.99 ppm is assigned to the C_3 protons of the 4,4'-bipyridine rings. The two doublets at 8.62 and 8.44 ppm are assigned

to the C_7, and C_{10}, protons respectively. The two triplets at 7.89 and 7.19 ppm are consistent with the protons at the C_8 and C_9 positions, respectively.

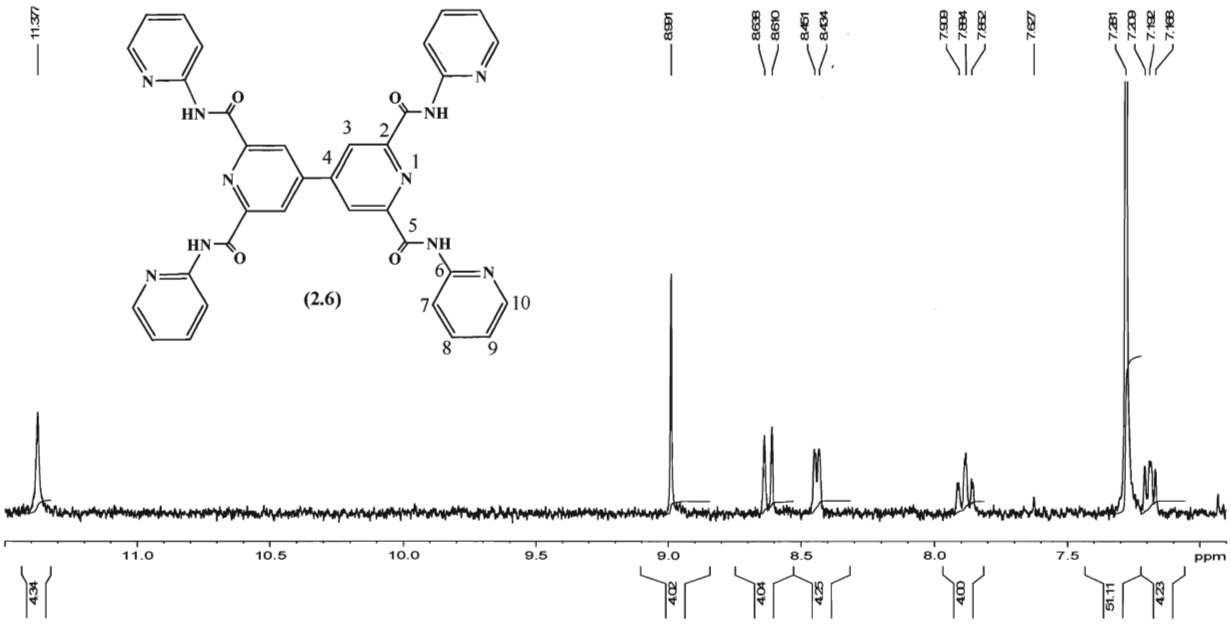

Figure 2.3. 300 MHz ^{1}H NMR spectrum of ligand **(2.6)** in $CDCl_3$.

The ^{13}C NMR of **(2.6)** is shown in Figure 2.4. The peak at 161.3 ppm is characteristic for the amide C=O. The five peaks at 151.4, 114.7, 123.4, 120.2, and 148.1 ppm are assigned to the five carbons (C_6-C_{10}) of the appended pyridine ring. The peaks at 150.1, 147.7 and 138.9 ppm are assigned to the bipyridine carbons at C_2, C_4 and C_3 positions respectively.

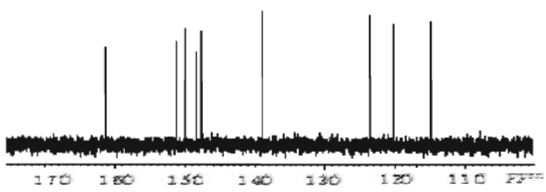

Figure 2.4. 150 MHz ^{13}C NMR spectrum of ligand **(2.6)** in $CDCl_3$.

The IR spectrum of ligand **(2.6)** displays the characteristic bands for an aromatic secondary amide. At 3455 cm^{-1} a broad band of medium intensity is observed and assigned to the amide NH stretching vibration. Other N-H bands (bendings and deformations) are located within the fingerprint region of the IR spectrum. An intense singlet at 1692 cm^{-1} is assigned to the Amide I [υ C=O]. A second band of weaker intensity is observed at 1524 cm^{-1} and assigned to the lower frequency Amide II band, which is considered to be a combination of C-N str and N-H bending *trans* to the carbonyl oxygen. A medium intensity band at 1227 cm^{-1} is assigned to the C-N str of the amide and is consistent with reported values for related pyridine amide ligands.[56] The high resolution FAB mass spectrum of the ligand, is consistent with its molecular structure, showing a parent ion at m/z = 637.20156 $[MH]^+$. Finally the elemental analysis data is within the acceptable ± 0.4 % limit for $C_{34}H_{24}N_{10}O_4$. Due to the poor solubility of this ligand, its coordination chemistry was problematic, so the decision was made to focus efforts on functionalizing the ligand in order to improve its solubility.

2.3 Preparation and characterization of ligand (2.7)

In this respect, ethyl groups were introduced into the *para* positions of the four pendant pyridyl rings. As expected, the ethyl groups afforded a slight increase in the solubility of the ligand. The modified ligand **(2.7)** was obtained following the same general procedure outlined in Scheme 2.2. The ligand was isolated as a pale yellow crystalline solid in 65% yield.

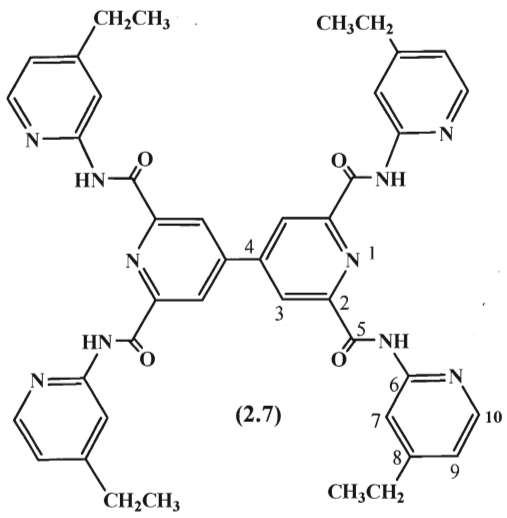

Figure 2.5. Molecular structure of ligand **(2.7)** with appropriate numbering scheme.

The ^{1}H NMR spectrum of the ligand, as expected, is very similar to that of **(2.6)** with additional peaks for the ethyl CH_2 and CH_3 protons at 2.80 and 1.36 ppms, respectively. The ^{13}C NMR spectrum has a peak at 161.2 ppm consistent with the amide carbonyl. Eight peaks between 156.4 and 114.0 ppm are once again consistent with the aromatic bipyridine and pyridine carbons. Two additional peaks at 28.7 and 14.4 ppm are assigned to the ethyl CH_2 and CH_3 carbons. The IR spectrum of **(2.7)** also contains very similar bands to the previous ligand. Above 3000 cm^{-1} a sharp band is present at 3377 cm^{-1} characteristic of an amide N-H str. A second broader band visible at 3270 cm^{-1} is assigned to the amide groups that are participating in hydrogen bonding interactions. H-bonding interactions involving amide groups broaden and lower their N-H stretching frequencies in the IR. The Amide I [υ C=O] band is visible at 1691 cm^{-1} and the Amide II band is present at 1527 cm^{-1}.[56] The direction and magnitude of the frequency of the Amide I and Amide II bands has often been used to determine the protonation state and mode of bonding in amides when X-ray data was not available. In recent years, however, it has

become apparent that this method is not reliable for the assignment of coordinated amides with complex spectra where two or more amide groups per molecule might not necessarily have the same vibrational modes. Furthermore, the bands of other functional groups in the complex often mask the Amide II band. The absence of NH stretching bands above 3200 cm^{-1} does indicate whether or not the amide is protonated, which is a particularly useful assignment when the coordination chemistry was carried out in the absence of base.[55] The electronic spectrum of the ligand has an intense band at λ= 285 nm assigned to overlapping low energy n to π^* and π to π^* transitions.[49] The high resolution FAB mass spectrum of this ligand has an $[MH]^+$ parent ion peak at *m/z* = 749.32123. Suitable single crystals of **(2.7)** were obtained via the slow evaporation of a (1:1) $MeOH/CHCl_3$ solution of this ligand at room temperature. The molecular structure of **(2.7)** was elucidated by X-ray crystallography.

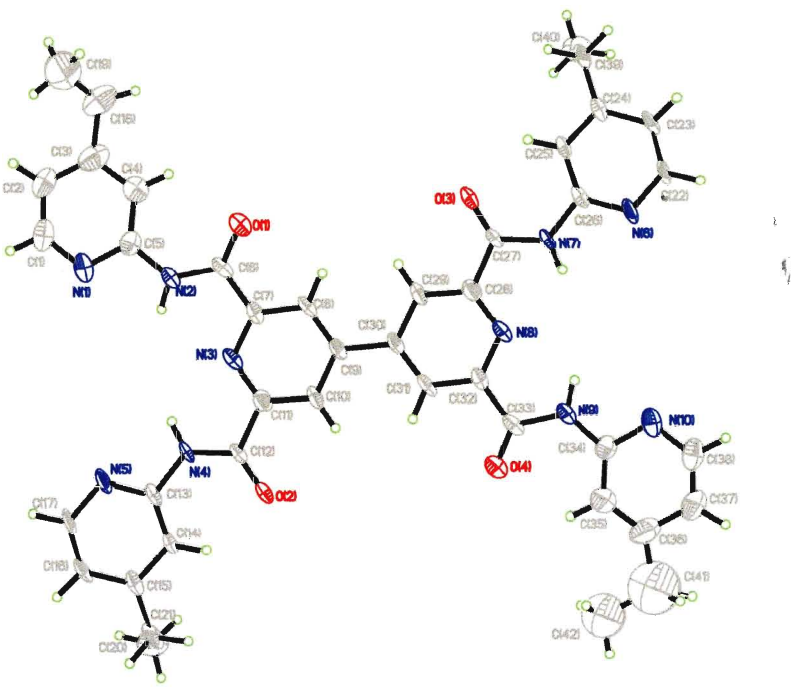

Figure 2.6. ORTEP[57] plot for the molecular structure of ligand **(2.7)** showing the numbering scheme.

The molecular structure of **(2.7)** together with the atom-numbering scheme is shown in Figure 6. Ligand **(2.7)** crystallizes in the triclinic space group P-1 with one independent molecule in the asymmetric unit. The two halves of the molecule are not symmetrical in the solid-state. The ethyl group at C(41) C(42) is disordered over two positions, but for clarity only one orientation is shown. Selected bond lengths and angles for this ligand are presented in Tables 2.1 and 2.2.

Table 2.1. Selected Bond Lengths [Å] for ligand (2.7).

N(3)-C(11)	1.336(15)	N(2)-C(6)	1.384(16)
C(10)-C(11)	1.405(18)	N(1)-C(5)	1.395(17)
C(9)-C(10)	1.371(17)	C(4)-C(5)	1.37(2)
C(9)-C(30)	1.516(18)	C(3)-C(4)	1.37(2)
C(8)-C(9)	1.387(17)	C(3)-C(18)	1.55(3)
C(7)-C(8)	1.394(17)	C(18)-C(19)	1.43(3)
N(3)-C(7)	1.337(15)	C(2)-C(3)	1.44(2)
C(6)-C(7)	1.491(17)	C(1)-C(2)	1.32(2)
O(1)-C(6)	1.210(14)	N(1)-C(1)	1.361(17)
N(2)-C(5)	1.386(16)		

Table 2.2. Selected Bond Angles [°] for ligand (2.7).

C(11)-N(3)-C(7)	117.3(10)	C(6)-N(2)-C(5)	127.8(11)
N(3)-C(11)-C(10)	123.0(12)	N(2)-C(5)-N(1)	111.7(11)
C(9)-C(10)-C(11)	119.4(12)	C(4)-C(5)-N(2)	125.0(13)
C(10)-C(9)-C(8)	117.9(11)	C(4)-C(5)-N(1)	123.2(13)
C(9)-C(8)-C(7)	119.5(11)	C(3)-C(4)-C(5)	121.0(16)
N(3)-C(7)-C(8)	123.0(11)	C(4)-C(3)-C(18)	119.9(17)
C(8)-C(9)-C(30)	120.8(11)	C(2)-C(3)-C(18)	122.8(16)
C(10)-C(9)-C(30)	121.3(11)	C(4)-C(3)-C(2)	117.3(14)
O(1)-C(6)-C(7)	122.5(12)	C(1)-C(2)-C(3)	117.0(15)
O(1)-C(6)-N(2)	123.4(12)	C(2)-C(1)-N(1)	129.1(16)
N(2)-C(6)-C(7)	114.0(10)	C(1)-N(1)-C(5)	112.4(11)

A summary of the crystallographic data including the structural refinement parameters for this ligand are presented in the appendix section of this thesis (Table 2.5 p.g. 214). The crystal structure of the neutral ligand reveals the carbonyl oxygen atoms are located *trans* to the pyridyl groups. The bipyridine ring and the amide group of the ligand are essentially co-planar. The C-N-C bond angles around the amide nitrogens are in the range 126.7°-127.9° and the sum of the angles around these nitrogens are very close to 360°. The amide C-N bond lengths are in the range of 1.33 - 1.40 Å which are about 0.5 Å shorter than the average C-N bond (1.45 Å). The amide C-O bond lengths range from 1.19-1.22 Å which are slightly longer than the average C=O bond length of 1.23 Å. These values are consistent with a conjugated amide and are comparable with the C-N and C-O bond lengths reported for the pyridyl analogue **(1.16)** reported by Woollins, Figure 2.7.[49]

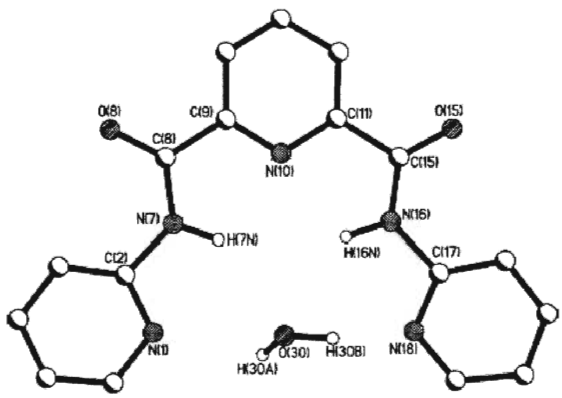

(1.16)

Figure 2.7. The molecular structure of N.N'-*bis*(2-pyridyl)pyridine-2,6-dicarboxamide showing the H-bound water in the coordination cavity.[49]- Reproduced by permission of the Royal Society of Chemistry (RSC).

As for the above pyridine ligand, the two pendant pyridyl nitrogens at both ends of **(2.7)** are facing towards the molecular cleft. In contrast to the co-planarity of the amide groups, the pyridyl rings are twisted out of bipyridine-amide plane by *ca.* 12°. This is fairly common in the structures of pyridine carboxamides and reflects a balance between the formation of an extended structure stabilized by H-bonding interactions and the preference for a resonance delocalized, fully conjugated planar structure. A single water molecule occupies each of the two coordination cavities at both ends of the molecule, Figure 2.8. These water molecules form weak H-bonds with the amide hydrogen atoms (O···H-N = 2.21 - 2.24 Å) and stronger H-bonds with the pendant pyridine nitrogen (N···H-O = 2.04 – 2.07 Å).

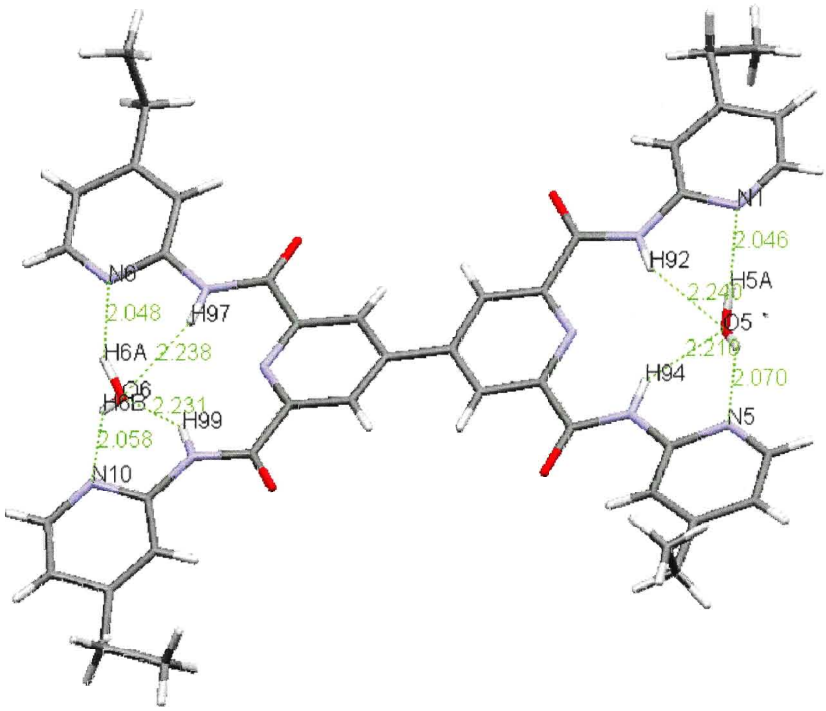

Figure 2.8. View of molecular structure of **(2.7)** showing the two coordinated water molecules. H-bonds are shown as green dashed lines and distances are given in Å.

The crystal packing of **(2.7)** reveals an offset arrangement of π-π stacked ligands with interplanar distances of 3.24 – 3.72 Å running along the *a*-axis of the unit cell, Figure 2.9. The interplanar separation is close to the graphite spacing of 3.35 Å[58] and ideal for π- π stacking interactions as determined by Hunter and Sanders.[59] Ligand molecules are connected in the crystal lattice via weak C-H···O interactions. Figure 2.10 shows packing diagram of ligand **(2.7)** along *c*-axis.

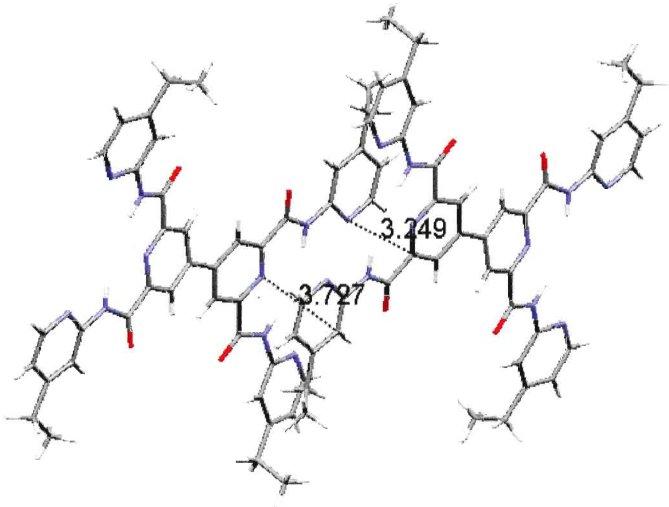

Figure 2.9. Packing of two adjacent molecules of **(2.7)**. π- π stacking interactions between molecules are shown as dashed lines, distances are in Å.

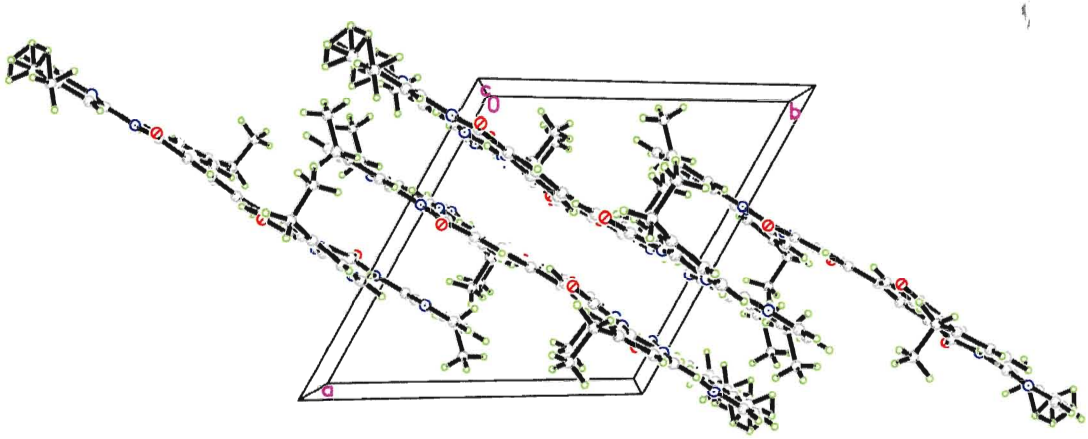

Figure 2.10. Packing diagram for ligand **(2.7)**. View down *c*-axis of the unit cell.

The molecular structure of this ligand clearly shows that it has two available tridentate pockets comprised of one central pyridine and two amidate nitrogen atoms which could coordinate metal ions in a meridional fashion leaving two tethered pyridine rings un-coordinated or hanging. After deprotonation, a tridentate binding pocket seems to be the most reasonable coordination mode for the ligand.

2.4 Coordination chemistry of ligand (2.7)

A series of coordination compounds were prepared by refluxing one equivalent of ligand **(2.7** together with two equivalents of a metal acetate salt ($M^{II}(OAc)_2$, M^{II} = Cu, Co, Ni and Zn) in a (1:4) ethanol : chloroform solution. All reactions were carried out in air. Although the presence of a base in the reaction mixture facilitates coordination of deprotonated amide nitrogens to metal ions, in this case no base was added. As previously discussed, Lewis acidic first row transition metal ions facilitate the deprotonation of N bound amides. It is most likely that the amide ligand in the complexes is in its anionic form, but the presence of a neutral ligand in one or more of the complexes cannot be completely ruled out. The resulting complexes were poorly soluble in common organic solvents which hindered their characterization.

2.4.1 Cobalt complex

The cobalt complex of ligand **(2.7)** was prepared as a dark brown crystalline powder in 48% yield. The UV-vis spectrum of the complex is plotted in red in Figure 2.11. In comparison with the free ligand, the UV-vis spectrum of the cobalt complex is broader and shows an absorption at λ_{max} = 285 nm consistent with the ligand transitions. For solubility issues, no weak CT or d-d transition were observed at longer wavelengths.

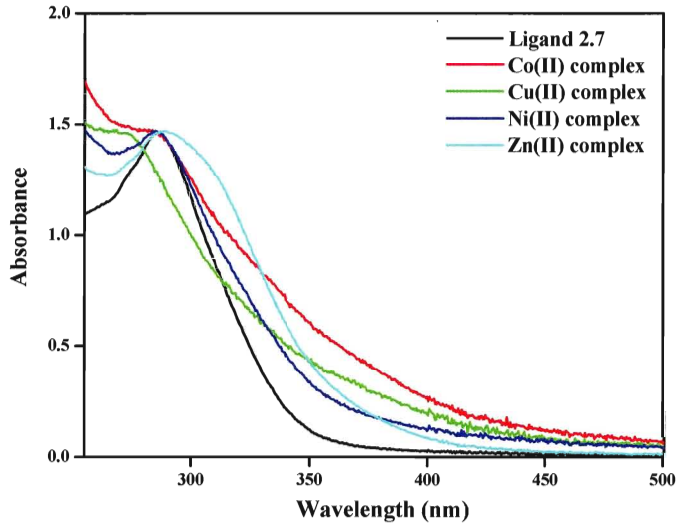

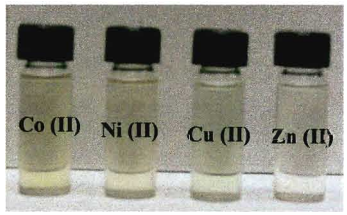

Figure 2.11. UV-vis spectra for ligand **(2.7)** (black) and its M^{II} complexes in a (1:1) mixture of CH_2Cl_2 : CH_3OH, where M^{II} = Co (red), Ni (blue), Cu (green) and Zn (cyan). Due to low solubility of these complexes, only qualitative UV-vis measurements were carried out, hence no extinction coefficients are given.

The fact that this band did not show any significant changes in position indicates the probable non-involvement of the carbonyl oxygen in coordination. No obvious charge transfer bands for this complex are observed at longer wavelengths. The FAB mass spectrum of the complex shows a parent peak at *m/z* = 1014 consistent with $[Co_2(L\text{-}4H)CH_3CO_2H{\cdot}2EtOH]^+$. The first fragment peak at *m/z* = 863 is consistent with one fully deprotonated ligand and two cobalt ions $[Co_2(L\text{-}4H)+H]^+$. The second fragment peak at *m/z* = 806 is consistent with $[Co(L\text{-}2H)+H]^+$ and the peak at 749 can be assigned to the uncoordinated ligand $[L+H]^+$. The IR spectrum of the cobalt complex contains an intense broad band at 3434 cm^{-1} consistent with the presence of coordinated water in the crystal lattice. No obvious bands at 3377 and 3270 cm^{-1} are visible for the amide NH str, but we cannot rule out the possibility that these bands are masked by the broad O-H band. The Amide I [υ C=O] band is red shifted by 74 cm^{-1} to 1617 cm^{-1} in the complex. This red

shift is of the same order of magnitude as that observed by Woollins *et al.* for the coordination complexes of closely related pyridyl systems which typically chelate metal ions through their amide nitrogens rather than their carbonyl group.[50] This weakening of the C=O str is consistent with structural studies of amide complexes of first row transition metal ions which typically show longer C-O bond lengths and shorter C-N bond lengths on coordination through a deprotonated amide N. This complex contains a number of intense bands between 1617 and 1400 cm^{-1}.

Acetate ligands bound to transition metal ions typically give bands in this region. Four additional bands are visible at 1564, 1528, 1475 and 1414 cm^{-1}. The first two bands can be tentatively assigned to υ_{asym} (OCO) of the acetate and the second bands to the υ_{sym} (OCO) of the acetate.[60] Comparison of the $\Delta\nu$ value of the respective carboxylate complexes with the $\Delta\nu$ value of the sodium salt of the same carboxylate can be used as a guideline in assigning the carboxylate coordination modes. Accordingly, (i) the chelating coordination mode occurs when $\Delta\nu$ of the studied complex << $\Delta\nu$ of the sodium salt; (ii) the bidentate bridging coordination mode occurs when $\Delta\nu$ of the studied complex $\leq \Delta\nu$ of the sodium salt, and (iii) the monodentate coordination mode exists when $\Delta\nu$ of the studied complex >> $\Delta\nu$ of the sodium salt.[60] For the cobalt complex, the $\Delta\nu$ = 150 cm^{-1}, which is lower than that reported for sodium acetate ($\Delta\nu$ = 164 cm^{-1}). As a consequence, it is likely that the acetate is chelating in a bidentate bridging manner. It should also be noted that the Amide II band for this complex expected between 1560 to 1585 cm^{-1} is now masked by the bands of acetate. It is very difficult to distinguish between N and O chelation when the IR spectrum is complex, and other characteristic bands for the amide, such as the C-N str and C-O out-of plane bend are masked and cannot therefore be confidently assigned. The CW EPR spectrum of the complex is shown in Figure 2.12. It

is narrower than would normally be expected for a low spin Co(II) (S=1/2) complex, suggesting that the unpaired electrons are not strongly localized on the metal center but perhaps delocalized over the complex. The spectrum shows g value which is an axial g-tensor with $g_{\|} = 2.0021$ and $g_{\perp} = 2.0008$.

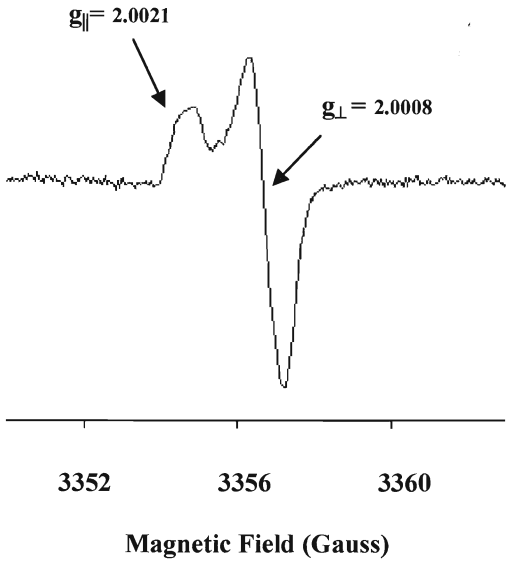

Figure 2.12. EPR spectrum of powder Co(II) complex of ligand **(2.7)** at 200 K, microwave frequency = 9.3998 x 10^9 Hz.

To summarize, the IR, EPR and mass spectrometry data are both consistent with the complex containing one ligand, two Co(II) metal ions and at least one bridging acetate together with solvent molecules. This is further supported by the elemental analysis data which is a good fit for a 2:1 metal to ligand complex of the stoichiometry $[Co_2(C_{42}H_{37}N_{10}O_4)(CH_3CO_2)]\cdot EtOH\cdot 5.45H_2O$. In this case, one of the nitrogen atoms in the complex must be protonated in order to balance the charge and give a neutral complex.

2.4.2 Nickel complex

The nickel complex of ligand **(2.7)** was isolated as a pale brown powder. The UV-vis data for this complex is plotted as a dark blue line in Figure 2.11. The spectrum does

not show any clear MLCT bands for this complex, just an intense band at λ_{max} = 285 nm consistent with the previously mentioned ligand transitions. Again, n to π^* transitions are not really shifted with respect to the free ligand which is suggesting that the carbonyl oxygen atom is not involved in chelation to the metal. The FAB mass spectrum shows the parent ion at *m/z* = 927 which can be assigned to one nickel ion coordinating to the deprotonated ligand plus a water, ethanol and an acetate ligand $[Ni(L\text{-}2H)CH_3CO_2+EtOH+H]^{+}$. The first fragment peak at *m/z* = 805 is consistent with the ligand coordinated to one nickel metal $[Ni(L\text{-}2H)+H]^{+}$ and a second fragment corresponding to just the free ligand as observed at *m/z* = 749.

The IR spectrum is almost superimposable with that of the cobalt complex. A broad band at 3419 cm^{-1} is consistent with solvent water in the crystal lattice. The NH str bands present in the ligand are absent from this spectrum. The Amide I band is visible at 1616 cm^{-1} and four bands characteristic of a chelating acetate are observed between 1564 - 1415 cm^{-1}. The $\Delta\nu$ for this acetate ligand is 150 cm^{-1} which supports a bridging bidentate mode of chelation.[60] Once again the IR and mass spectroscopy data is consistent with the amide binding to at least one nickel through its deprotonated amide nitrogens, most probably in the tridentate pocket of the ligand. The coordination geometry of the metal ion is most likely satisfied by at least one bridging acetate ligand together with coordinating solvent molecules.

2.4.3 Copper complex

Following the above procedure, a copper complex of ligand **(2.7)** was isolated as dark green crystalline powder in 56% yield. The FAB mass spectrum of this complex shows a peak at *m/z* = 937 which can be assigned to $[Cu_2(L\text{-}4H)+ H_2O+ EtOH+ H]^{+}$.

Fragment peaks consistent with the ligand plus one and two copper ions and an $[MH]^+$ peak for the ligand are also observed. The UV-vis spectrum of the copper complex is plotted in green in Figure 2.11. This spectrum has an intense absorption centered at λ_{max} 274 nm consistent with the n to π^* and π to π^* transitions of the ligand. Closer inspection reveals the presence of a much weaker second band at λ = 350 nm visible as a shoulder on the first absorption band. MLCT bands of copper(II) complexes of diimine ligands are typically observed around 350 nm.[61] No additional bands were visible past 500 nm.

The IR spectrum revealed that the two NH bands at 3377 and 3270 cm^{-1} visible in the ligand are now absent in the complex and a broader absorption band is visible in the region 3350-3500 cm^{-1}. This broad band is most likely due to the presence of coordinated water in the crystal lattice. An intense Amide I [C=O] band is present at 1617 cm^{-1}. This band is red shifted to lower frequency by 70 cm^{-1} when compared to that of the free ligand. The C-N stretch of the amide is now masked by the broad Amide I band. The lack of the N-H stretch together with the red shift of the C=O amide stretch is supportive of the involvement of anionic N amide in the coordination.[62] Woollins *et al.* have prepared and characterized two copper (II) complexes of pyridine carboxamide ligands by reacting ligand **(2.13)** with copper acetate in the absence of any base. In both cases, the amide nitrogens are deprotonated and take part in chelation to the metal centres. Furthermore, in these complexes, the acetate also bridges neighbouring copper centres facilitating the formation of a trimetallic species.[49] Figure 2.13 shows the molecular structure of a trimetallic species formed from ligand **(2.13)** and copper acetate.

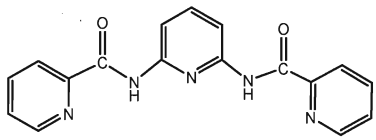

(2.13)

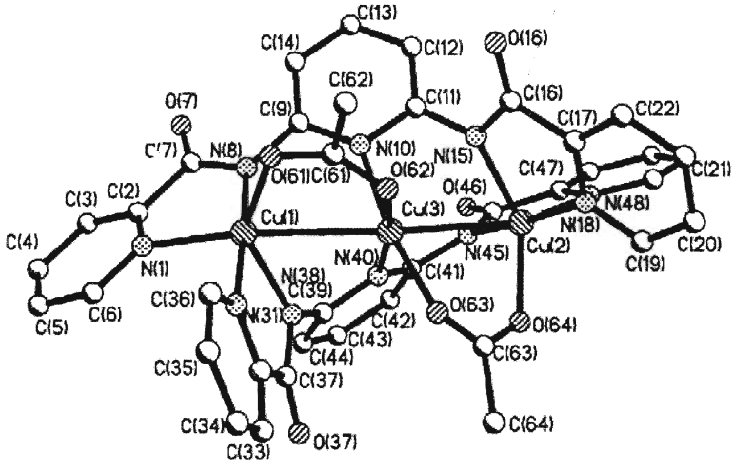

(2.14)

Figure 2.13. Molecular structure of a trimetallic species prepared from reacting a pyridine dicarboxamide ligand **(2.13)** with copper acetate in a methanol : chloroform solution at room temperature.[49] - Reproduced by permission of the Royal Society of Chemistry (RSC).

A red shift in the Amide I [υ C=O] band of 70 cm^{-1} for the above trinuclear copper complex when compared with the free ligand was also reported. For our complex, the region 1600-1375 cm^{-1} contains a larger number of intense bands when compared with the previously characterized two complexes which could be due to acetate ligands binding in more than one type of chelation mode to the copper centres. The elemental analysis is an excellent fit for a 2:1 metal to ligand complex of stoichiometry $[Cu_2(C_{42}H_{37}N_{10}O_4)(CH_3CO_2)]\cdot 4.45H_2O\cdot EtOH$. This structure could very likely be a 1-D chain with acetate ligands connecting neighbouring metal centres in the chain. An alternative suggestion is a cluster comprising of $[Cu_6(L)_2(CH_3CO_2)_4]_n$ units. In this case,

all amide nitrogens would be deprotonated and each of the binding pockets of the ligand would chelate three copper ions and two bridging acetates. This makes more chemical sense with respect to the charge balance. For $[Cu_6(L)_2(CH_3CO_2)_4]\cdot H_2O\cdot CH_3CH_2OH$, the largest deviation between the calculated and experimental values for C, H and N are 0.2, 0.74 and 0.75 % respectively. The elemental analysis data would seem to be a better fit for a 2:1 structure, but without X-ray crystallographic data it is not possible to fully elucidate the structure of this complex. We cannot completely rule out a multinuclear species where bridging acetates, solvent molecules and/or the pendant pyridyl groups participate in coordination.

Given the lack of success in growing single crystals of these complexes, the Zn(II) complex was targeted. The thinking was that due to the diamagnetic nature of this complex, NMR spectroscopy could then also be used to shed more light on the coordination preferences of this ligand.

2.4.4 Zn complex

The zinc complex was isolated as a yellow crystalline powder in 53% yield, following the previously discussed synthetic route shown in Scheme 1. The UV-vis spectrum of the complex is plotted in blue in Figure 2.11. The spectrum is the broadest of all of the coordination complexes and once again shows a broad band centered around λ_{max} = 300 nm. The FAB mass spectrum has a peak at *m/z* = 956 which can be assigned to $[Zn_2(L\text{-}4H)+EtOH+2H_2O+H]^+$. A fragment ion at *m/z* = 895 is consistent with $[Zn_2(L\text{-}2H)+EtOH+2H_2O+H]^+$, loss of water from this fragment gives a peak at *m/z* = 877 and loss of one Zn from this gives a peak at *m/z* = 811. As for the previous complexes, a fragment ion for the ligand is observed at *m/z* = 749. The IR spectrum of this complex

differs slightly from the previous complexes. Although a band due to lattice water is present at 3414 cm^{-1}, this is much broader then for the previous complexes and a second band is just about visible at 3257 cm^{-1} which is consistent with an H-bonded NH str. It should be noted that the broadness of the band due to the O-H str makes this region difficult to interpret. An intense band at 1619 cm^{-1} for the amide I [υ C=O] str is visible. This band also has a fairly intense shoulder at 1693 cm^{-1} that matches the stretch of the C=O bond observed in the free neutral ligand. Once again, a number of bands are visible between 1565 and 1417 cm^{-1} consistent with bridging acetate ligands.

The ^1H NMR spectrum of the Zn complex is not particularly easy to interpret. A peak for the NH proton is clearly visible at 11.49 ppm. In comparison with the ^1H NMR for the uncoordinated ligand, the H_3 proton is now observed at 8.97 ppm as a triplet. The H_7 and H_{10} protons of the pyridyl pendant arms are now no longer present as two distinct peaks, but a multiplet is present at 8.40 ppm. A broad peak is now present at 7.03 ppm which is very close to the resonance for the H_9 proton in the free ligand. In addition, two smaller sets of multiplets are present centered at 7.84 and 6.37 ppm. Two singlets are observed for CH_2 protons of ethyl groups at 2.99 and 2.77 ppm overlapping with a water peak. CH_3 protons assigned to bound acetate molecules are observed as a broad singlet at 1.84 ppm. At least two peaks are observed at 1.60 and 1.54 ppm consistent with ethyl CH_3 groups. From the integration, it is possible to roughly estimate that the zinc complex contains two acetate molecules for every one ligand. The ligand is clearly not symmetrical in the complex and at least one of the amide nitrogen atoms could still be protonated. Without the help of additional data it is impossible to confidently assign the peaks in the aromatic region. It seems that at least one set of aromatic peaks are shifted upfield.

To summarize, initial data is encouraging to support coordination of two zinc ions to this ligand. Mass spectroscopy data supports the formation of a metal complex, but additional data is needed for a more comprehensive characterization together with proof of purity. Ideally, the molecular structures of these coordination complexes need to be determined by X-ray crystallography, but the growth of suitable single crystals remains a challenge. Since these complexes were problematic to crystallize, the decision was made to focus on the preparation and study of the third ligand **(2.8)**. This ligand was more soluble in comparison with **(2.6)** and **(2.7)** and crystallized more easily from organic solvents which enabled the characterization of two of its copper complex by X-ray diffraction.

2.5 Preparation and characterization of ligand (2.8)

As mentioned, the search for a more soluble carboxamide bipyridine ligand in common organic solvents motivated us to choose 3-amino-5-*tert*-butyl-pyrazole as a pendant arm attached to the four *ortho* positions of the 4,4′-bipyridine rings, Figure 2.14.

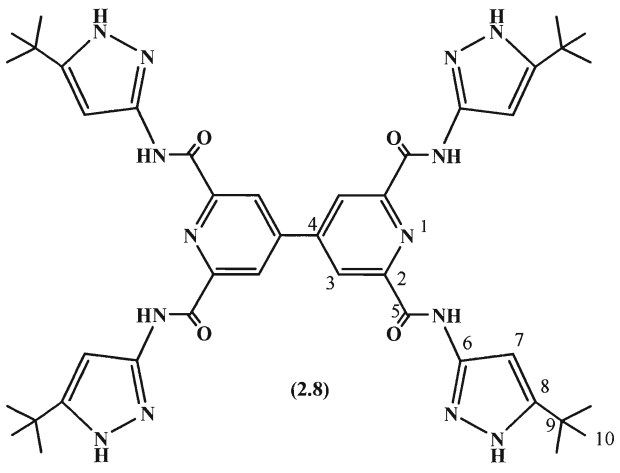

Figure 2.14. Molecular structure of ligand **(2.8)** with appropriate numbering scheme.

These pendant groups improve the solubility of the ligand and modify its binding pocket enough to change its coordination preferences. Pyrazolate ligands are known to form complexes with diverse structural motifs. They are able to bind two or more closed-shell d^{10} metal centers together in distances close to the sum of the covalent radii of the two metals and are thus suitable linkeages for the construction of metal aggregates with metal-metal interactions. There are many examples of dimers, trimers and tetranuclear complexes,[63] and more recently, two examples of higher nuclearity complexes namely, the two octanuclear copper(I) complexes of bis(pyrozalate) pyridyl ligands, **(2.16)**, Figure 2.15 (where R = CH_3 or Ph) have been reported. These complexes are neutral and are comprised of eight copper (I) ions held together by four dianionic ligands. The complexes were prepared via hydrothermal reactions.[63]

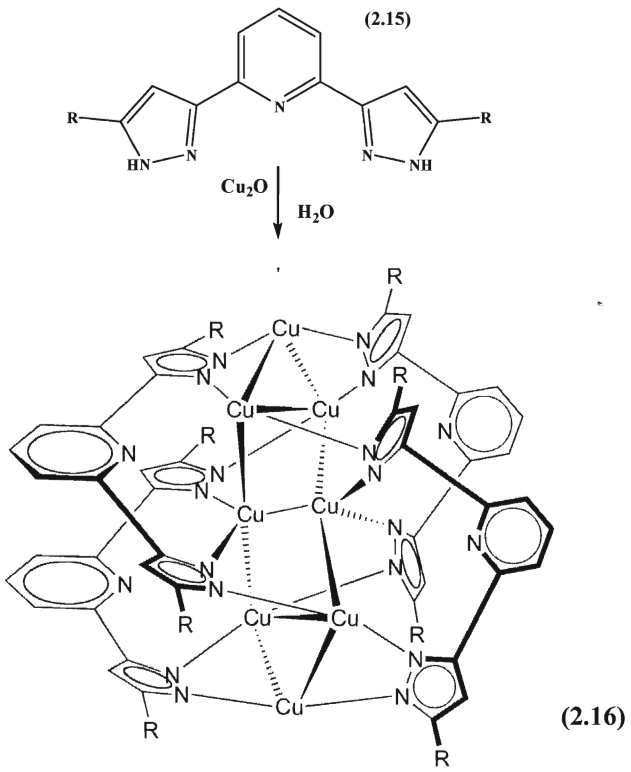

Figure 2.15. Molecular structure of **(2.16)**, where R = CH_3 or Ph.[63]- Reproduced by permission of the Royal Society of Chemistry (RSC).

These results highlight the versatility of pyridyl ligands containing pyrazole arms for the self-assembly of large copper clusters. The condensation reaction between 2,2',6,6'-tetrachloroformyl-4,4'-bipyridine **(2.5)** and an excess of 3-amino-5-*tert*-butyl-pyrazole in toluene afforded **(2.8)** as a pale yellow solid in 66% yield, Scheme 1.

The ^{1}H NMR spectrum of **(2.8)** shows two N-H peaks for the pyrazole and amide protons at 12.36 and 11.83 ppm, respectively. Singlets at 8.70 and 6.58 ppm were assigned to the two aromatic C_3 and C_7 protons. A singlet at 1.33 ppm is present for the protons of the *tert*-butyl CH_3's. The ^{13}C NMR spectrum of **(2.8)** has a peak at 161.5 ppm for the amide carbon. Peaks at 153.0, 146.7, 94.8 ppm are assigned to C_6, C_8 and C_7 carbons of the pyrazole ring. Peaks at 150.8, 147.5, and 123.1 ppm are assigned to bipyridine carbons at the C_2, C_4 and C_3, positions, respectively. The final peaks at 31.2 and 30.4 ppm are consistent with the quaternary and methyl carbons of the *tert*-butyl group.

The IR spectrum displays a number of bands above 2900 cm^{-1} assigned to both the amide and pyrazole NH. A second broader band is visible at 3171 cm^{-1} due to the O-H str of coordinated water molecules overlapping with the NH str of the amide and pyrazole groups participating in hydrogen bonding interactions. H-bonded NH groups in pyrazoles typically give bands in the IR around 3175 cm^{-1}. An Amide I [υ C=O] band is visible at 1689 cm^{-1} and the Amide II band is present at 1541 cm^{-1}. The high resolution FAB mass spectrum of this ligand, is consistent with its molecular structure, showing an $[MH]^+$ peak at m/z = 817.43742. Single crystals suitable for X-ray diffraction were grown via the slow diffusion of diethyl ether into a DMF solution of the ligand. An ORTEP view of the molecular structure of one independent molecule along with the atom-numbering scheme is shown in Figure 2.16. The *tert*-butyl group at C(18) is highly disordered and for clarity

only one orientation is shown. The ligand crystallizes in the orthorhombic space group $Pna2_1$. The asymmetric unit contains one independent molecule in the unit cell. In the solid state, the ligand is not completely planar.

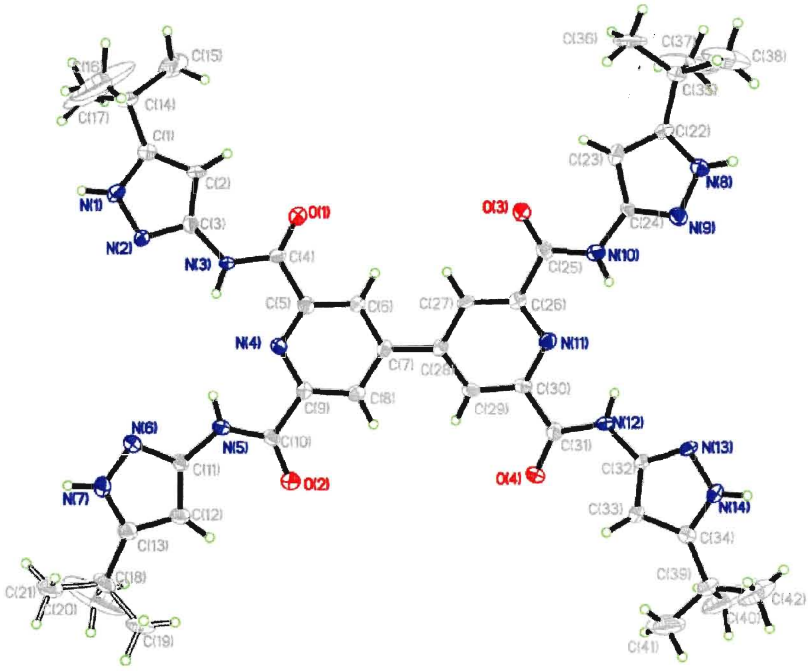

Figure 2.16. ORTEP[57] plot for the molecular structure of ligand **(2.8)**.

The two pyridine rings of the bipyridine are twisted away from each other such that the dihedral angle between their best planes is 16.9°. Selected bond lengths and angles for **(2.8)** are presented in Tables 2.3 and 2.4. The two 5-membered pyrazole rings coordinated to the N(4)-C(9) bipyridine ring are fairly co-planar with this ring, with torsion angles of 8.4 and 11.3° for the N(1)N(2) and N(6)N(7) rings, respectively. The pyrazole N(8)N(9) group attached to the N(11)-C(30) bipyridine ring is almost co-planar. In this case, the torsion angle between the best planes of the two rings is only 6°. In contrast, the second pyrazole N(13)N(14) ring is quite considerably twisted out of the plane of the pyridine ring to which it is attached by a torsion angle of 21.

Table 2.3. Selected bond lengths [Å] for ligand (2.8).

N(4)-C(9)	1.334(8)	N(3)-C(3)	1.390(8)
C(8)-C(9)	1.393(8)	N(2)-C(3)	1.326(8)
C(7)-C(8)	1.370(9)	N(1)-N(2)	1.348(7)
C(6)-C(7)	1.403(8)	N(1)-C(1)	1.360(9)
C(7)-C(28)	1.462(9)	C(1)-C(2)	1.378(11)
C(5)-C(6)	1.382(9)	C(2)-C(3)	1.388(9)
N(4)-C(5)	1.316(8)	C(4)-C(5)	1.516(8)
N(3)-C(4)	1.356(8)	O(1)-C(4)	1.208(8)
C(1)-C(14)	1.497(11)	C(14)-C(15)	1.50(2)
C(14)-C(16)	1.73(2)	C(14)-C(17)	1.44(2)

Table 2.4. Selected bond angles [°] for ligand (2.8).

C(5)-N(4)-C(9)	117.4(5)	N(2)-C(3)-C(2)	112.1(6)
N(4)-C(9)-C(8)	123.4(5)	C(2)-C(3)-N(3)	130.3(6)
N(4)-C(9)-C(10)	115.5(5)	C(3)-N(2)-N(1)	104.5(5)
C(7)-C(8)-C(9)	118.9(5)	N(2)-N(1)-C(1)	112.3(5)
C(8)-C(7)-C(6)	117.9(5)	N(2)-C(3)-N(3)	117.5
C(8)-C(7)-C(28)	123.1(5)	C(1)-C(2)-C(3)	105.1(6)
C(6)-C(7)-C(28)	118.9(5)	N(3)-C(4)-C(5)	112.5(5)
C(5)-C(6)-C(7)	118.6(6)	C(17)-C(14)-C(1)	113.5(10)
C(6)-C(5)-C(4)	119.1(5)	C(17)-C(14)-C(15)	135.4(12)
N(4)-C(5)-C(6)	123.8(6)	C(1)-C(14)-C(15)	107.1(9)
N(4)-C(5)-C(4)	117.1(5)	C(17)-C(14)-C(16)	104.3(11)
O(1)-C(4)-C(5)	123.5(6)	C(1)-C(14)-C(16)	100.9(11)
O(1)-C(4)-N(3)	124.0(6)	C(15)-C(14)-C(16)	84.8(13)
C(4)-N(3)-C(3)	125.6(5)		

The carbonyl oxygen and amide hydrogen adopt the *trans* configuration as observed for the previously characterized pyridine carboxamide ligand **(2.7)**. The amide C-N bond lengths are in the range of 1.33 -1.35 Å and the C=O bond lengths are in the range 1.20-1.23 Å. These are shorter than the average C-N bond and longer than the average C=O bond lengths, consistent with a conjugated structure.[64] The C-N-C angles around the amide nitrogen's are in the range 124.85 -127.75°. The sum of the bond angles around the amide N are very close to 360°.

The crystal structure of this ligand contains three DMF and three water molecules per formula unit, Figure 2.17. Interestingly, the two binding pockets of the ligand coordinate the solvent molecules a little differently. The first binding pocket contains a single tightly bound water molecule. H-bonds from the amide NH group and from the pendent pyrazole nitrogens to the water are in the range of 2.21 – 2.26 Å. The oxygen atom of two independent DMF solvent molecules are H-bonded to a pyrazole NH groups such that N(1)H···O(9) = 1.940 Å and N(14)H···O(8) = 1.960 Å. The second cavity contains two water molecules. The first O(6) is H-bonded to a pyrazole N such that N(13)H···O6 = 1.989A. This water is also H-bonded to the carbonyl oxygen atom of an amide group from a second ligand molecule. The second water molecule O(7) is H-bonded to both the amide and pyrazole groups on the same arm such that the distances are N(10)H ···O(7) = 2.164 Å and O(7)-H…N(9) = 2.050 Å. The two waters are H-bonded to each other such that O(7)-H···O(6) = 1.903 Å, Figure 2.17.

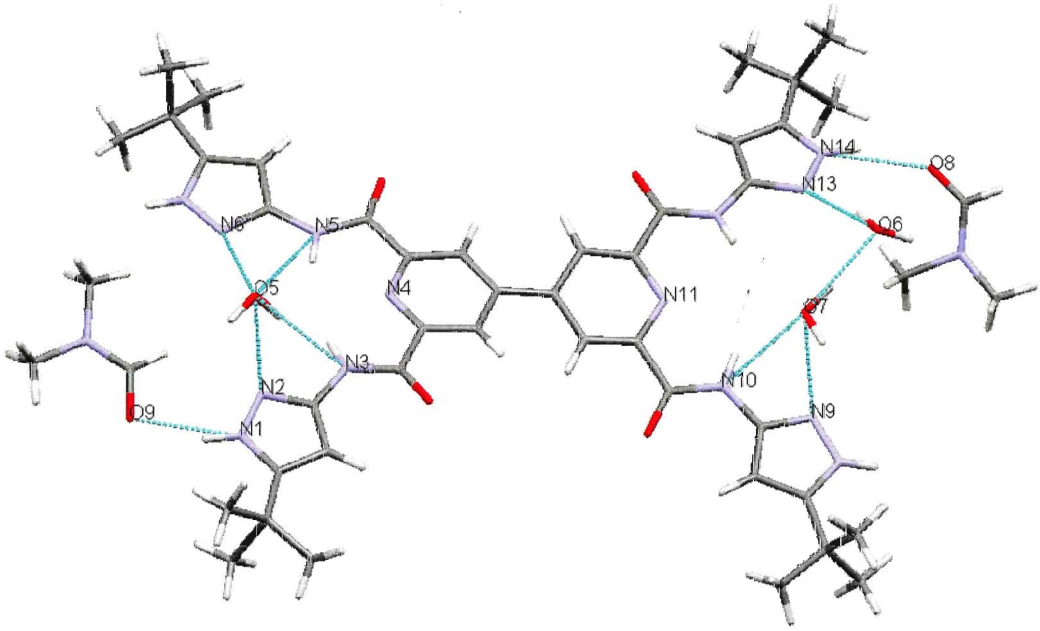

Figure 2.17. View of the molecular structure of **(2.8).** H-bonding interactions to neighboring solvent molecules are shown as blue dashed lines.

There are intermolecular H-bonds of 2.042 Å between the amide carbonyl groups of one molecule and a pyrazole NH of a neighbouring molecule. π-π Stacking is present between the pyrazole and pyridine rings of adjacent molecules of **(2.8)**. The interplanar separations are shown in Figure 2.18 and are within the ideal limit for π-stacking interactions as determined by Hunter and Saunders.[59] The molecules π-π stack in a herringbone fashion along the *c*-axis of the unit cell. In this stacking arrangement, there is some loss in the planarity of the structure which is offset by the formation of an extended structure that is most likely stabilized by the formation of the H-bonds.

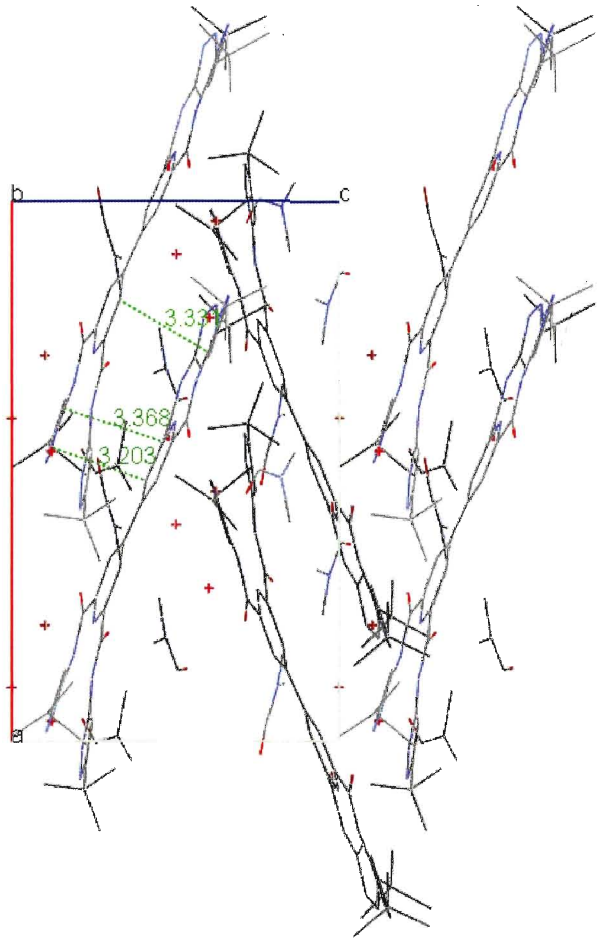

Figure 2.18. Packing diagram of ligand **(2.8)** viewed down the *b*-axis. Herringbone arrangement of ligands, π-π stacking interactions and distances in Å are indicated in green.

2.5.1 Coordination chemistry of (2.8)

The coordination chemistry of ligand **(2.8)** together with a range of metal salts was attempted, but the growth of single crystals for the elucidation of their molecular structures has not been successful to-date. These complexes have not been fully characterized and as such are not included in the body of this thesis. The poor solubility of these complexes after isolation renders it impossible to redissolve them in organic solvents for the growth of single crystals. In order to circumvent this problem, we adopted an alternative, "serendipitous strategy" for the preparation of coordination

complexes that has been largely successful for the self-assembly of large polymetallic cages.[65] In this respect, the complex was not isolated and fully characterized before attempting to grow single crystals. In contrast, solutions of various metal salts and the ligand were allowed to slowly diffuse together over time. Following this strategy, slow diffusion of a methanol solution of copper chloride into a chloroform solution of ligand **(2.8)** at room temperature, afforded green plates, after 2 weeks that were suitable for X-ray diffraction. No base was added. The molecular structure reveals that the assembled complex is a large cluster of stoichiometry $[Cu_8(L)_4Cl_{16}]$, Figure 2.19. The refinement of the crystal structure was non-trivial.

Due to its low symmetry there were hundreds of atoms to independently refine as well as disordered ligands and solvent. In this respect, we acknowledge the help of Professor Clegg from the University of Newcastle, who was able to assist us with the final stages of the data refinement and help us treat successfully the disorder in the structure. One disordered chloroform molecule is modeled in the structure and the remaining solvent was removed by applying the SQUEEZE command in PLATON.[66] Elemental analysis data for single crystals of **(2.17)** are within +/- 0.4 % for the stoichiometry $[Cu_8(L)_4Cl_{16}].CHCl_3.5H_2O.7CH_3OH$. This amount of solvent fits well for the amount of electron density removed from the .hkl file of the crystal structure by applying the SQUEEZE command.[66] Compound **(2.17)** crystallized in the triclinic space group P-1 with one unique cluster in the asymmetric unit. Cluster **(2.17)** has approximate S_4 symmetry and is comprised of four ligands and eight copper (II) centers. A view of the molecular structure of the cluster along its approximate S_4 axis is shown in Figure 2.19. All of the amide Ns are protonated in the cluster and chelation takes place between amide O atoms, and pyrazole and pyridine nitrogens. The C-N and C=O lengths of the amide

bonds are in the range of 1.31 -1.35 Å and 1.21-1.25 Å consistent with a conjugated amide. Since the amide Ns remain protonated, the ligand cannot chelate via its tridentate binding pocket and so adopts a rather different mode of chelation which affords a very interesting octanuclear saddle-shaped complex.

The pentacoordinate geometry around each copper center is best interpreted as intermediate between trigonal bipyramidal and square-based pyramidal. According to the procedure described by Addison[67] the copper (II) atoms have distortion parameter τ values of 0.66, 0.34, 0.76, 0.43, 0.55, 0.54, 0.58 and 0.8 for Cu(1) to Cu(8) respectively. ($\tau = (\theta_1-\theta_2)/60)$), where θ_1 and θ_2 are the largest angles in the coordination sphere), where τ = 0 for square pyramidal and 1 for trigonal bipyramidal.[65] This indicates that the coordination geometry for the copper(II) ions Cu(1), Cu(3), Cu(5), Cu(6), Cu(7) and Cu(8) are best described as distorted trigonal bipyramidal. Here, the axial positions are occupied by two pyrazole nitrogens from two different ligands, while the equatorial positions or basal plane, are occupied by an oxygen of a carboxamide unit and two chloride ions which serve as the 4th and 5th ligands to complete the five-coordinate geometry. In the case of Cu(2) and Cu(4), the geometries are closer to distorted square pyramidal with an oxygen of a carboxamide unit and two pyrazole nitrogen's from two different ligands and one chloride ion occupying the basal plane and second chloride ion occupying the axial position. At each copper center, different Cu-Cl bond lengths are observed. For the Cu(2) and Cu(4) centers, the axial Cu-Cl bond lengths (2.44 Å) are longer than the equatorial bond lengths (2.25 Å). A similar trend was observed for the copper centers with distorted trigonal bipyramidal geometry, however the differences between the two bond lengths were less pronounced as both Cu-Cl bonds are in equatorial positions. In order for the ligand to chelate all four of its pendant arms to copper centers,

the two bipyridine rings are substantially twisted. The dihedral angles between the best planes of the two bipyridine rings are 40.97°. The structure of **(2.17)** consists of a non-planar saddle-like loop comprised of eight Cu(II) centres. Although there are a number of reported metal complexes that adopt this saddle-type geometry,[68] this complex is unique being the first reported example of a octanuclear copper cluster with a saddle-shaped hyperboloid structure that has a double surface, Figure 2.20. To visualize this more clearly, the core structure of the cluster is shown in Figure 2.20(a). Here Cu(2) and Cu(6) at the bottom of the front and back-sides of the saddle represent points A and B respectively in Figure 22(b). Similarly, Cu(8) and Cu(4) correspond to points C and D. The Cu····Cu distances between the two points at the upper (C and D) and lower faces (A and B) of the saddle are shown in the Figure 2.20. The intramolecular distances for adjacent Cu(II)····Cu(II) centres along the saddle rim are in the range of 7.462 - 8.624 Å.

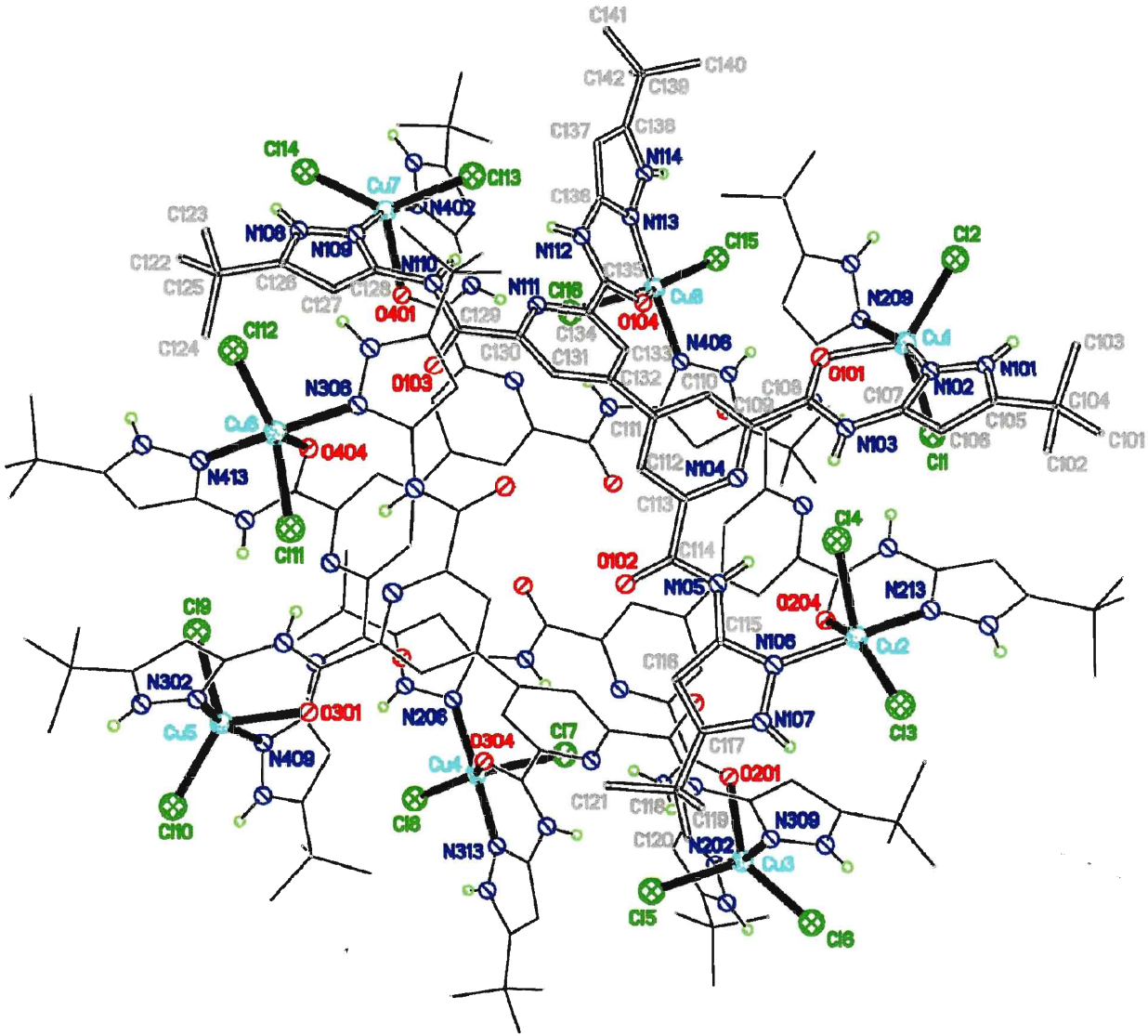

Figure 2.19. View of the molecular structure of cluster **(2.17)** along its approximate S_4 axis together with the labeling scheme. For clarity all H-atoms with the exception of the NH's are omitted. The minor disorder components and the chloroform molecule are omitted.

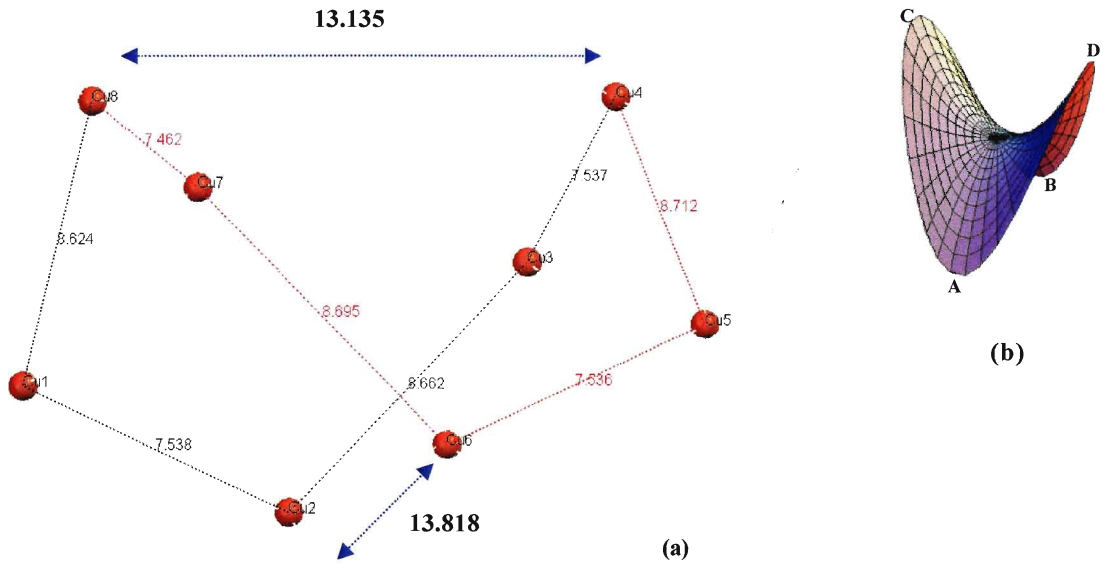

Figure 2.20. (a) The saddle shape of the Cu_8 core in cluster **(2.17)**. The black and red dashed lines represent the front and back sides of the saddle, respectively. (b) Representation of a 3-D hyperboloid saddle shape.

The best view to visualize the saddle shape arrangement of copper ions in the molecular structure of the cluster is along the y-axis of the unit cell. Rotating consecutively by 90° along the y-axis, the saddle shape can be observed in four different directions. Two of these views are shown in Figure 2.21.

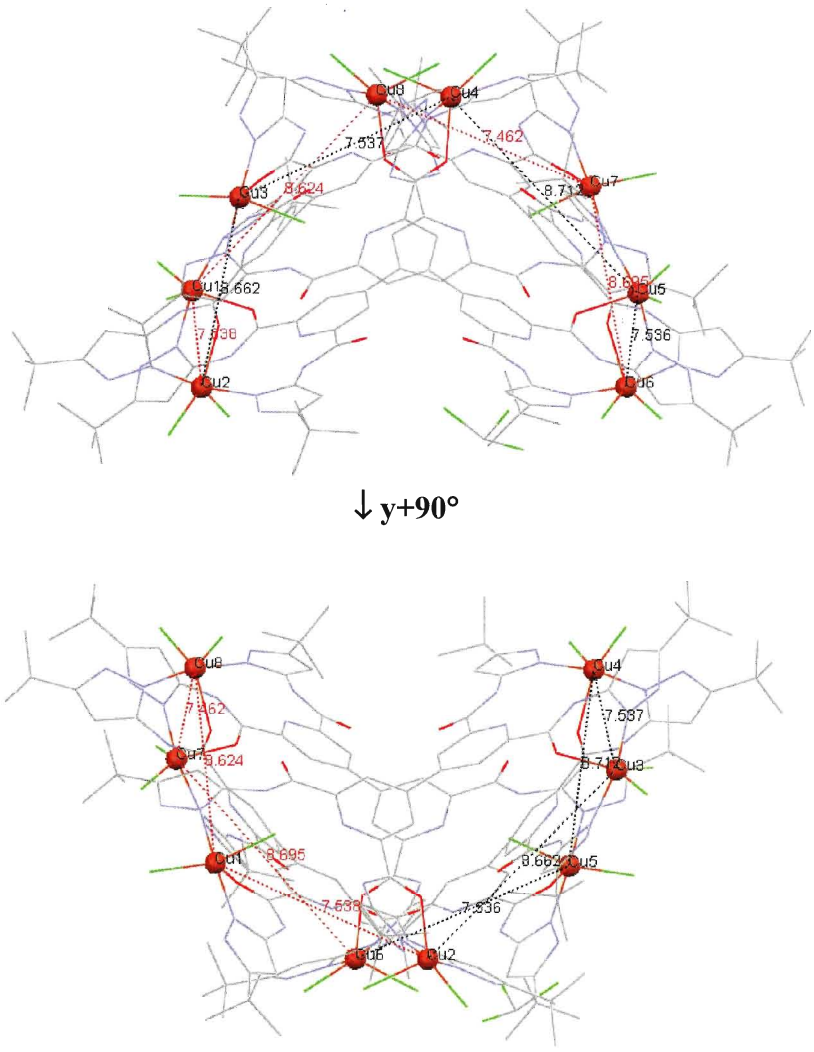

Figure 2.21. Perspective views (perpendicular to the screen) showing the saddle shape of the Cu_8 cluster and intermolecular Cu····Cu distances. The bottom view (inverted saddle) of the cluster core was obtained by flipping 90° along the vertical axis (y-axis).

In terms of magnetic clusters, the structure of this cluster is reminiscent of the Mn_8 single molecule magnet reported by Christou *et al.* that consists of a nonplanar saddle-like $[Mn_8O_8]^{8+}$ loop attached to central Ce^{4+} and O^{2-} ions, Figure 2.22.

.

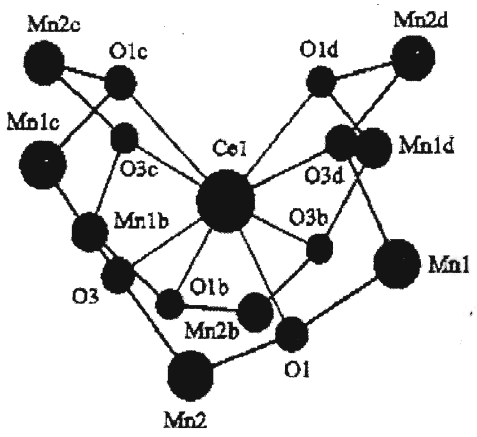

(2.18)

Figure 2.22. PovRay plot of the $[CeMn_8O_8]^{2+}$ core of a Mn_8 SMM emphasizing its saddle-like folding of the $[MnO_8]$ ring.[69] "Reprinted with permission from reference 38. Copyright {2003} American Chemical Society."

The cluster **(2.17)** packs in a head-to-tail arrangement along the *c*-axis of the unit cell, Figure 2.23. All chloride ions show H-bonds to neighbouring amide H atoms in the range of 2.33-2.49 Å. In the case of Cu(2) and Cu(4), the axial chloride ion makes these H-bonds, while for the other copper centers, one of the basal plane chloride ions takes part in the H-bond. Three H-bonds in the range 2.77-2.9 Å between the oxygen and amide H atoms of neighbouring ligands can be observed. Intermolecular Cu(II)···Cu(II) distances are quite long, in the range of 10.32-45.96 Å. Since the majority of the solvent was highly disordered and removed from the model, we are not able to comment in any detail regarding the intermolecular interactions between clusters in the solid state. The FAB mass spectrum of the cluster exhibited only fragmentation peaks. Peaks at *m/z* = 1089, 977 and 942 are consistent with $[Cu_3(L)Cl+H_2O+CH_3OH]^+$, $[Cu_2(L\text{-}2H)Cl]^+$ and $[Cu_2(L)]$. An intense fragment peak at *m/z* = 879 is also observed for [Cu(L)].

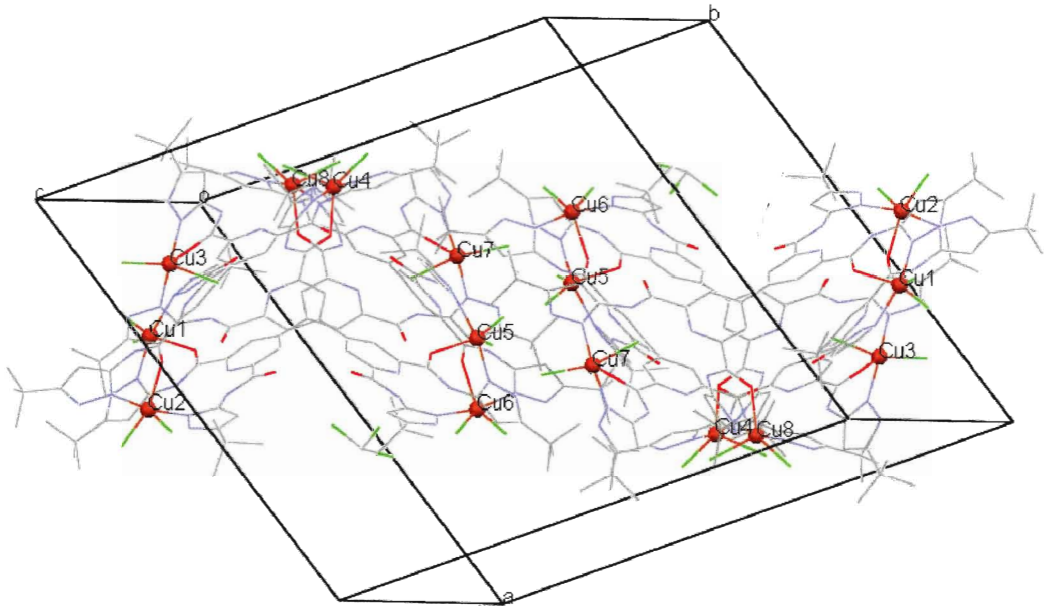

Figure 2.23. Packing diagram of complex **(2.17)** showing the head to tail arrangement of clusters in the unit cell.

The UV-vis spectrum of the complex has a band at λ = 261 nm (ε = 81048 $M^{-1}cm^{-1}$) consistent with π to π^* transitions of the bipyridine ligands, Figure 2.24. The cluster also shows a broad absorption broad band at λ_{max} = 797 nm (ε = 854 $M^{-1}cm^{-1}$) assigned as *d-d* transitions. Five-coordinated Cu(II) complexes that typically show *d-d* absorptions in the range 588–769 nm tend to approximate a square-pyramidal geometry, while complexes with a trigonal-bipyramidal geometry show absorption bands at longer wavelengths typically in the range 685–952 nm, with highest absorption intensities in the range 666-877 nm.[70] From the crystal structure we were able to elucidate that we have metal ions with both geometries present in the molecule. The IR spectrum of **(2.17)** has four peaks above 3000 cm^{-1} characteristic of amide N-H and solvent O-H str's. In comparison with

the IR data for the copper complex of ligand **(2.7)**, the IR spectrum of the cluster contains sharp intense peaks in this region above 3000 cm^{-1} giving us a clear indication that the amide nitrogens remain protonated in the cluster. Two Amide I [$\upsilon_{C=O}$] bands are present at 1694 and 1640 cm^{-1} which are consistent with the two types of amide C=O bonds in the structure since six of the carbonyl oxygen atoms remain uncoordinated. The red shifted band at 1640 cm^{-1} can be assigned to the C=O str of those carbonyl groups involved in coordination to the copper centers. As previously discussed, upon complexation, the C=O bond of a neutral carboxamide becomes longer and weaker and the C-N bond becomes shorter and stronger.[45] Two Amide II bands are observed at 1574 and 1548 cm^{-1} which once again reflects the two different chemical environments of the amide groups.

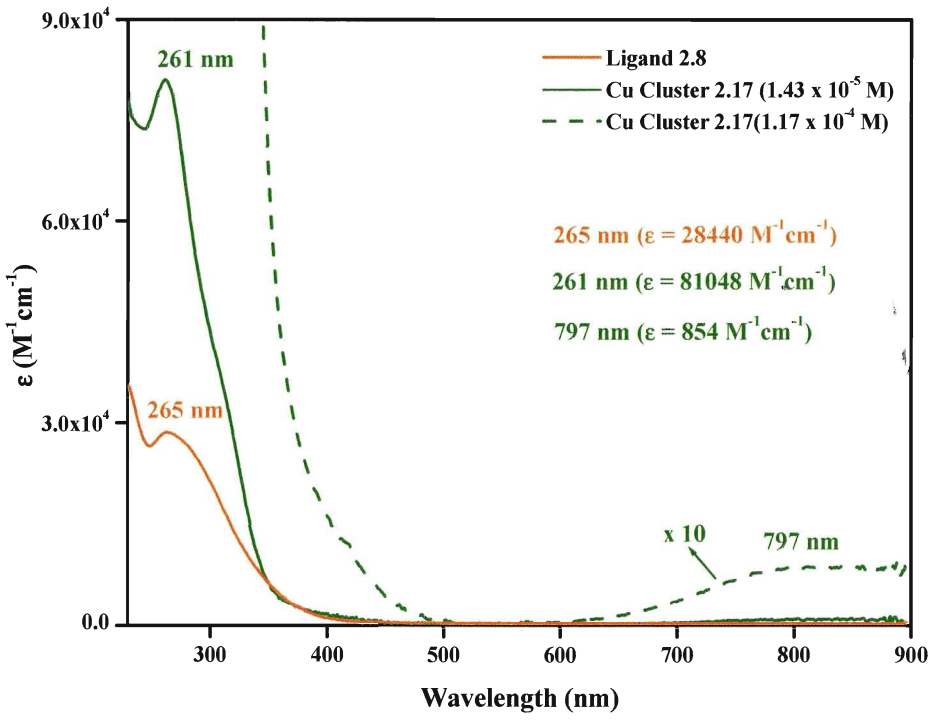

Figure 2.24. UV-vis absorption spectra of copper(II) complex **(2.17)** and corresponding ligand **(2.8)** in mixture of DCM: methanol (3:1) at room temperature.

The EPR spectrum of complex was recorded in a frozen methanol solution, Figure 2.25. The near axial nature of the EPR spectrum was confirmed by the simulation which revealed g_x = 2.224, g_y = 2.065 and g_z = 2.035. This pattern, $g_x >> g_y \sim g_z > g_e$ is consistent with a pseudo-square planar or Jahn-Teller elongated octahedral Cu^{II} centre.

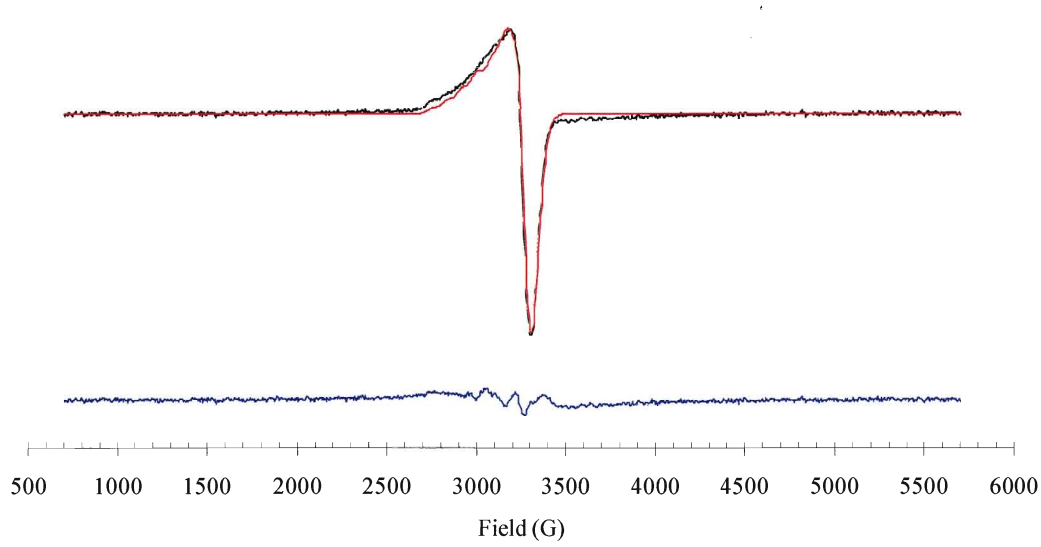

Figure 2.25. X-band EPR spectrum of **(2.17)** in methanol at 100K. (black = experimental; red = simulation; blue = difference)[77]

In addition, the low field component reveals some evidence for hyperfine coupling, although the features were not sufficiently well-resolved to determine unambiguously the nature of the hyperfine coupling (the low field features revealed a coupling of *ca.* 80 G consistent with hyperfine coupling to Cu).

The magnetic susceptibility data for this cluster shows that at room temperature, the experimental value of χT of 3.64 cm^3Kmol^{-1} is close to the value of 3.31 $cm^3.K.mol^{-1}$ expected for eight uncoupled copper(II) ions (S = ½, g = 2.1). The applied Curie-Weiss law leads to a value of θ = – 0.74 K (C = 3.59 cm^3Kmol^{-1}), indicating the presence of antiferromagnetic interactions.

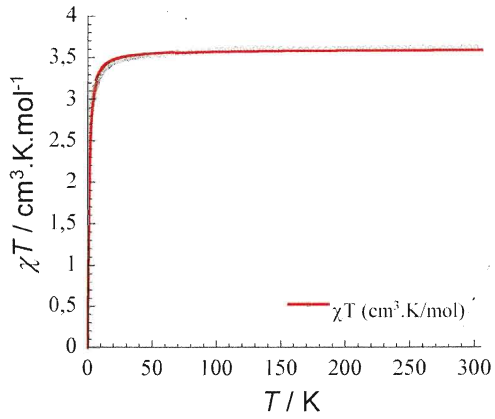

Figure 2.26. Curie-Weiss law fit applied to the χT product at 1T. The red solid line corresponds to the best fit.

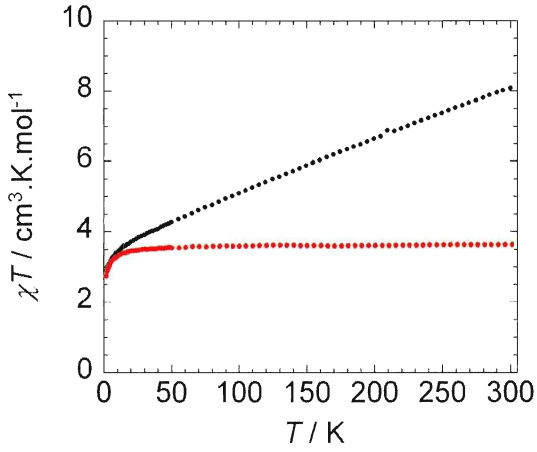

Figure 2.27. Temperature dependence of the χT product at 1 T (red line) and 7 T (black line) (with χM being the molar susceptibility per complex defined as M/H).

The *dc* magnetic properties of the Cu_8 compound were investigated under a 1 and 7 T fields in the temperature range 1.8-300 K. The χT *vs.* T under a 1 T field shows that χT remains constant until 50 K before slowly decreasing to reach the value of 2.76 $cm^3.K.mol^{-1}$ at 1.8 K. The field dependence of the magnetization reveals a typical variation for uncoupled or weakly coupled spins. The value of the magnetization at 7 T of 7.61 $cm^3.K.mol^{-1}$ is slightly lower than the value of 8.15 $cm^3.K.mol^{-1}$ expected for eight

uncoupled $S = ½$ and $g = 2.1$. From the magnetic data for the cluster we can conclude that until about 50 K, the metal centres behave as isolated spins, as the metal to metal distances are too far apart to facilitate any significant magnetic exchange interactions.

It is however quite remarkable that such a large polydentate ligand is able to facilitate the assembly of cluster. It should be possible to change the coordination preferences of the ligand by deprotonating the amide nitrogens using a base. The use of larger metals such as lanthanides could open up an interesting strategy for the preparation of lanthanide or mixed transition metal ion/lanthanide clusters. Multinuclear metal clusters are ubiquitous to many areas of chemistry, and biochemistry including main group, and organometallic chemistry, lanthanide and bioinorganic chemistry.

Particular interest in polynuclear copper clusters has been sparked in recent years by the characterization of several unusual metalloenzymes that contain copper clusters.[71] Cyclic metal arrays containing large numbers of spin-coupled paramagnetic metal centres are frequently synthesized from a large number of components in an uncontrolled self-assembly process that employs simple organic molecules and/or bridging ligands.[72] A good example of this strategy is the octanuclear tennis ball prepared from the small organic ligand N-(2-pyridylmethyl)acetamide **(2.19)** with copper perchlorate, Figure 2.28. This cluster comprises eight copper(II) ions, eight deprotonated ligands and four bridging hydroxide ligands.

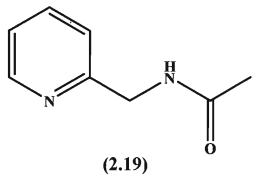

(2.19)

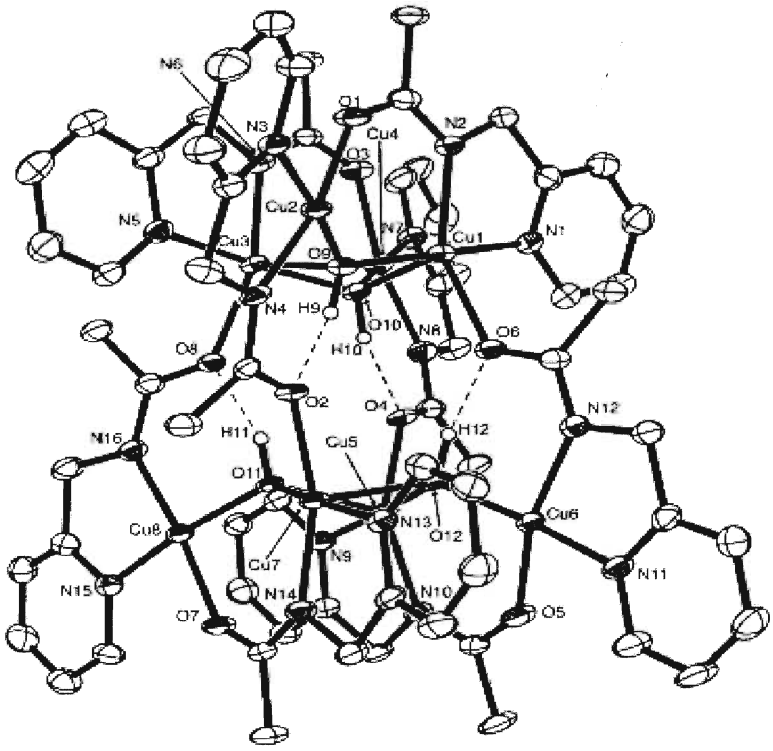

(2.20)

Figure 2.28. ORTEP plot of the molecular structure of $[Cu_8L_8(OH)_4]^{4+}$.[72] "Reprinted with permission from reference 72. Copyright {2004} American Chemical Society."

Polynuclear cyclic arrays comprised of more than six metal ions assembled from large, flexible multidentate organic ligands via a more controlled approach that proceeds through an algorithm defined by the coordination preferences of the metal ion and the steric information contained within the ligand structure are much more rare. Matthews *et al.* demonstrated that the polytopic diazine ligand **(2.21)** with $Cu(ClO_4)_2.6H_2O$ could afford a circular array of eight copper (II) centres, Figure 2.29.[73]

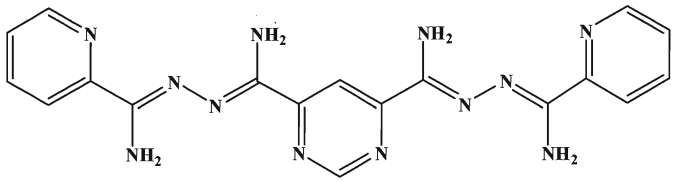

(2.21)

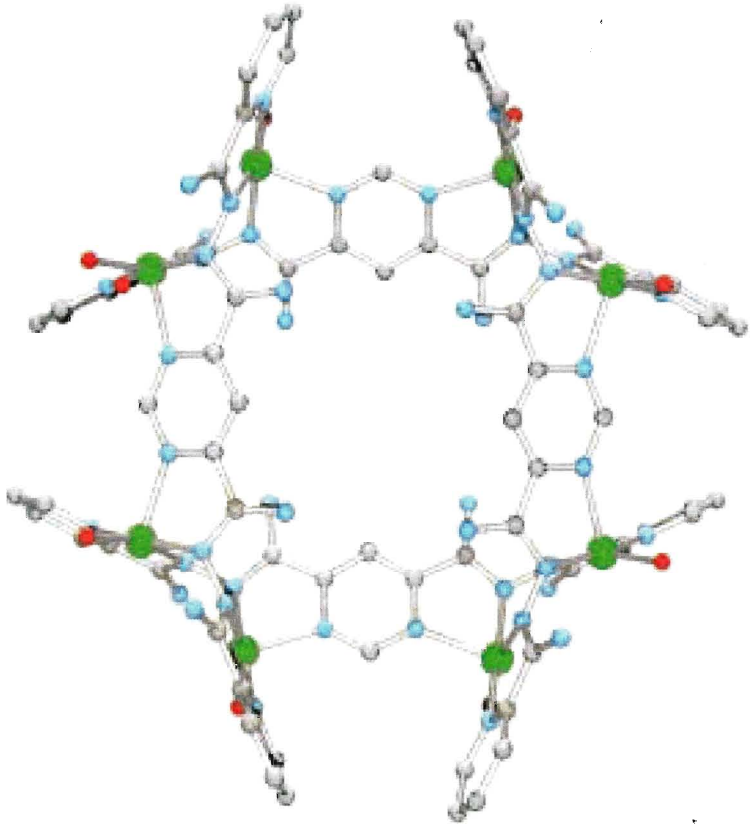

(2.22)

Figure 2.29. POV-Ray representation of the X-ray structre of an octanuclear copper(II) circular array.[73] Reproduced with permission from reference 73. Copyright 2004 Wiley-VCH.

More recently a novel octanuclear copper(II) nucleoside wheel was reported by De Munno *et al.*[74] Since nucleoside bases contain a large number of oxygen and nitrogen donor sites of different basicity they are also suitable ligands for the self-assembly of cyclic polynuclear metal complexes. The complex was obtained by the serendipitous

method of self-assembly and exhibits a fascinating calixarene-like structure which is made up of octanuclear $[Cu_8(Hcyd)_8(CF_3SO_3)_4]^{4+}$ (**2.23**) rings that include mononuclear $[Cu(H_2O)_6]^{2+}$ cations, Figure 2.30. Uncoordinated triflate anions and water molecules are also present in the structure.

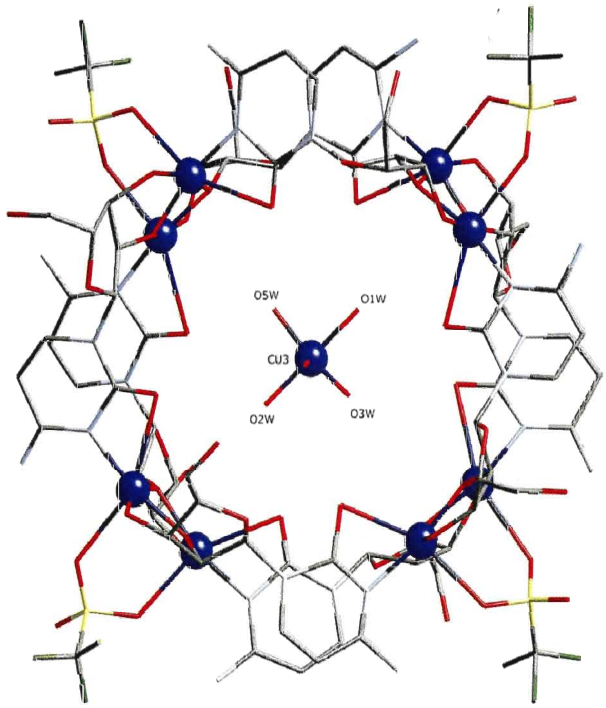

(2.23)

Figure 2.30. View of the octanuclear $[Cu_8(Hcyd)_8(CF_3\text{-}SO_3)_4]^{4+}$ host together with the mononuclear $[Cu(H_2O)_6]^{2+}$ guest.[74] "Reprinted with permission from reference 74. Copyright {2007} American Chemical Society."

2.6 Preparation and characterization of ligand (2.25)

Given that ligand **2.8** afforded such a unique cluster we turned our attention to investigate the coordination chemistry of the closely related pyridine system **(2.25)**, Figure 2.31. Although the tert-Bu pyrazole ligand was not reported in the literature, its methyl analogue of this ligand was known.[75]

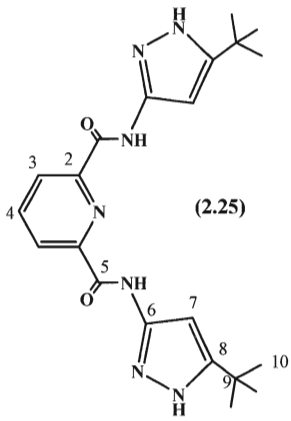

Figure 2.31. Molecular structure of **(2.25)** with appropriate numbering scheme.

The methyl derivative was previously prepared and studied for the treatment of diseases based on abnormal protein structures.[75] To the best of our knowledge, no coordination complexes of this ligand have been reported to-date. Ligand **(2.25)** was prepared from following the strategy outlined previously in Scheme 2.4 and isolated as a pale yellow solid in 71% yield. 2,6-Pyridinedicarbonyl dichloride **(2.24)** was prepared in one step from commercially available 2,6-pyridinedicarboxylic acid following modification of literature methods.[76]

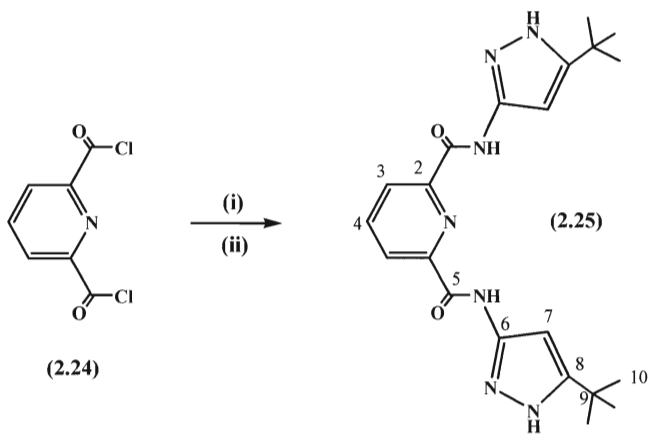

Scheme 2.4. Synthetic route for the preparation of ligand **(2.25)**. **Reagents and conditions:** (i) 3-amino-5-*tert*-butyl-pyrazole; (ii) toluene, reflux, 4 h.

The molecular structure of **(2.25)** was confirmed by NMR, IR and high resolution FAB mass spectroscopy. The ^{1}H NMR spectrum showed peaks for N-H pyrazole and amide protons downfield at 13.04 and 12.21 ppm, respectively. A doublet at 8.39 and multiplet at 8.31 ppm were assigned to the C_3 and C_4 protons of the pyridine ring. The singlet at 6.66 was assigned to the proton at C_7 position of the pyrazole ring. Finally, the singlet at 1.49 is consistent for the *tert*-butyl CH_3 protons.

The ^{13}C NMR spectrum of **(2.25)** has a peak at 162.2 ppm characteristic of the amide C=O. Peaks at 155.3, 126.3, 94.5 are assigned to the C_6, C_3 and C_7 of the pyrazole ring. Peaks at 148.7, 144.2, and 140.6 ppm are assigned to the bipyridine carbons at the 2, 8 and 4 positions respectively. The final two peaks at 31.6 and 30.1 ppm are consistent with C_9 and C_{10} carbons of the *tert*-Bu groups. The IR spectrum of **(2.25)** has a single broad band above 3000 cm^{-1} consistent with the N-H str of the amide and pyrazole groups. Two additional bands, a sharp singlet at 2974 cm^{-1} and a broad intense band at 2608 cm^{-1} are also present. The Amide I [υ C=O] band is present as a sharp band at 1712 cm^{1}. The Amide II band is also present at 1554 cm^{-1}. The FAB mass spectrum of this ligand, is consistent with its molecular structure, showing a parent ion $[MH]^+$ peak at *m/z* = 410.22867 for $C_{21}H_{27}N_7O_2$.

2.6.1. Coordination chemistry of ligand (2.25)

Coordination of ligand **(2.25)** together with $CuCl_2$ in the presence of triethylamine was carried out in methanol. Fortunately, single crystals of complex **(2.26)** were grown via the slow diffusion of diethyl ether into a concentrated reaction solution of the complex. Dark green blocks were obtained after 3 days, Figure 2.32.

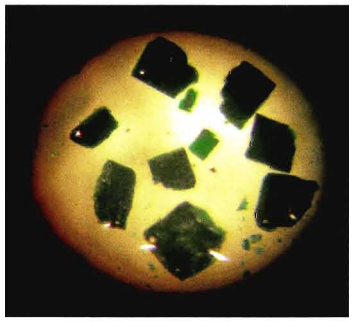

Figure 2.32. Single crystals of **(2.26)**.

Although the crystals were large enough and well formed, they only diffracted out to about 1.2 Å resolution. This observation is unfortunately fairly typical for a large structure that contains a lot of disordered solvent in the crystal lattice. Nevertheless, as much data as possible was collected on the diffractometer and we were able to solve and partially refine the crystal structure applying suitable constrains to the model. The X-ray data are reasonable enough to elucidate the molecular structure of the complex. A more intense X-ray source, such as a synchrotron, is needed in order to improve the resolution of the data for publication. This complex is a large copper cluster of stoichiometry $[Cu_9(L)_6Cl_6]$. It crystallizes in the trigonal space group R-3c. Only part of the cluster is crystallographically unique and this is shown in Figure 2.33 together with the appropriate labeling scheme. A view of the molecular structure of the cluster, viewed down its 3-fold axis is shown in Figure 2.34.

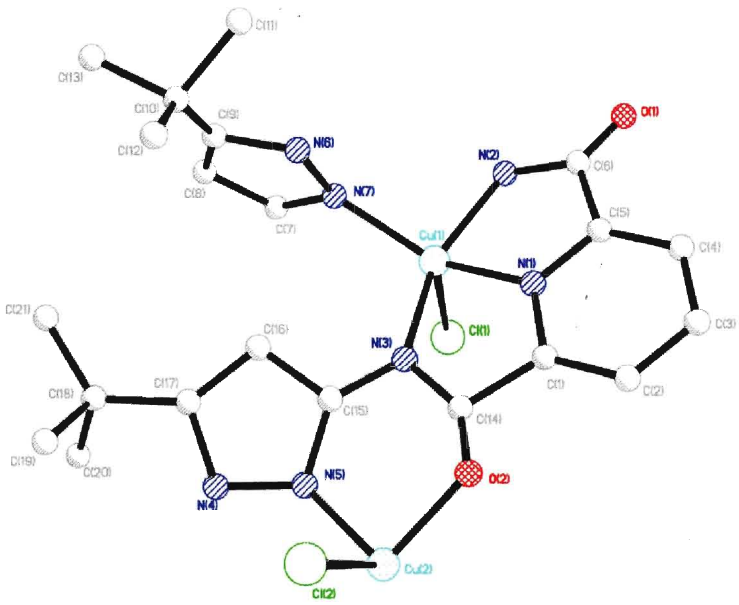

Figure 2.33. Molecular structure of the crystallographically unique fragment of the cluster **(2.26)** with labeling scheme. H-atoms are omitted for clarity.

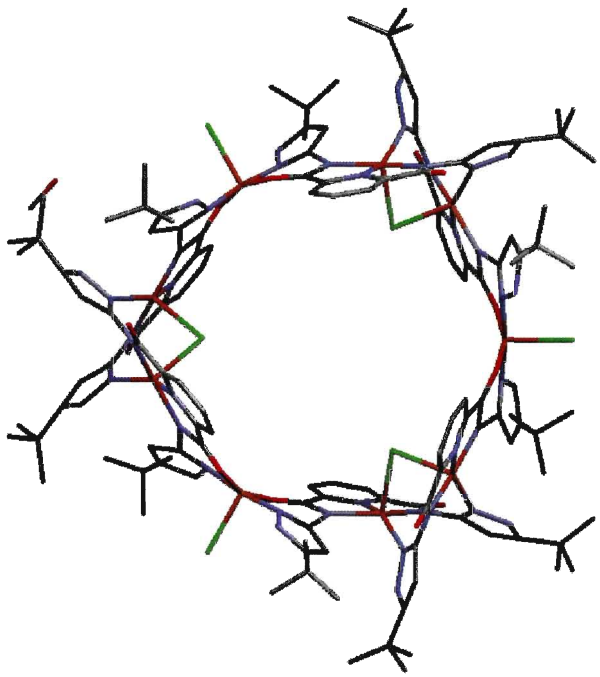

Figure 2.34. View of the molecular structure of $[Cu_9(L)_6Cl_6]$, **(2.26)**. View down the 3-fold axis.

The cluster contains a large amount of disordered solvent. Elemental analysis data on the single crystals is a reasonable fit for $[Cu_9(C_{21}H_{25}N_7O_2)Cl_6]\cdot CH_3OH\cdot 5H_2O\cdot (C_2H_5)_3N$. Each ligand coordinates three copper centers and each copper ion shares two ligands to connect six ligands with nine copper ions. The amide nitrogens are completely deprotonated in the complex. Interestingly, both amide N and O atoms coordinate metal centres. There are six chloride ions, three of which are bridging two neighbouring Cu(II) centers. A view of the cluster showing the coordination geometry around the two crystallographically unique copper centers Cu1, Cu2, and the shortest intermolecular Cu···Cu distances are shown in Figure 2.35.

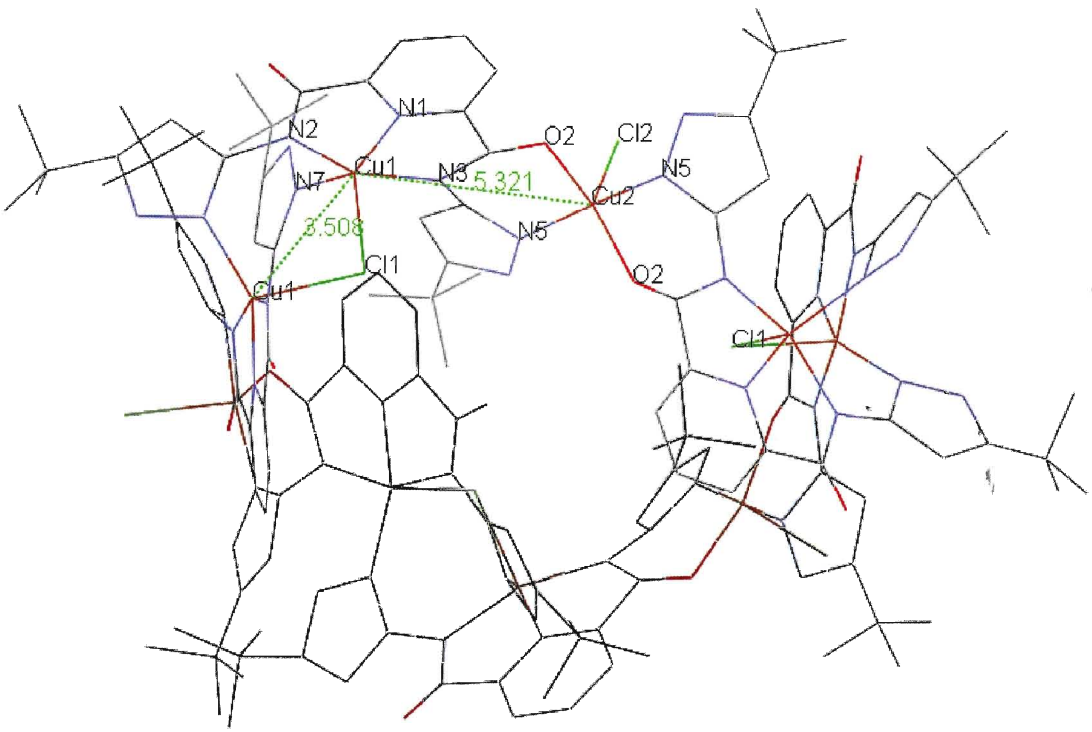

Figure 2.35. View of **(2.26)** showing the coordination geometry around the copper centres. The shortest intramolecular Cu···Cu distances are shown as green dashed lines, distances are given in Å.

Given the low resolution of our data, we have not carried out a detailed geometrical analysis of the coordination geometry around the copper centres. It is however clear that both copper centres are five-coordinate. The first copper centre, Cu1 is coordinated in the tridentate binding pocket of the ligand via the pyridine (N1) and two amide nitrogens (N2 and N3). The pyrazole nitrogen from a second ligand (N7) completes the equatorial ligands around the copper. The axial position is occupied by a chloride ion (Cl1) which also acts as bridge between neighbouring, symmetry related, copper ions. The second copper is equatorially coordinated via a carbonyl oxygen (O2) and a pyrazole N (N5) from two symmetry related ligands. Once again an axial chloride ligand (Cl2) completes the five-coordinate geometry, Figure 2.35.

In order to chelate in this manner the pyridyl amide part of the ligand remains planar, but the pyrazole rings are rotated in order to facilitate their chelation to metal ions. In this respect, one of the pyrazole nitrogens is facing towards the binding pocket of the ligand, whereas the second pyrazole nitrogen is rotated away by 180^0 so that it is *cis* with respect to the amide carbonyl group. In this manner it can chelate a neighbouring copper centre and facilitate the assembly of the cyclic structure. The cluster has a cavity 11 Å in diameter, Figure 2.34, which is acts as a guest for disordered solvent molecules. There is disordered solvent in the cavity of the cluster that is H-bonded to atoms of the cluster however the majority of solvent was removed from the model during the refinement since it was disordered, so we cannot comment in any detail regarding the H-bonding interactions between solvent molecules and the clusters. The packing diagram of **(2.26)** shows a honeycomb arrangement of clusters, Figure 2.36.

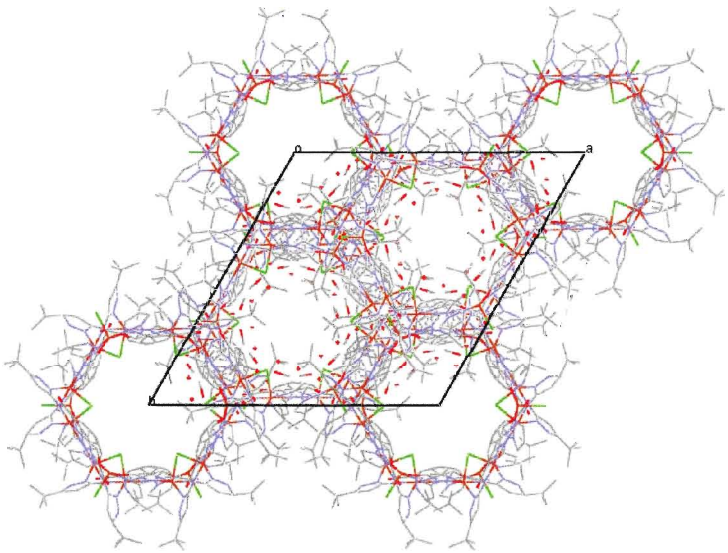

Figure 2.36. Packing diagram of **(2.26)**. View down the c-axis.

The UV-vis spectrum of this complex shows two bands at $\lambda = 254$ ($\varepsilon = 67339\ M^{-1}cm^{-1}$) and 299 nm ($\varepsilon = 52477\ M^{-1}cm^{-1}$) assigned to the low energy n to π^* and π to π^* transitions of the ligand, Figure 2.37. A band observed at $\lambda = 673$ nm ($\varepsilon = 1354\ M^{-1}cm^{-1}$) is consistent with *d-d* transitions.

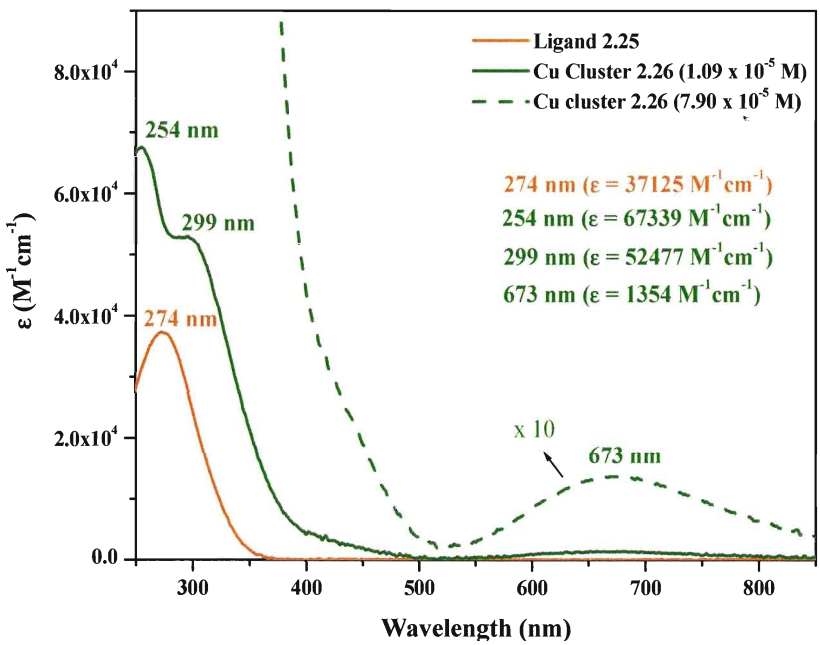

Figure 2.37. UV-vis absorption spectra of copper(II) complex **(2.26)** and its corresponding ligand in methanol at room temperature.

The FAB mass spectrum of this complex shows fragment ion peaks at *m/z* = 1067, 1005, 533 and 472 for $[Cu_2(L)_2Cl_2+ H_2O+ CH_3OH]^+$, $[Cu(L)_2Cl_2+H_2O+CH_3OH]^+$, $[Cu_2(L\text{-}2H)]^+$ and $[Cu(L]]^+$ respectively. The IR spectrum of complex **(2.26)** contains a number of intense peaks in the range 2852 - 2957 cm^{-1}due to NH and OH str's. A sharp singlet cannot be clearly assigned to the amide I [υ C=O] band, but an intense band at 1465 cm^{-1} can be assigned to the amide II band.

An EPR spectrum of complex **(2.26)** in frozen methanol solution revealed a broad singlet around g = 2.05 (ΔH_{pp} = 284 G), Figure 2.38.[77]

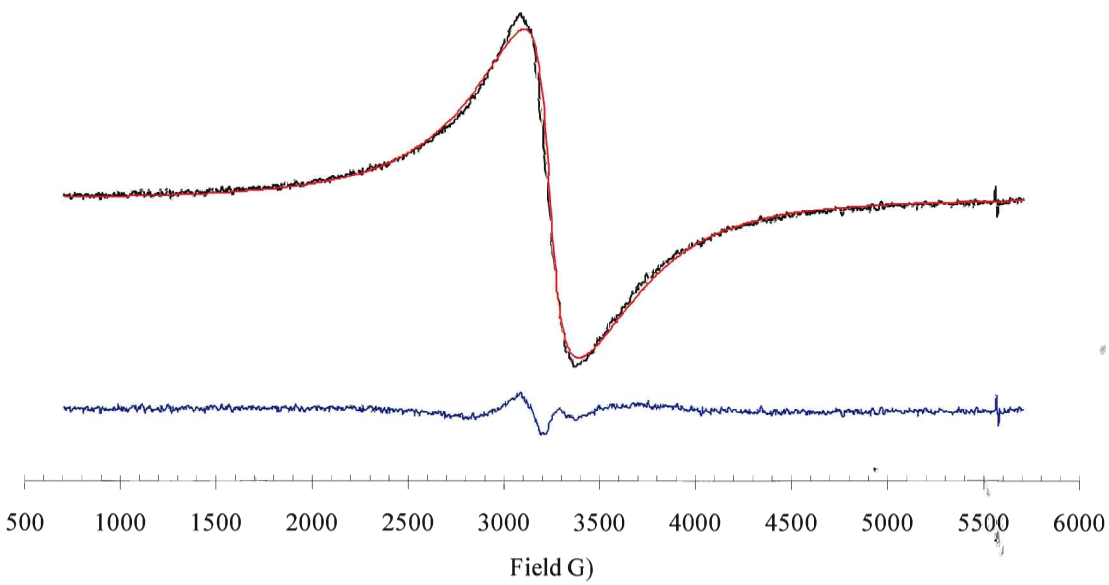

Figure 2.38. EPR spectrum of **(2.26)** in methanol at 100K. (black = experimental; red = simulation; blue = difference).[77]

However, the lineshape was slightly asymmetric indicative of some anisotropy and the spectrum was simulated with three Gaussians of differing linewidths (g_x = 2.042, g_y = 2.052 and g_z = 2.062 with ΔH_{pp} = 660, 540 and 90 G respectively). The broadness of the

EPR spectrum is consistent with significant dipolar line broadening consistent with retention of the structure in MeOH solution.

Magnetic susceptibility of **(2.26)** was carried under fields of 2000 Oe in the temperature range of 5-300 K, Figure 2.39. After correction for diamagnetism, the field dependence of the magnetization reveals a typical variation for uncoupled or weakly coupled spins. The value of the magnetization at room temperature is 3.53 cm^3Kmol^{-1} which is slightly lower than the value of 3.72 expected for nine uncoupled S = ½ and g = 2.1. From the magnetic data for the cluster we can conclude that until about 80 K, the metal centers behave as isolated spins. The $\chi_M T$ value slightly decreases from 3.47 cm^3Kmol^{-1} at 80 K to reach a minimum of 2.15 cm^3Kmol^{-1} at 5 K indicating a presence of weak antiferromagnetic interactions.

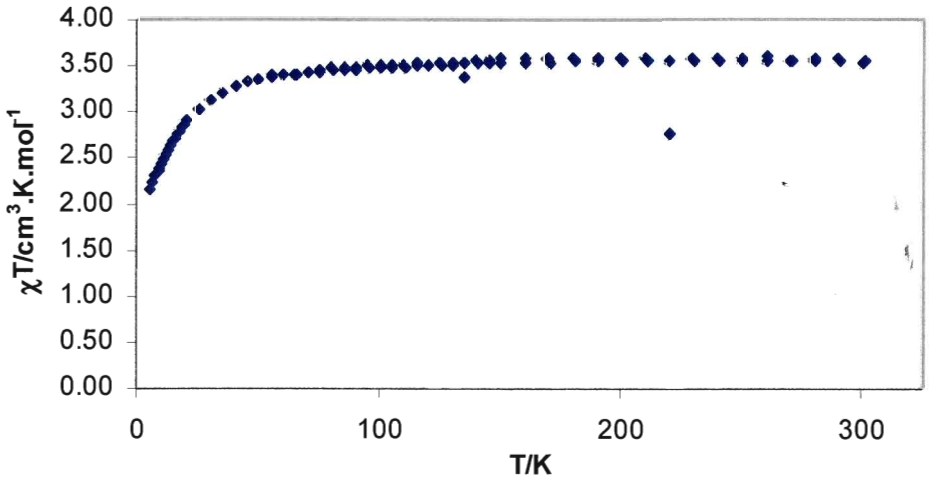

Figure 2.39.Temperature dependence of the χT *vs* temperature for **(2.26)**.

Nonanuclear copper clusters assembled from organic ligands are much less common than their octanuclear neighbours. A nonanuclear copper(II) complex was assembled from a small, rigid pentadentate Schiff-base ligand with N_2O_3 donor atoms

(2.27). This structure consists of four dincuclear $[Cu_2L]^+$ units linked covalently to a central copper atom by four μ-OH, thus yielding a nonacopper core, Figure 2.40.[78]

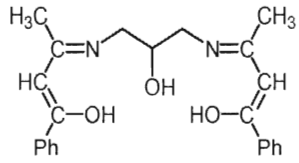

(2.27)

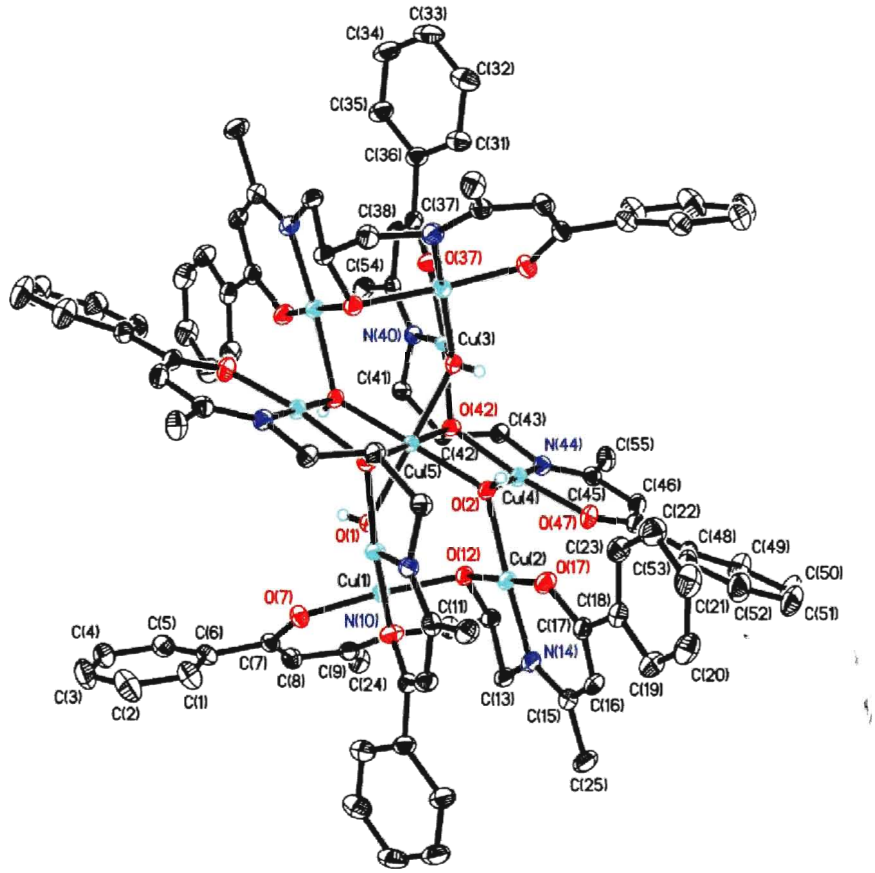

(2.28)

Figure 2.40. Molecular structure of nonanuclear copper(II) cluster.[78]. Reproduced by permission of the Royal Society of Chemistry (RSC).

Powell *et al.* have reported a series of high nuclearity clusters prepared from small organic ligands. In this respect, a nonanuclear Cu(II) carboxylate-bridged cluster aggregate $[Cu_9(cpida)_6(MeOH)_6]\cdot 6(MeOH)$ {H_3cpida = 2-(carboxyphenyl)iminodiacetic

acid **(2.29)**}, **(2.30)** was reported in 2004, Figure 2.41.[78] This cluster is made up of two weakly ferromagnetically coupled carboxylate-bridged Cu_4 units that are antiferromagnetically linked through a central Cu(II) to give a Cu_9 core with an $S = 7/2$ spin ground state.[79]

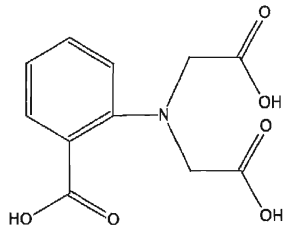

(2.29)

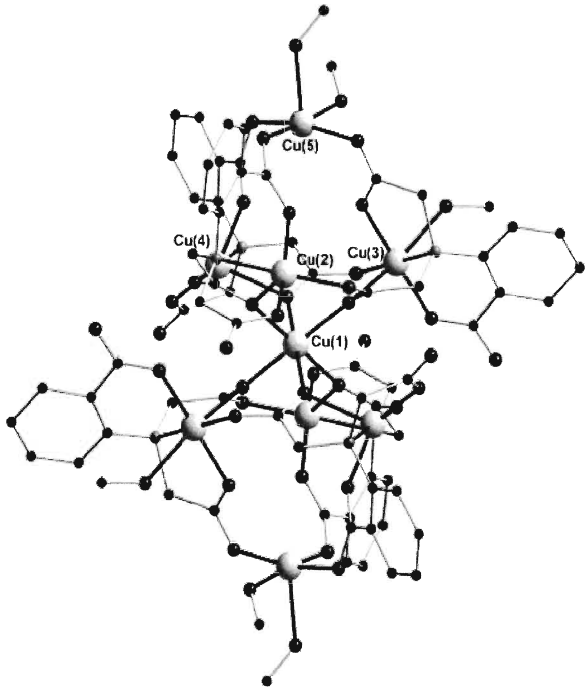

(2.30)

Figure 2.41. Molecular structure of **(2.30)**, all hydrogen atoms have been removed for clarity.[79] Reproduced by permission of the Royal Society of Chemistry (RSC).

In contrast, nonanuclear clusters prepared from larger flexible polydentate organic ligands are rare. A search of the chemical literature reveals only two examples. The first, a Cu_9 complex assembled from a tripodal amido ligand with a central non-chelating

phosphorus donor that allows for the facile assembly of a pentanesoluble organometallic copper cluster, with a central copper atom surrounded by a nonplanar chain of eight copper atoms and two terminal amido-copper bonds, Figure 2.42.[80]

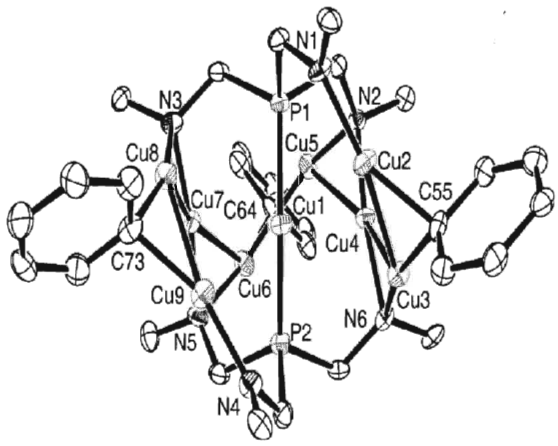

(2.31)

Figure 2.42. ORTEP depiction of the solid-state structure of **(2.31)**, with 50% probability ellipsoids. Hydrogen atoms are omitted. Only the ipso carbons of the 3,5 bis(trifluoromethyl)phenyl substituents are shown. The 1,3,5 methyl substituents of the mesityl groups and short contacts between the central and outer copper atoms are omitted for clarity.[80]. Reproduced by permission of the Royal Society of Chemistry (RSC).

The second example is the M_9 [3 x 3] grid-like structure that includes these complexes assembled by Thompson *et al.* from a series of tritopic ligands containing a linear arrangement of coordination pockets, Figure 2.43.[81]

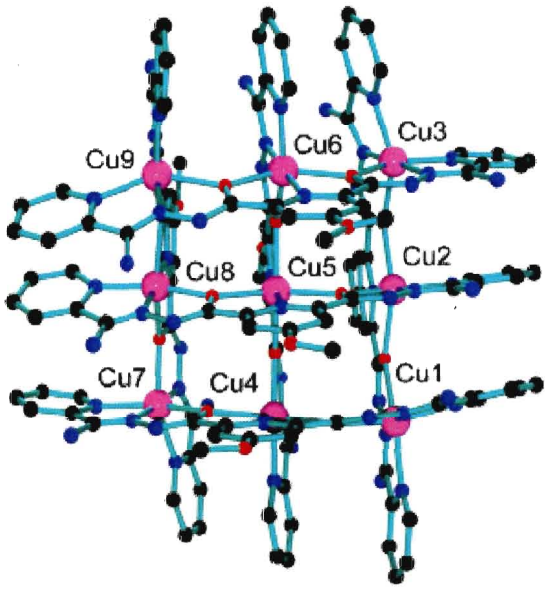

(2.32)

Figure 2.43. Cu_9 grid reported by Thompson *et al.*[81a] "Reprinted with permission from reference 81a. Copyright {2004} American Chemical Society."

Although there are examples of mixed copper/lanthanide clusters and nonanuclear clusters of other transition metals e.g. Ni(II),[72] the majority of these high nuclearity clusters are assembled from small organic ligands by serendipitous self-assembly rather than via a rational self-assembly approach involving the design of larger more flexible polytopic ligands.

2.7 Summary and future work

The design of ligands that support transition metal clusters or organized assemblies of metals has multiple goals. Such complexes can exhibit novel reactivities based on cooperativity or electron transfer between metal centres, as well as unique physical properties such as luminescence or magnetism that result from interactions between metal centres. Unfortunately, the design of ligands that can support clusters or assemblies of metals with a variety of transition metals is rarely straightforward.

Within the timeframe of these studies, four new pyridine carboxamide ligands **(2.6)**, **(2.7)**, **(2.8)** and **(2.25)** have been prepared and characterized. Ligands **(2.6)**, **(2.7)** and **(2.8)** contain a 4,4'-bipyridine backbone, while the core of **(2.25)** is a pyridine ring. The molecular structures of ligands **(2.7)** and **(2.8)** have been characterized by X-ray crystallography which reveals they adopt fairly planar conjugated structures that are π-π stacked in the solid state.

Coordination of ligand **(2.8)** with copper(II) acetate in the absence of base resulted in the assembly of the first hyperboloid saddle-like octanuclear complex. Here the Cu(II) ions adopt two different geometrical environments, distorted trigonal bipyramidal and distorted square pyramidal. The shortest intramolecular Cu(II)···Cu(II) distances within the cluster are 7.462 Å. The magnetic susceptibility data for **(2.17)** is consistent with very weakly antiferromagnetically coupled spins below 50 K. Coordination of ligand **(2.25)** with copper(II) in the presence of base resulted in the assembly of a cluster that comprises nine Cu(II) ions. Because of the chloride bridge between the Cu(1) and Cu(2) centers in this compound, the ligand is forced to twist and the structure takes on a wheel like, cyclic

form. This circular array possesses an S_6 axis that holds nine copper (II) ions in a hexagonal shape. Here the Cu (II) ions adopt five coordinate geometries. The shortest intramolecular Cu(II)···Cu(II) distances in the cluster are 3.51 Å.

Our results show that this series of bipyridyl carboxamide ligands are promising building blocks for the preparation of multinuclear complexes. The most challenging part of this work has been dealing with the poor solubilities of both the ligands and their complexes. This problem, however, can be rectified by the introduction of alkyl chain subsituents onto the appended arms. Although this thesis only contains a description of two complexes from ligands **(2.8)** and **(2.25)**, a number of coordination complexes were prepared with other transition metal ions, but we have been unscuccessful to-date in growing suitable crystals of these complexes to elucidate their molecular structures. More work is needed to carefully characterize these complexes. Furthermore, both clusters **(2.17)** and **(2.26)** have uncoordinated binding sites, so they could also perhaps bind a second metal ion which could allow for the preparation of larger heterometallic clusters.

The EPR data of cluster **(2.26)** is quite promising in this respect as it indicates that the cluster remains intact in solution. Finally the coordination chemistry can be repeated, but this time systematically varying the metal salts, the base used and the solvent. With respect the cluster **(2.26)**, we are in the process of obtaining higher resolution X-ray diffraction data so that we can refine the model to a fit acceptable for publication. Additional magnetic measurments are also required to fully characterized its magnetic properties. The lack of examples of higher nuclearity complexes containing greater than six metal ions in the chemical literature assembled via a rational approach, employing

ligand design, highlights the challenges faced in this field of supramolecular coordination chemistry.

CHAPTER 3

Introduction to Spin Crossover and a Review of the Chemistry of an $[N_3O_2]$ Macrocycle

3.1. Spin crossover systems

The phenomenon of spin crossover was discovered by Cambi and Szegö as part of a study on iron(III) *tris*(N,N-dialkyl-dithiocarbamato) complexes in the early 1930s, whose magnetic moments were shown to be temperature-dependent.[82] Their initial interpretation of this unusual magnetic behaviour was in terms of thermal equilibrium between two different magnetic isomers. The high temperature isomer having μ_{eff} = 5 B.M. and the low temperature isomer having μ_{eff} = 1 B.M. This suggestion was only clarified 30 years later, when the physics behind spin crossover was first proposed.[83] The magnetic isomers of these compounds do not have different chemical structures, as had been proposed. Rather they reflect the ability of the same molecule to adopt one of two different electronic states, with different distributions of electrons in its frontier d orbitals.

3.2. Ligand field strength and SCO

In octahedral ligand fields, transition metal ions with $[Ar]3d^4$–$3d^7$ electronic configurations can be distinguished by different occupations of the antibonding e_g and the nonbonding t_{2g} d orbitals of the central metal ion. If the spin pairing energy P, is large compared to Δ (ligand field strength), the d electrons are arranged according to Hund's rule to give the maximum number of unpaired electrons. In this case, the complex is referred to as high-spin (HS). If the splitting of the d orbitals is large with respect to the pairing energy ($\Delta > P$), it is more favourable for electrons to pair in the t_{2g} level, and the

metal complex adopts the low-spin state (LS). Most Cr(II), Mn(II), Mn(III), Fe(II), Fe(III), Co(II) and Co(III) complexes can be classified in one of these two families. When the two interactions are comparable ($\Delta \approx P$), *i.e.*, close to the critical point (Δ_c), an electron in the highest suborbital may transfer into the lowest suborbital and change its spin direction in a controlled, detectable and reversible manner, by the applied action of temperature, pressure or via light irradiation. This gives birth to a new family of complexes called spin crossover. Thus, the spin transition (ST) phenomenon corresponds to an intra-ionic transfer of electron between the t_{2g} and the e_g orbitals centered in the immediate environment of the metal ion.

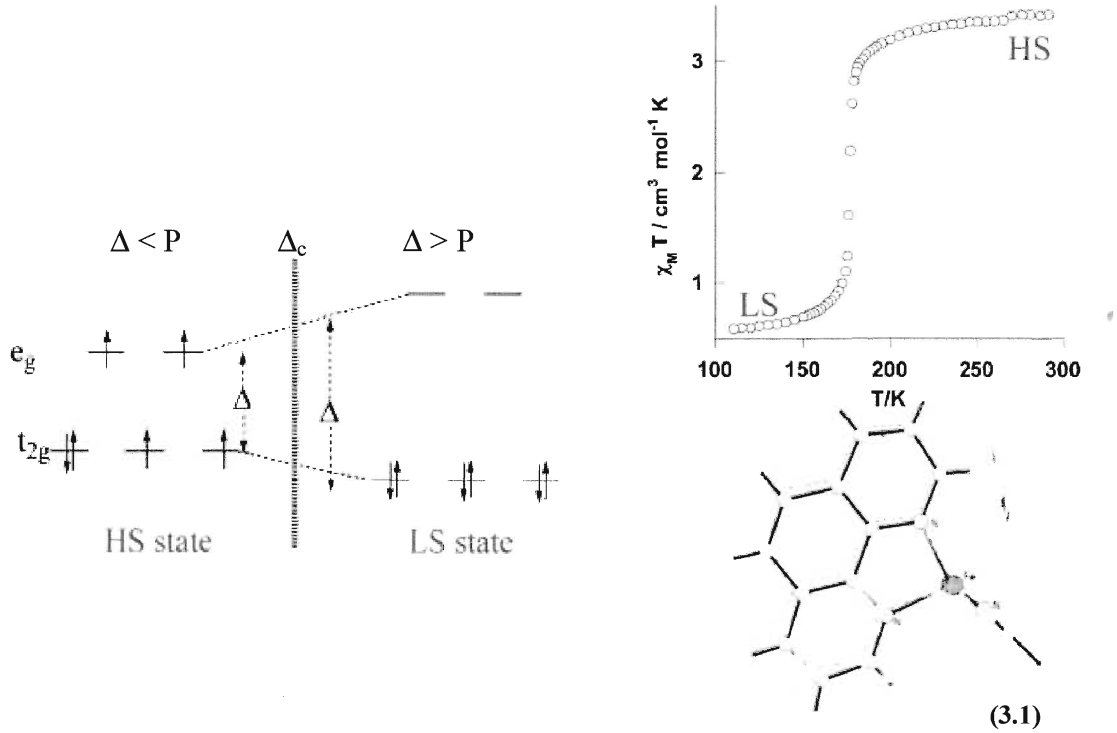

(3.1)

Figure 3.1. The electron configuration of HS and LS states for the [Ar] $3d^6$ (left).The magnetic behaviour (top right) and overlay of the HS (dotted line) and LS (black line) structural unit for $[Fe(phen)_2(NCS)_2]$ (bottom right).[84] Reproduced by permission of the Royal Society of Chemistry (RSC).

Figure 3.1 shows, the electronic configuration of HS and LS states for an octahedral d^6 system as well as the overlay of the HS and LS of $[Fe(phen)_2(NCS)_2]$, **(3.1)** and its magnetic behaviour. Compound **(3.1)** is one of the first Fe(II) spin crossover compounds whose spin transition was discovered in 1964 , Figure 3.2.[85]

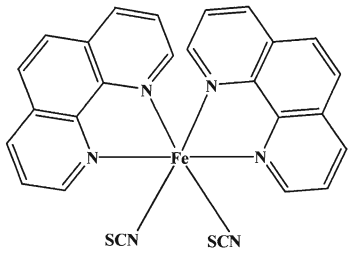

(3.1)

Figure 3.2. Molecular structure of **(3.1)**.

3.3. Photo-conversion of spin states and the relaxation process

The first example of photoinduced magnetization changes of spin state were observed by McGarvey and Lawthers in solution at high temperature,[86] however, the resulting light-induced states were of the order of submicroseconds to microseconds. Following this pioneering discovery, Decurtins *et al.* observed a photoinduced LS → HS transition for the Fe(II) SCO compound $[Fe(ptz)_6][BF_4]_2$, **(3.2)** where ptz = 1-propyltetrazole in the solid state at 10 K, Figure 3.3.

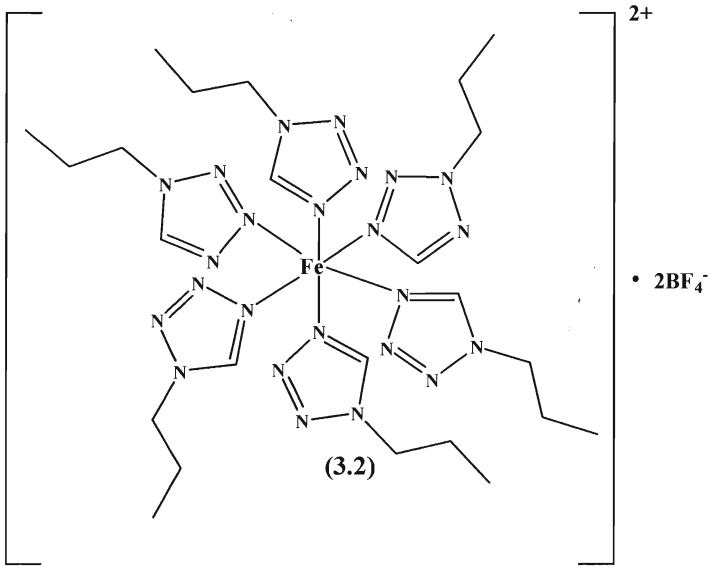

Figure 3.3. Molecular structure of (**3.2**).

Subsequently, the term "light-induced excited state spin trapping (LIESST)" was used to describe this effect.[87,88] In fact, irradiating a crystal of **(3.2)** at 10 K with green light (λ = 514.5 nm) into the spin allowed $^1A_1 \rightarrow {}^1T_1$ d–d absorption band gives access to a metastable state $^1T_1$ or to the intermediate state $^3T_1$ (if pumping with light of λ = 980 nm), Figure 3.4.[89] The excited state $^1T_1$, rapidly decays through the intermediate state $^3T_1$ to either return back to its original ground state $^1A_1$ or to reach the $^5T_2$ high spin ground state. Figure 3.4 indicates the possibility of pumping the system back to the low-spin state by selectively irradiating with red light (λ = 820 nm), into the maximum of the $^5T_2 \rightarrow {}^5E$ band of the trapped high-spin compound.[90]

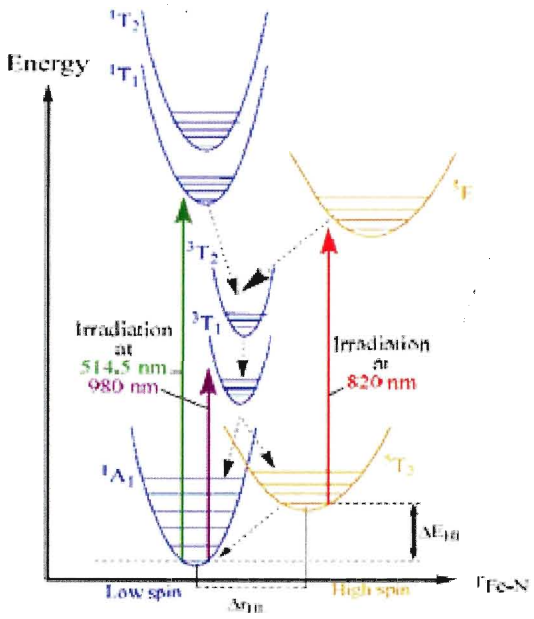

Figure 3.4. Electronic structure of Fe(II) spin crossover complexes and mechanisms of LIESST and reverse-LIESST.[84] Reproduced by permission of the Royal Society of Chemistry (RSC).

3.4. Spin crossover and cooperativity

Spin crossover behaviour is observed for systems in both solution and the solid state, although the material will not necessarily display the SCO transition in both phases. In solution, interactions between the molecules undergoing spin change are virtually negligible and thus the course of the transition can be described using a temperature dependent Boltzmann distribution over all HS vibronic states and the LS state. The thermal transition is a molecular process and not subject to cooperative interactions. That is, an interaction of the constituent subunits of a system causing a conformational change in one subunit to be transmitted to all others. In this instance, the transition occurs essentially at the molecular level without the constraints of lattice interactions.

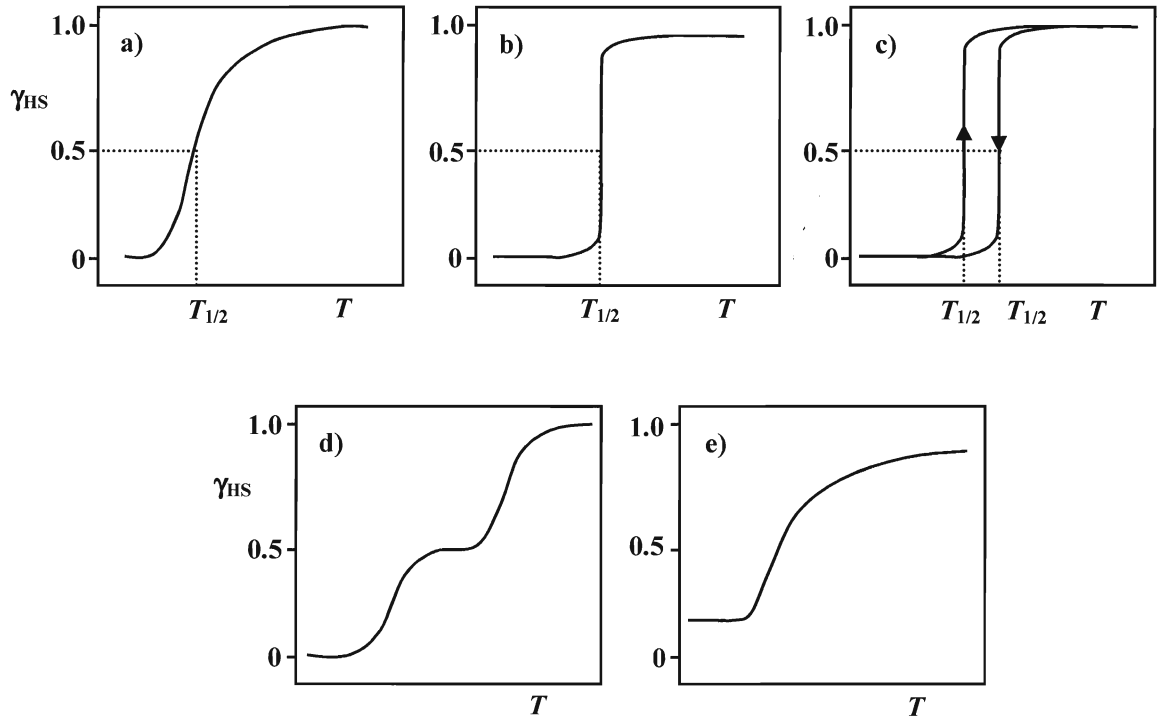

Figure 3.5. The nature of ST curves for SCO systems in the solid state: (a) gradual (b) abrupt (c) with hysteresis (d) with steps (e) incomplete.[91] "Adapted from figure 1 of reference 91."

For solid systems, lattice effects play a role, Figure 3.5 (a–e). The transition may be gradual and continuous over an extended temperature range, Figure 3.5(a), or it may be abrupt and occur within a narrow temperature range, Figure 3.5(b). The transition may be associated with a thermal hysteresis loop, Figure 3.5(c) or be a two-step process, Figure 3.5(d). In certain cases, the transition may also be incomplete, Figure 3.5(e). When the cooperativity is poor, the transition is a gradual/continuous process, Figure 3.5(a). The transition becomes more abrupt as the cooperativity increases, and sometimes can be associated with a phase change and thermal hysteresis, Figure 3.5(c). The transition temperature, $T_{1/2}$, is defined at which the fractions of HS and LS species are equal. For

transitions displaying hysteresis, two transition temperatures, $T_{1/2\downarrow}$ and $T_{1/2\uparrow}$, define the width of the hysteresis loop. The cooperative behaviour is effected by the following factors:

3.4.1. Influence of molecular shape on triggering cooperative behaviour

The largest group of compounds with available high-spin and low-spin crystal structures are from the $[Fe(1\text{-}bpp)_2]^{2+}$ series. One such example is $[Fe((3'\text{-}Me)_2\text{-}1\text{-}bpp)_2][BF_4]_2.xH_2O$ **(3.3)**, where $(3'\text{-}Me)_2$-1-bpp = 2,6-bis(3-methylpyrazol-1-yl)pyridine **(3.4)**, Figure 3.6. Compound **(3.3)** undergoes spin-crossover in two steps, both with hysteresis, Figure 3.8 (bottom), whose temperatures depend on the number of solvent H_2O's.

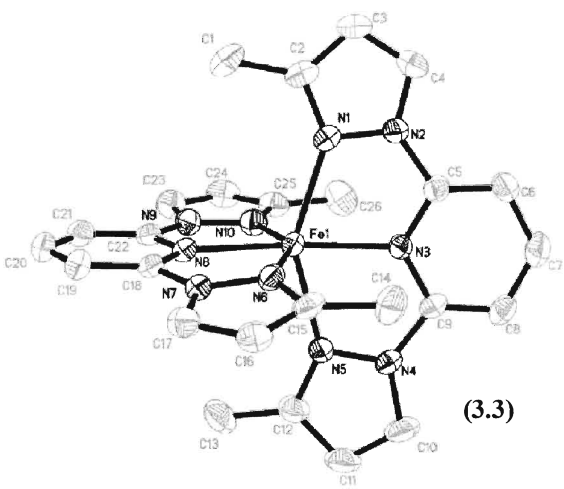

(3.3)

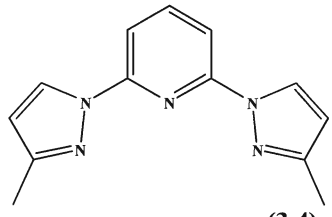

(3.4)

Figure 3.6. ORTEP plot of **(3.3)**, for clarity, all H atoms have been omitted (left). Molecular structure of ligand **(3.4)** (right).[92] Reproduced with permission from reference 92. Copyright 2005 Wiley-VCH.

The novel spin transitions in this compound are mediated by multiple crystallographic phase changes.[92] However, here the complex undergoes a larger than usual change in shape between the high- and low-spin states. This change is measured as a distortion parameter ($\Delta\theta$) where θ is the N-Fe-N angle measured on the projection of

two triangular faces of the octahedral along their common pseudo-threefold axes.[93] The value of $\Delta\theta$ for $[Fe((3'\text{-}Me)_2\text{-}1\text{-}bpp)_2][BF_4]_2$ **(3.3)** is 5.5° between their high- and low-spin structures. In contrast, all other $[Fe(1\text{-}bpp)_2]^{2+}$ complexes such as $[Fe(1\text{-}bpp)_2][BF_4]_2$, **(3.5)**, where 1-bpp = 2,6-bis(pyrazole-1-yl) pyridine **(3.6)**, Figure 3.7, have $\Delta\theta$ value of ≤ 0.61° for comparison.[94] These compounds show abrupt spin-crossover without hysteresis, Figure 3.8 (top).

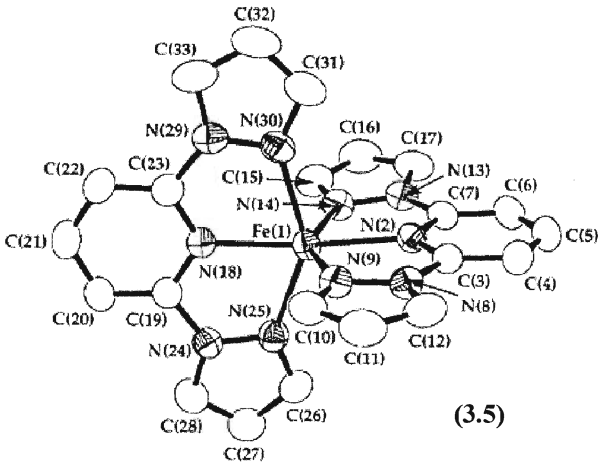

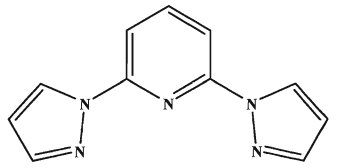

(3.6)

Figure 3.7. ORTEP view of **(3.5)**, for clarity, all H atoms have been omitted, (left). Molecular structure of ligand **(3.6)**, (right).[95] Reproduced by permission of the Royal Society of Chemistry (RSC).

Figure 3.8 shows the molecular structures of high- and low-spin $[Fe((3'\text{-}Me)_2\text{-}1\text{-}bpp)_2][BF_4]_2$ **(3.3)** and $[Fe(1\text{-}bpp)_2][BF_4]_2$ **(3.5)** as well as their magnetic behaviour. The high value of $\Delta\theta$ reflects this change in ligand conformation. It seems that the lattice rearrangements required to accommodate these additional changes in molecular shape are responsible for the complicated phase behaviour shown by this compound.

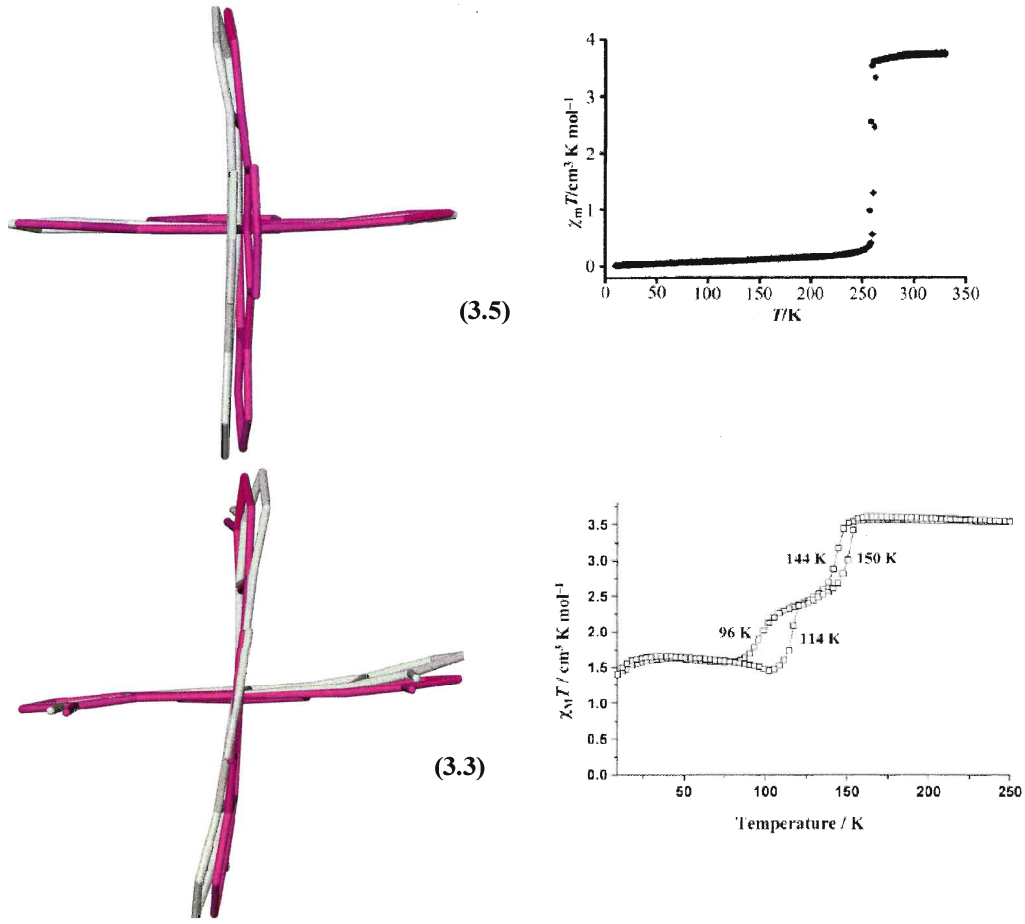

Figure 3.8. Overlays of the high-spin (white) and low-spin (purple) structures of the complexes [Fe(1-bpp)$_2$][BF$_4$]$_2$ and [Fe({3′-Me}$_2$-1-bpp)$_2$][BF$_4$]$_2$ and their magnetic behaviour (top and bottom).[92] Reproduced with permission from reference 92. Copyright 2005 Wiley-VCH.

3.4.2. Crystallographic disorder

Crystallographic disorder also proved to be responsible for unusual spin crossover cooperativity. This could result in a discontinuous spin-transition or abrupt and hysteretic low - high spin transitions.[94] Changes in anion or solvent disorder associated with spin-crossover are also common. One such example is the [Fe(pic)$_3$]Cl$_2$.ROH series (where pic

= 2-{aminomethyl}pyridine) that show multiple phase changes during the progress of their spin-transitions.[96]

3.4.3. Crystal packing

3.4.3.1. Interatomic contact

Another important factor, which effects spin crossover cooperativity is crystal packing. Crystal packing is strongly influenced by inter-atomic distances and non-covalent interactions that include, hydrogen bonding and π-π stacking. A relationship between crystal packing and cooperativity was noted in the crystal structures of $[Fe(NCS)_2(PM\text{-}R)_2]$, (R = aryl, PM = N-2-pyridylmethylene).[97] These compounds undergo spin crossover if 'R' is not too large, with widely varying degrees of cooperativity, and crystallise in one of two closely related crystal forms. In both lattices, the closest intermolecular interactions are C–H----S contacts between the 'R' substituents on one molecule and the thiocyanate ligands of its nearest neighbour, Figure 3.9.

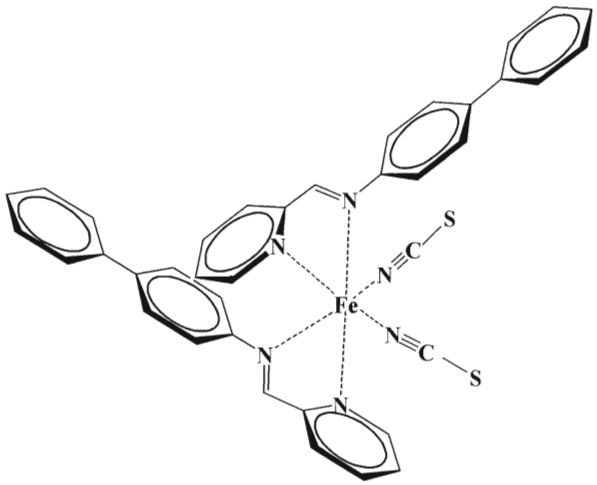

(R = biphenyl **3.8)**

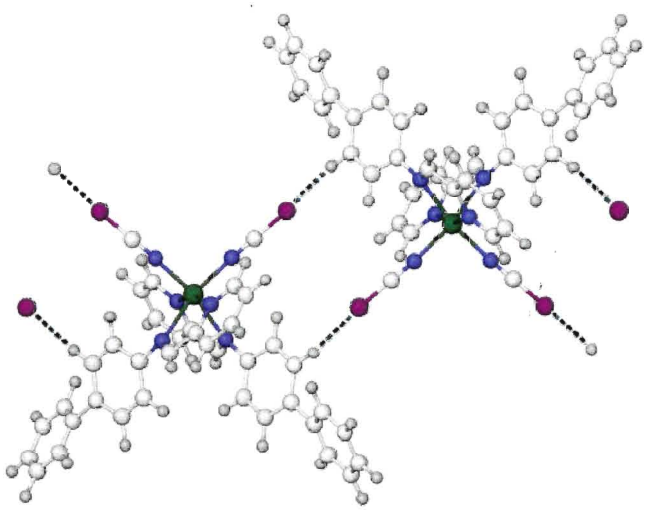

Figure.3.9. Molecular structure of **(3.8)** (top), Partial packing diagram of **(3.8)** in its high-spin state, showing the short intermolecular C–H----S contacts that are believed to mediate spin crossover cooperativity in this material (H----S = 2.8 Å).[97] Reproduced by permission of the Royal Society of Chemistry (RSC).

A good linear relationship was found between the width of the spin-transition, from susceptibility measurements, and the length of this crystallographic intermolecular contact in the high-spin state of the materials.[97] This result indicates that $[Fe(NCS)_2(PM\text{-}R)_2]$ compounds reproduced their different cooperativities (weak when R = $C_6H_4N{=}NPh$, **(3.7)** moderate when R = biphenyl, **(3.8)** and very strong when R = $C_6H_4C{\equiv}CPh$, **(3.9)**), and implied that changes in the electrostatic environment of the crystal lattice during spin crossover were important in generating a cooperative transition, Figure 3.10.[98]

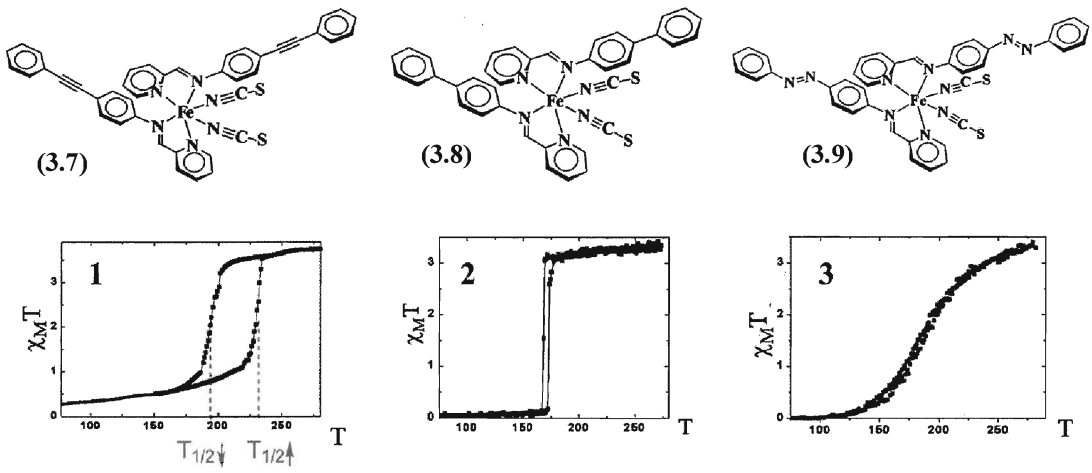

Figure 3.10. Molecular structure and magnetic behaviour of (**3.7**), (left), (**3.8**) (center) and (**3.9**) (right).[98]"Reprinted with permission from reference 98. Copyright {2009} American Chemical Society."

Significantly, the aryl substituents in these compounds crystals do not take part in intermolecular π–π interactions, ruling that out as an alternative mechanism for the transmission of cooperativity.

3.4.3.2. Hydrogen bonding

Direct hydrogen bonding (N–H----X or O–H----X) between spin crossover centres in a crystal would be expected to transmit cooperativity most efficiently. Hydrogen bonding between a complex and anions or lattice solvent is more common, showing abrupt and gradual transitions.[99]

3.4.3.3. π-π interactions

Since the majority of spin crossover complexes contain N-heterocyclic and/or phenoxy ligand donors, it is common for them to associate in the crystal through π-π interactions. It was proved that concerning the four related complexes $[Fe(NCS)_2L_2]$,

whose spin-crossover cooperativity increases along the series: L = btz (gradual)[100]; bipy or phen (abrupt, no hysteresis)[101]; dpp (abrupt, 40 K hysteresis loop)[102], where btz = 2,2′-bi-4,5-dihydrothiazine, bipy = 2,2′-bipyridine, phen = 1,10-phenanthroline and dpp = dipyrido [3,2-a:2′3′-c] phenazine, Figure 3.11.

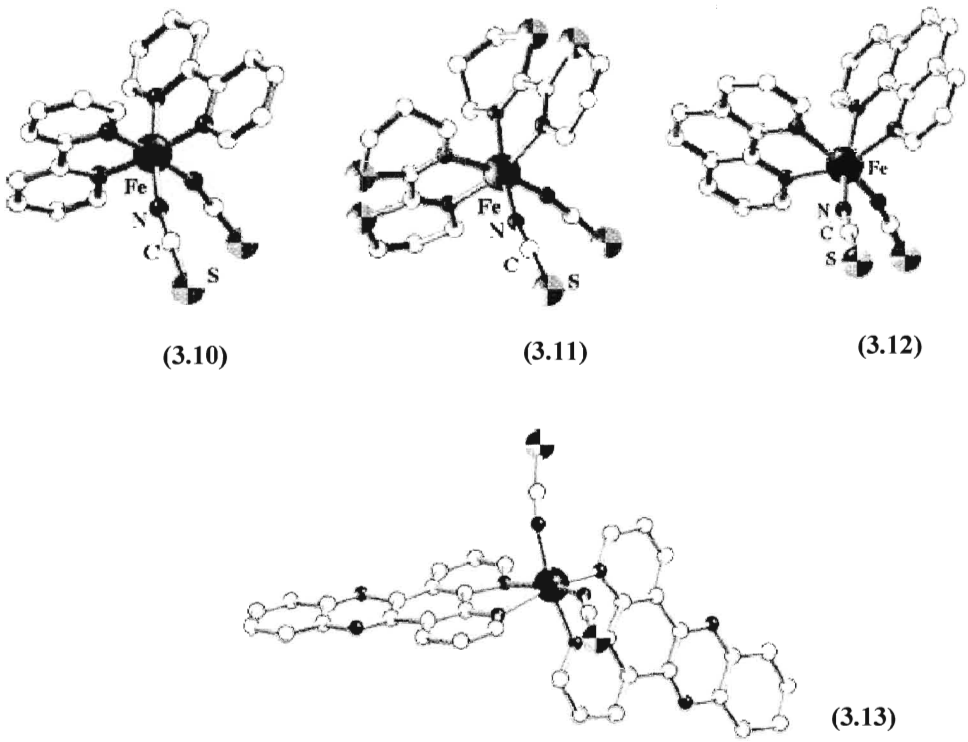

(3.10) **(3.11)** **(3.12)**

(3.13)

Figure. 3.11. Molecular structure of **(3.10)** left, **(3.11)** centre, **(3.12)**, right and **(3.13)**, bottom.[103] "Reprinted from Coordination Chemistry Reviews, 236, Real, J. A.; Gaspar, A. B.; Niel, W.; Muñoz, M. C. Communication between iron(II) building blocks in cooperative spin transition phenomena 124, 125., Copyright (2003), with permission from Elsevier.

Although the materials are not isostructural, their molecules each associate in the crystal through similar modes of face-to-face overlap of the L ligands on neighbouring molecules (which leads to π-π stacking for L = bipy, phen and dpp). Figure 3.12 shows π-π stacking between two dpp ligands. It is striking that the strength of these inter-ligand interactions perfectly parallels the cooperativity of spin-crossover in these complexes.

The btz, bipy and phen compounds all have a similar distribution of short intermolecular C–H----S contacts in their room temperature crystal structures. So, the influence of interatomic interactions is unlikely to be important for these complexes, and their π-π interactions are probably governing their different cooperativities. Figure 3.13 shows intra and inter molecular contacts in $[Fe(bipy)_2(NCS)_2]$.

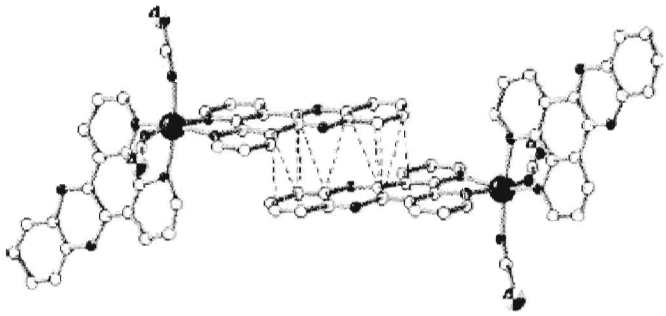

Figure. 3.12. Perspective view emphasising the stacking between two dpp ligands of two **(3.13)** units.[103]"Reprinted from Coordination Chemistry Reviews, 236, Real, J. A.; Gaspar, A. B.; Niel, W.; Muñoz, M. C. Communication between iron(II) building blocks in cooperative spin transition phenomena 127., Copyright (2003), with permission from Elsevier.

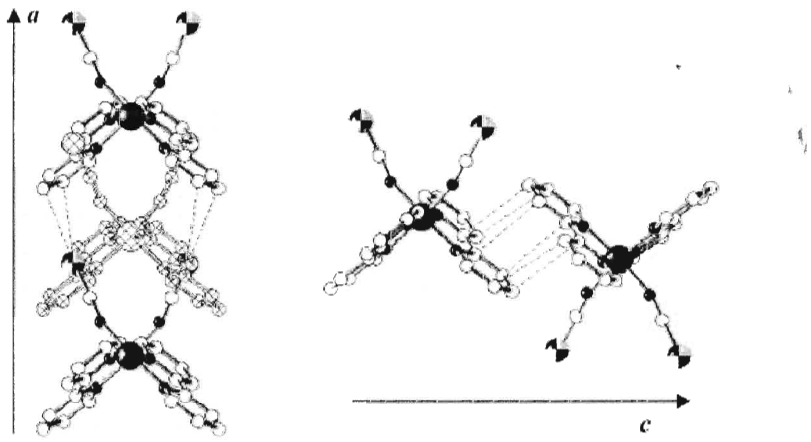

Figure. 3.13. Short intra-sheet S ---- C(left) and inter-sheet C ---- C(right) intermolecular contacts in **(3.10)**.[103] " Reprinted from Coordination Chemistry Reviews, 236, Real, J. A.; Gaspar, A. B.; Niel, W.; Muñoz, M. C. Communication between iron(II) building blocks in cooperative spin transition phenomena 127., Copyright (2003), with permission from Elsevier.

The design of new SCO complexes has a great interest. Up to now most of the SCO Fe(II) complexes involve polydentate ligands combining both N-heterocyclic and amino-aliphatic groups.[104] In this regard, the use of alternative polydentate ligands such as macrocyclic derivaties of **(3.14)** could provide different building blocks for new SCO systems. Since Fe(II) complexes of **(3.14)** present hysteresis as well as high LIESST temperatures,[105] new derivaties of this macrocycle lend themselves well to a range of potential applications in preparation of new materials potentially useful for rewritable optical, thermal, or pressure memories.[106]

3.5. $[N_3O_2]$ Schiff base-type ligand

It has been found that Fe(II) complexes of ligand **(3.14)** comprising on $[N_3O_2]$ pendentate macrocycle can form spin crossover compounds.[109] This ligand had attracted the interest of chemists for more than thirty years, Figure 3.14.[107] Complexes of ligand (**3.14**) were prepared via the metal templated condensation of 2,6-diacetylpyridine with 3,6-dioxaoctane-1,8-diamine in the presence of a metal salt.[107]

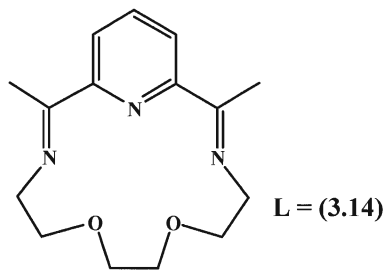

L = (3.14)

Figure 3.14. Molecular structure of ligand **(3.14)**

In 1864, Hugo Schiff discovered condensation of carbonyl compounds with primary amines.[108] The classical Schiff-base condensation of monocarbonyl compounds together with amines as the starting compounds occurs with high yields. However, the reactions of dicarbonyl compounds with diamines can result in a wide spectrum of

products, Scheme 3.1. This reaction (1:1 molar ratio) initially gives the acyclic product of a [1+1]-condensation **I**. Compound **I** can react with a dicarbonyl compound or a diamine to give the corresponding [2+1]-condensation product **II** or a [1+2]-condensation product **III**. By reacting compounds **II** and **III** together with a diamine and a dicarbonyl compound, respectively, the [2+2]-macrocycle **IV** and linear oligomers **V** can be obtained. It is very rare to get one of the products **I-IV** in the pure state. Usually a mixture of these compounds contains oligomeric products (oligomers **V**) of polycondensation are obtained.

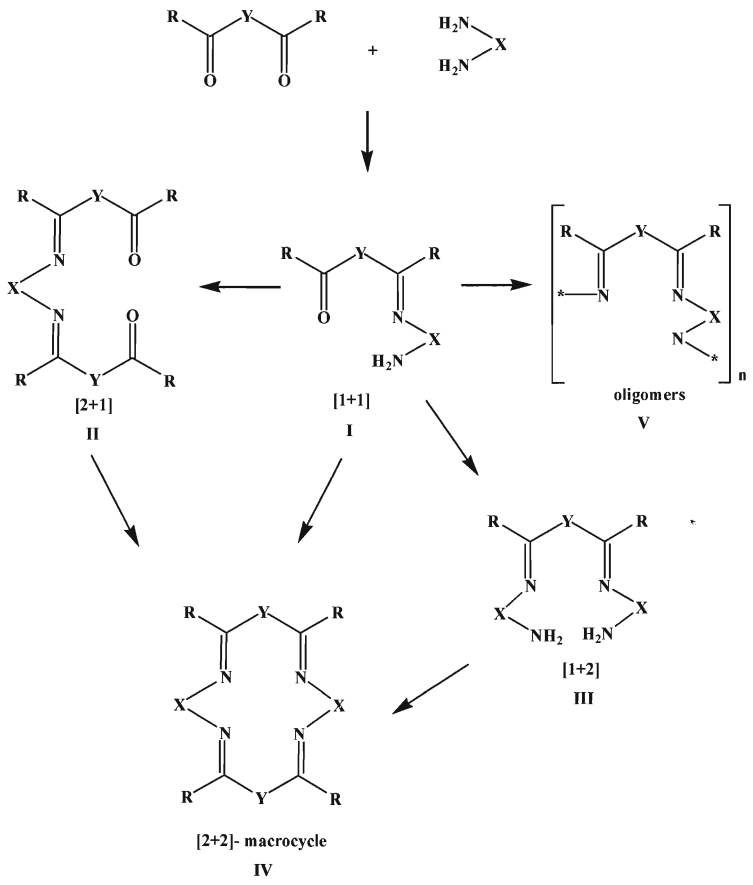

Scheme 3.1. Main condensation products of dicarbonyl compounds with diamines.[109] "Adapted from scheme 2 of reference 109."

Coordination of the starting compounds into the metal cation, which acts as a template agent, fixes their mutual orientation favorable for C=N bond formation. The

importance of the metal ion is in promoting the cyclic condensation of the reactants and /or in stabilising the macrocycle once formed. In general, the reaction in the absence of a metal salt yielded only gums with properties consistent with an oligomeric (or mixture of products) having residual unchanged carbonyl group.[109] In 1977, Nelson reported complexes of the 15-membered $[N_3O_2]$ macrocycle (**3.14**) that included the metal ions Mn(II) and Fe(II).[107] Formation of the macrocycles was confirmed by (a) the X-ray structure determination of $[MnL(NCS)_2]$ **(3.15)**, Figure 3.15, (b) the IR spectra of the complexes which showed an imino C=N str as a strong band at 1650 cm^{-1}, no absorption at 1700 and 3100-3300 cm^{-1} for any residual carbonyl or primary amine, and (c) a peak of *m/z* 275 in the mass spectra assigned to $[L]^+$, where L= the pendentate macrocycle.

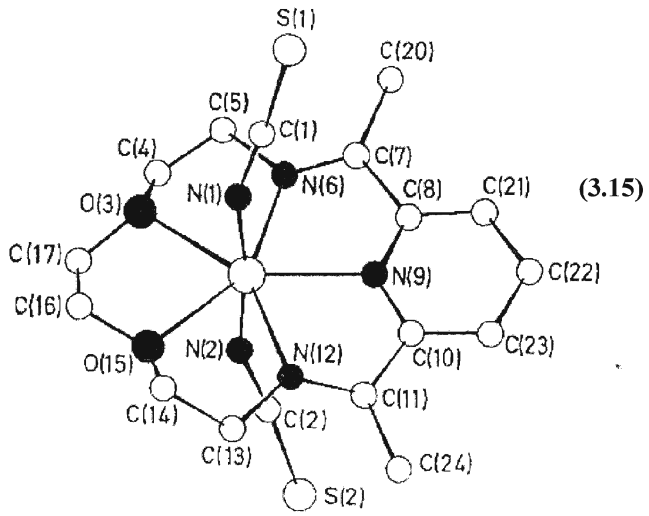

(3.15)

Figure 3.15. Molecular structure of $[MnL(NCS)_2]$.[107] Reproduced by permission of the Royal Society of Chemistry (RSC).

The crystal data for the thiocyanate derivative, **(3.15)** indicates the Mn(II) is in a pentagonal bipyramidal environment in which the macrocycle occupies the pentagonal girdle and the thiocyanate nitrogen atoms are axially coordinated. The metal atom and the five donor atoms are almost coplanar. Furthermore, the X-ray powder diffraction pattern

show the same pentagonal bipyramidal geometry for the metal ion.[107] Within these studies it was found that Mn(II), Fe(III), Fe(II), Co(II) and Zn(II) are effective templates for the preparation of pentagonal bipyramidal complexes from 2,6-diacetylpyridine with an appropriate primary diamine. In all of these complexes, the five donor atoms of the macrocycle coordinate in a the pentagonal plane and the axial sites of the pentagonal bipyramid are occupied by unidentate anionic or solvent ligands.[107] The magnetic studies of the $[M(II)L(SCN)_2]$, where M(II) = Fe(II), Fe(III) and Mn(II) complexes confirmed the high spin state for metal ion of these complexes. In continuation of this research, the *bis* cyanide derivative $[FeL(CN)_2].H_2O$ was prepared and its magnetic properties were studied.[110] The IR spectrum of this complex shows a sharp red shifted band at 2100 cm^{-1} consistent with the coordinated CN^- groups. The UV-vis spectrum also showed the presence of charge transfer band around 657 nm.[110]

The magnetic studies of this complex were carried out using a Gouy balance and Mössbauer spectroscopy. The results showed that the Fe(II) has a spin singlet ground state at temperature below 150 K. The ground state of S = 0 excluded the seven-co-ordinate (pentagonal bipyramidal) structure for this complex at low temperature. This is due to the fact that spin singlet ground states are not possible for d^6 ions in D_{5h} symmetry.[110] That implies, this structure was different from other Fe(II) complexes of the same macrocycle contain weaker field anionic ligands such as NCS^-which were prepared previously.[107] As a result, it was concluded that the complex most likely adopted a six-co-ordinate, approximately octahedral geometry at low temperature. The CN^- groups are co-ordinated, in a *trans* fashion, a hypothesis that is supported by the small splitting of the $\nu(C\equiv N)$. In this case, the ligand must be co-ordinated equatorially in a quadridentate

rather than a quinquedentate fashion. In order to facilitate this, one of the oxygen atoms is excluded from the co-ordination sphere, structure (I), Figure 3.16.

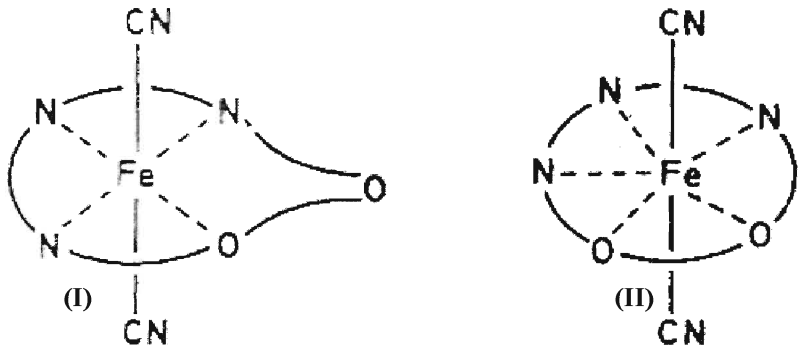

Figure 3.16. Molecular structure of $[FeL(CN)_2]$ at low temperature (LS, left) and high temperature (HS, right).[110] Reproduced by permission of the Royal Society of Chemistry (RSC).

At temperatures between 160 and 200 K, the stable form of the complex is a mixture of low spin (S = 0) and high spin(S = 2) forms in a 1:1 ratio. At room temperature the complex in the high spin (S = 2) state. In the 1970's when the system was first charecterized, it was assumed that the complex could be either six- (I) or seven- co-ordinate, pentagonal bipyramidal, structure (II) as in the complex $[FeL(NCS)_2]$. However, at the time there was no literature proof for that, it would be consistent with lattice reorganisation accompanying the spin change as reflected in the observed hysteresis effects. In addition, the large crystal-field stabilisation energy is also favourable for the six-co-ordinate geometry at low temperature. In 1987 the study of high-resolution X-ray powder diffraction of this complex was carried out.[111] The change in X-ray powder diffraction pattern as a function of temperature reveals that the unit cell dimensions of the HS state and of the HS : LS = 1 : 1 form are different from the LS state. For slow heating between 130 and 265 K, result showed a diffraction pattern at 130 K which is

characteristic for the HS : LS = 1 : 1 form and that obtained at 265 K for the pure HS form, Figure 3.17. In the intermediate temperature range, the intensity of the lines originating from the HS : LS = 1 : 1 form is gradually decreasing while that of the HS state is increasing at the same rate. For the cooling process, the changes occur in the opposite order and at a lower transition temperature, confirming that hysteresis effects are present in X-ray diffraction.

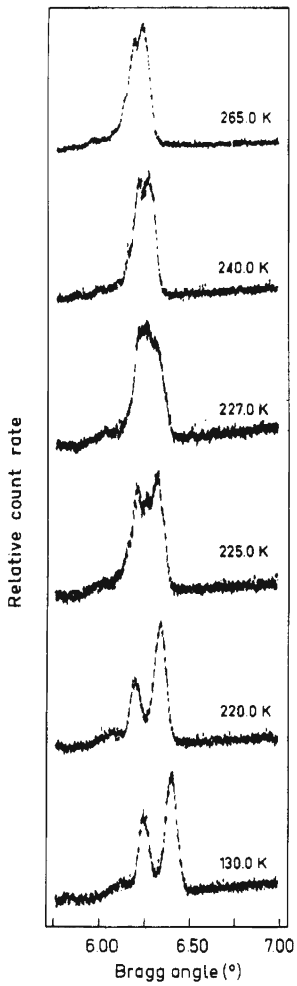

Figure 3.17. X-ray powder diffraction of the complex for slow heating between 130 and 265 K.[111]"Reprinted with permission from reference 111. Copyright {1987} American Chemical Society."

In 2001, the room temperature crystal structure of the complex **(3.16)** was reported by Sato *et al,*[105] and later revised by Letard in 2004, Figure 3.18.[112] The Fe(II) is in a 7- coordinate pentagonal bipyramidal coordination environment. The $[N_3O_2]$ macrocycle occupies the pentagonal girdle around the metal ion and the CN^- ligands are axially coordinated via their carbon atoms. The Fe(II) macrocycles complex are linked through the water molecules into infinite 1-D chains. with the $[Fe(L)(CN)_2]$ complex lying along the *a*- axis of the unit cell.[105]

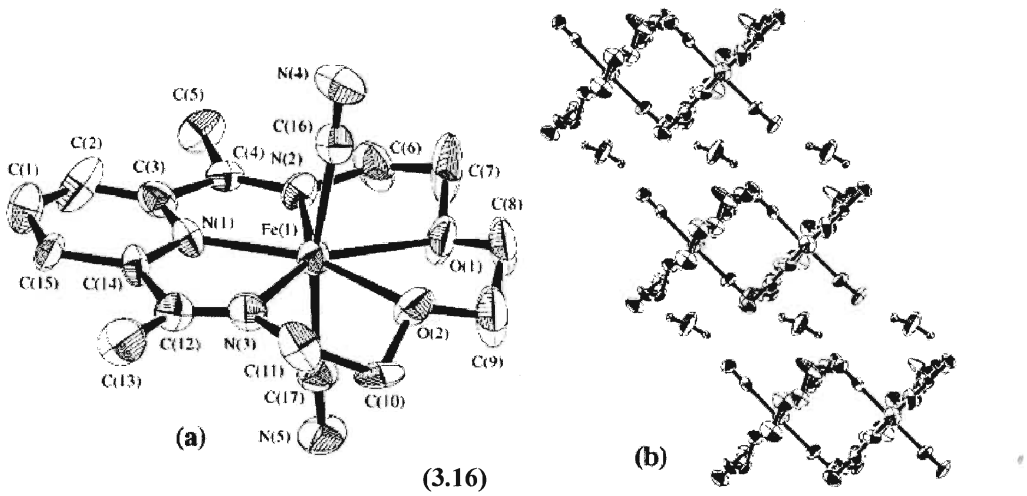

Figure 3.18. (a) ORTEP view for complex **(3.16)** (with the exception of the hydrogen atoms and a water molecule). (b) Projection of the crystal structure of complex **(3.16)** along the *ac* plane.[105] "Reprinted with permission from reference 105. Copyright {2001} American Chemical Society."

The magnetic properties of this complex were elucidated by magnetic susceptibility experiments and Mössbauer Spectroscopy. In addition a LIESST effects with a relaxation temperature above 130 K, which was the highest temperature at the time for a SCO compound was also reported. The magnetic susceptibility of **(3.16)** showed a value of 3.3 cm^3Kmol^{-1} for $\chi_m T$, at 300 K, which is corresponding to HS state, Figure 3.19. In cooling mode of the first cycle (▼), a slight and abrupt decrease of the $\chi_m T$,

between 193 and 159 K was observed. At 130 K, $\chi_m T$ is almost zero. In warming mode of the first cycle (▲), there is an abrupt increase of $\chi_m T$ to 3.2 cm^3Kmol^{-1} around 172 K. A thermal hysteresis of 13 K in the magnetic susceptibility was observed. More warming, resulted first in a decrease of $\chi_m T$ to 1.7 cm^3 K mol^{-1} at 207 K, then an increase in 3.4cm^3 K mol^{-1} at 225 K respectively.

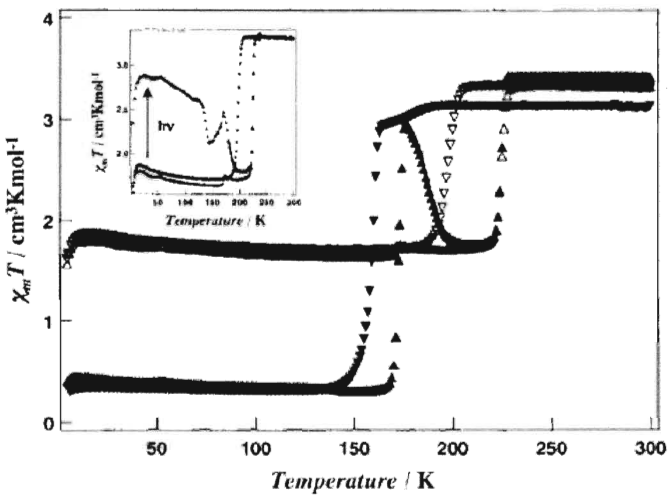

Figure 3.19. $\chi_m T$ versus T plots for complex $[Fe(\mathbf{L})(CN)_2]\cdot H_2O$ **(3.16)**. (▼): Cooling mode of first cycle, (▲): Warming mode of first cycle, (∇): Cooling mode of second cycle, (Δ): Warming mode of second cycle. The temperature was varied at the rate of 1 $Kmin^{-1}$ without temperature overshoot. The $\chi_m T$ versus T plot in the inset was recorded in the warming mode after the sample was exposed to light illumination for 1 h.[105] "Reprinted with permission from reference 105. Copyright {2001} American Chemical Society."

The magnetic properties of the second thermal cycle were similar to powder sample of this complex reported previously showing a conventional one step transition with a pronounced hysteresis loop around 210 K.[111] This abrupt transition with hysteresis is only observed when the cooperative effects are strong enough. In this case, the cooperative effects mainly arise from the formation of a 1-D chain mediated by the N-H--

--O interactions. Mössbauer Spectroscopy also confirms a HS state at 300 K and LS on cooling. This transition was accompanied with a bluish violet to dark purple color change as well as changes in the ν (C-N) stretching mode from 2106 and 2103 cm^{-1} at 300K to 2095 cm^{-1} at low temperatures. During the magnetic measurements on single crystals, it was possible to 'freeze-in' the HS state. When the sample was rapidly cooled (over a few seconds), the $\chi_m T$ value of 3.5 $emuKmol^{-1}$ indicated the presence of a HS Fe(II) complex that could be retained for several days and there was no HS↔LS transition until the crystal was slowly warmed up to 150 K. Following on from these studies, it was also discovered that this complex also displays a LIESST effect, Figure 3.19 (inset). At 15 K, the complex was irradiated with red light via a Hg-Xe lamp (λ = 550 nm, 1.5 mW/cm^2) and a critical temperature of T_c = 130 K for the SCO transition was recorded. By illumination of sample at 5 K, an increase in the dc susceptibility was observed. Even after the illumination was stopped, the change in the magnetization continued for many hours, which indicate that the transition from the LS state to the HS state can be induced by illumination. Here, the relaxation occurs in two steps. First, the magnetization value decreases from 2.9 to 2.1 cm^3Kmol^{-1} at around 130 K, and then, it is completely returned to the original value, 1.7 cm^3Kmol^{-1} at around 180 K.

As it mentioned before, the HS crystal structure of complex **(3.16)** was first reported by Sato but the space group was not correct. The revised structure was reported by Letard *et al* in 2004.[112] In the correct space group *C2/c*, the iron lies on a two-fold axis. As a result, the two Fe-O bonds are crystallographically equivalent and of identical length. The iron is thus clearly seven-coordinate at 293 K in the HS state. If there is a transition to a six-coordinate geometry at low temperature, it will most likely be accompanied by a change in the crystal symmetry. If one of the Fe-O bonds is broken

then clearly the two Fe-O bonds will be inequivalent and the iron complex can not lie on a two-fold axis. In 2007, the crystal structure of this complex at LS state and the detailed structural changes between HS and LS were reported by Létard *et al.*[113] These results confirmed Nelson hypothesis of a thermal transition in the solid state from a hepta-coordinate HS-7 state, to a hexa-coordinate LS-6 state, Figure 3.20.

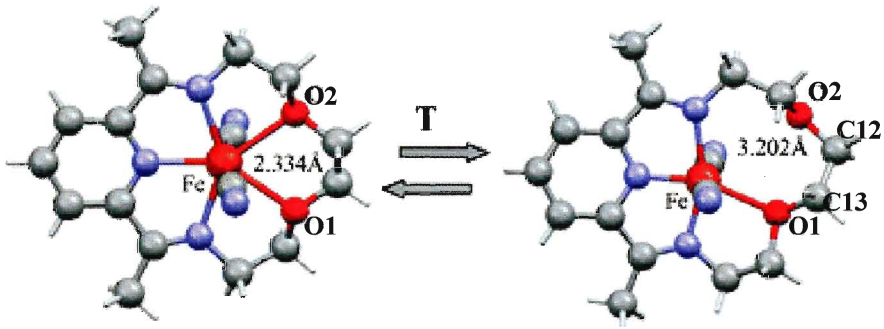

High spin-7, Fe[N_3O_2] CN_2 **Low spin-6, Fe[N_3O_2] CN_2**

Figure 3.20. View of the two X-ray diffraction molecular structures of compound **(3.16)** at 293 and 120 k.[113] Reproduced by permission of the Royal Society of Chemistry (RSC).

At low temperature, the complex crystallize in the monoclinic $P2_1/c$ space group, with the loss of the two-fold axis. This symmetry breaking corresponds to the differentiation of the two Fe ---- O distances. The latter split from 2.334(1) Å in the HS structure to 2.243(1) Å for Fe–O1 and 3.202(1) Å for Fe–O2 in LS structure. Also, the Fe–N distances clearly show the complex is in the LS state. Another notable change in the molecular structure of the complex from HS-7 to LS-6 is the inversion of the O–CH_2–CH_2–O ethylene ring conformation, Figure 3.20. This change of conformation is confirmed by the distance of the two carbon atoms of the ethylene group, C12 and C13, from the plane defined by the two oxygen atoms and the iron atom. Due to the symmetry,

in HS-7, the distances from C12 and C13 to the plane are identical and these atoms are located on opposite sides of the macrocyclic plane, +0.353 Å for C13 and –0.353 Å for C12. In contrast, in LS-6, C12 and C13 are located on the same side of the plane at different distances to the plane, +0,872 Å for C13 and +0.303 Å for C12. The crystal packing is also strongly affected by the broken symmetry, Figure 3.21.

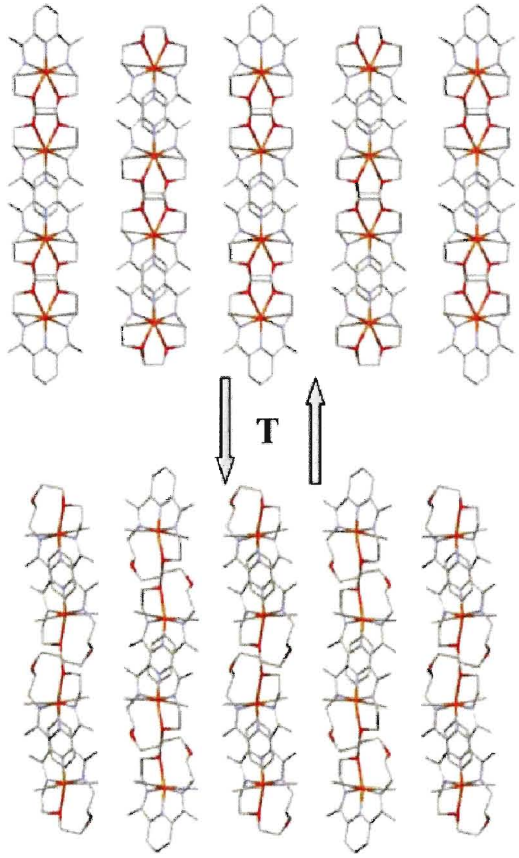

Figure 3.21. Temperature dependence of the crystal packing of X from HS-7(top) to LS-6 (bottom).[113]

Reproduced by permission of the Royal Society of Chemistry (RSC).

In HS-7, the two oxygen atoms involved in the coordination sphere, do not participate in any intermolecular interactions due to their internal positions. But, in LS-6, the oxygen atom that leaves the coordination sphere, O2, is turns a H-bond with a methyl group of a neighbouring complex. The hydrogen bonds involving the water of solvation

are also affected. In contrast, the H-bonds between a water molecule and the nitrogen atoms of the cyanide groups are only slightly affected.

As was mentioned previously, the spin transition behaviour is greatly influenced by the cooperativity of the intermolecular forces within the crystal lattic.[114] One way of increasing cooperativity is to introduce dimensionality into spin-transition compounds.[115] In addition, spin-transition compounds that feature dimensionality can be expected to exhibit magnetic interactions between the central metal ions when the distance between the metal ions is sufficiently short. One such an example is shown in Figure 3.22, a 1-D LIESST compound, $[Fe(L)(CN)_2][Mn(hfac)_2]$, **(3.17)**, which reveals a magnetic interaction between Fe(II) and Mn(II) ions. Formation of **(3.17)** was confirmed using EXAFS and IR spectroscopy. This 1-D –NC–Fe–CN–Mn– structure was constructed by exploiting the bidentate coordinating ability of the axial CN groups. The heterometallic structure, **(3.17)** revealed LIESST effects. After illumination, antiferromagnetic coupling is observed between iron(II) and manganese(II) ions.[116]

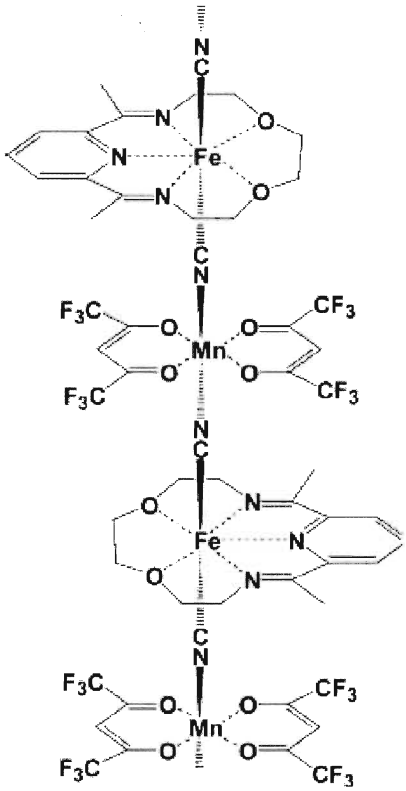

(3.17)

Figure 3.22. Schematic representation of **(3.17)**.[116] "Reprinted with permission from reference 116. Copyright {2005} American Chemical Society."

The Mn(II) complex **(3.15)** is a promising building block for the self-assembly of low-dimensional cyanide-bridged heterometallic complexes. The preparation and characterization of such compounds has recently attracted attention in the field of molecular magnetism. In particular, much synthetic compounds such as single-molecule magnets (SMM) and single-chain magnets (SCM).[117] For the preparation this cyanide bridged compounds, several factors must be considered that include the number and positioning of the cyanide groups, the number and nature of the charge of the cyanide-containing building blocks, and the steric effects of the reactants. In this regard, introducing an ancillary ligand into the cyanide containing polycyanide metal precursor could be as an efficient method due to induced steric effect.[118] The strategy is to exploit

the axially position of the macrocycle complex for coordination to a second ancillary ligand. The ancillary ligands play an important role in influencing the structure and as a result, the magnetic properties of the resulting complexes. As described previously, the macrocycle **(3.14)** is able to coordinate Mn(II) in the equatorial plane, forming a seven-coordinated complex with two *trans* replaceable sites that can be occupied by other ligands such as H_2O , Cl^-or ClO_4^-, Figure 3.23.

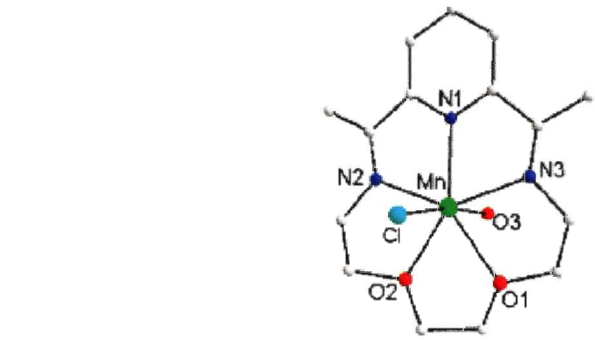

(3.18)

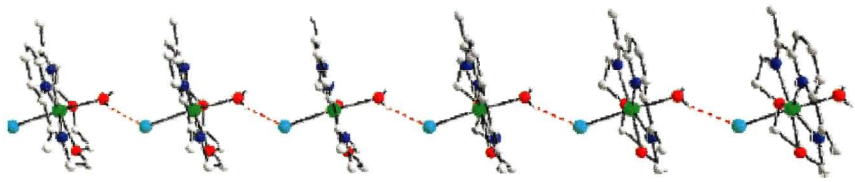

Figure 3.23. Crystal structure of compound **(3.18)** and its 1-D chain supramolecular structure formed via hydrogen bonds. The free ClO_4^- group, solvent methanol molecule, and all the hydrogen atoms except those used to form hydrogen bond have been omitted for clarity.[119] "Reprinted with permission from reference 119. Copyright {2009} American Chemical Society."

Figure 3.24 shows an example where the ancillary ligand is K[Fe(salen)$(CN)_2$], (H_2salen = N,N′-bis(salicyl)-ethylenediamine) **(3.19)**.[120] Co-crystallising the two complexes of **(3.18)** and **(3.19)** together afforded a cyanide-bridged heterometallic Fe(III)–Mn(II) single chain complex **(3.20)** comprised of alternating Fe–C≡N–Mn cationic units, and free ClO_4^- counter ions, Figure 3.25. Magnetic studies of this

compound show an overall antiferromagnetic interaction between the Fe(III) and Mn(II) ions bridged by cyanide ligands.

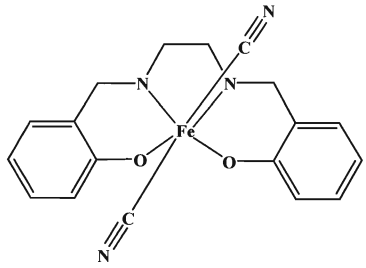

(3.19)

Figure 3.24. Molecular structure of **(3.19)**.

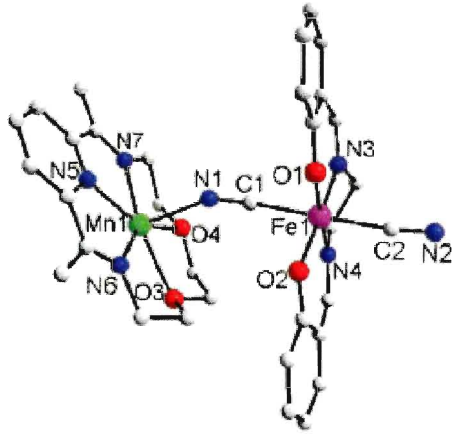

(3.20)

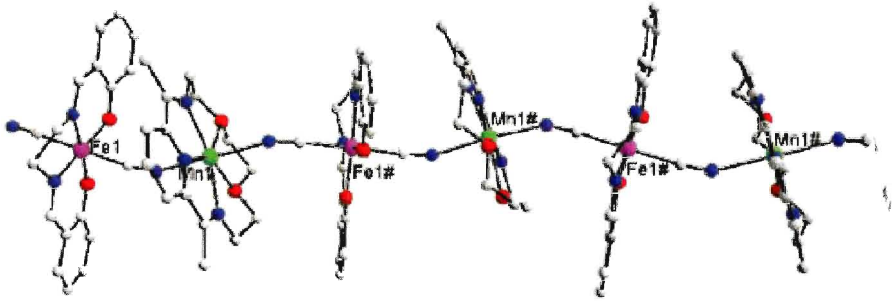

Figure 3.25. The cationic unit and one-dimensional cationic chain structure of complex **(3.20)**. All the hydrogen atoms, free ClO_4^-, and solvent methanol molecule have been omitted for clarity.[120] Reproduced by permission of the Royal Society of Chemistry (RSC).

Second ancillary ligand also used for the preparation of a 1-D chain is the dicyanide-containing Fe(II) complex $[Fe(bpb)(CN)_2]^-$,(bpb^{2-} = 1,2-bis(pyridine-2-

carboxamido) **(3.21)** that has a relatively large planar equatorial pyridine carboxamido ligand and two *trans* cyanide groups, Figure 3.26. Reaction of 1eq of **(3.21)** and 1 eq of $[Mn(L)(H_2O)Cl]ClO_4$ afforded single crystals of the heterometallic cyanide-bridged complex **(3.22)** which exhibits an infinite 1-D cyanide-bridged chain structure with free ClO_4^- groups as the counter ion, Figure 3.27.[119]

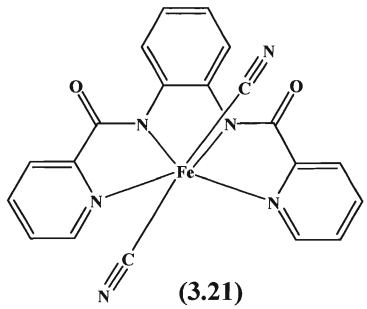

(3.21)

Figure 3.26. Molecular structure of **(3.21)**.

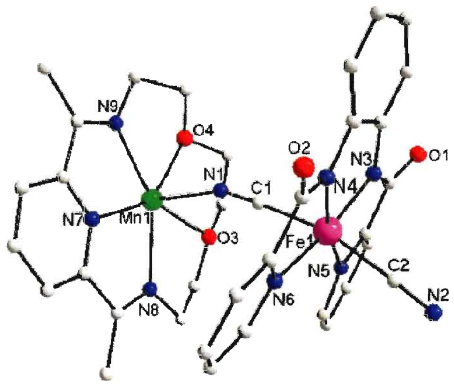

(3.22)

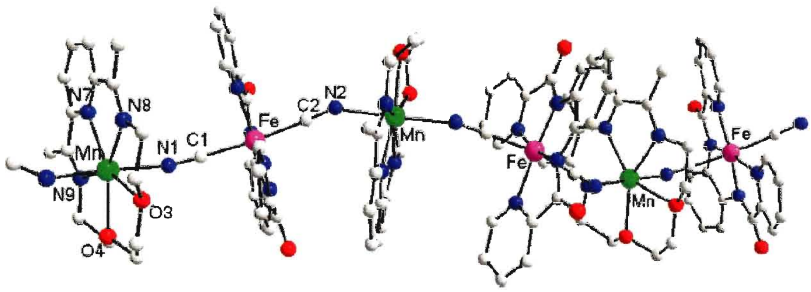

Figure 3.27. The cationic unit and 1-D cationic chain structure of complex **(3.22)**. All the hydrogen atoms, free ClO_4^-, and solvent water molecules have been omitted for clarity.[119] "Reprinted with permission from reference 119. Copyright {2009} American Chemical Society."

This 1-D Fe(III)-Mn(II) complex exhibits overall antiferromagnetic coupling between Fe (III) and Mn(II) ions through the cyanide bridges.

Another promising building block for preparation of extended structure is $[M(CN)_n]^{m-}$ where M= Cr(III), Mn(III), Fe(III), Fe(II) complexes. Following this strategy compounds **(3.23)** and **(3.24)** with 1-D chain structures were obtained by using $K[M(CN)_2]$ (M = Ag^{2+} or Au^{2+}), Figure 3.28. The magnetic studies of these networks demonstrate the weak antiferromagnetic interaction between the Mn(II) ions through [–NC–M–CN–] unit.[121]

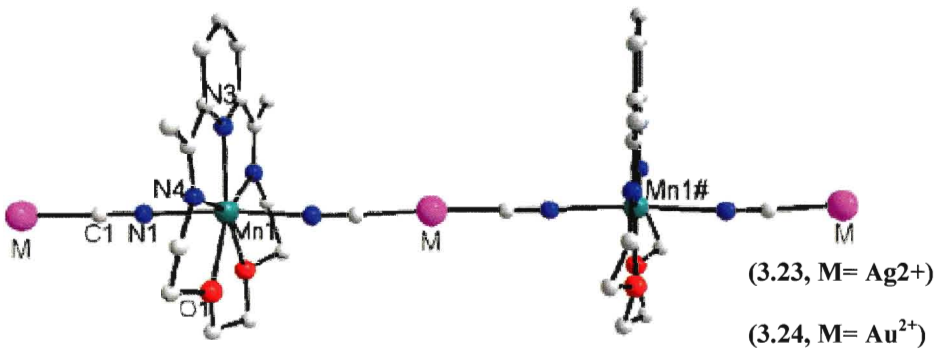

Figure 3.28. Perspective view of the one dimensional chain structure in complex **(3.23)** M = Ag^{2+} and **(3.24)** M = Au^{2+}.[121] Reproduced by permission of the Royal Society of Chemistry (RSC).

Compound **(3.25)** is another example where, $K_2[Pt(CN)_4]$ connects the macrocycle units to form a linear chain. This compound was prepared by liquid diffusion of $K_2[Pt(CN)_4]$ into a methanol solution of $[Mn(L)Cl_2]$, Figure 3.29.[122] Compounds **(3.25)** are the neutral chains where the paramagnetic Mn(II) ions are linked through diamagnetic $[Pt^{II}(\mu\text{-}CN)_4]^{2-}$ units, hence in total a paramagnetic material is obtained.

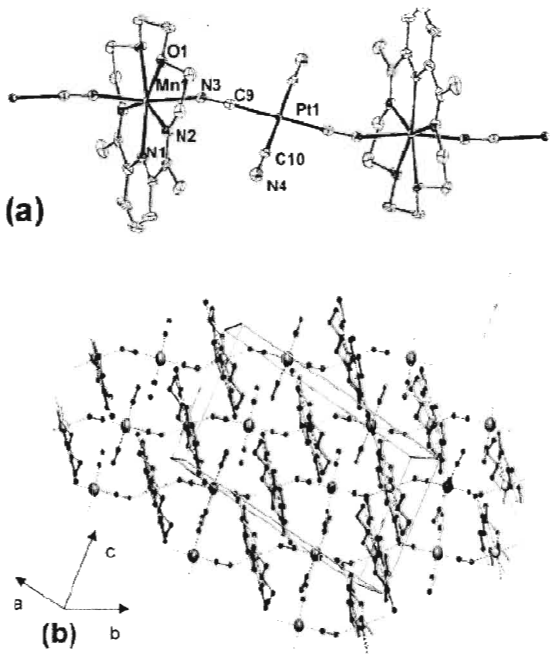

(3.25)

Figure 3.29. (a) ORTEP representation (ellipsoids at 30% probability) of **(3.25)**, H atoms are omitted for clarity. (b) View of the crystal packing of **(3.25)**.[122] "Reprinted with permission from reference 122. Copyright {2005} American Chemical Society."

Slow diffusion of a solution of $[NMe_4]_3[Fe(CN)_6]$ into a solution to the solution of $[Mn(L)Cl_2]$ resulted in the formation of a different structural topology, namely, a 2-D layer system, **(3.26)**, Figure 3.30.

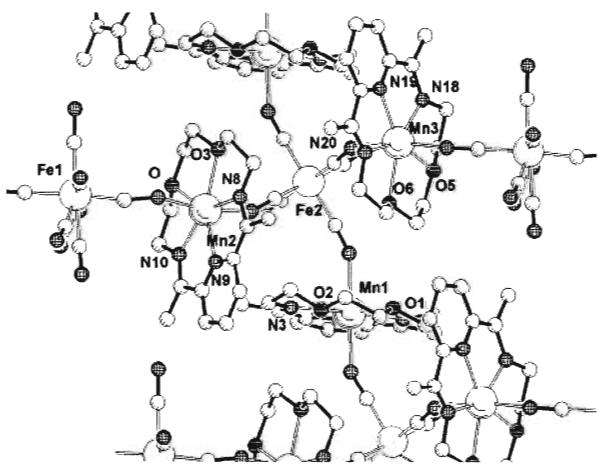

(3.26)

Figure 3.30. Crystal structure of **(3.26)**.[122] "Reprinted with permission from reference 122. Copyright {2005} American Chemical Society."

The magnetic studies of **(3.26)** indicate antiferromagnetic exchange interactions between Mn(II) and Fe(III) ions through the CN^- ligands.[121]

Reaction of 1.5 equivalents of [Mn(L)(NCS)] and 1 equivalents of $[Fe(CN)_6]^{3-}$ resulted in the formation of a tri-nuclear cluster **(3.27)**, Figure 3.31.[123] The analysis of the packing diagram indicates the formation of layers resulting from hydrogen bonds established between the terminal cyano groups from one unit and the aqua ligands from two other trinuclear species, Figure 3.32.

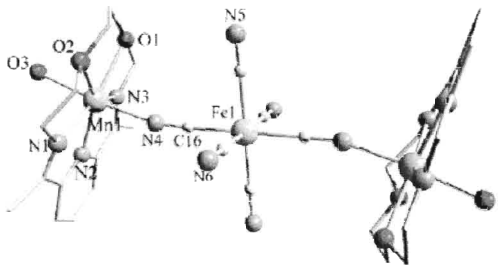

(3.27)

Figure 3.31. Crystal structure of **(3.27)**.[123] Reproduced by permission of the Royal Society of Chemistry (RSC).

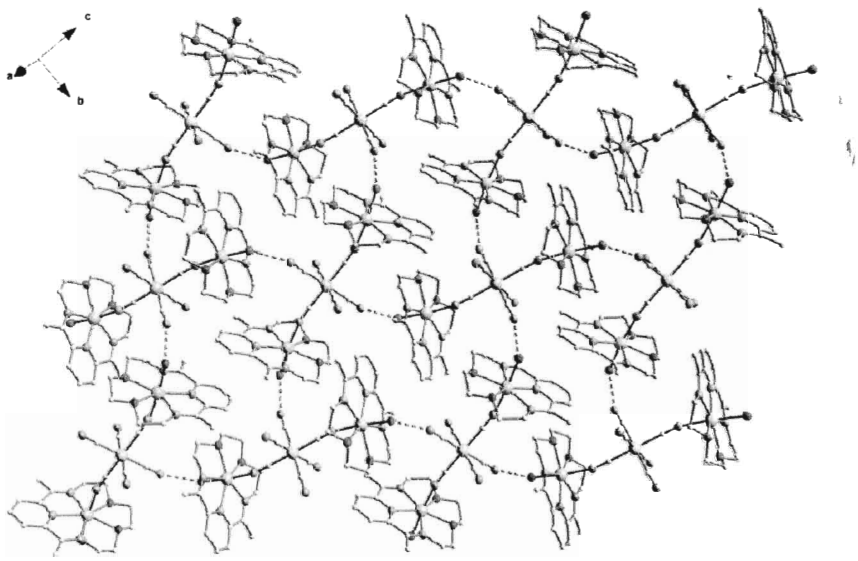

Figure 3.32. Packing diagram of **(3.27)**.[123] Reproduced by permission of the Royal Society of Chemistry (RSC).

There are graphite-like π–π stacking interactions between the pyridyl rings of the macrocyclic ligands. These layers are further interconnected through hydrogen bonds involving water molecules and NCS^- ions, resulting in a complex three-dimensional supramolecular architecture. This compound exhibits a ferromagnetic coupling between the cyano-bridged Mn(II) and Fe(III) ions.

More recently it was found that the Co(II) complex of **(3.14)** together with a hexacyanometallate ligand can form a chiral nanotubular structure, Figure 3.33.[124] In this respect, the complex of stiochiometry $[\{Co(L\text{-}N_3O_2)\}_2Cr(CN)_6][ClO_4].8H_2O$, **(3.28)**, was obtained by reaction of 1eq of $K_3Cr(CN)_6$ together with 1eq of $[Co(L\text{-}N_3O_2)(H_2O)_2][ClO_4]_2$.

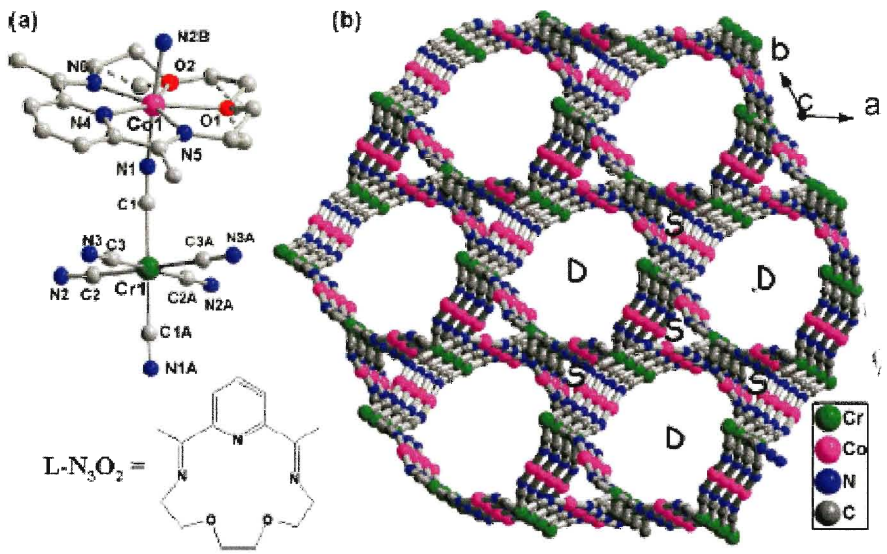

(3.28)

Figure 3.33. (a) View of the ball-and-stick structure of an asymmetric unit of **(3.28)**, where $L\text{-}N_3O_2$ is partly disordered. (b) Chiral 3-D tubular network down the c axis interlocked by single or double helices.[124](Only bridging cyanide and corresponding metallic ions are reserved for clarity.) "Reprinted with permission from reference 124. Copyright {2010} American Chemical Society."

The complex is comprised of a periodically ordered nanotubular structure composed of left-handed single helices and right-handed double-helical strands, Figure 3.34.

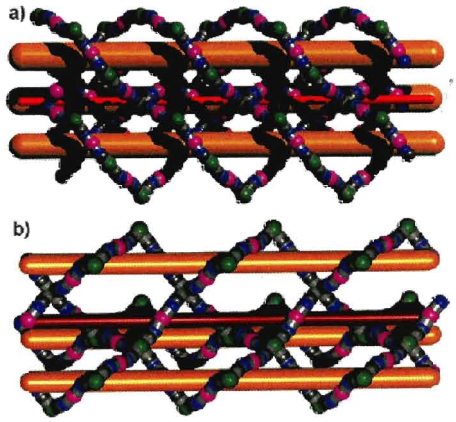

Figure 3.34. View of the ball-and-stick structures of (a) the interlocking of three neighboring right-handed double helices and (b) the interlocking of four neighboring left-handed single helices, along the c-axis.[124](only metallic ions and corresponding cyanide bridges are included for clarity.) "Reprinted with permission from reference 124. Copyright {2010} American Chemical Society."

No circular dichroism spectrum was observed for **(3.28)** at room temperature, indicating that the material is racemic, although the single crystal X-ray diffraction study on several crystals show that the crystals themselves are chiral. The magnetic study of **(3.28)** reveals ferromagnetic coupling between the adjacent Co(II) and Cr(III) ions for this compound and strongly confirmed long-range ferromagnetic order below 12 K. This complex represents the first example of a cyano-bridged magnetic chiral helical compound assembled from achiral components.

3.6. Conclusion

This review highlights the importance of the $[N_2O_3]$ macrocycle ligand **(3.14)**. The results show that ligand **(3.14)** is as an excellent starting point for the design of new macrocyclic compounds not only for preparation of new spin crossover compounds but also for other types of interesting magnetic materials such as SCM and chiral magnets. There are many possible ways to modify this ligand for example, by changing the number of atoms in the ring, by changing the nature of macrocycle and/or introduction new substituents.

CHAPTER 4

The Synthesis and Study of Novel Fe(II)[N_3O_2] Macrocyclic Complexes

Combining two physical properties within the same molecule such as chirality and magnetism, as well as the possibility of investigating cooperative interactions in SCO properties of macrocyclic compounds were the motivations behind the design of the ligands and complexes in this project. In the introduction section to this chapter, several examples of multinuclear complexes with extended structures assembled from mononuclear [N_3O_2] macrocyclic building blocks have been reviewed. As part of a strategy to prepare SCO compounds where two or more SCO centers are covalently attached, the dimeric macrocycle $\{[Mn(N_3O_2)]ClH_2O\}_2 2Cl \cdot 10.5H_2O$, **(4.1)** containing two Mn(II) ions was prepared and characterized by a previous member of Pilkington group.[54b] Single crystals of this compound were obtained and its molecular structure was characterized by X-ray crystallography, Figure **4.1**.[54b]

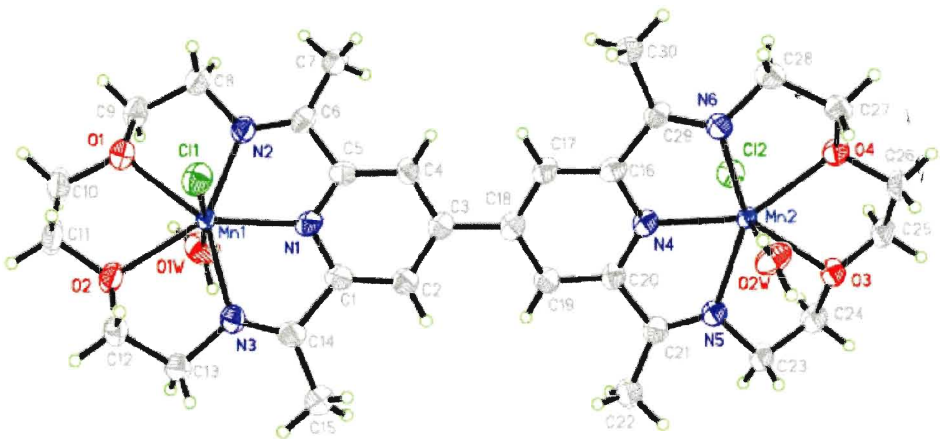

(4.1)

Figure 4.1. ORTEP[57] representation of the molecular structure of compound **(4.1)** (ellipsoids at 50% probability). The Cl^- counter ions are omitted for clarity.[54b] "Reprinted with permission from reference 54b. Copyright {2007} American Chemical Society."

The structural characterization of **(4.1)** reveals that Mn(II) ions contain labile axial chloride and water ligands. Both Mn(II) ions are in a pentagonal-bipyramidal environment, with the macrocycles occupying the equatorial plane, similar to the HS mononuclear complexes of **(3.14)** discussed previously.[106] Magnetic measurements on this macrocycle show the presence of weak antiferromagnetic interactions between Mn(II)-Mn(II) dimeric units. Originally, the dimeric Mn(II) macrocycle was prepared as Mn(II) is more stable with respect to air and moisture than Fe(II) which allowed the macrocycle to be more easily prepared and characterized. The synthetic strategy for the preparation of this macrocycle is shown in Scheme 4.1.

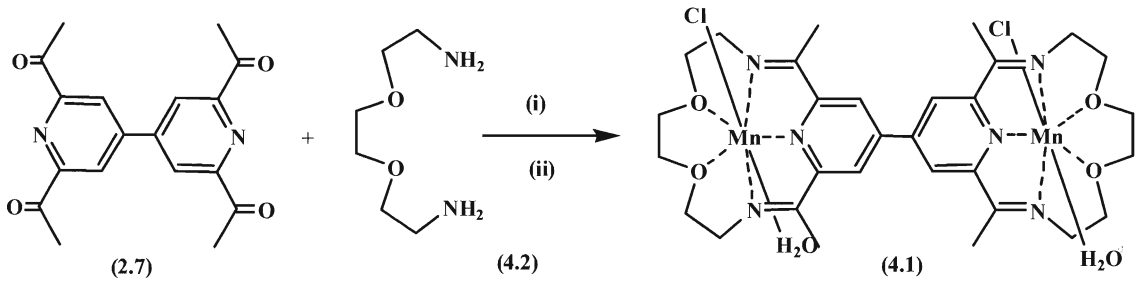

Scheme 4.1. Synthetic route for the preparation of the macrocycle **(4.1)**. **Reagents and conditions:** (i) $MnCl_2$, MeOH (ii) reflux, 6h.[54b]

The success to the preparation of this macrocycle lies in the synthetic strategy for the preparation of the 2,2′,6,6′-tetraacetyl-4,4′-bipyridine **(2.7)** which is not commercially available.[53] It is also an important intermediate in the preparation of the carboxamide ligands described in Chapter 2 of this thesis. The starting material 2,2′,6,6′-tetraacetyl-4,4′-bipyridine (**2.7**), for preparation of **(4.1)** was synthesised following the strategy outlined in Scheme 4.2.[54b] During the course of this project, the final yield of **2.7** was

improved from 30 to 61%. This increased yield was obtained by adding **(2.5)** in small portions to the reaction mixture containing 2,2′-dimethyl-1,3-dioxane-4,6-dione (Meldrum's acid) in acetic acid.

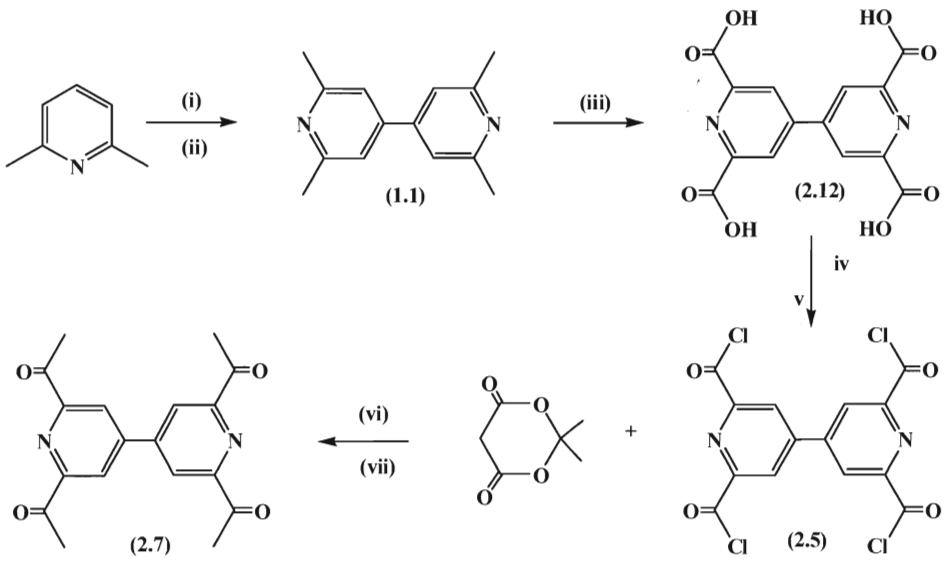

Scheme 4.2. Synthetic route for the preparation of 2,2′, 6,6′-tetraacetyl-4,4′- bipyridine **2.7**. **Reagents and conditions:** (i) Na/THF (ii) SO_2 (iii) CrO_3/conc. H_2SO_4 (iv) $SOCl_2$ (v) DMF, reflux, 5 h (vi) HCl (vii) CH_3COOH, reflux, 16 h .

The initial objectives of this project were to follow the synthetic route outlined in Scheme 4.1 for the preparation of a new dimeric Fe(II) macrocycle **(4.4)** (X = CN) which could be a good candidate for a dinuclear SCO compound. Covalently tethering two Fe(II) centers in close proximity should enable us to study whether or not this has any effect on the cooperativity of the molecules in the crystal lattice. Furthermore, the axial ligands of these macrocycles could also be exploited as linkers for the self-assembly of multi-dimensional SCO compounds. Due to the toxicity of cyanide salts which need caution for handling, we initially decided to prepare the much less toxic thiocyanate macrocycle **(4.3)**. In this way we could determine the ideal reaction conditions for the

preparation and purification of the macrocycle and establish whether or not the compound was soluble in conventional organic solvents for further coordination chemistry. In this respect, macrocycle **(4.3)**, was prepared and characterized.

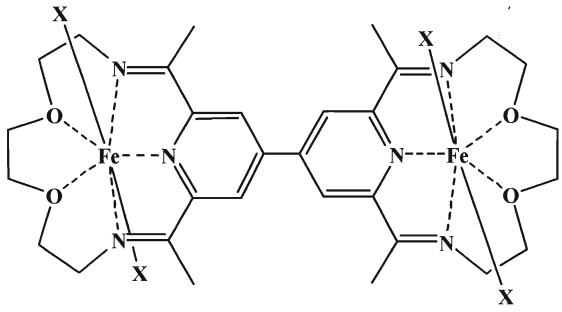

(4.3) X= NCS
(4.4) X= CN

Figure 4.2. Molecular structures of **(4.3)** and **(4.4)**.

4.1. Preparation and characterization of $[Fe(N_3O_2)(SCN)_2]_2$ (4.3)

The dimeric macrocycle **(4.3)** was prepared following the original strategy presented in Scheme 4.1, using $FeCl_2$ as the template metal salt. Once the macrocycle had formed, a solution of the resulting chloride complex was directly filtered into a solution of NaSCN in order to exchange the axial Cl^- and H_2O for $[NCS]^-$ ligands. A reducing agent, $Na_2S_2O_4$ was added during the formation of the macrocycle to keep the Fe(II) ions from undergoing any oxidation during the reaction. Complex **4.3** was isolated as a dark blue powder in 61% yield.

The IR spectrum of macrocycle **(4.3)** was carried out. In general, the $[NCS]^-$ group displays three fundamental frequencies, *a* v_1 (asymmetric stretch), v_2 (symmetric stretch), and v_3 (bend). The positions of v_1, v_2 and v_3 bands depend on whether or not the ligand is coordinated to the metal ion via N or S. For N-bonded thiocyanate ligands, the

following absorption ranges are expected: v_1, 2040-2080; v_2, 780-860 and v_3, 465- 480 cm^{-1}, whereas for S-bonded thiocyanate the ranges are: v_1, 2080-2120; v_2, 690-720; v_3,410-470cm^{-1}.[125, 25] The presence of an intense NCS str at 2061 cm^{-1} is evidence for co-ordination via the nitrogen atom. The position of the v_2, v_3 bands at 802 and 480 cm^{-1} are also consistent with this conclusion. There is also a band at 1632 cm^{-1} which can be attributed to the C=N str of the imine. The C-O-C str's are noticeable at 1119 and 1025 cm^{-1}. The FAB mass spectrum of this macrocycle, is consistent with its molecular structure, showing a parent ion peak at *m/z* = 892. Two fragment ion peaks at *m/z* = 834 and *m/z* = 776 are also observed which correspond to $[M\text{-}NCS]^+$ and $[M\text{-}2NCS]^+$, respectively.

Due to the poor solubility of this macrocycle in most common organic solvents, all attempts to grow suitable single crystals for X-ray diffraction have been unsuccessful to-date. In order to increase the solubility of this macrocycle, *tert*-butyl groups were induced and the new tetraketone starting material, 2,2′,6,6′-tetra(2,2′-dimethyl-1-propanone)-4,4′- bipyridine **(4.5)** was targeted, Figure 4.2.

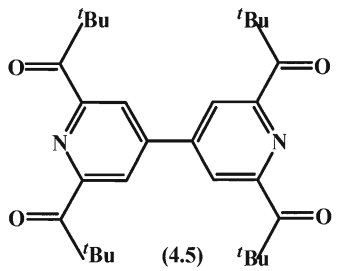

(4.5)

Figure 4.3. Molecular structure of **(4.5)**.

4.2. Preparation and characterization of tetra ketone (4.5)

Compound **(4.5)** was prepared from 2,2′,6,6′-tetrachloroformyl-4,4′-bipyridine via the Gilmann reaction highlighted in Scheme 4.3.[126,127]

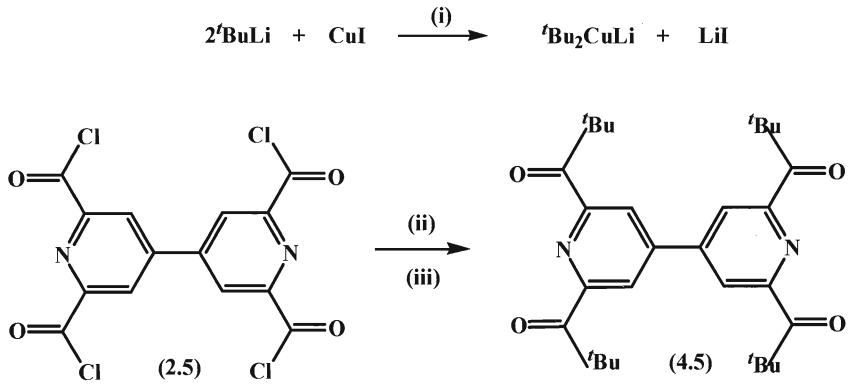

Scheme 4.3. Synthetic route for the preparation of **(4.5)**. **Reagents and conditions:** (i) THF,-40° C; (ii) ^{t}BuCu/THF, -78°, 1 h; (iii) MeOH, -78°C.

In the first step, reaction of *tert*-butyllithium and CuI led to formation of the active Gilman reagent, $^{t}Bu_2CuLi$. In the second step the carbon-carbon bond formation was achieved via the cross coupling of acyl chloride (**2.5**) with the Gilman reagent. The crude compound was purified *via* column chromatography on neutral alumina eluting with CH_2Cl_2 to afford **4.5** as a pale yellow solid in 30% yield. This new precursor was characterized by 300 MHz ^{1}H and ^{13}C NMR and mass spectroscopy. The ^{1}H NMR spectrum of **4.5** has two singlets at 8.26 and 1.51 ppm for the aromatic CH and the *tert*-butyl CH_3 protons, respectively, Figure 4.4.

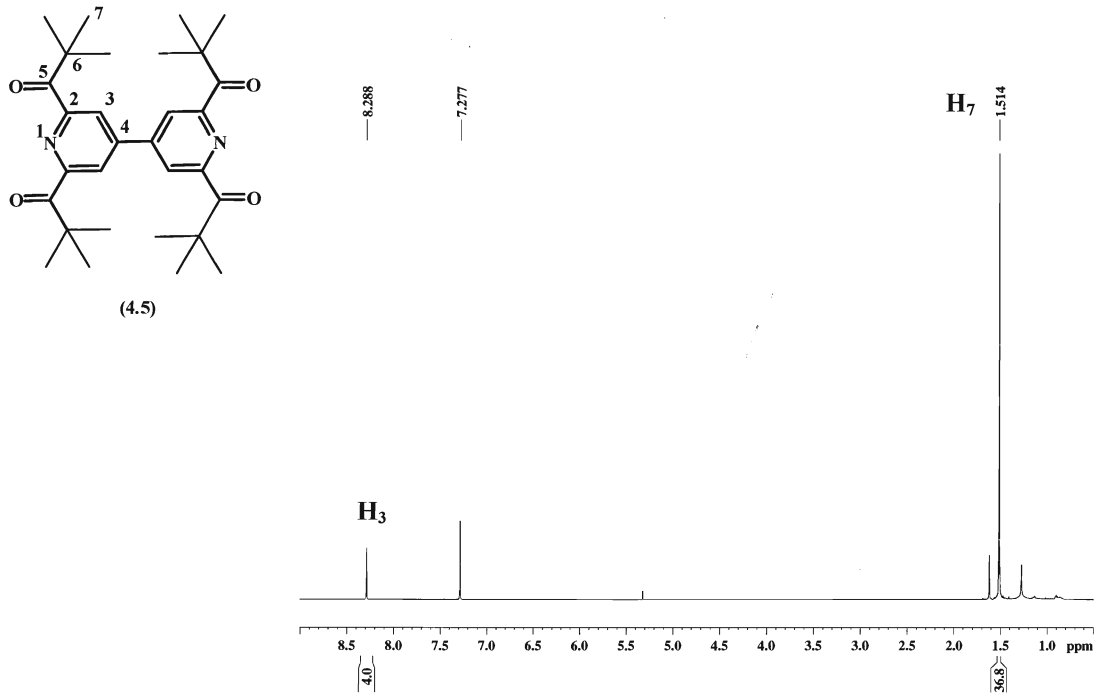

Figure 4.4. 600 MHz ^{13}H NMR spectrum of **(4.5)** in $CDCl_3$.

The ^{13}C NMR spectrum of the tetraketone shows six signals at 206.2, 154.8, 146.6, 123.5, 44.0 and 27.2 ppm consistent with C_5, C_2, C_4, C_3, C_6, C_7 positions, respectively.

The EI mass spectrum of this compound is consistent with its molecular structure, showing a parent ion peak at m/z = 492. Unfortunately, the metal-templated Schiff base condensation reaction of this tetraketone together with 3,6-dioxa-1,8-diamine failed to give the desired macrocycle even though the reaction was repeated several times varying the reaction conditions. During these reactions there were no obvious colour changes indicating that no reaction was taking place since the Fe(II) macrocycles are a deep blue colour. In addition, mass and IR spectroscopy of the isolated products did not show any evidence for the formation of the macrocycle. The failure of this reaction could be due to inductive effect of the *tert*-butyl groups which makes the ketone less reactive in

comparison with the original tetra-methyl ketone. In addition, the steric hindrance of bulky *tert*-butyl groups may also make this reaction more difficult.

During the initial stages of this project it became apparent the dimeric macrocycle is difficult to characterize since it is insoluble in common organic solvents which makes its characterization and the growth of single crystals for X-ray diffraction problematic. Given these issues we turned out attention to modify the skeleton of the macrocycle. One of the common themes in the Pilkington group is to prepare dual property materials where magnetism is combined with a second physical property such as conductivity. In recent years it has become apparent that developing systems which are both chiral and magnetic could afford new materials with interesting optical, electrical and magnetic properties. As discussed towards the end of Chapter 3, the Co(II) macrocycle **(3.28)** afforded a chiral network.[42] The chirality of this system comes from a spontaneous resolution during the crystallization process. The disadvantage here is that this approach is not rational. Applying this methodology it is not possible to study the properties of the chiral systems versus the racemic and impossible to apply the strategy for the preparation of other systems. By modifying the macrocyclic ligand by introducing chiral centres, it should be possible to prepare new chiral macrocyclic building blocks for the rational self-assembly of chiral ferromagnets. In this respect the ligand induced chirality should ensure that the resulting self-assembled material is chiral. Furthermore, both enantiomers can be targeted and the magnetic properties of the enantiomers can be compared with their racemic counterparts. In this regard, we targeted the preparation of the novel chiral diamine **(4.11)** which has two phenyl rings on adjacent carbons both of which have R stereochemistry.

The objectives of this project were the preparation and characterization of the chiral macrocycles **(4.12)** and **(4.13)** from the chiral diamine **(4.11)**, Figure 4.5. On the

one hand the phenyl rings could increase the cooperative interactions in the solid-state facilitating π-to- π interactions. On the other, the bulky nature of the phenyl rings may prevent the macrocycle from undergoing the conformational change from 7 to 6 coordinate hampering or preventing the SCO transition in the Fe(II) complexes.

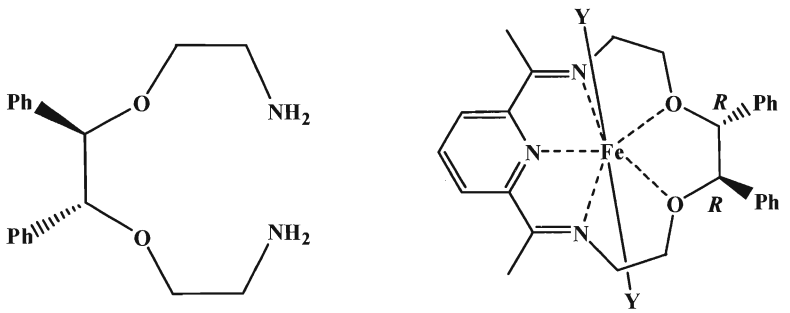

(4.11)

Y = NCS (4.12)
Y = CN (4.13)

Figure 4.5. Molecular structure of **(4.11)**, **(4.12)** and **(4.13)**.

4.3. Preparation and characterization of (4R,5R)-4,5-diphenyl-3,6-dioxa-1,8-octanediamine (4.11)

The novel chiral R,R- diamine **(4.11)** was prepared following the synthetic route shown Scheme 4.4.[128,129] The commercially available (R,R)-(+)-hydrobenzoin was the starting material for this synthesis. In the first step, (R,R)-(+)-hydrobenzoin was reacted with allyl bromide to afford **(4.7)** as pale yellow oil in 90% yield. Compound **(4.7)** was characterized by ^{1}H and ^{13}C NMR and FAB mass spectroscopy. In the second step, oxidation of **(4.7)** with $OsO_4/NaIO_4$ afforded **(4.8)** which were then reduced with $NABH_4$ to afford the corresponding alcohol **(4.9)** as yellow oil in 48% yield. In the third step, reaction of compound **(4.9)** with phthalimide, triphenylphosphine and di-iso-propylazodicarboxylate afforded **(4.10)** as white solid in 37% yield. In the final step,

compound **(4.10)** was reduced with hydrazine monohydrate to afford the chiral amine **(4.11)** as colourless oil in 78% yield. **(4.11)** was characterized by 300 MHz ^{1}H and ^{13}C NMR spectroscopy. Taking the symmetry of the molecule into consideration, the aromatic protons at the C_7 and C_8 positions are observed as a multiplet at 7.22 ppm. A second multiplet at 7.15 ppm corresponds to protons at C_6. A singlet at 4.48 ppm is assigned to the two CH protons at the C_4 chiral centers. Two multiplets at 3.49 and 3.36 ppm are consistent with the CH_2 protons at C_3. A triplet at upfield at 2.82 pm is assigned to the CH_2 protons at the C_2 position. The NH protons are observed as a broad peak at 1.4 ppm. The ^{13}C NMR spectrum shows seven signals at 138.8, 127.9, 127.6, 127.5, 86.0, 71.9 and 41.9 ppm. The four peaks at 138.8, 127.9, 127.6, 127.5 ppm are assigned to the aromatic C carbons of phenyl rings. The peaks at 86.0, 71.9 and 41.9 ppm are assigned to C_4, C_3 and C_2 carbons. The FAB mass spectrum of this compound is consistent with its molecular structure, showing an $[MH]^+$ parent ion peak at m/z = 301. Finally, the elemental analysis data is within the acceptable ± 0.4 % error for $[C_{18}H_{24}N_2O_2]\cdot H_2O$.

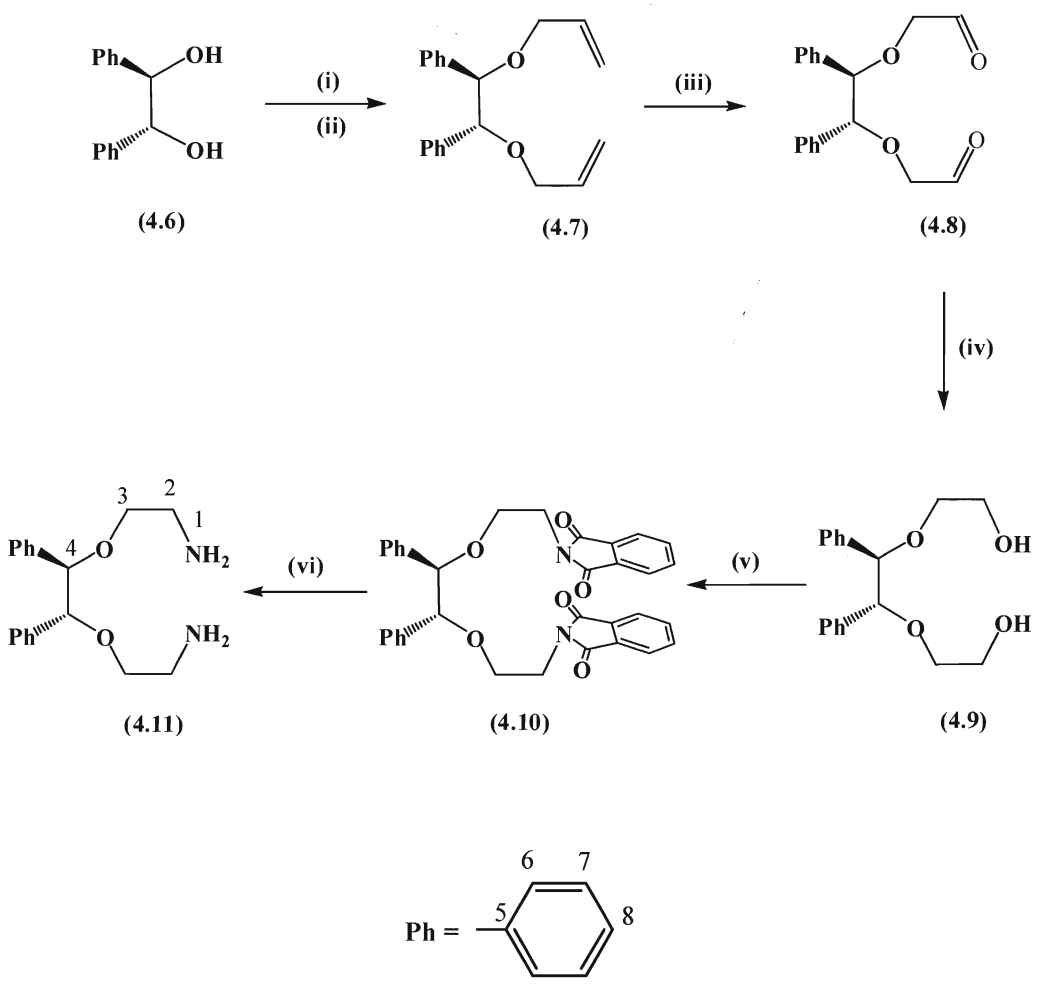

Scheme 4.4. Synthetic route for the preparation of **(4.11)**. **Reagents and conditions**: (i) NaH, THF; (ii) allyl bromide, reflux 24 h; (iii) $OsO_4/NaIO_4$, THF, stirring 24 h; (iv) $NaBH_4$, DCM, MeOH, 20 h; (v) phthalimide, triphenylphosphine and di-iso-propylazodicarboxylate, THF, 4 days stirring; (vi) N_2H_4, EtOH, reflux 24 h.

4.4. Preparation of the R,R $[Fe[N_3O_2](SCN)_2]$ macrocycle (4.12)

Macrocycle **(4.12)** was prepared via the reaction of commercially available 2,6-diacetyl pyridine with one equivalent of the chiral diamine **(4.11)** in the presence of one equivalent of $FeCl_2$. The axial chloride and aqua ligands of the complex were exchanged by adding the reaction mixture to an excess of NCS^-. The resulting blue precipitate was

washed with water to remove unreacted $FeCl_2$, $Na_2S_2O_4$ and NaSCN and then washed with a (1:1) Et_2O : THF mixture to remove any unreacted starting material. The target macrocycle **(4.12)** was isolated as dark blue powder in 59 % yield, Scheme 4.5.

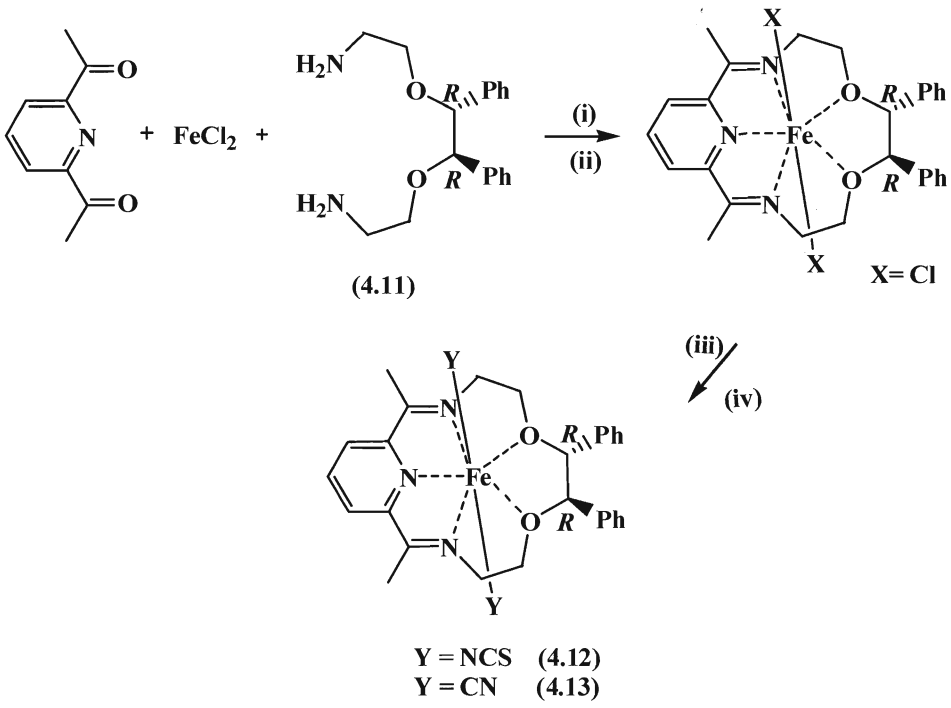

Scheme 4.5. Synthetic route for the preparation of **(4.12)** and **(4.13)**. **Reagents and conditions:** (i) $Na_2S_2O_4$ in H_2O/MeOH; (ii) reflux, 20 h;. (iii) NaSCN/NaCN; (iv) stirring, 4 h.

The IR spectrum of macrocycle **(4.12)** shows an intense band at 2067 cm^{-1} consistent with NCS coordination through the nitrogen atom.[106] A band at 1637 cm^{-1} can be attributed to the C=N stretching band of the imine. The C-O-C stretching bands are noticeable at 1082 , 1058 and 1025 cm^{-1}. The high resolution FAB mass spectrum of this compound, is consistent with its molecular structure showing a parent ion peak at *m/z* = 599.11461 which is in close agreement with the predicted value of 599.11120 for $C_{29}H_{29}FeN_5O_2S_2$. Also a fragment peak at *m/z* = 541 is observed which can be assigned to $[M\text{-}NCS]^+$. The

elemental analysis data indicated that there was a trace of an impurity present in the sample. The UV-vis spectra of macrocycle **(4.12)** recorded at 293 and 77 K. These spectra show two distinct bands centered at λ_{max}= 490 and 672 nm (ε =1081 and 1860 $M^{-1}cm^{-1}$) at 77K which are shifted to λ_{max}= 493 and 660 nm (ε =763 and 1231 $M^{-1}cm^{-1}$) at 293K, Figure 4.6.

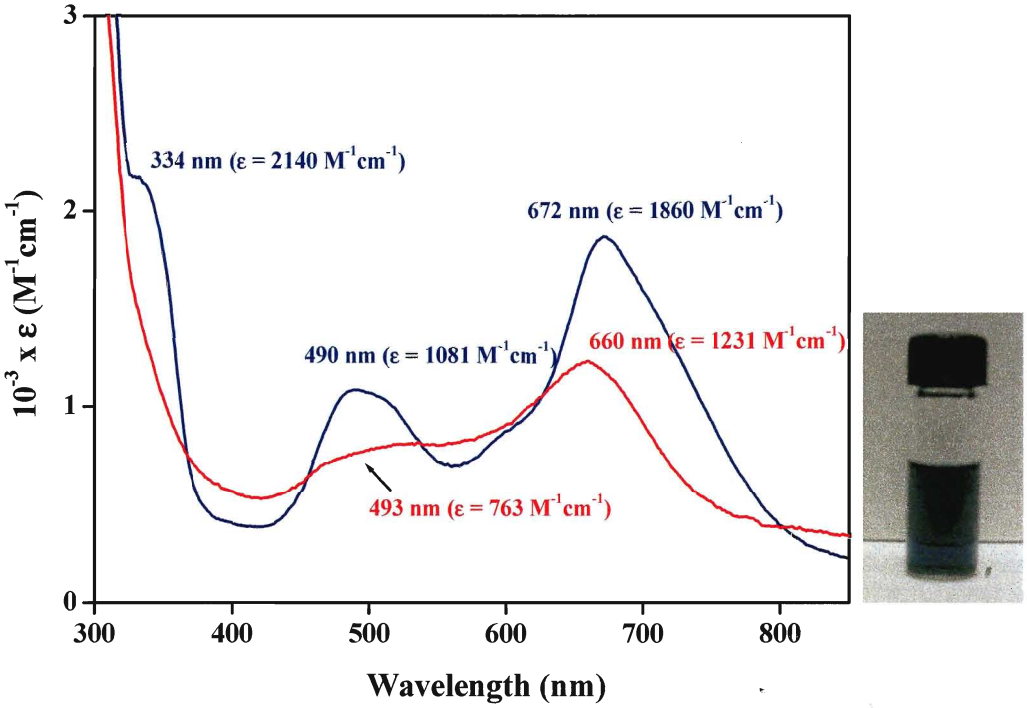

Figure 4.6. UV-Vis spectra of **(4.13)** in EtOH at 293 K (red line) and 77 K (blue line).

The band at 490 nm is assigned to an MLCT band. A second broad band at λ_{max}= 672 nm can be assigned to the $^5T_2 \rightarrow {}^5E$ transition of the HS Fe (II) complex. In general, the SCO transition of octahedrally coordinated Fe(II) coordination compounds can be characterized by UV-vis spectroscopy. The HS complexes of Fe(II) generally contains one UV-vis band centered at around 672 nm, arising from an $^5T_2 \rightarrow {}^5E$ transition, while for LS Fe(II) complexes, two bands occur, the first in the visible region and a second band at

UV-vis part of the spectrum.[130] No change in the position of the bands were observed for **(4.12)**, which suggests that no spin crossover is taking place as the samples are cooled or warmed. There is also a shoulder on the low temp spectrum at 334 nm ($\varepsilon = 2140\ M^{-1}cm^{-1}$) corresponding to intra ligand transitions.

The chirality of the macrocycle was probed by circular dichroism (CD) spectroscopy, Figure 4.7. The Cotton effect was observed in the CD spectrum of **(4.12)** at 372 nm indicating that the molecule is optically active.

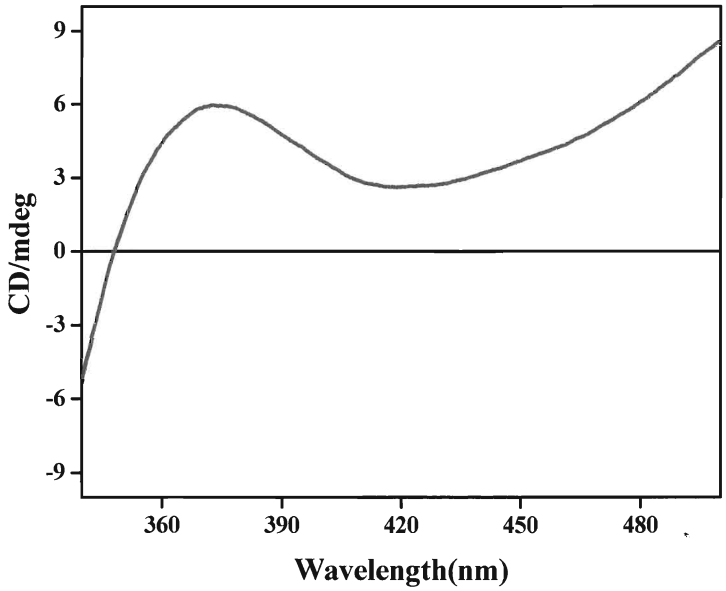

Figure 4.7. Circular dichroism spectrum of **(4.12)** in ethanol.

4.4.1 The molecular structure of R,R $[Fe[N_3O_2](SCN)_2]$ (4.12)

X-Ray quality single crystals of the macrocycle were obtained by liquid diffusion of Et_2O into a THF solution of **(4.12)**. Dark blue plates were obtained after 3 days. The crystal structure was measured at 200 K. To treat the disordered solvent the SQUEEZE command was applied in PLATON[65] during the crystal structure refinement. Compound **(4.12)** crystallizes in the triclinic space group P1, with two independent molecules per

unit cell, **A** and **B**. The molecular structure of **(4.12)** along with the atom-numbering scheme is shown in Figure 4.8. Both NCS groups are disordered which is quite common for this ligand.[131] For clarity, only one of the disordered positions of the NCS molecules are shown in the below.

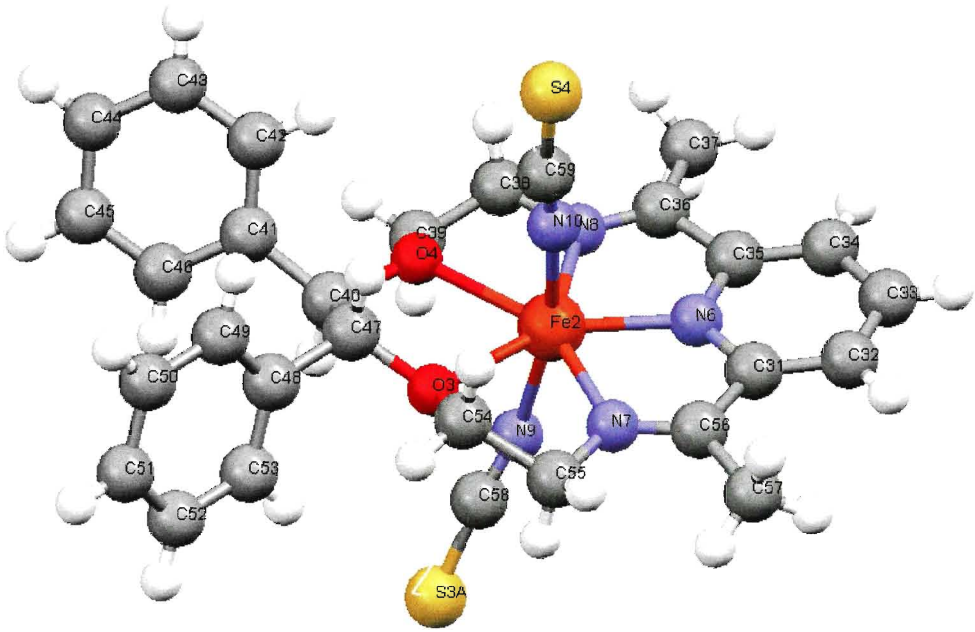

Figure 4.8. Molecular structure of macrocycle **(4.12).**

The Fe(II) ions in both independent molecules are hepta-coordinated in a pentagonal bipyramidal environment, with the $[N_3O_2]$ macrocycle occupying the pentagonal girdle and two axial NCS ligands coordinated via their nitrogen atoms. This structure is very similar to the molecular structures of the Fe(II) and Mn(II) macrocycles described in Chapter 3.[106] The Fe-O bond lengths are 2.395 Å for Fe(1)-O(1), 2.295 Å for Fe(1)-O(2), 2.315 Å for Fe(2)-O(3) and 2.267 Å for Fe(2)-O(4). The Fe-$N_{pyridine}$ bond lengths are 2.083 and 2.105 Å. The Fe-NCS bond angles are 165.13 and 166.55° for N(5)-Fe(1)-N(4) and N(9)-Fe(2)-N(10), respectively, indicating that the ligand is quite bent. It has been

suggested that inter- and intra-molecular forces in the crystal packing affect this angle.[132] Two resonance structures (I) and (II) for thiocyanate metal complexes, representing, respectively, linear and non-linear bonding, may be written, Figure 4.9.

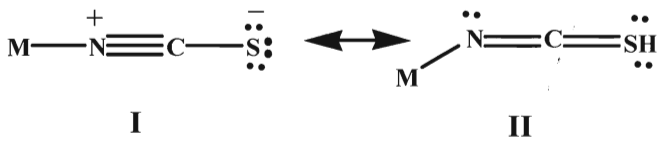

Figure 4.9. Resonance structures (I) and (II) for thiocyanate metal complexes.

Since linear N-bonded $[NCS]^-$ is a potential acceptor of π-electrons, the occurrence of the bent form (II) in the present complex could be a consequence of the non availability of the metal d_π electrons, which are involved in π-overlap with the macrocycle.[133] In addition, the NCS disorder could also have effect on the Fe-NCS bond angle. Selected bond lengths and angles for both independent molecules **A** and **B** in the structure are presented in Tables 4.1- 4.4.

Table 4.1 Selected bond lengths for R,R [Fe[N_3O_2]($SCN)_2$] at 200 K. Molecule A

Fe(1)-N(1)	2.084(7)	N(5)-C(29)	1.1205(10)
Fe(1)-N(4)	2.132(8)	N(5)-C(29A)	1.1202(10)
Fe(1)-N(3)	2.180(12)	S(1)-C(29)	1.6504(10)
Fe(1)-N(2)	2.198(13)	S(1A)-C(29A)	1.6502(10)
Fe(1)-N(5)	2.237(9)	S(2)-C(30)	1.6501(10)
Fe(1)-O(2)	2.295(11)	S(2A)-C(30)	1.6501(10)
Fe(1)-O(1)	2.395(11)	S(2)-S(2A)	0.799(13)
N(4)-C(30)	1.1203(10)	C(29)-C(29A)	1.62(3)

Table 4.2 Selected bond angles [°] for R,R [Fe[N_3O_2]($SCN)_2$] at 200 K. Molecule A

C(30)-N(4)-Fe(1)	153.9(14)	N(1)-Fe(1)-N(3)	71.6(5)
C(29A)-N(5)-C(29)	93(3)	N(4)-Fe(1)-N(3)	94.6(5)
C(29A)-N(5)-Fe(1)	119(2)	N(1)-Fe(1)-N(2)	73.8(5)
C(29)-N(5)-Fe(1)	143.6(14)	N(4)-Fe(1)-N(2)	92.1(5)
S(2A)-S(2)-C(30)	76.0(3)	N(3)-Fe(1)-N(2)	145.3(5)
S(2)-S(2A)-C(30)	76.0(3)	N(1)-Fe(1)-O(2)	142.9(4)
N(4)-C(30)-S(2)	170.2(17)	N(4)-Fe(1)-O(2)	86.0(5)
N(4)-C(30)-S(2A)	161.8(16)	N(3)-Fe(1)-O(2)	71.9(5)
N(5)-C(29)-S(1)	173.7(18)	N(2)-Fe(1)-O(2)	142.6(5)
N(5)-C(29A)-S(1A)	178(4)	N(1)-Fe(1)-O(1)	146.3(4)
N(4)-Fe(1)-N(5)	165.2(5)	N(4)-Fe(1)-O(1)	81.8(5)
N(1)-Fe(1)-N(4)	103.0(5)	N(3)-Fe(1)-O(1)	141.9(4)

Table 4.3 Selected bond lengths [Å] for R,R [Fe[N_3O_2](SCN)$_2$] at 200 K. Molecule B

Fe(2)-N(10)	2.092(6)	N(10)-C(59)	1.1204(10)
Fe(2)-N(6)	2.104(8)	S(3)-S(3A)	0.688(14)
Fe(2)-N(9)	2.139(8)	S(3)-C(58)	1.6501(10)
Fe(2)-N(8)	2.202(12)	S(3A)-C(58)	1.6502(10)
Fe(2)-N(7)	2.204(13)	S(4)-S(4A)	0.70(4)
Fe(2)-O(4)	2.267(11)	S(4)-C(59)	1.6501(10)
Fe(2)-O(3)	2.315(11)	S(4A)-C(59)	1.6501(10)
N(9)-C(58)	1.1203(10)		

Table 4.4 Selected bond angles [°] for R,R [Fe[N_3O_2](SCN)$_2$] at 200 K. Molecule B

C(59)-N(10)-Fe(2)	173.4(13)	N(6)-Fe(2)-N(8)	72.9(4)
C(58)-N(9)-Fe(2)	153.1(15)	N(10)-Fe(2)-O(4)	84.5(4)
S(3)-S(3A)-C(58)	78.0(3)	N(6)-Fe(2)-O(4)	143.7(4)
S(4A)-S(4)-C(59)	77.7(7)	N(9)-Fe(2)-O(4)	86.6(5)
N(10)-Fe(2)-N(9)	166.5(5)	N(8)-Fe(2)-O(4)	71.4(4)
N(10)-Fe(2)-N(6)	92.2(5)	N(7)-Fe(2)-O(4)	142.9(4)
N(6)-Fe(2)-N(9)	101.0(5)	N(10)-Fe(2)-O(3)	83.7(4)
N(9)-Fe(2)-N(8)	91.1(5)	N(6)-Fe(2)-O(3)	144.6(4)
N(10)-Fe(2)-N(7)	88.5(5)	N(9)-Fe(2)-O(3)	83.8(5)
N(10)-Fe(2)-N(8)	95.7(5)	N(8)-Fe(2)-O(3)	142.4(4)
N(7)-Fe(2)-O(3)	71.9(5)		

The Fe-$N_{pyridine}$ bond distance is slightly shorter than the Fe-N_{imino} bond distances, 2.203 Å (Fe-N8) and 2.204 Å (Fe-N7). This is in agreement with the structures of previously reported [N_3O_2] macrocycles.[11] The Fe-NCS distances are 3.178 Å for Fe(2)-C(58)) and 3.207 Å for Fe(2)-C(59). The dihedral angle between the best planes of phenyl rings is 50.80°. The carbon atoms of the O-CH(Ph)-CH(Ph)-O unit, C40 and C47 are located on opposite sides of the plane defined by the two oxygen atoms and the Fe(II) atom at distances of -0.317 and 0.544 for Molecule A and -0.241 Å and +0.466 Å for molecule B, Figure 4.10.

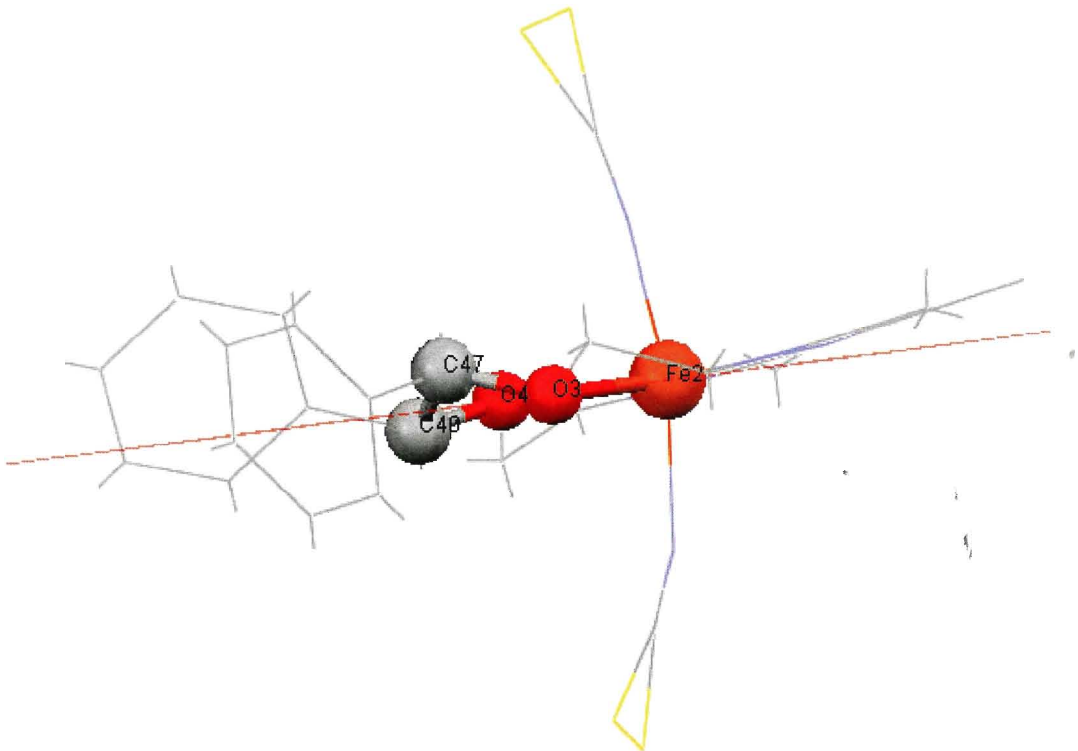

Figure 4.10. View of the positions of the O-CHPh-CHPh-O carbons in the macrocycle **(4.12)** , molecule **B**, with respect to the plane defined by the two oxygen atoms and the iron atom at 200 K.

The macrocycles pack in a head - to - head fashion, Figure 4.11. The shortest distance between neighbouring Fe(II) ions is 7.660 Å. The shortest intermolecular distance

between neighbouring phenyl rings is 4.587 Å. The molecules are well separated from each other. There are no π-π interactions. Since the solvent molecules were removed from the structure we are not able to comment on the intermolecular interactions involving the solvent molecules or the degree of H-bonding in the structure. A summary of the crystallographic data including the structural refinement parameters for this ligand are presented in the appendix section of the thesis (Table 4.9 p. 215).

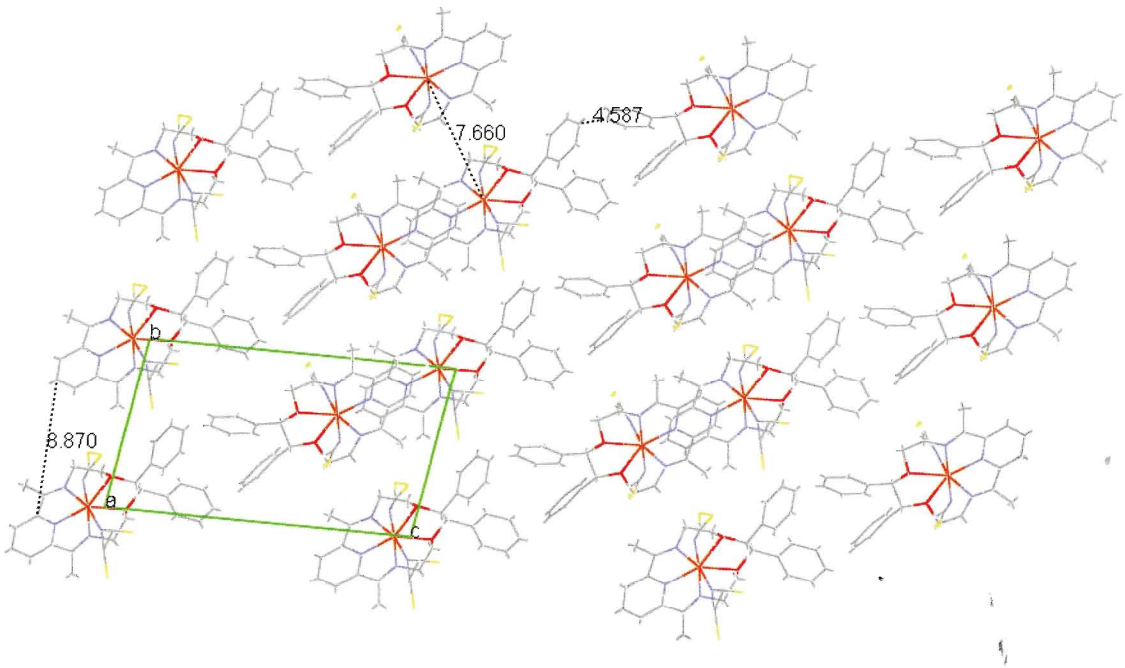

Figure 4.11. Packing diagram for compound **(4.12)** showing intermolecular distances between pyridine rings, 8.870 Å, the shortest distance between neighbouring Fe(II) ions, 7.660 Å and the shortest intermolecular distance between neighbouring phenyl rings, 4.587 Å. viewed down the *a*-axis.

4.4.3 Magnetic studies of R,R $[Fe[N_3O_2](SCN)_2]$ (4.12)

Variable temperature magnetic susceptibility studies were carried out on **(4.12)** on the SQUID magnetometer at Brock University. A plot of $\chi_M T$ vs T is shown in Figure 4.12. The value of $\chi_M T$ decreases gradually from 300 to 20 K. Below 20 K, a decrease in $\chi_M T$ can be observed down to 2.6 cm^3Kmol^{-1}. On warming, a very small hysteresis is observed between 40 and 200 K. This can be either interpreted as an artefact due to the very low change of intensity signal and/or the presence of the trace impurity presenting a spin or phase transition. No traces of any spin transition were observed for this macrocycle. The $\chi_M T$ value of 3.5 cm^3 K mol^{-1} indicates that the Fe(II) in this complex is in the high spin state. Since this value does not change considerably over the temperature range we conclude that this complex does not undergo a SCO transition in the solid state.

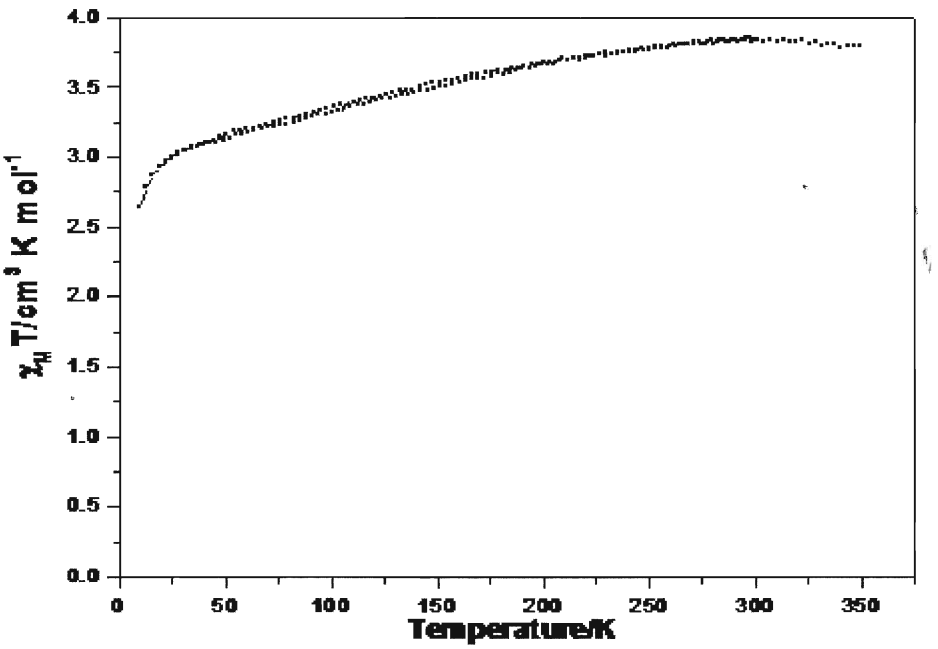

Figure 4.12. $\chi_M T$ vs T for $[Fe[N_3O_2](SCN)_2]$ **(4.12)** between 350 and 10 K.

This finding is not surprising since SCN^- is a weaker field ligand than CN^-. In this respect, the Δ_{oct} for this complex is less than the pairing energy across the temperature range so the electrons occupy the higher energy e_g state instead of pairing up, giving rise to a HS Fe(II) complex. No photomagnetism was observed for this complex. Since the compound high-spin, the only effect that could have been recorded is a reverse-LIESST, transforming under irradiation some of the high spin molecules into their low spin states, thus leading to a decrease of $\chi_M T$ under irradiation. However, no such effect was observed.

4.5. The preparation of R,R $[Fe[N_3O_2](CN)_2]$, (4.13)

The chiral *bis* cyanide macrocycle **(4.13)** was prepared following the strategy previously discussed for the preparation of the thiocyanate derivative. In this case, the reaction mixture was added to an excess solution of NaCN in order to exchange the Cl^- and H_2O ligands for cyanide. The complex was isolated as a blue/purple powder in 54% yield. The IR spectrum of **(4.13)** has an intense C≡N str at 2096 cm^{-1} that is red shifted when compared with ionic CN^-. A band at 1633 cm^{-1} can be attributed to the C=N str of the imine. The C-O-C stretching bands of the macrocyclic ring are observed at υ = 1082 and 1021 cm^{-1}. The FAB mass spectrum of this complex shows a fragment ion at *m/z* = 509 corresponding to $[M–CN]^+$. The elemental analysis data of **(4.13)** powder is within the acceptable ±0.4 % margin of error for $[C_{29}H_{31}N_5O_3Fe]\cdot H_2O$.

At room temperature, the UV-vis spectrum of **(4.13)** contains two bands at λ_{max} = 500 and 645 nm. On cooling the solution to 100 K a dramatic colour change is observed from a dark blue to a very pale pink. The UV-vis spectrum of a frozen solution of **(4.13)** at 100

K, reveals a marked increase in the absorption band at λ_{max} = 490 nm (ε =1421 $M^{-1}cm^{-1}$), together with a new broad absorption band centered at λ_{max} = 711 nm (ε =136 $M^{-1}cm^{-1}$), Figure 4.13.

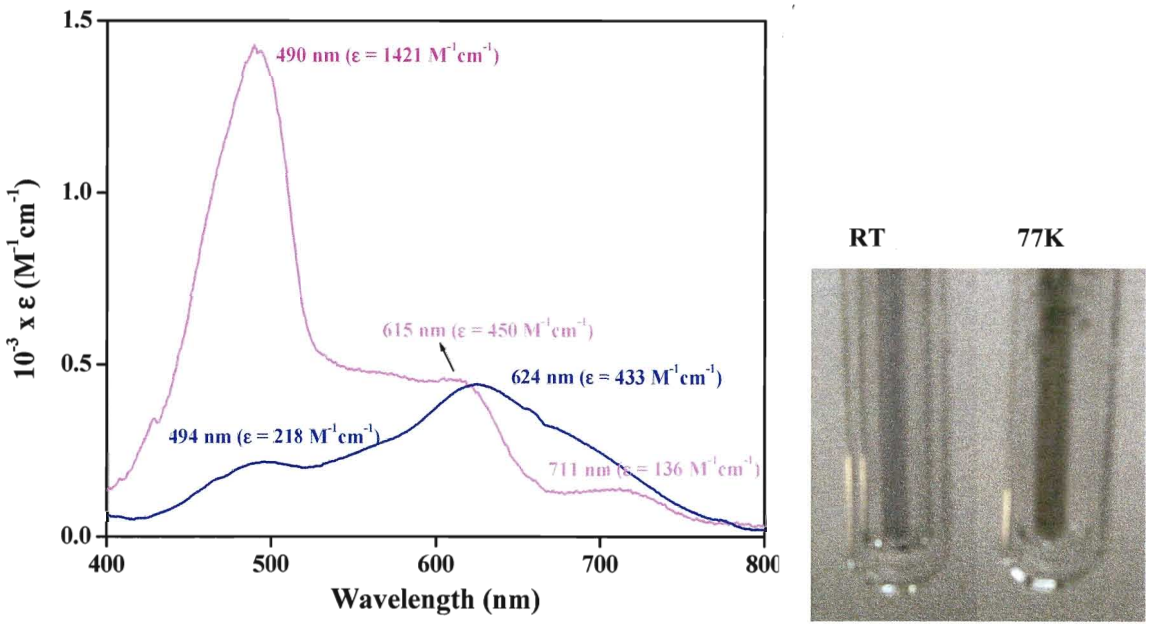

Figure 4.13. UV- vis spectra of **(4.13)** in EtOH at 100K (pink line) and RT(blue line).

The band at λ = 490 nm corresponds to the LS Fe(II) $^1A \rightarrow {}^1T$ transition.[6] There is an increase in the intensity of this band as the temperature is decreased and the complex undergoes a SCO from HS to LS. The bands at λ_{max} = 615, 624 nm (ε =450, 433 $M^{-1}cm^{-1}$) are assigned as a charge transfer interaction from the d_{xz} and d_{yz} orbitals on the metal ion into the low lying antibonding p_{π^*} orbital of the unsaturated segment of the macrocycle.[25] The band at 711 nm corresponds to the HS Fe(II) $^5T_2 \rightarrow {}^5E$ transition.[11]

The chirality of the macrocycle was probed by circular dichroism (CD) spectroscopy, Figure 4.14. Positive Cotton effects were observed at 370 nm and a

negative dichroic signal was observed at 305 nm, confirming that the complex is optically active.

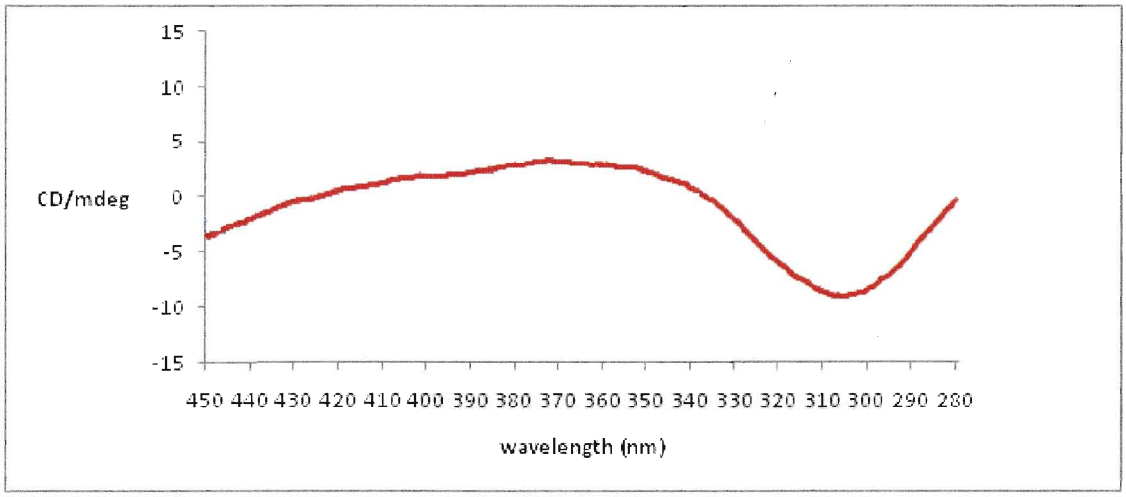

Figure 4.14. Circular dichroism spectrum of **(4.13)** in ethanol.

4.5.1 Crystal structure of R,R $[Fe[N_3O_2](CN)_2]$ (4.13)

X-Ray quality single crystals of **(4.13)** were obtained via liquid diffusion of Et_2O into a CH_3CN solution of the complex. Deep purple/blue needles were obtained after approximately 2 weeks. The crystal structure of **(4.13)** was measured at two temperatures namely, 250 and 100 K. Above 250 K, the crystals were unstable, breaking into pieces. This could be due to the loss of solvent from the crystal lattice, air sensitivity, or to a SCO transition at or around room temperature which causes the crystals to crack. Since the crystals also broke when suspended in paraffin oil, it is unlikely that the decomposition was due to a loss of solvent from the crystal lattice. The crystals were quickly placed in paraffin oil and a single crystal was mounted inside a nylon loop and flashed cooled to 250 K on the X-ray diffractometer where they were stable. Slowly warming the crystal on

the diffractometer to above 270 K caused the crystal to split. We attempted to mount small crystals in the hope that they would be less likely to crack on warming, but measurements of the complex above 250 K have been unsuccessful to-date. At 250 K the macrocycle adopts the chiral monoclinic space group $P2_1$ with two independent molecules in the unit cell. An ORTEP view of the molecular structure of the two molecules **A** and **B**, along with the atom-numbering scheme is shown in Figure 4.15. In contrast to the previously discussed room temperature molecular structure of the original Fe(II) macrocycle (**3.16**), the crystal structure of the chiral system at 250 K contains two independent molecules in the unit cell. Surprisingly, the Fe(II) centers crystallize in two different geometries corresponding to low- and high spin states of the Fe(II). The Fe (II) in molecule **A** is closest to a six-coordinate octahedral environment with one short Fe-O distance Fe(1)-O(1) at 2.263 Å and a longer Fe(1)-O(2) distance at 3.097 Å. In this respect, it seems that one of the oxygen atoms is outside the coordination sphere of the metal and the geometry is more consistent with a LS Fe(II). In contrast, the Fe(II) in molecule **B** is closest to a pentagonal bipyramidal environment, with the macrocycle occupying the pentagonal girdle and two cyanide carbon atoms in the axial positions. For this molecule, the two Fe-O bond lengths are a little long, but very similar namely, 2.418 Å for Fe(2)-O(3) and 2.475 Å for Fe(2)-O(4). In this case the Fe(II) ion is closest to a hepta-coordinated geometry and the Fe-O bond distances are more consistent with a HS Fe(II).

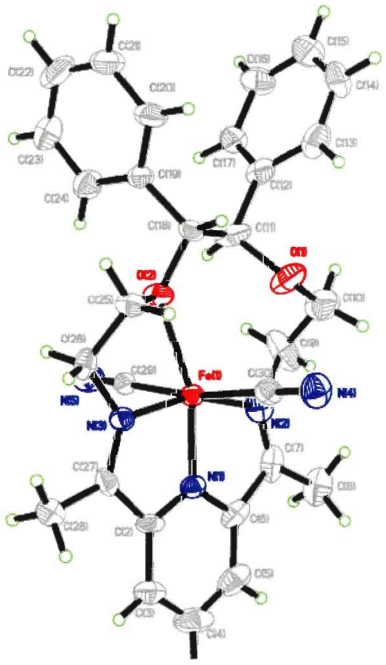

(4.13) Molecule A, LS

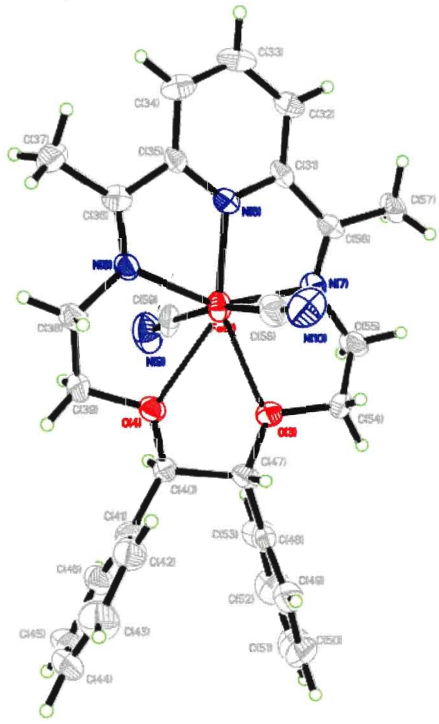

(4.13) Molecule B, HS

Figure 4.15. ORTEP plot of molecular structure of R,R[Fe[N_3O_2]$(CN)_2$] **(4.13)** showing the two independent molecules **A** and **B** in the unit cell at 250 K. Thermal ellipsoids are plotted at 50%.

The Fe-$N_{pyridine}$ bond lengths for molecules **A** and **B** are 1.872 and 2.040 Å, respectively. The Fe-N_{imino} bond distances for molecule **A** are 2.036 Å and 1.956 Å. The corresponding bond distances for molecule **B** are 2.141 Å and 2.123 Å. The Fe-CN bond angles in molecules **A** and **B** are 170.32° for C(29)-Fe(1)-C(30) and 169.56° for C(58)-Fe(2)-C(59). The Fe-CN distances are 1.987 Å for Fe(1)-C(29) and 1.988 Å Fe(1)-C(30) in molecule **A** and 2.106 Å for Fe(2)-C(58) and 2.092 Å for Fe(2)-C(59) for molecule **B**. The dihedral angle between the best planes of phenyl rings for molecules **A** and **B** are 47.01 and 47.05° respectively. Another noteworthy difference between the two molecules is the inversion of the O-CHPh-CHPh-O ethylene chain conformation. The difference in conformation is defined by the distance of the two carbon atoms of ethylene group, C(40)

and C(47) in molecule **B** and C(11) and C(18) in molecule **A** from the plane defined by the two oxygen atoms and the iron atom. In molecule **A**, the C11 and C18 atoms are located on the same side of the FeO2 plane at distances of +0.914 and +0.125 Å respectively, Figure 4.14, top. In contrast in molecule **B**, the C40 and C47 are located on opposite sides of the plane at distances of +0.493 Å and -0.305 Å respectively, Figure 4.16, bottom. This is essentially reflecting the fact that when the Fe(II) is 7-coordinate, the macrocyclic ring is essentially planar facilitating [N_3O_2] coordination. However, this planarity is lost during the SCO transition as one of the oxygen atoms is rotated out of the coordination sphere of the metal and the Fe(II) becomes 6-coordinate.

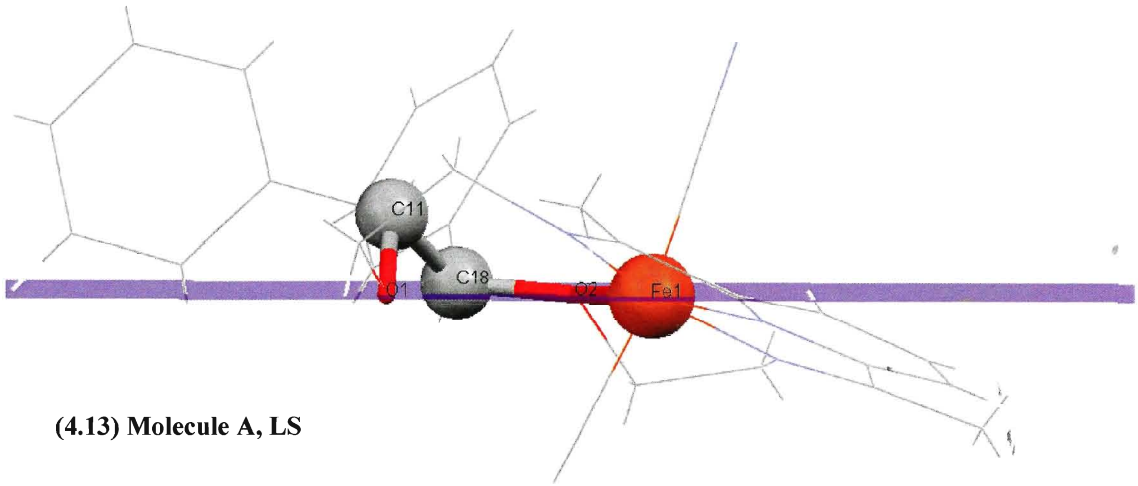

(4.13) Molecule A, LS

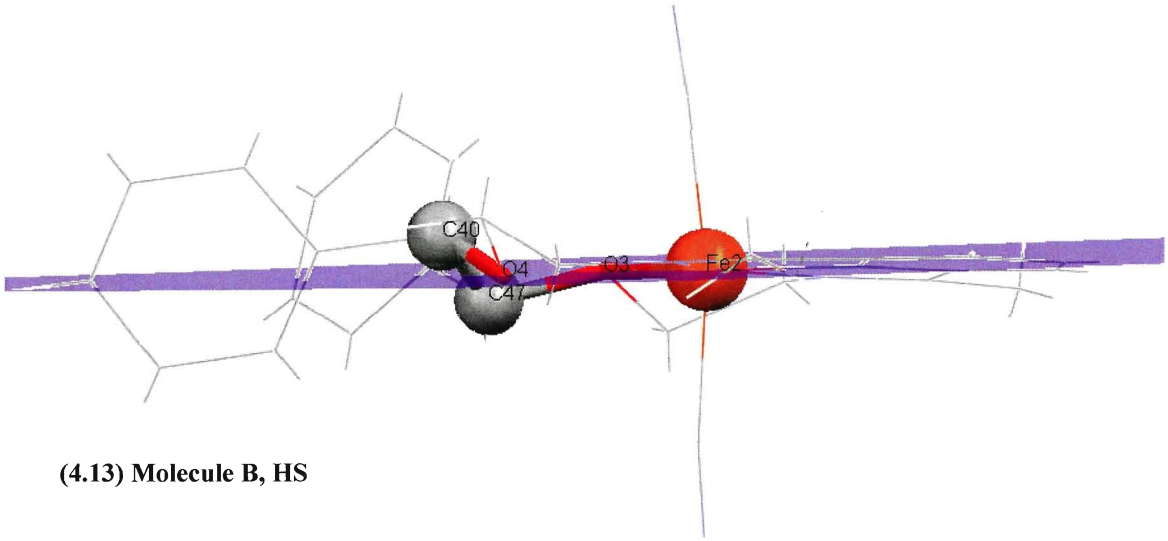

(4.13) Molecule B, HS

Figure 4.16. View of positions of O-CHPh-CHPh-O carbons in molecules **(4.13) A** and **(4.13) B** with the respect to the plane defined by the two macrocyclic oxygen atoms and the Fe(II) atom at 250 K.

Macrocycle **(4.13)** was crystallized along with two CH_3CN and one Et_2O molecules. Figure 4.17 shows the crystal packing of **(4.13)** at 250 K. The aromatic Ph-H's form weak H-bonds to both the cyanide N atoms (H···N-C= 2.562-2.626 Å) and the oxygen atoms of the diethylether solvent molecules (H···O-C= 2.571 Å). In addition, the cyanide nitrogen atoms form weak H-bonds with the hydrogen atoms of the acetonitrile solvent molecules (N··H-C= 2.734 Å) and stronger H-bonds with the macrocyclic CH_2 hydrogen atoms (C-N···H-C= 2.626 Å). The closest intermolecular distances between Fe(II) centers are 10.542 Å.

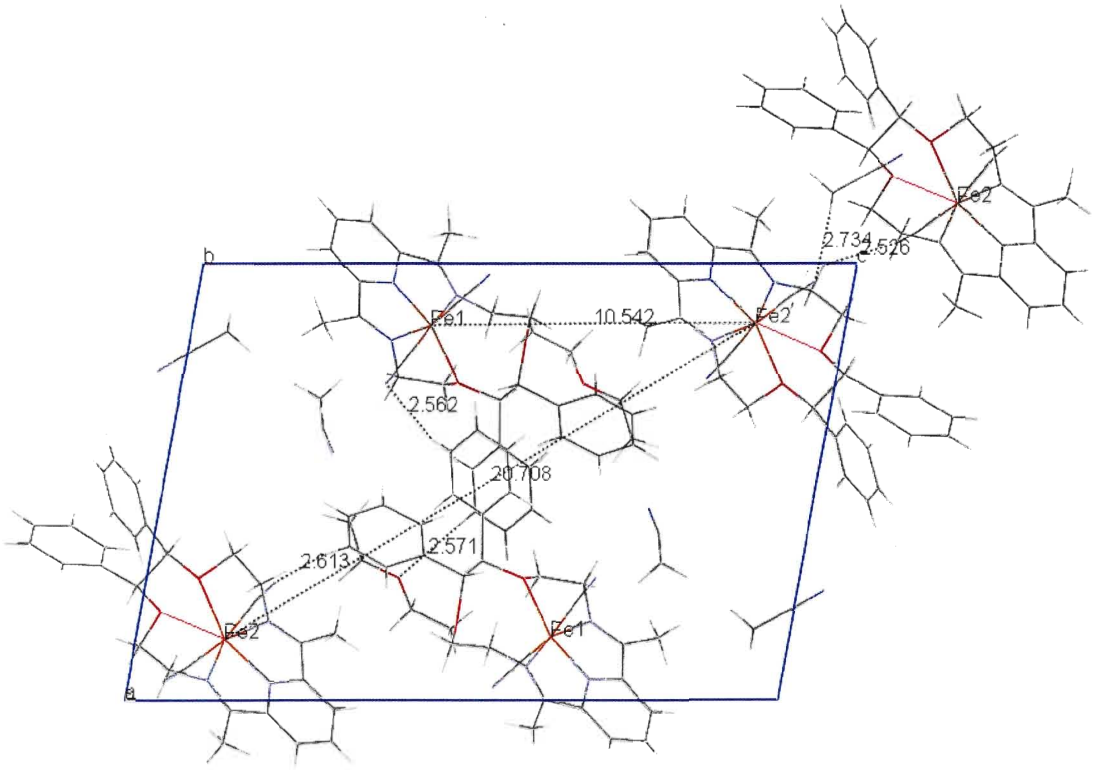

Figure 4.17. Packing diagram for compound **(4.13)** at 250 K showing H-band (2.562-2.613 Å) and the shortest and longest intermolecular Fe-Fe distances (10.542 Å, 20.708 Å). viewed down the *b*-axis.

Table 4.5 Selected bond lengths [Å] for $[Fe[N_3O_2](CN)_2]$ at 250 K.

Fe(1)-N(1)	1.872(4)	Fe(2)-N(6)	2.040(5)
Fe(1)-N(2)	2.036(6)	Fe(2)-N(7)	2.140(5)
Fe(1)-N(3)	1.956(5)	Fe(2)-N(8)	2.123(5)
Fe(1)-O(2)	2.264(4)	Fe(2)-C(58)	2.107(8)
Fe(1)-C(29)	1.986(7)	Fe(2)-C(59)	2.093(8)
Fe(1)-C(30)	1.989(7)		

Table 4.6. Selected bond angles [°] for $[Fe[N_3O_2](CN)_2]$ at 250K.

N(1)-Fe(1)-C(29)	94.5(2)	N(6)-Fe(2)-C(59)	97.8(3)
C(29)-Fe(1)-C(30)	170.2(3)	C(59)-Fe(2)-C(58)	169.7(3)
N(1)-Fe(1)-N(2)	79.6(2)	N(6)-Fe(2)-N(8)	74.5(2)
C(29)-Fe(1)-N(2)	89.0(2)	C(59)-Fe(2)-N(8)	93.2(2)
C(30)-Fe(1)-N(2)	88.4(2)	C(58)-Fe(2)-N(8)	90.3(3)
N(3)-Fe(1)-N(2)	159.2(2)	N(6)-Fe(2)-N(7)	74.8(2)
N(3)-Fe(1)-O(2)	77.45(19)	C(58)-Fe(2)-N(7)	90.4(2)
C(29)-Fe(1)-O(2)	85.6(2)	C(59)-Fe(2)-N(7)	91.5(2)
N(2)-Fe(1)-O(2)	123.2(2)	N(6)-Fe(2)-C(58)	92.5(2)
N(1)-Fe(1)-O(2)	157.2(2)	N(8)-Fe(2)-N(7)	149.2(2)

At 100 K, the macrocyle **(4.13)** retains its chiral monoclinic space group $P2_1$ with two independent molecules in the unit cell. An ORTEP plot of the molecular structure of the two molecules **A** and **B** along with the atom-numbering scheme is shown in Figure 4.18. In this case molecule **A** remains hexa-coordinated with one short and one long Fe-O bond length. In comparison with the bond lengths of the 6-coordinate Fe(II) in molecule **A** at 250 K, the bond lengths at 100 K do not change significantly, which means that the Fe(II) in molecule **A** does not change its spin state and remains in the LS configuration as the temperature is lowered. In contrast, the Fe-O bond distances for molecule **B** at 100 K are significantly longer than those determined at 250 K. The Fe(2)-O(3) and Fe(2)-O(4) distances change from 2.418 Å and 2.475 Å at 250 K to 2.583Å and 2.638 Å at 100 K. This is consistent with the Fe(II) center in molecule **B** undergoing a SCO transition. In this case, the Fe(2)-O(4) bond length becomes longer as the oxygen atom moves out of the coordination sphere of the transition metal ion. By examining the Fe-O and Fe-N bond lengths and angles for this molecule, it would seem that the coordination geometry of the Fe(II) centre is actually closer to being 5 coordinate than 6, where both oxygen atoms have moved out of the coordination sphere of the Fe(II) ion. In this case, a square pyramidal coordination geometry is consistent with a LS Fe(II). What is not clear at this time is if the 5-coordinate Fe(II) is an intermediate in the structural rearrangement that takes place during the spin crossover process. Unfortunately we have not been able to measure the crystal structure of this complex below 100 K or above 250 K to study its coordination geometry in the pure HS or LS state. Given that the crystals break at room temperature it is likely that a large structural reorganization in the crystal lattice accompanies the SCO transition to pure HS. This seems reasonable given that the Fe(II) center in molecule **A** has to change its geometry quite considerably and move from a 6- to

a 7-coordinate environment. Given the steric hindrance inflicted on this macrocycle by the phenyl rings at the chiral centers it seems reasonble to suggest that it is difficult for this complex to structurally accomodate this transition.

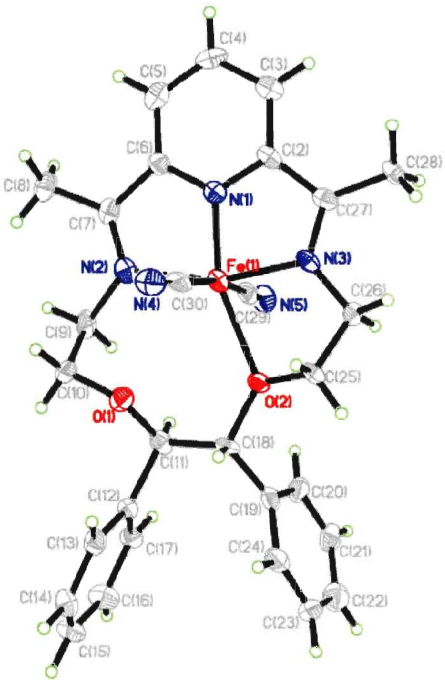

(4.13) Molecule A, LS

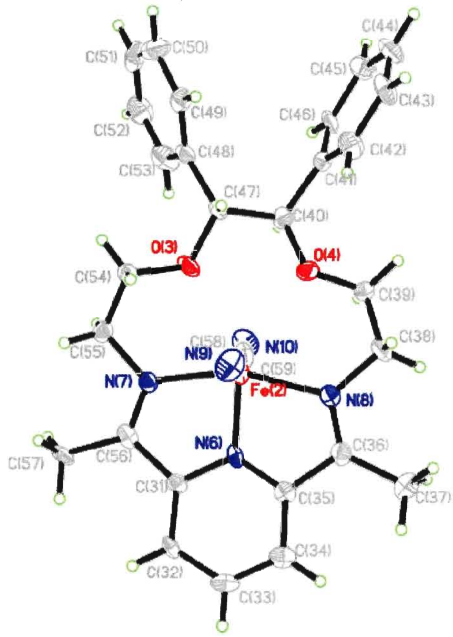

(4.13) Molecule B, LS

Figure 4.18. ORTEP plot of molecular structure of **(4.13)** showing the two independent molecules **A** and **B** in the unit cell at 100 K. Thermal ellipsoids are plotted at 50%.

As for molecule **A** at 250 K, the C11 and C18 atoms are once again located on the same side of the FeO2 plane at distances of +0.895 Å and +0.113 Å from the defined plane, Figure 4.19, top. For molecule **B**, C40 and C47 are located on opposite sides of the plane at distances of +0.503 Å and -0.292 Å from the FeO2 plane, Figure 4.19, bottom.

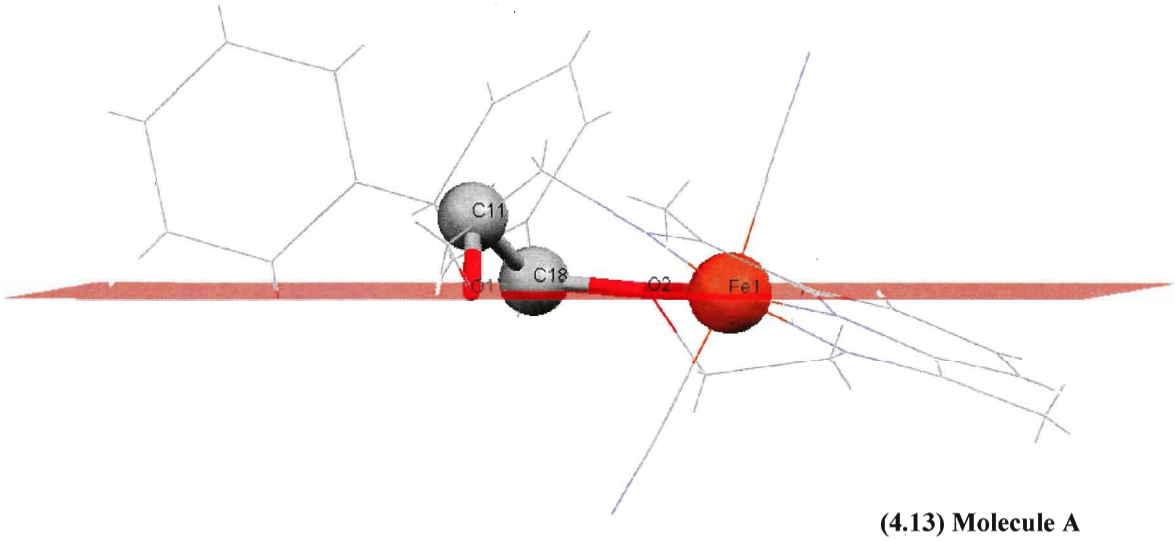

(4.13) Molecule A

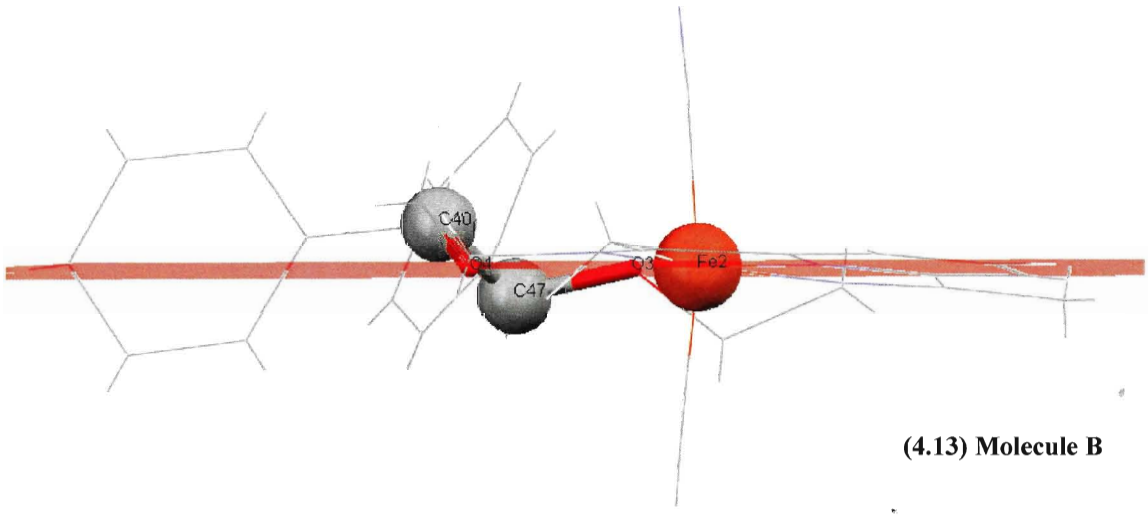

(4.13) Molecule B

Figure 4.19. View of the positions of the O-CHPh-CHPh-O carbons in **(4.13),** molecules **A** and **B** with respect to the plane defined by the two oxygen atoms and the Fe(II) at 100 K.

The dihedral angle between the best planes of phenyl rings for molecules **A** and **B** are 46.19° and 45.31°, respectively, which are slightly smaller in comparison with the values measured at 250 K. Figure 4.18 shows the crystal packing of **(4.13)** at 100 K. Here the phenyl ring H atoms form weak H- bonds with neighbouring cyanide nitrogen atoms (H···N-C= 2.540-2.557 Å) and the oxygen atom of a diethylether solvent molecules

(H···O-C= 2.482 Å). In addition, the cyanide nitrogen atoms form weak H-bonds with macrocyclic –CH_2- hydrogen's (N···H-C = 2.532 Å). All the H-bonds are slightly shorter at 100 K. In this respect, the number of H-bonding interactions does not change with temperature, but the strength of the bonds increase at lower temperatures. Neighbouring Fe(II) centers are slightly closer at 100 K. The shortest Fe-Fe distance in the crystal structure is 10.328 Å, Figure 4.20.

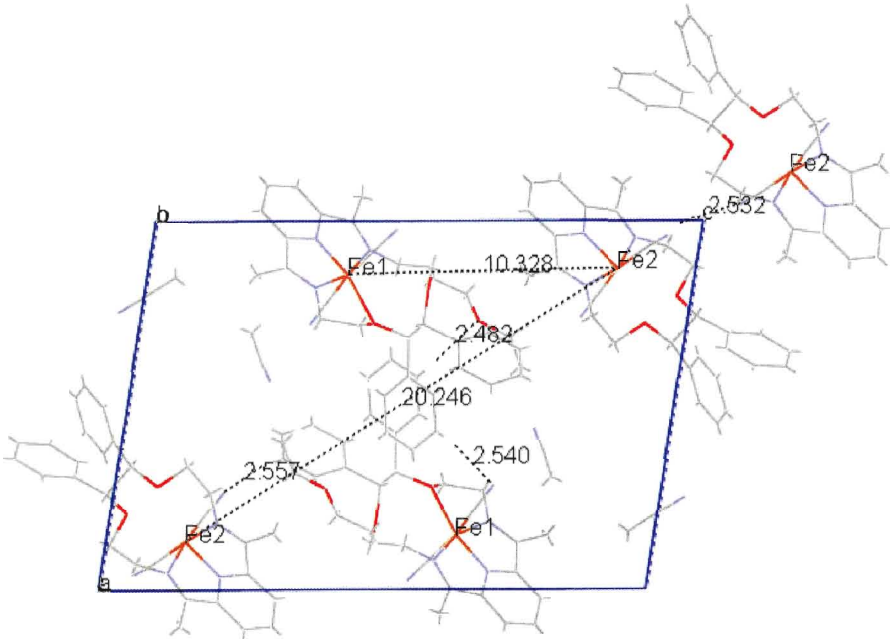

Figure 4.20. Packing diagram for compound **(4.13)** at 100 K showing H-bond (2.532-2.557 Å) and the shortest and longest intermolecular Fe-Fe distances (10.328 Å, 20.246 Å). viewed down the *b*-axis.

A comparison of the molecular structures at 100 K and 250 K indicates that as the temperature is increased, structural changes in the molecular structure of the complexes are consistent with a LS to HS transition that is not complete at 298 K.

Table 4.7 Selected bond lengths [Å] for R,R [$Fe(N_3O_2)CN_2$] at 100 K.

Fe(1)-N(1)	1.831(5)	Fe(2)-N(6)	1.860(5)
Fe(1)-N(2)	2.042(7)	Fe(2)-N(7)	2.015(6)
Fe(1)-N(3)	1.917(6)	Fe(2)-N(8)	2.013(6)
Fe(1)-O(2)	2.249(5)	Fe(2)-C(58)	1.976(9)
Fe(1)-C(29)	1.939(8)	Fe(2)-C(59)	1.976(9)
Fe(1)-C(30)	1.950(9)		

Table 4.8. Selected bond angles [°] for R,R [$Fe(N_3O_2)CN_2$] at 100K.

N(1)-Fe(1)-C(29)	94.0(3)	N(6)-Fe(2)-C(59)	99.2(3)
C(29)-Fe(1)-C(30)	170.4(3)	C(59)-Fe(2)-C(58)	167.3(3)
N(1)-Fe(1)-N(3)	81.5(3)	N(6)-Fe(2)-N(8)	78.7(3)
C(29)-Fe(1)-N(2)	88.5(3)	C(59)-Fe(2)-N(8)	92.7(3)
C(30)-Fe(1)-N(2)	88.3(3)	C(58)-Fe(2)-N(8)	89.9(3)
N(3)-Fe(1)-N(2)	161.8(3)	N(6)-Fe(2)-N(7)	80.0(3)
N(3)-Fe(1)-O(2)	78.4(2)	C(59)-Fe(2)-N(7)	91.4(3)
C(29)-Fe(1)-O(2)	86.6(3)	C(58)-Fe(2)-N(7)	90.6(3)
N(2)-Fe(1)-O(2)	119.7(2)	N(6)-Fe(2)-C(58)	93.5(3)
N(1)-Fe(1)-O(2)	159.9(2)	N(8)-Fe(2)-N(7)	158.6(2)

A summary of the crystallographic data for the complex at 100 and 250 K including the structural refinement parameters are presented in the appendix section of the thesis (Table 4.9 p. 215).

4.5.2 Magnetic studies of R,R $[Fe(N_3O_2)CN_2]$ (4.13)

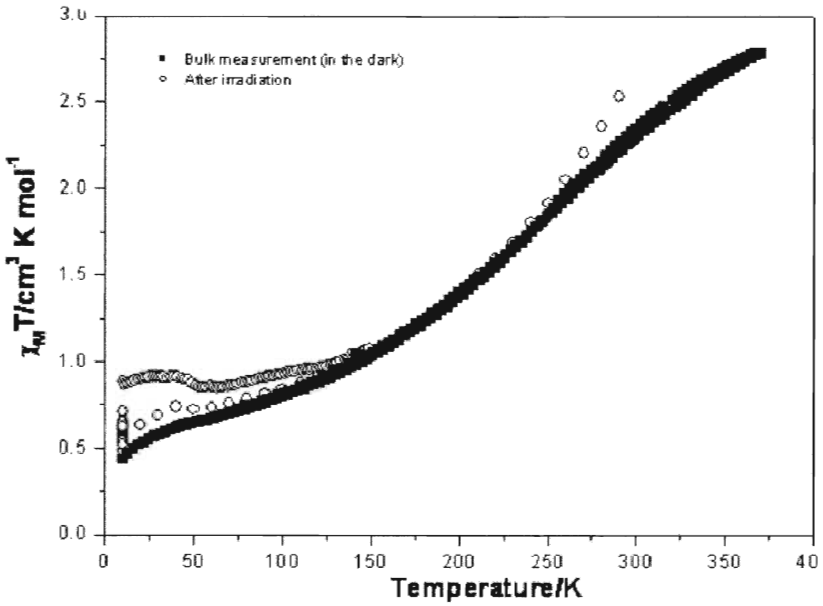

Figure 4.21. : Temperature dependence of the χT product for **(4.13).**

The magnetic properties were recorded on a powder sample of **(4.13)**. Elemental analysis data for the powder is consistent with the stoichiometry $[Fe(N_3O_2)CN_2]H_2O$. The sample was introduced into the SQUID at 300 K and the magnetic susceptibility was recorded on slow cooling from 300 to 10 K in 3 K steps. Care was taken not to freeze in the LS state by flash cooling the sample. The magnetic susceptibility was further recorded in warming mode to from 10 to 300 K in 3 K steps. The magnetic properties in the high temperature region (280 to 370 K) were recorded in one circle starting at 280 K warming up to 370 K and then cooling back to 280 K in 3 K steps, Figure 4.21. At 370 K, the $\chi_M T$

value is 2.78 cm^3Kmol^{-1}. Decreasing the temperature leads to a continuous and very smooth decrease in $\chi_M T$ down to 50 K at which $\chi_M T$ reaches the value 0.64 cm^3Kmol^{-1}. Between 50 and 25 K, $\chi_M T$ remains roughly constant, whereas it decreases again below 25 K to reach the value of 0.43 cm^3 K mol^{-1} at 10 K. Increasing the temperature shows that no thermal hysteresis is present. The spin transition is very gradual, with incomplete conversion at low (10 K) and high temperature (370) K. Taking a mean value of $\chi_M T$ of 3 cm^3 K mol^{-1} for the high spin state as a rough approximation, the high spin fraction can be evaluated as 2.78/3= 92.6% at 370 K and 0.64/3= 21.3% at 50 K. The small decrease in $\chi_M T$ below 25 K can be attributed to zero field splitting of the remaining high spin fraction. The very gradual nature of the spin transition can possibly be traced back to the absence of any strong cooperativity between molecules and/or distribution of the molecular environment if the compound is not perfectly crystalline. Thermal quenching of the high spin state was attempted by cooling the sample very rapidly from room temperature to 10 K. However, the high spin fraction at 10 K was the same as that obtained via slow cooling; suggesting that thermal quenching of the high spin state is not feasible for this compound.

Photomagnetic experiments were performed in collaboration with the Letard group at the CNRS in Bordeaux, France. Attempts to photoexcite the compound in the SQUID cavity with light of different wavelengths were performed. The best photomagnetic conversion was obtained by illuminating the sample with green light (λ = 514 nm) at 10 K. After photoexciting the compound for 10 hours with a power source of 70mW at the entry of the glass fiber, the light was switched off. $\chi_M T$ reached a value of 0.86 cm^3Kmol^{-1}, compared with 0.43 cm^3Kmol^{-1} before irradiation. In order to approximate the temperature at which the photoexcited spin state relaxes, the temperature

was continuously increased in the dark at 0.3 $Kmin^{-1}$ and the magnetization recorded in 1 K steps. The $\chi_M T$ plot is almost constant up to 40 K, when it decreases slightly and remains more or less constant up to 125 K, the temperature at which the curve merges with the thermal spin transition recorded in the dark. It should be emphasized that the photoconversion of this complex is small and very far from being complete. If we estimate the value as a percentage of the conversion observed between 10 and 370 K, where the $\chi_M T$ values are respectively of 0.43 and 2.78 cm^3Kmol^{-1}, the photoconversion is about (0.86-0.43)/ (2.78-0.43) = 18.3%. It can be recalled here that for the original $Fe[N_3O_2]CN_2$ complex reported by Sato *et al.*[134], the photo-induced conversion was complete at 370 K. Accurately defining a T(LIESST) for such a low conversion is difficult. Possibly, the very slow decrease of $\chi_M T$ with increasing temperature is a consequence of a larger energy barrier to lattice reorganization for this complex since the structural rearrangements taking place in the crystal lattice could hindered by the bulky nature of the phenyl substituents on the macrocyclic ring. However, it remains clear that this complex displays a modest LIESST effect which is the first time such a photoconversion from LS to HS has been observed for an enantiomerically pure Fe(II) spin crossover complex where the chirality is ligand-based.

4.6 Summary and future work

To summarize, three new Schiff-base Fe(II) macrocycles **(4.3)**, **(4.12)** and **(4.13)** were prepared and characterized. Compound **(4.3)** is the first dinuclear Fe(II) macrocycle $[N_3O_2]$ in which Fe(II) ions are covalently attached through a 4, 4′- bipyridine bridge. Two chiral macrocycles **(4.12)** and **(4.13)** were prepared from an R,R-chiral dimer. Within the timeframe of this project, a synthetic strategy has been developed for the facile synthesis of new chiral diamines. This strategy is versatile so that the R groups at the two chiral centres can be varied. The macrocycles have been characterized by mass, IR and UV-vis spectroscopy as well as X-ray crystallography. The data for complex **(4.12),** is consistent with a HS Fe(II) and there is no evidence of a thermal or light induced spin crossover. In contrast, the structural data for the *bis* CN macrocycle **(4.13)** shows presence of two independent molecules with different coordination geometries at both low and room temperatures. The structural data is consistent with the presence of a spin crossover transition which is confirmed by magnetic studies. Most interestingly this complex shows a photoinduced spin crossover transition that is far from quantitative. It is likely that the steric hindrance of the bulky phenyl rings increases the energy barrier to the reorganization of the coordination geometry of the Fe(II) during the spin crossover process. The results described in this thesis represent the first example of a chiral SCO complex prepared from a pentadentate $[N_3O_2]$ macrocycle. Following this strategy, new families of Fe(II)$[N_3O_2]CN_2$ complexes can be prepared and characterized and their SCO properties elucidated. In the longer term, the axial coordination sites of the macrocycles can be exploited with suitable ancillary ligands for the preparation of chiral cyanide bridged frameworks. In this respect, the long term goal is to work towards the assembly

of molecule-based multiferroic and magneto-chiral materials where ferromagnetism and chirality co-exist.

CHAPTER 5

Experimental

5.1 General Procedures:

All reagents were purchased from commercial sources and used as received unless otherwise stated. Anhydrous solvents were obtained from a Puresolve PS MD- 4 solvent purification system, and all air and /or moisture sensitive reactions were carried out using standard Schlenk techniques, unless otherwise stated. Silica gel (75-250 Mesh, 60Å) for column chromatography was purchased from Desican Inc. For thin layer chromatography (TLC), silica gel plates were obtained from EMD chemicals *Inc*. Elemental analyses were obtained from Atlantic Microlab, *Inc*. Norcross, GA, USA.

5.2 Instrumentation:

FT-IR: Spectra were recorded on a Bomem MB-100 spectrometer as KBr discs.

UV-vis: Spectra were recorded on a Shimadzu 3600 UV-Vis-NIR spectrophotometer or Thermo Spectronic/ Unicam UV-4 UV spectrophotometer. Room temperature spectra were acquired from solutions in appropriate solvents. Spectra at 77 K were obtained as ethanol glasses in 5 mm NMR tubes immersed in a transparent liquid nitrogen dewar.

Mass spectroscopy: Electron Impact (EI) Ionization and Fast Atom Bombardment (FAB) spectra were recorded on a Kratos Concept 1S high resolution E/B mass spectrometer.

NMR: ^{1}H NMR and ^{13}C NMR spectra were obtained on Bruker Advance DPX-300 and DPX-600 MHz digital spectrometers with deuterated solvents. Chemical shifts for NMR were determined relative to the internal standard tetramethylsilane. Multiplicity is

assigned following the abbreviations: s (singlet), d (doublet), t (triplet), q (quartet), dd (doublet of doublet), m (multiplet), br (broad).

Melting point: A Stuart Scientific SMP 10 apparatus was used to measure melting points.

EPR: Electron paramagnetic resonance (EPR) data were obtained by Dr. Poddutoori at Brock University. The spectra were recorded as powders in quartz tubes on a Bruker Elexsys E580 pulsed and CW X-band (9 GHz) spectrometer, equipped with a liquid nitrogen setup. The simulation of EPR data of clusters **(2.17)** and **(2.26)** was carried out by Prof. J. M. Rawson at University of Windsor.[77]

Variable temperature magnetic susceptibility measurments: Magnetic susceptibility measurements of cluster **(2.17)** were obtained by Prof. Jerome Long and Prof. Muralee Murugesu at University of Ottawa using a Quantum Design SQUID magnetometer MPMS-XL7 operating between 1.8 and 300 K. Dc analyses were performed on polycrystalline samples, wrapped in a polyethylenemembrane and under a field ranging from 0 to 7 T. Magnetic susceptibility measurements of cluster **(2.26)** were obtained by Prof. Martin Lemaire at Brock university using a Quantum Design SQUID magnetometer MPMS in an applied field of 5000 G between 5 and 300 K. Dc analyses were performed on polycrystalline samples, carefully weighted into gelatine capsules, which were loaded into plastic straw and attached to the sample transport rod. Magnetic susceptibility measurements of the R,R-chiral macrocycles **(4.12)** and **(4.13)** were obtained in collbaoration with Dr.Cédric Desplanches and Dr. Hongfeng Wang at the CNRS in Bordeaux, France using a Quantum Design SQUID magnetometer. The magnetization was recorded from 10 K to 350 K. Photomagnetic experiment has also been performed

using different wavelength. The compound were irradiated for 10 hours with power 70 mW at the entry of a glass fiber.

X-ray structure determination and powder diffraction: Crystals of a suitable size were mounted on a small loop mounted on a copper pin. Data were collected on a X8 APEX II CCD diffractometer located with Mo Kα radiation (λ = 0.71073 Å) and an Oxford low temperature device. The data were processed using the Bruker SHELXTL software package[135]. The structures were solved by direct methods (SHELXS-97).[135] The structures were refinement using SHELX-97[135] in the Bruker SHELXTL suite. PlATON/SQUEEZE[65] was used to correct the data for the presence of disordered solvent. Molecular structures and packing diagrams were prepared using ORTEP[66] and Mercury.[136] The single crystal data were collected and solved by Prof. Pilkington and Niloofar Zarrabi. The refinement of data was carried out by Prof. Pilkington unless otherwise stated.

5.3. Experimental for project 1

5.3.1. Synthesis of (2.11)[76]

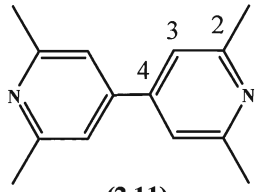

(2.11)

Dry hexane (100 mL) was added to Na (30%-35% in paraffin wax, 13.87 g, 196.0 mmol) under nitrogen, and the mixture was sonicated for 5 min. The solvent was then removed with a syringe and the operation was repeated three times. Distilled THF (80 mL) and 2,6-lutidine (10 mL, 86 mmol) were added to the reaction mixure that was stirred vigorously under nitrogen overnight to afford a light yellow solution. SO_2 gas was then passed over the reaction mixture slowly over a period of 5 h. The reaction mixture was then quenched with ethanol (100 mL), and the pH of the solution was adjusted to approximately pH = 8 by the addition of an aqueous solution of 12 M NaOH. The resulting mixture was extracted with CH_2Cl_2 (6 × 50 mL), and the organic layers were combined and dried over Na_2SO_4. Removal of the solvent under vacuum afforded the crude product as a pale yellow solid, which was re-crystallized from water to afford ligand (**2.11**) as a white solid. Yield = 15.54 g (85%).

^{1}H NMR ($CDCl_3$, 300 MHz, ppm):	δ = 7.19 (s, 4H, H_3), 2.62 (s, 12H, CH_3).
^{13}C NMR ($CDCl_3$,75 MHz, ppm):	δ = 158.5, 146.8, 118.1, 24.5.
Mass spectrum (FAB):	*m/z* 212 $[M]^+$.
IR (KBr, cm^{-1}):	3010 (w), 2955 (w), 2915, 1434, 1383, 1099, 1030 , 989, 485, 446.
Mpt.	152-154 °C Lit[152 °C][76]

5.3.2 Synthesis of (2.12)[76]

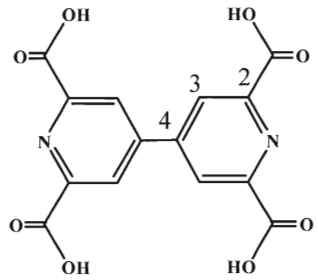

(2.12)

Compound **(2.11)** (1.95 g, 9.20 mmol) was dissolved in concentrated H_2SO_4 (35 N, 32 mL, 0.57 mol) and cooled in ice bath, after which time CrO_3 (11.02 g, 11.02 mmol) was cautiously added in portions over 3 h with continuous stirring. The resulting reaction mixture was slowly heated to 75°C and then kept at that temperature for 2 h. The resulting dark green sticky solution was poured into ice water (200 mL) with continuous stirring. A white precipitate was collected by filtration. It was washed with distilled water and dried under vacuum to afford **(2.12)** as a white solid. Yield = 2.05 g (67%).

^{1}H NMR (DMSO-d_6, 300 MHz, ppm):	δ = 13.62 (s, 4H, OH), 8.61 (s, 4H, H_3).
^{13}C NMR (DMSO-d_6, 75 MHz, ppm):	δ = 165.8 , 150.1, 146.7, 125.8.
Mass spectrum (FAB):	*m/z* 332 $[M]^+$.
IR (KBr, cm^{-1}):	3300 (br), 1732 , 1965, 1429 , 1231, 1255, 1309, 909.
Mpt.	272-274°C Lit[270 °C][76]

5.3.3. Synthesis of (2.5)[76]

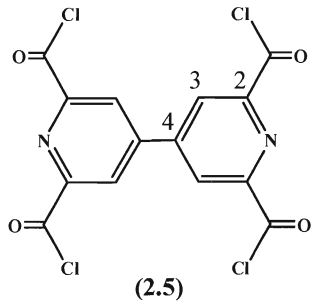

(2.5)

To a solution of **(2.12)** (2.80 g, 8.43 mmol) in distilled $SOCl_2$ (15 mL) under nitrogen was added two drops of distilled DMF. The resulting reaction mixture was then refluxed for 5 h. The solvent was then removed to afford **(2.5)** as a pale green solid. Yield = 3.03 g (89%).

^{1}H-NMR ($CDCl_3$, 300 MHz ppm):	δ = 8.62 (s, 4H, H_3).
^{13}C-NMR ($CDCl_3$, 75 MHz ppm):	δ = 169.2, 150.8, 146.7, 126.1.
Mass spectrum (FAB):	*m/z* = 404 $[M]^+$.
Mpt.	204 -206°C Lit[205-206°C][76]

5.3.4. Synthesis of (2.6)

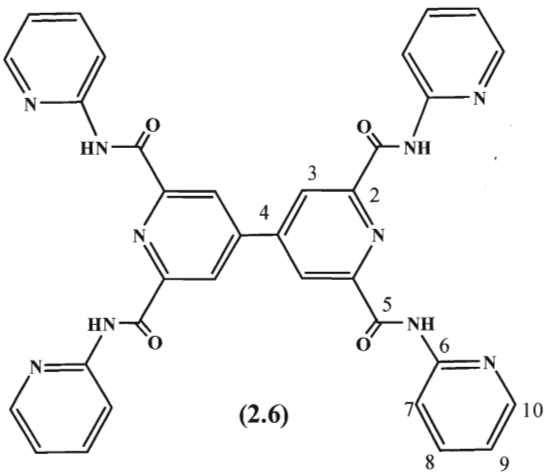

(2.6)

A mixture of **(2.12)** (2.80 g, 8.43 mmol) and $SOCl_2$ (15 mL) were refluxed for 5 h under nitrogen. The excess $SOCl_2$ was then removed under reduced pressure. The resulting product was cooled in an ice bath for 15 min. Dry toluene (30 mL) followed by 2-aminopyridine (3.17 g, 33.72 mmol) was then added and the solution was further refluxed overnight. The solvent was removed under reduced pressure and the resulting crude pale yellow solid was dissolved in CH_2Cl_2 and neutralized with 5% $NaHCO_3$. The organic layers were separated, washed with water and dried over Na_2SO_4. Removal of the solvent gave a solid which was washed with ethanol to afford ligand **(2.6)** as a pale yellow solid. Yield = 3.37 g (63%).

^{1}H NMR ($CDCl_3$, 300 MHz, ppm): δ = 11.36 (s, 4H, NH), 8.99 (s, 4H, H_3), 8.62 (d, 4H, J = 8.4 Hz, H_7), 8.44 (d, 4H, J = 5.1 Hz, H_{10}), 7.89 (t, 4H, J = 14.1, 7.5 Hz, H_8), 7.19 (t, 4H, J = 12.3, 5.1 Hz, H_9).

^{13}C NMR ($CDCl_3$, 150 MHz, ppm): δ = 161.3, 151.4, 150.1, 147.7, 138.9, 123.4, 120.2, 114.7.

HRMS (FAB):	Found m/z = 637.19241 $[M]^+$, Calcd. 637.20156 for $C_{34}H_{24}N_{10}O_4$
CHN:	Found C 64.23, H 3.76, N 22.10%. Calcd. for $C_{34}H_{24}N_{10}O_4$: C 64.15 H 3.80 N 22.00%.
IR (KBr, cm^{-1}):	3455, 1692 , 1524, 1227.
Mpt.	> 300 °C

5.3.5 Synthesis of (2.7)

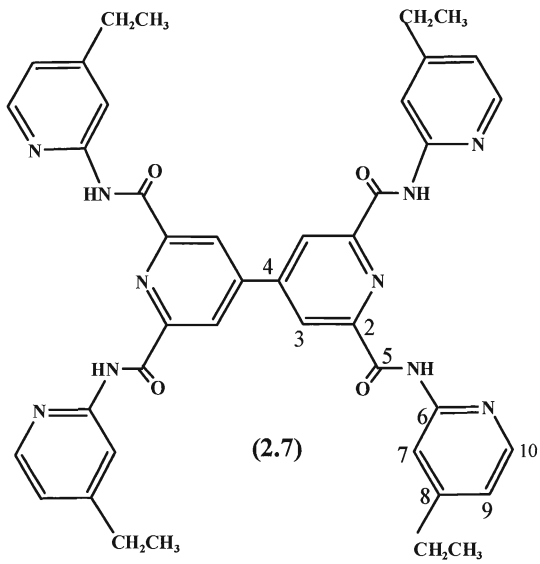

(2.7)

A mixture of **(2.12)** (2.80 g, 8.43 mmol) and $SOCl_2$ (15 mL) were refluxed for 5 h under nitrogen. The excess $SOCl_2$ was then removed under reduced pressure. The resulting compound **(2.5)** was cooled in an ice bath for 15 min. Dry toluene (30 mL) followed by 4-ethyl-2-aminopyridine (4.1 g, 33.72 mmol) was then added to the above solution that was further refluxed overnight. The solvent was removed under reduced pressure and the resulting pale yellow solid was dissolved in CH_2Cl_2 and neutralized by the addition of 5% $NaHCO_3$. The organic layers were separated, washed with water and

dried over Na_2SO_4. Removal of the solvent under vacuum afforded the crude product, which was washed with ethanol to afford ligand **(2.7)** as a pale yellow solid. Yield = 4.09 g (65%). Single crystals of **(2.7)** suitable for X-ray diffraction were grown from the slow evaporation of a MeOH:$CHCl_3$ (1:1) solution of **(2.7)** at RT.

^{1}H NMR ($CDCl_3$, 600 MHz, ppm):	δ = 11.19 (s, 4H, NH), 8.96 (s, 4H, H_3), 8.44 (s, 4H,H_7), 8.30 (d, 4H, J = 4.8 Hz, H_{10}) 7.02 (d, 4H, J = 4.2 Hz, H_9), 2.80 (q, 8H, J = 22 Hz, CH_2), 1.36 (t, 12H, J = 15, 7.2 Hz, CH_3).
^{13}C NMR ($CDCl_3$, 150 MHz, ppm):	δ = 161.2, 156.4, 151.2, 150.3, 148.0, 147.5, 123.3, 120.2, 114.0, 28.4, 14.4.
HRMS (FAB):	Found m/z = 749.32123 $[M]^+$, Calcd. 749.32676 for $C_{42}H_{40}N_{10}O_4$.
CHN:	Found C 63.41, H 5.49, N 17.74%. Calcd. for $C_{42}H_{40}N_{10}O_4 \cdot 2.45\ H_2O$: C 63.62 H 5.71 N 17.66%.
IR (KBr, cm^{-1}):	3377 , 3270 (br), 1691, 1527.
UV-vis (DCM :MeOH, 1 :1):	λ_{max}= 285 nm.
Mpt.	> 300 °C

5.3.6 Preparation of coordination complexes of ligand (2.7)

Coordination with $Co(OAc)_2$

Carboxamide ligand **(2.7)** (400 mg, 0.53 mmol) was dissolved in chloroform (20 mL). To this solution was added $[Co(OAc)_2 \cdot H_2O]$ (190 mg, 1.07 mmol) in ethanol (5 mL). The reaction mixture was then refluxed overnight. The resulting brown precipitate was filtered, washed with ethanol and dried. Yield = 222 mg (48%).

Mass spectrum (FAB): *m/z* = 1014 $[Co_2(L\text{- }4H)CH_3CO_2H.2EtOH]^+$ 47% , 863 $[Co_2(L\text{- }4H) +H]^+$ 74%, 806 $[Co(L\text{- }2H) +H]^+$ 100%, 749 $[L+H]^+$ 28%.

IR(KBr, cm^{-1}): 3434 (br), 1617 (sh), 1564 (sh), 1528 (sh), 1475 (sh), 1414 (sh).

UV-vis (DCM /MeOH, 1 :1): λ_{max}= 285 nm.

EPR (200K): $g_{\|} = 2.0021$, $g_{\perp} = 2.0008$

CHN: Found C 51.44, H 5.07, N 13.46.% Calcd. for $[Co_2(C_{42}H_{37}N_{10}O_4)(CH_3CO_2)]\cdot EtOH\cdot 5.45H_2O$; C 51.78, H 5.38, N 13.13%.

Coordination with Ni $(OAc)_2$

Carboxamide ligand **(2.7)** (400 mg, 0.53 mmol) was dissolved in chloroform (20 mL). To this solution was added $[Ni(OAc)_2 \cdot 4H_2O]$ (266 mg, 1.07 mmol) in ethanol (5 mL). The reaction mixture was then refluxed overnight. The resulting pale brown precipitate was filtered, washed with ethanol and air-dried. Yield = 273 mg (59%).

Mass spectrum (FAB): *m/z* = 927 $[Ni(L\text{-}2H)CH_3CO_2+ EtOH+ H]^+$ 10% , 805 $[Ni(L\text{-}2H)+H]^+$ 20%, 749 $[L]^+$ 90%.

IR (KBr, cm^{-1}): 3419 (br), 1616 (sh), 1564 (sh), 1527 (sh), 1475 (sh, w), 1415 (sh).

UV-vis (DCM : MeOH, 1 : 1): λ_{max}= 285 nm.

Coordination with $Cu(OAc)_2$

Carboxamide ligand **(2.7)** (400 mg, 0.53 mmol) was dissolved in chloroform (20 mL). To this solution was added [$Cu(OAc)_2.H_2O$] (195 mg, 1.07 mmol) in ethanol (5 mL). The reaction mixture was then refluxed overnight. The resulting green precipitate was filtered, washed with ethanol and air-dried. Yield = 262 mg (56%).

Mass spectrum (FAB): *m/z* = 937 $[Cu_2(L- 4H) +H_2O + EtOH +H]^+$ 15%, 874 $[L+Cu]^+$ 15%, 811 $[L+2Cu]^+$ 30%, 749 $[L]^+$ 30% .

IR (KBr, cm^{-1}): 3411(br), 1617(sh), 1600(sh), 1477, 1419(sh), 1375(sh).

UV-vis (DCM :MeOH, 1 :1): λ_{max}= 274 nm.

CHN: Found C 51.81, H 5.01, N 13.65%. Calcd. for $[Cu_2(C_{42}H_{37}N_{10}O_4)(CH_3CO_2)]\cdot EtOH\cdot 4.45\ H_2O$; C 51. 21, H 5.23, N 13.24%.

Coordination with Zn $(OAc)_2$

Carboxamide ligand **(2.7)** (400 mg, 0.53 mmol) was dissolved in chloroform (20 mL). To this solution was added [$Zn(OAc)_2\cdot 2H_2O$] (235 mg, 1.07 mmol) in ethanol (5 mL).

The reaction mixture was then refluxed overnight. The resulting yellow precipitate was filtered, washed with alcohol and air-dried. Yield = 249 mg (53%).

^{1}H NMR ($CDCl_3$, 300 MHz, ppm):	δ = 11.49 (s, 2H, NH), 8.97 (t, 4H, H_3), 8.40 (m, 6H) 7.84 (m, 4H), 7.03 (bs, 4H, H_9), 6.37 (m), 2.99 (s, CH_2), 2.77 (s, CH_2), 1.84 (bs, CH_3COO), 1.60 (CH_3), 1.54 (CH_3).
Mass spectrum (FAB):	*m/z* = 956 $[Zn_2(L- 4H) + 2H_2O + EtOH + H]^+$ 15%, 895 $[Zn_2(L- 2H) +2H_2O + EtOH + H]^+$ 20%, 877 $[Zn_2(L- 2H) + H_2O + EtOH +H]^+$ 55% , 811 $[Zn(L-2H) +H_2O + EtOH + H]^+$ 65%, 749 $[L]^+$, 100%.
IR (KBr, cm^{-1}):	3414 (br), 3257 (br), 1693 (sh), 1619 (sh), 1565 (sh, s), 1533 (sh), 1483 (sh, w), 1417 (sh).
UV-vis (DCM : MeOH, 1 :1):	λ_{max}= 300 nm.

5.3.7 Synthesis of ligand (2.8)

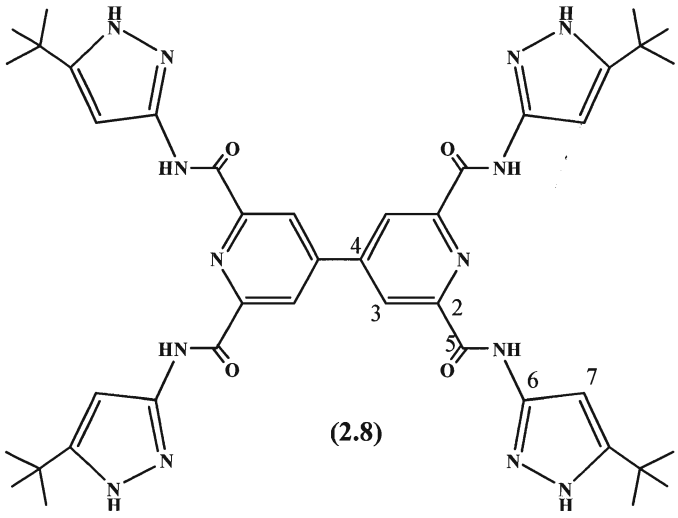

(2.8)

A mixture of **(2.12)** (2.80 g, 8.43 mmol) and $SOCl_2$ (15 mL) were refluxed for 5 h under nitrogen. The excess $SOCl_2$ was then removed under reduced pressure. The resulting compound **(2.5)** was cooled in an ice bath for 15 min. Dry toluene (30 mL) followed by 3-amino-5-*tert*-butyl-pyrazole (4.7 g, 33.72 mmol) was then added to the above solution that was further refluxed overnight. The solvent was removed under reduced pressure and the resulting crude pale yellow solid was dissolved in CH_2Cl_2 and neutralized with 5% $NaHCO_3$. The organic layers were separated washed with water and dried over Na_2SO_4. Removal of the solvent afforded the crude product, which was washed with EtOH to afford ligand **(2.8)** as a pale yellow solid. Yield = 4.53 g (66%). Single crystals of **(2.8)** suitable for X-ray diffraction were grown via diffusion of Et_2O into a DMF solution of ligand **(2.8)** at RT.

^{1}H NMR (DMSO-d_6, 600 MHz, ppm): δ = 12.36 (s, 4H, NH pyr), 11.83 (s, 4H, NH

	amide), 8.70 (s, 4H, H_3), 6.58 (s, 4H, H_7), 1.33 (s, 36H, CH_3).
^{13}C NMR (DMSO-d_6, 150 MHz, ppm):	δ = 161.5, 153.0, 150.8, 147.5, 146.7, 123.1, 94.8, 31.2, 30.4.
HRMS (FAB):	*m/z* = 817.43742 $[M]^+$; Calcd.817.43295 for $C_{42}H_{52}N_{14}O_4$.
CHN:	Found C 56.91, H 6.65, N 20.86%. Calcd. for $C_{42}H_{52}N_{14}O_4 \cdot 3.3\ H_2O \cdot C_2H_5OH$: C 57.29 H 7.06 N 21.26%.
IR (KBr, cm^{-1}):	3339 (sh), 3175(br), 1689 (sh), 1541 (sh).
UV-vis (DCM:MeOH = 3: 1):	265
Mpt.	> 300 °C

5.3.8 Preparation of coordination complexes of ligand (2.8)

$[Cu_8\ (L)_4Cl_{16}]\cdot CHCl_3\cdot 5H_2O\cdot 7CH_3OH$

Carboxamide ligand **(2.8)** (400 mg, 0.49 mmol) was dissolved in chloroform (15 mL). A solution of $CuCl_2\cdot 2H_2O$ (167 mg, 0.98 mmol) in methanol (5 mL) was then carefully layered over the top of the chloroform solution. Green plates suitable for X-ray diffraction were obtained after 2 weeks. Yield = 486 mg (21%).

Mass spectrum (FAB):	*m/z* = 1089 $[Cu_3(\mathbf{L})Cl + H_2O + CH_3OH]^+$ 5%, 977 $[Cu_2(\mathbf{L}\text{-}2H)Cl]^+$ 10%, 942, $[Cu_2\ (\mathbf{L})]^+$ 35%, 879 [Cu $(\mathbf{L})]^+$ 100%.
IR (KBr, cm^{-1}):	3329 (sh), 1694 (sh), 1640 (sh), 1574(sh), 1548 (sh).

UV-vis (MeOH): λ_{max}= 261 nm (ε = 81048 $M^{-1}cm^{-1}$), 797 nm (ε = 854 $M^{-1}cm^{-1}$).

CHN: Found C 44.29, H 5.11, N 16.44%. Calcd. for [$Cu_8(L)_4Cl_{16}$]·$CHCl_3$·$5H_2O$·$7CH_3OH$] C 44.25, H 5.21, N 16.42%.

EPR (100K): g_x= 2.224, g_y= 2.065, g_z= 2.035.

5.3.9 Synthesis of (2.24)[76]

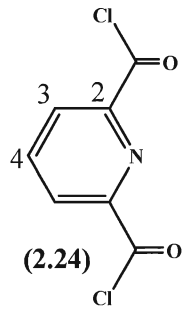

(2.24)

To a solution of distilled $SOCl_2$ (15 mL) was added 2,6-pyridine dicarboxylic acid (2.80 g, 8.43 mmol) and two drops of distilled DMF under nitrogen. The resulting reaction mixture was refluxed for 5 h. The solvent was then removed under vacuum to afford **(2.24)** as a pale green solid. Yield = 3.08 g (91%).

^{1}H NMR ($CDCl_3$, 300 MHz, ppm): δ = 8.23 (m, 4H, H_3, H_4).

^{13}C NMR ($CDCl_3$, 75 MHz ppm): δ = 165.8, 148.4, 139.8, 128.0.

Mass spectrum (FAB): *m/z* = 203 $[M]^+$.

Mpt. 56 °C Lit[57-61°C][76]

5.3.10 Synthesis of ligand (2.25)[137]

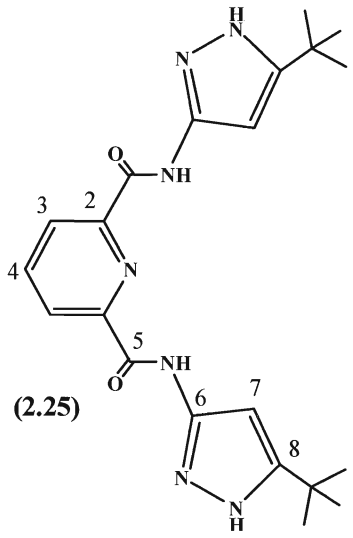

(2.25)

A mixture of 2,6-pyridine dicarboxylic acid (2.80 g, 8.43 mmol) and $SOCl_2$ (excess, 15 mL) were refluxed for 5 h under anhydrous conditions. Excess $SOCl_2$ was removed under reduced pressure. The resulting ligand **(2.24)** was cooled in an ice bath for 15 min. Dry toluene (30 mL) followed by 3-amino-5-*tert*-butylpyrazole (2.35 g, 16.86 mmol) was then added and the solution was further refluxed overnight. It was filtered in hot condition and washed with hot toluene and Et_2O to afford ligand **(2.25)** as a pale yellow solid. Yield = 4.88 g (71%).

^{1}H NMR (DMSO-d_6, 300 MHz, ppm): δ =13.04 (br, 2H, NH_{pyr}), 12.21 (s, 2H, NH_{amide}), 8.39 (d, 2H, J = 8.7 Hz, H_3), 8.31 (m, 1H, H_4), 6.66 (s, 2H, H_7), 1.49 (s,18H, CH_3).

^{13}C NMR (DMSO-d_6, 75 MHz, ppm): δ = 162.2, 155.3, 148.7, 144.2, 140.6, 126.3, 94.5, 31.6, 30.1.

HRMS (FAB): Found *m/z* = 410.22867 $[M]^+$; calculated 410.22598 for $C_{21}H_{27}N_7O_2$.

CHN: Found C 51.91, H 6.02, N 19.80%. Calcd. for $C_{21}H_{27}N_7O_2 \cdot 0.56\ CH_3Cl_3 \cdot 1.23\ H_2O$ C 51.96, H 6.07, N 19.68%.

IR (KBr, cm^{-1}): 3287 (sh), 2974 (sh), 2608 (sh), 1712 (sh), 1554 (sh).

UV-vis (MeOH): λ_{max}= 274 nm (ε = 37125 $M^{-1}cm^{-1}$).

Mpt. > 300 °C

5. 3.11 Preparation of coordination complexes of ligand (2.25)

$[Cu_9\ (L)_6Cl_6]\cdot CH_3OH\cdot 5H_2O\cdot(C_2H_5)_3N$

The carboxamide ligand **(2.25)** (400 mg, 0.97 mmol) was dissolved in MeOH (15 mL). After which time, Et_3N (0.28 mL, 2 mmol) was added and the solution was refluxed for 2 h. $CuCl_2$ (165 g, 0.97 mmol) was then added and the reaction mixture was refluxed further overnight. The resulting clear solution was reduced in volume by 50% after which time Et_2O was slowly diffused in at RT affording dark green blocks after 3 days. Yield = 475 mg (60%).

Mass spectrum (FAB): *m/z* = 1067 $[Cu_2(\mathbf{L})_2Cl_2+H_2O+CH_3OH]^+$ 10%, 1005 $[Cu(\mathbf{L})_2Cl_2+H_2O+\ CH_3OH]^+$ 15%, 533 $[Cu_2(\mathbf{L}\text{-}2H)]^+$ 100% , 472 $[Cu(L)]^+$ 95%.

IR (KBr, cm^{-1}): 2957 (sh), 2923 (sh), 1465 (sh).

UV-vis (MeOH):	λ_{max}= 254, 299, 678 nm, (ε = 67339, 52477, 1354 $M^{-1}cm^{-}1$).
CHN:	Found C 45.04 H 6.78 N 15.14%. Calcd. for $[Cu_9(L)_6Cl_6]\cdot CH_3OH\cdot 5H_2O\cdot(C_2H_5)_3N$ C 44.30 H 5.16 N 16.53%.
EPR (100K):	g_x= 2.042, g_y= 2.052, g_z= 2.062.

5.4 Experimental for project 2

5.4.1 Synthesis of (2.7)[138]

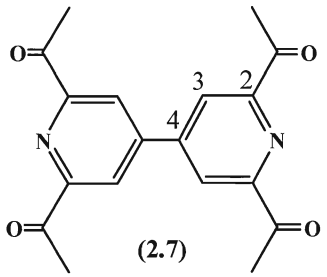

(2.7)

Compound (**2.5**) (3.03 g, 7.46 mmol) was added in portions to a solution of Meldrum's acid (4.45 g, 30.9 mmol) in distilled CH_2Cl_2 (25 mL) and distilled pyridine (6.20 mL, 76.9 mmol). A dark brown solution formed immediately that was stirred at 0 °C for one hour and then room temperature for a further hour. The reaction mixture was diluted with dry CH_2Cl_2 (40 mL), and then poured into an aqueous solution of 2N HCl containing crushed ice (50 mL). The organic layer was separated and the aqueous layers were washed with CH_2Cl_2 (6 × 50 mL). The organic layers were combined, washed with 2N HCL (2 × 50 mL) and dried over anhydrous Na_2SO_4. The solvent was removed to

afforded the intermediate as a dark brown solid (5.05 g), which was then refluxed in a (1:1) solution of acetic acid at 115 °C for 16 h. The reaction mixture was then diluted with H_2O (200 mL) andextracted with CH_2Cl_2 (6 × 50 mL). The combined organic layers were washed with a 5% $NaHCO_3$ solution (50 mL), water (50 mL) and dried over anhydrous Na_2SO_4. Removal of solvent afforded **(2.7)** as a yellow solid. Yield = 1.52 g (61%).

^{1}H NMR ($CDCl_3$,300 MHz, ppm):	δ = 8.56 (s, 4H, H_3), 2.85(s, 12H,CH_3).
^{13}C NMR ($CDCl_3$,75 MHz, ppm):	δ = 198.7, 154.0, 146.7, 122.2, 25.6.
Mass spectrum (FAB):	*m/z* = 325 $[M]^+$.
IR (KBr, cm^{-1}):	2920 , 1704 , 16590 , 1408,
	1364 , 1100 , 958 , 895.
M.pt.:	> 300°C

5.4.2 Synthesis of $[Fe(N_3O_2)SCN_2]_2$ (4.3).[54b]

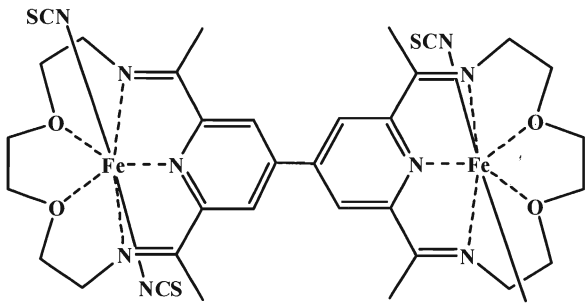

(4.3)

To a solution of $FeCl_2.4H_2O$ (0.153g, 0.767 mmol) in degassed MeOH (4 mL) was added a solution of $Na_2S_2O_4$ (85%, 92mg, 0.44mmol) in degassed H_2O (2 mL). To this mixture added the tetaketone (**2.7**) (0.125g, 0.383 mmol) followed by a solution of diamine (0.23g, 0.767mmol) in degassed MeOH (7 mL). The mixture was gently refluxed for 20 h under an N_2 atmosphere. After cooling, the volume of the solution was reduced to 50 % and the reaction mixture was filtered into a degassed solution of NaSCN (1.27 g, 15.6 mmol) in H_2O (5 mL) containing $Na_2S_2O_4$(38mg) under N_2. The mixture was stirred for a futher 4 h and the resulting blue precipitate was collected by filtration. The solid was washed with degassed water, THF and Et_2O and then dried under vacuum to afford (**4.3**). Yield = 0.21 g (61%).

Mass spectrum (FAB): *m/z* = 892 $[M]^+$ 20%, 834 $[M\text{-}SCN]^+$100%, 776$[M\text{-}2SCN]^+$ 70% .

CHN: Found C 41.21 H 4.49 N 12.24%. Calcd. for $C_{34}H_{40}Fe_2N_{10}O_4S_4 \cdot 2.35\ CH_3OH \cdot 2.9\ H_2O$ C 42.58 H 5.92 N 13.36%.

IR(KBr, cm^{-1}): 2061,1632,1119, 1025.

Mpt. > 300°C

5.4.3 Synthesis of (4.5)[126,127]

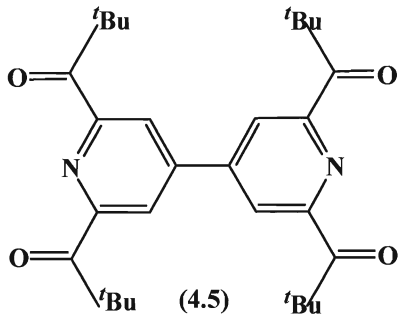

(4.5)

A solution of 3N *tert*-butyl lithium in pentane (14 ml) was added in one portion to a suspension of 4.0 g (21 mmol) of CuI in THF (20 ml) at -40 C° with vigorous stirring. The reaction mixture was stirred for 1 h at this temperature, after which time 0.75 g (1.85 mmol) of tetrachloroformyl bipyridine in THF (40 ml) was added. The reaction mixture was allowed to warm to room temperature and then poured into saturated aqueous ammonium chloride (50 mL) and extracted with three 50 ml portions of DCM. The combined organic phases were washed with water and dried over magnesium sulphate. The solvent was evaporated and the crude product was purificatied *via* column chromatography using neutral alumina gel and CH_2Cl_2 as the eluent. Pure **(4.5)** was obtained as a pale yellow solid. Yield = 340 mg (30%).

^{1}H NMR ($CDCl_3$,300 MHz, ppm): δ = 8.5 (s, 4H, H_3), 2.8 (s, 12H, CH_3).

^{13}C NMR ($CDCl_3$,75 MHz, ppm): δ = 206.2, 154.8, 146.6, 123.5, 44.0, 27.2.

Mass spectrum (FAB): $m/z = 492\ [M]^+$.

5.4.3 Synthesis of (4.7)[128,129]

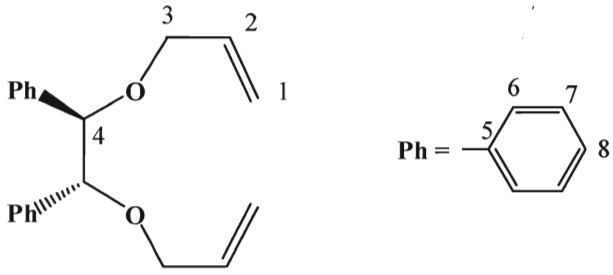

(4.7)

To a solution of (R,R)-(+)-Hydrobenzoin (6.03 g, 28.18 mmol) in dry THF (150 mL) was added sodium hydride (2.17 g, 85.90 mmol) and the mixture was stirred for 1 h at 30 °C under N_2 after which time a solution of allyl bromide (11.94 g, 98.72 mmol) in dry THF (25 mL) was added dropwise. The reaction mixture was then warmed to 40 °C and stirred at this temperture for 2 h and then refluxed for an additional 24 h or until TLC (silica gel) (DCM:MeOH = 9.5:0.5) showed the presence of no starting material. The mixture was cooled to RT and filtered to remove a white precipitate. The filtrate was collected and the solvent was removed under vacuum to give a pale yellow oily residue that was dissolved in CH_2Cl_2 (150 mL) and washed with H_2O (50 mL) and brine (50 mL). The solution was dried over $MgSO_4$ and the solvent was removed to afford (**4.7**) as pale yellow oil. Yield = 7.42 g (90%).

^{1}H NMR ($CDCl_3$, 300 MHz, ppm): δ = 7.19 (m, 6H, H_7, H_8), 7.08 (m, 4H, H_6), 5.87 (m, 2H, H_2), 5.23 (m, 4H, H_1), 4.55 (s, 2H, H_4), 3.80 (m, 4H, H_3).

^{13}C NMR ($CDCl_3$, 75 MHz, ppm): δ = 138.8, 135.1, 128.1, 127.7, 127.4, 116.5, 85.1, 70.2.

HRMS (FAB): Found *m/z* = 294.16254 $[M]^+$; Calculd 294.16198 for $C_{20}H_{22}O_2$.

5.4.5 Synthesis of (4.9)[128,129]

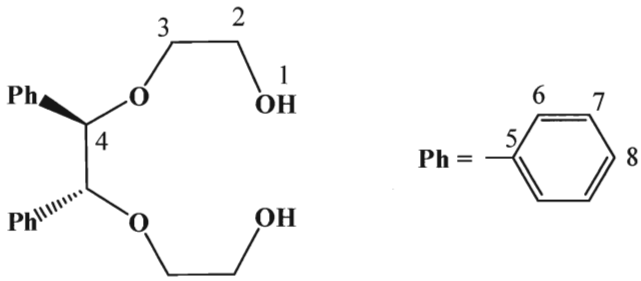

(4.9)

A solution of **(4.7)** (7.38 g, 25.1 mmol) and OsO_4 (0.19 g, 0.74 mmol) in THF/H_2O (60 mL, 3:1) was stirred at 25 °C for 2 h. $NaIO_4$ (31.4 g, 147 mmol) was then added dropwise over a 4 h period in the dark. The reaction mixture was stirred in the dark for an additional 20 h or until TLC (petroleum ether: Et_2O = 25:1) showed no evidence of any starting material. Removal of the solvent afforded a paste which was suspended in a (1:1) solution of CH_2Cl_2/MeOH (200 mL). A white solid was removed by filtration and the resulting pale brown filtrate was stirred vigorously and cooled to 0 °C. $NaBH_4$ (6.5 g, 170 mmol) was then added in portions over a 1 h period and the solution was stirred was for a further 19 h at room temperature under N_2. The solvent was removed and the resulting residue was added to a large amount of water (700 mL) and the mixture was stirred for 1 h to destroy unreacted $NaBH_4$ and $NaIO_4$ and other salts formed during the reaction. The

aqueous solution was extracted with CH_2Cl_2 (3 x 100 mL) and the organic phases were combined and washed with 1 M HCl, water (50 mL) and brine (50 mL). After drying over $MgSO_4$, the solution was filtered and the filtrate was concentrated to afford the crude produce as a yellow oil. The compound was purified by flash chromatography on silica gel eluting with a (20:1) mixture of $CHCl_3$:MeOH (20:1) to give **(4.9)** as a yellow oil. Yield = 3.62 g (48%).

^{1}H NMR ($CDCl_3$, 300 MHz, ppm): 7.21 (m, 6H, H_7,H_8), 7.08 (m, 4H, H_6), 4.50 (s, 2H, H_4), 3.78 (bs, 4 H, H_2), 3.71 (m, 2H, H_3), 3.52 (m, 2H, H_3), 3.03 (bs, 2H, H_1).

^{13}C NMR ($CDCl_3$, 75 MHz, ppm): 138.3, 128.2, 127.9, 127.5, 86.9, 71.2, 61.8.

HRMS (FAB): Found *m/z* = 303.15820 $[M]^+$; Calcd. 303.15963 for $C_{18}H_{22}O_4$.

5.4.6. Synthesis of (4.10)[128,129]

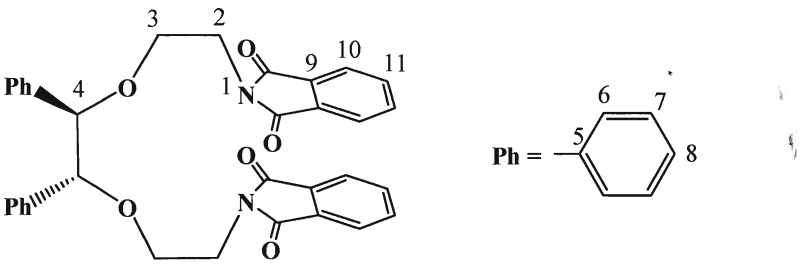

(4.10)

Di-iso-propyl azodicarboxylate (2.58, 95%, 12.17 mmol) was added dropwise to a solution of **(4.9)** (1.67 g, 5.53 mmol), phthalimide (1.79 g, 12.17 mmol) and triphenylphosphine (3.19 g, 12.17 mmol) in dry THF (45 mL), The mixture was stirred at RT under N_2 for 4 days. Removal of the solvent resulted in a solid residue. The solid was

suspended in CH_2Cl_2 and purified by flash chromatography, first by eluting with a 2:1 mixture of hexane:EtOAc and then by redissolving the product in DCM and carrying out a second column on silica gel eluting with a (3:1) mixture of petroleum ether/EtOAc. Removal of the solvent afforded **(4.10)** as white solid. Yield = 1.26 g (37%).

^{1}H NMR ($CDCl_3$, 300 MHz, ppm): 7.84 (s, 4H, H_{10}), 7.74 (s, 4H, H_{11}), 6.94 (m, 6H, H_7,H_8), 6.83 (m, 4H, H_6), 4.41 (s, 2H, H_4), 3.78 (m, 4H, H_3), 3.61 (m, 4H, H_2).

^{13}C NMR ($CDCl_3$, 75MHz, ppm): 168.1, 137.8, 133.8, 132.2, 127.7, 127.4, 127.3 123.1, 85.6, 66.0, 37.7.

Mass spectrum (FAB): *m/z* = 561 $[M]^+$.

CHN: Found C 71.65, H 5.24, N 4.84%; Calcd. for $(C_{34}H_{28}N_2O_6)\cdot$ 0.5 H_2O C 71.69, H 5.13, N 4.92%.

Mpt. 188°C

5.4.7 Synthesis of (4.11)[128,129]

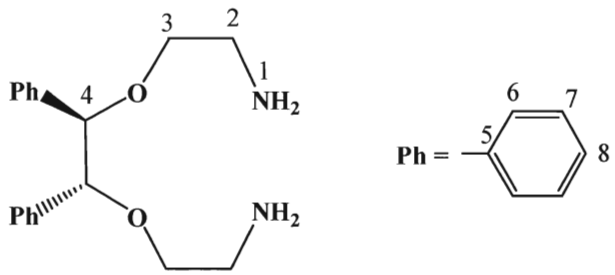

(4.11)

Compound **(4.11)** (0.5 g, 0.89 mmol) was suspended in warm ethanol (96%, 30 mL) after which time hydrazine monohydrate (0.45 g, 8.9 mmol) was added and the solution

was refluxed for 27 h. The mixture was cooled to RT and a white gel-like precipitate was removed by filtration. The precipitate was washed with cold EtOH (6 mL) and CH_2Cl_2 (9 mL). The filtrate was evaporated and the resulting white residue was dissolved in CH_2Cl_2 (100 mL) and extracted with 2N HCl (3 × 40 ml). 20% aqueous NaOH (100 mL) was them added to the combined aqueous extracts in order to adjust the pH to ≥ 10 and the mixture was stirred for 30 min. The aqueous solution was extracted with CH_2Cl_2 (3 × 60 mL). The combined extracts were washed with H_2O (2 x 50 mL) and brine (2 x 50 mL) respectively and dried over anhydrous $NaSO_4$. Removal of solvent afforded **(4.11)** as colourless oil. Yield = 0.2 g (78%).

^{1}H NMR ($CDCl_3$, 300 MHz, ppm):	7.22 (m, 6H, H_7,H_8), 7.15 (m, 4H, H_6), 4.48 (s, 2H, H_4), 3.49 (m, 2H, H_3), 3.36 (m, 2H, H_3), 2.82 (t, 4H, J = 1.8, 0.6, H_2), 1.4 (bs, 4H, NH).
^{13}C NMR ($CDCl_3$, 75 MHz, ppm):	139.8, 127.9, 127.6, 127.5, 86.0, 71.9, 41.9.
Mass spectrum (FAB):	m/z = 301 $[M]^+$.
CHN:	Found C 68.39, H 8.04, N 8.34%; Calcd. for $(C_{18}H_{24}N_2O_2)\cdot H_2O$ C 67.9, H 8.23, N 8.8%.

5.4.8 Synthesis of (4.12)[107]

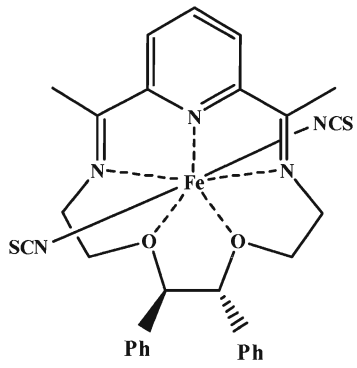

(4.12)

To a solution of $FeCl_2 \cdot 4H_2O$ (0.153 g, 0.767 mmol) in degassed MeOH (4 mL) was added a solution of $Na_2S_2O_4$ (92 mg, 0.44 mmol) in degassed H_2O (2 mL) followed by 2,6-diacetyl pyridine (0.125 g, 0.767 mmol) and a solution of **(4.11)** (0.23 g, 0.767 mmol) in degassed MeOH (7 mL). The reaction mixture was gently refluxed for 20 h under an N_2 atmosphere. After cooling to RT, the volume of solution was reduced to 50% and it was filtered into a solution of NaSCN (1.27 g, 15.6 mmol) in degassed H_2O (5 mL) containing $Na_2S_2O_4$ (38 mg) under N_2. The resulting mixture was stirred for a futher 4 h after which time a blue-precipitate was obtained. The solid was collected by filtration and washed with degassed water, a (3:1) mixture of Et_2O and THF and Et_2O and then dried under vacuum to afford **(4.12)** as a dark blue solid. Yield = 0.27 g (59%).

HRMS (FAB): Found *m/z* = 599.11461 $[M]^+$; Calcd 599.11120 for $C_{29}H_{29}FeN_5O_2S_2$.

CHN: Found C 48.34, H 4.13, N 9.68%; Calcd. for $C_{29}H_{29}FeN_5O_2S_2 \cdot 1.94\ CH_2Cl_2 \cdot 0.13H_2O$ C 48.48, H 4.36, N 9.14%.

IR (KBr, cm^{-1}): 2067, 1637, 1082, 1058.

UV-vis (in EtOH): λ_{max}= At 77 K: 334, 490, 672 (ε = 2140, 1081, 1860

$M^{-1}cm^{-1}$), At 293 K: 493, 660 nm (ε = 763, 1231 $M^{-1}cm^{-1}$)

Mpt. > 300°C

5.4.9 Synthesis of (4.13) [107]

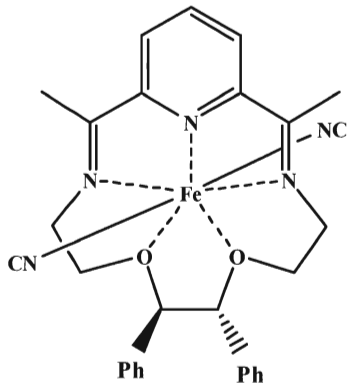

(4.13)

To a solution of $FeCl_2 \cdot 4H_2O$ (0.153 g, 0.767 mmol) in degassed MeOH (4 mL) was added a solution of $Na_2S_2O_4$ (85%, 92 mg, 0.44 mmol) in degassed H_2O (2 mL) followed by 2,6-diacetyl pyridine (0.125 g, 0.767 mmol) and the diamine **(4.11)** (0.23 g, 0.767 mmol) in degassed MeOH (7 mL). The blue reaction mixture was gently refluxed for 20 h under a N_2 atmosphere. After cooling to RT, the volume of solution was reduced to 50% and it was filtered into a solution of NaCN (0.77 g, 15.6 mmol) in degassed H_2O (5 mL) containing $Na_2S_2O_4$ (38 mg) under N_2. The mixture was stirred for a future 4 h. The blue-purple precipitate was collected by filtration. It was washed with degassed water, a 1:1 mixture of Et_2O : THF (1:1) and Et_2O to afford **(4.13)**. Yield = 0.22 g (54%).

Mass spectrum (FAB): *m/z* = 509 $[M\text{-}CN]^+$ 100% for $C_{29}H_{29}FeN_5O_2$.

CHN: Found C 63.16 H 5.47 N 12.44%; Calcd. for $(C_{29}H_{29}FeN_5O_2) \cdot H_2O$ C 62.93 H 5.61 N 12.66%.

IR (KBr, cm^{-1}): 2096, 1633, 1082, 1021.

UV-vis (in EtOH):	λ_{max}= At 100 K: 490, 615, 711 nm (ε = 1421, 450, 136 $M^{-1}cm^{-1}$). At 293 K: 494, 624nm (ε = 218,433 $M^{-1}cm^{-1}$).
Mpt.	> 300°C

CHAPTER 6

References

[1] Coronado, E.; Day, P. *Chem. Rev.* **2004**, *104*, 5419.

[2] Bleaney, B.; Bowers, K.D. *Proc.R. Soc. A*. **1952**, *214*, 451.

[3] Sessoli, R.; Gatteschi, D.; Caneschi, A.; Novak, M.A. *Nature*. **1993**, *365*, 141.

[4] Brown, J. *Philos. Trans*. **1724**, *33*, 17.

[5] Gilbert,W. *De Magnete*,**1600**, translation, Gilbert Club: London, **1900**.

[6] Mattis, D. C. *The Theory of Magnetism Made Simple*; World Scientific Publishing: **2006**.

[7] Weiss, P. *J. de Phys*. **1907**, *6*, 661.

[8] Dirac, P.A.M. *Proc. Royal Soc. London*. **1931**, *A133*, 60.

[9] Jiles, D. *Magnetism and Magnetic Materials*; Chapman and Hall: London, **1989**.

[10]Maxwell, J.C. *A Treatise on Electricity and Magnetism*; Dover: New York, **1954**.

[11]Aktas, B. *Nanostructred Magnetic Materials and their Applications*; Springer: **2001**.

[12] Moriya, T. *Spin Fluctuations in Itinerant Electron Magnetism*; Springer-Verlag: Berlin, **1985**.

[13]Curie, P. *Ann.Chim.Phys.* **1895**, *5*, 289.

[14]Blundell, S. *Magnetism in Condensed Matter*; Oxford University Press: **2001**.

[15] Majlis, N. *The Quantum Theory of Magnetism*; World Scientific: New Jersey: **2007**.

[16]Trémolet de Lacheisserie, E. D.; Gignoux, D.; Schlenker, M. *Magnetism: Fundamentals*; springer: **2005**.

[17]Kronmullel, F. *Micromagnetism and the Microstructure of Ferromagnetic solids*; Cambridge University Press: **2003**.

[18]Culity, B. D., Graham, C. D. *Introduction to Magnetic Materials*; John Wily & Sons: inc. **2008**.

[19] Miller, S. J., Drillon, M. *Molecules to Materials V*; Wiley-VCH: Weinheim. **2005**.

[20] Standly, K. J. *Oxide Magnetic Materials*; Clarendon Press: Oxford, **1972**.

[21] Morish, A. H. *The Physical Principals of Magnetism*; John Wily & Sons: inc. **1965**.

[22] Constable, E.C. *Coord. Chem. Rev.* **2008**, *252*, 842.

[23] Suh, M. P.; Cheon, Y. E.; Lee, E.Y. *Coord..Chem. Rev.* **2008**, *252*, 1007.

[24] (a) Huc, I.; Krische, M.J.; Funeriu, D. P.; Lehn, J. M. *Eur. J. Inorg. Chem.* **1999**, 1415. (b) Mazik, M.; Bandmann, H.; Sicking, W. *Angew. Chem., Int. Ed.* **2000**, *39*, 551.

[25] Kurmoo, M. *Chem. Soc. Rev.* **2008**, *38*, 1353.

[26] (a) Pilkington, M.; Decurtins. S. *Chimia*, **2000**, *54,* 593. (b) Lehn, J. M. *Supramolecular chemistry*; VCH: New York, USA, **1995**. (c) Kahn, O. *Molecular Magnetism*; VCH: New York, USA, **1993**.

[27] (a) Kato, M.; Muto, Y. *Coord.Chem. Rev.* **1988**, *92*, 45. (b) Kahn, O. *Angew. Chem., Int. Ed. Engl.* **1985**, *24*, 834. (c) Tandon, S. S.; Thompson, L. K.; Manuel, M. E.; Bridson, J. N. *Inorg. Chem.* **1994**, *33*, 5555.

[28] (a) Gatteschi, D.; Sessoli, R.; Villain, J. *Molecular Nanomagnets*; Oxford University Press: UK, **2006**. (b) Beltran, L. M. C.; Long. J. R. *Acc. Chem. Res*, **2005**, *38*, 325. (c) Kim, J. Yoo. H. S.; Koh. E. K.; Hong. C. S.; *Inorg. Chem.* **2007**, *46*, 10461.

[29] (a) Goodenough, J. B. *Phys. Rev,* **1955**, *100*, 564. (b) Goodenough, J. B. *J. Phys. Chem. Solids,* **1958**, *6*, 287. (c) Kanamori, J. *J. Phys.Chem. Solids,* **1959**, *10*, 87. (d) Ginsberg, A. P. *Inorg. Chim. Acta* Rev. **1971**, *5*,45.

[30] (a) Kahn, O. *Struct. Bonding* **1987**, *68*, 89, (b) Kahn, O., Galy, J., Journaux, Y., Jaud, J.; Morgenstern- Badarau, I. *J. Am. Chem. Soc.* **1982**, *104*, 2165. (c) McCleverty, J. A.; Ward. M.D. *Acc. Chem. Res*, **1998**, *31*, 842.

[31] Julve, M.; Lloret, F.; Cano, J.; Ottenwaelder, X.; Journaux, Y.; Munäoz, M. C. *Angew Chem*, **2001**, *113*, 3129.

[32] Ung, V. A.; Cargill Thompson, A. M. W.; Bardwell, D. A.; Gatteschi, D.; Jeffery, J. C.; McCleverty, J. A.; Totti, F.; Ward, M. D. *Inorg. Chem.* **1997**, *36*, 3447.

[33] Lloret, F.; De Munno, G.; Julve, M.; Cane, J.; Ruiz, R.; Caneschi, A. *Angew. Chem. Int. Ed.* **1998**, *37*, 135.

[34] Ottenwaelder, Ruiz-Garcia, R.; Blondin, G.; Carrasco, R.; Cano, J.; Lexa, D.; Journaux, Y.; Aukauloo, A. *Chem. Commun.* **2004**, 504.

[35] Kahn, O. *Acc. Chem. Res.* **2000**, *33*, 647.

[36] Dougherty, D. A. *Acc. Chem. Res.* **1991**, 24, 88.

[37] Pardo, E.; Ruiz-Garcia, R.; Lioret, F.; Julve, M.; Cano, J.; Pasan, J.; Ruiz- Perez, C.; Filali, Y; Chamoreau, L. M.; Journaux, Y. *Inorg. Chem.* **2007**, *46*, 4504.

[38] Pardo, E.; Bernot, K.; Ruiz-Garcia, R.; Lioret, F.; Julve, M.; Cano, J.; Delago, F. S.; Ruiz- Perez, C.; Ottenwaelder, X.; Journaux, Y. *Inorg. Chem.* **2004**, *43*, 2768.

[39] Fonseca, M. A.; Koning, B. *Adv.Synth.Catal.* **2003**. *345*, 1173.

[40] Epperson, J. D.; Ming, L. J.; Baker, E. R.; Newkome, E. R. *J.Am.Chem. Soc.* **2001**, *123*, 8583.

[41] Collinson, S. R.; Gelbrick, T.; Hursthouse, M. B.; Tucker, J. H. R. *Chem. Commun.* **2001**, 555.

[42] Sakai, K.; Ozawa, H.; Yamada, H.; Tsubomura, T.; Hara, M.; Higuchi, A.; Haga, M. A. *J. Chem. Soc., Dalton Trans*. **2006**, 3300.

[43] Hirao, T.; Moriuchi, T.; Ishikawa, T..; Nishimura, K.; Mikami, S.; Oshiro, Y.; Ikeda, I. *J. Mol. Catal*. **1996**, *A 113*, 117.

[44] Sigel, H.; Martin, R. B. *Chem. Rev*. **1982**, *82*, 385.

[45] Ma, Q. J.; Zhou, H. L.; Choi, M.C.K.; Chan, A.S.C., Yang, Q. *Chem. Commun*. **2003**, *111*, 1294.

[46] Morsali, A.; Ramazini, A.R.; Mahjoub. J. *Coord. Chem*. **2003**, 56, 1555.

[47] (a) Mishra, A.; Ali, A.; Upreti, S.; Gupta, R. *Inorg. Chem*. **2008**, *47*, 154. (b) Singh, A. P.; Ali, A.; Gupta, R. *Dalton Trans*. **2010**, *39*, 8135.

[48] Kalagouda, K.; Ali, A.; Vadavi, R.; Shenoy, R.; Patil, M.; Patil, S. A.; Nethaji, M. *Inorg. Chim. Acta*. **2005**, *358*, 3799.

[49] Jain, S. L.; Bhattacharyya, P.; Milton, H. L.; Stawin, A. M. Z.; Crayston, J. A.; Woollins, J. *Dalton Trans*. **2004**, 862.

[50] Reed, E. J.; White, A. J. P.; Neidle, S.; Vilar, R. *Dalton Trans*. **2009**, 2558.

[51] Qin, Z., Jennings, M. C., Puddephatt. J. *Inorg. Chem*. **2003**, *42*, 1956.

[52] Hou, H.; Wei, Y.; Song, Y.; Mi, L.; Tang, M.; Li, L.; Fan, Y. *Angew.Chem. Int. Ed*. **2005**, *44*, 6067.

[53] Tzeng, B. C.; Chen, B. S.; Yeh, H. T.; Lee, G. H.; Peng, S. M. *New J. Chem*, **2006**, *30*, 1087.

[54] (a) Lin, Y-i.; Jr, S. A. L. *Synthesis* **1977** , 345.(b) Wang, J.; Slater, B.; Alberola, A.; Stoeckli-Evans, H.; Razavi, F. S.; Pilkington, M. *Inorg. Chem*. **2007**, *46*, 4763.

[55] Lin, X.; Blake, A. J.; Wilson, C.; Sun, X.-Z.; Champness, N. R.; George, M.W.; Hubberstey, P.; Mokaya, R.; Schröder, M. *J. Am. Chem.Soc.* **2006**, *128*, 10745.

[56] (a) Terheijden, J.; Driessen, W. L.; Groeneveld, W. L.;*Trans.Met. Chem.* **1980**, *5*, 346. (b) Chapman, R. L.; Vagg. R. S. *Inorg. Chim. Acta,* **1979**, *33*, 227.

[57] Farrugia, L.J. *J. Appl. Cryst,* **1997**, *30*, 565.

[58] Bacon, G. E. *Acta Cryst.* **1951**, *4*, 558.

[59] Hunter, C.A.; Saunders, J. K. N. *J. Am. Chem. Soc.* **1990**, *112*, 5525.

[60] Kumar, U.; Thomas, J.; Thirupathi, N. *Inorg Chem.* **2010**, *49*, 62.

[61] Escuer, A.; Comas, T.; Vicente, R.; Ribas, J. *Transition Met. Chem. 18*, **1993**, 42.

[62] Mishra, A.; Kaushik, N. K.; Verma, A. K.; Gupta, R. *Eur. J. Med. Chem.* **2008**, 2189.

[63] Zhou, Y.; Chen, W. *Dalton Trans.* **2007**, 5123.

[64] Orgen, A. G.; Bremmer. L. *J. Chem. Soc. Dalton Trans.* **1989**, 51.

[65] Winnpenny, R. E. P. *J. Chem. Soc. Dalton Trans.* **2002**, 1.

[66] Spek, A.L. *Acta Cryst.* **2009**, D65, 148.

[67] Addison, A. W.; Rao, T. N.; Redi, J. K.; van Riju, J.; Vershoor, G. C. *J. Chem. Soc., Dalton Trans.* **1984**, 1349.

[68] Nanda, K. K.; Addison, A. W.; Paterson, N., Sinn, E.; Thompson, L. K.; Sakaguchi, U. *Inorg. Chem.* **1998**, *37,* 1028.

[69] Tasiopoulos, A. J., Wernsdorfer, W.; Moulton, B.; Zaworotko, M. J., Christou, G. *J. Am. Chem. Soc.* **2003**, *125*, 15274.

[70] Hathaway B. J. *Comprehensive Coordination Chemistry*: Vol. 5, Pergamon Press; New York, NY, USA, **1987**.

[71] Mondal, A.; Li, Y.; Khan, M. A.; Ross, J. H., Jr.; Houser, R. P. *Inorg. Chem,* **2004**, *43*, 7075.

[72] Pardo, E.; Dul, M. C.; Lescouëzec, R.; Chamoreau, L. M.; Journaux, Y.; Pasán, J.; Ruiz-Pérez, C.; Julve, M.; Lloret, F.; Ruiz-García, R.; Cano, J. *Dalton Trans.*, **2010**, *39*, 4786.

[73] Onions, S. T.; Heath, S. L.; Price, D. J.; Harrington. R. W.; Clegg. W.; Matthews . C. J. *Angew. Chem. Int. Ed.* **2004**, *43*, 1814.

[74] Armentano, D.; Mastropietro, T. F.; Julve, M.; Rossi, R.; Rossi, P.; De Munno, G. *J. Am. Chem. Soc.* **2007**, *129*. 2741.

[75] Rzepecki, P.; Nagel- Steger, L.; Feuerstein, S.; Linne, U.; Molt, O.; Zadmard, R.; Aschermann, k.; Wehner, M.; Schrader, T.; Riesner, D. *J. Bio. Chem.* **2004**, *279*, 47497.

[76] Lin, Y-i.; Jr, S. A. L. *Synthesis* **1977**, 345.

[77] Simulation were undertaken by Prof. J. M. Rawson using PIP (M.Nilges, Illinois EPR Research Center) via a windows interface (PIP for windows v1.2, J. M. Rawson, University of Windsor, 2011).

[78] Khanra, S.; Weyhermüller, T.; Chaudhuri, P. *Dalton Trans.*, **2009**, 3847.

[79] Murugesu, M.; King, P.; Clérac, R.; Anson, C. E.; Powell, A. K.; *Chem. Commun.* **2004**, 740.

[80] Keen, A. L.; Doster, M.; Han, H.; Johnson, S. A. *Chem. Commun.***2006**, 1221.

[81] (a) Milway, V. A.; Niel, V.; Abedin, T. S. M.; Xu, Z.; Thompson, L.; K. Grove. H.; Miller, D. O.; Parsons, S. R. *Inorg. Chem.* **2004**, *43*, 1875. (b) Zhao. L.; Xu, Z.;

Thompson, L. K.; Heath, S. L.;Miller, D. O.; Ohba, M. *Angew. Chem. Int. Ed,* **2000**, *39*, 3114.

[82] (a) L. Cambi, L. Szegö, *Chem. Ber. Dtsch. Ges.***1931**, *64,* 2591. (b) L. Cambi, L. Szegö, *Chem. Ber. Dtsch. Ges.***1933**, *66*, 656 L. (c) L. Cambi, L. Malatesta, *Chem. Ber. Dtsch. Ges.***1931**, *64,* 2591.

[83] A. H. Ewald, R. L. Martin, I. G. Ross, A. H. White, *Proc. Roy. Soc. London Ser.*, **1964**, *280*, 235.

[84] J. A. Real, A. B. Gaspar, M. C. Muñoz, *Dalton Trans.*, **2005**, 2062.

[85] (a). Baker W. A.; Bobonich. Jr, H. M. *Inorg. Chem.* **1964**, *3*, 1184. (b) König, E.; Madeja, K. *Inorg. Chem.* **1967**, *6*, 48.

[86] J.J. McGarvey, I.J. Lawthers, *Chem. Soc., Chem. Commun.* **1982**, 906.

[87] (*a*) S. Decurtins, P. Gütlich, C. P. Köhler, H. Spiering, A. Hauser, *Chem. Phys. Lett.*, **1984**, *139*, 1. (*b*) S. Decurtins, P. Gütlich, C. P. Köhler, H. Spiering, A. Hauser, *Inorg. Chem.*, **1985**, *24*, 2174.

[88] A. Hauser, J. Jeftić, H. Romstedt, R. Hinek, H. Spiering, *Coord. Chem. Rev.,* **1999**, *190–192*, 471.

[89]P. Gütlich, H.A. Goodwin, Spin Crossover in Transition Metal Compounds II, Topics in Current Chemistry, Eds. Springer., **2004**, 234, 155.

[90] A. Hauser, *Chem. Phys. Lett.* **1986**, *124*, 543.

[91] Gütlich, P.; Goodwin, H. A. *Spin crossover in transition metal compounds*, Springer, 2004.

[92] Money, V. A.; Carbonera, C.; Elhaık, J.; Halcrow, M. A.; Howard, J. A. K.; Lé tard, J.F. *Chem.Eur. J.*, **2007**, *13*, 5503.

[93] McCusker, J. K.; Reheingold, A.L.; Hendrickson, D. N. *Inorg Chem.* **2001**, 577.

[94] Halcrow, M. A. *Coord. Chem. Rev.*, **2009**, *253*, 2493.

[95] Holland, J. M.; McAllister, J. A.; Lu, Z.; Kilner, C. A.; Thornton-Pett, M.; Halcrow, M. A. *Chem. Commun.* **2001**, 577.

[96] Hostettler, M.; Trnroos, K. W.; Chernyshov, D.; Vangdal. B.; Bürgi, H.B. *Angew. Chem., Int. Ed.*, **2004**, *33*, 4589.

[97] Marchivie, M.; Guionneau, P.; Létard, J.-F. Chasseau, D. *Acta Crystallogr., Sect. B: Struct. Sci.*, **2003**, *59,* 479.

[98] Kepenekian, M.; Guennic, B. Le.; Robert, V. *J. Am. Chem. Soc.*, **2009**, *131*, 11498.

[99] (a) Yamada, M.; Hagiwara, H.; Torigoe, H.; Matsumoto, N.; Kojima, M.; Dahan, F.; Tuchagues, J.-P.; Re. N.; Iijima, S.; *Chem.Eur. J.*, **2006**, *12*, 4536. (b) Hagiwara, H. ; Matsumoto, N.; Iijima, S.; Kojima, M. *Inorg. Chim. Acta*, **2011**, *366*, 283.

[100] Galet, A.; Gaspar, A. B. ; Munoz, M. C.; Levchenko. G.; Real, J. A. *Inorg. Chem.*, **2006**, *45*, 9670.

[101] Gallois, B. ; Real, J. A.; Hauw. C.; Zarembowitch, J. *Inorg. Chem.*, **1990**, *29*, 1152.

[102] Zhong, Z. J.; Tao, J.-Q.; Yu, Z.; Dun, C.-Y.; Liu. Y.-J.; You, X.-Z. J. *Chem. Soc., Dalton Trans.*, **1998,** 327.

[103] Real, J. A.; Gaspar, A. B.; Niel, W.; Muñoz, M. C. *Coord. Chem. Rev.* **2003**, *236*, 121.

[104] Toftlund, H.; McGarvey, J.J. *Top. Curr. Chem.* **2004**, *233*, 151.

[105] Hayami, S.; Gu, Z.; Einaga,Y.; Kobayasi, Y.; Ishikawa, Y.; Yamada, Y.; Fujishima,A.; Sato, O. *Inorg. Chem.* **2001**, *40*, 3240.

[106] (a) Galet, A.; Gaspar, A. B.; Muñoz, M. C.; Bukin, G. V.; Levchenko, G.; Real, J. A. *Adv. Mater.* **2005**, *17*, 2949. (b) Kahn, O.; Martinez, C. J. *Science* **1998**, *279*, 44. (c) Kahn, O.; Krber, J.; Jay, C. *Adv. Mater.* **1992**, *4*, 718.

[107] Drew, M.G. B.; Othman, A. H. B.; Mcfall, S. G.; Mcllory, P. D. A.; Nelson, S. M. *Dalton Trans.*, **1977**, 1173.

[108] Schiff, H. *Annalen.* **1864**,*131*,118.

[109] Borisova, N. E.; Reshetova, M. D.; Ustynyuk, Y. A. *Chem. Rev.* **2007**,46.

[110] Nelson, S. M.; Mcllroy. P. D. A.; Stevenson. C. S. *J. Chem. Soc. Dalton Trans.***1986**, 991.

[111] König, E.; Ritter, G.; Dengler, J.; Nelson, S. M. *Inorg. Chem.* **1987**, *26*, 3582.

[112] Guionneau, P.; Sánchez Costa, J.; Létard, J. F. *Acta Cryst.* **2004**, *C60*, m587.

[113] Guionneau, P.; Le Gac, F.; Kaiba, A.; Sánchez Costa, J.; Chasseau, D.; Létard, J. F. *Chem. Commun*, **2007**, 3723.

[114] Létard, J. F.; Capes, L.; Chastanet, G.; Moliner, N.; Létard, S.; Real, J. A.; Kahn, O. *Chem. Phys. Lett.* **1999**, *313*, 115.

[115] (a) Kahn, O.; Martinez, J. C. *Science* **1998**, *279*, 44. (b) Sugiyarto, K.H.; Goodwin, H. A. *Aust. J. Chem.* **1994**, *47*, 263. (c) Real, J. A.; Andrés, E.; Munöz, M. C.; Julve, M.; Granier, T.; Bousseksou, A.;Varret, F. *Science* **1995**, *268*, 265. (d) Garcia, Y.; Kahn, O.; Rabardel, L.; Chansou, B.; Salmon, L.; Tuchagues, J. P. *Inorg. Chem.* **1999**, *38*, 4663.

[116] Hayami, S.; Juhász, G.; Maeda,Y.; Yokoyama,T.; Sato, O. *Inorg. Chem.* **2005**, *21*, 7289.

[117] (a) Atanasov, M.; Comba, P.; Daul, C.A. *Inorg. Chem.* **2008**, *47*, 2449. (b) Atanasov, M.; Busche, C.; Comba, P.; Hallak, F. E.; Martin, B.; Rajaraman, G.; Slageren, J. van.;

Wadepohl, H. *Inorg. Chem.* **2008**, *47*, 8112. (c) Lescouëzec, R.; Vaissermann, J.; Ruiz-Pérez, C.; Lloret, F., Carrasco, R.; Julve, M.; Verdaguer, M.; Dromzee, Y.; Gatteschi, D.; Wernsdorfer, W. *Angew. Chem., Int. Ed.* **2003**, *42*, 1483.

[118] (a) Ni, Z. H.; Kou, H. Z. ; Zhao, Y. H.; Zheng, L.; Wang, R. J.; Cui, A. L.; Sato, O. *Inorg. Chem.*, **2005**, *44*, 2050; (b) Ni, Z. H.; Zhang, L. F.; Tangoulis, V.; Wernsdorfer, W.; Cui, A. L.; Sato, O. Kou, H. Z. *Inorg. Chem.* **2007**, *46*, 6029.

[119] Zhang, D.; Wang, H.; Chen, Y.; Ni, Z.H.; Tian, L.; Jiang, J. *Inorg. Chem.* **2009**, *48*, 5488.

[120] Zhang, D.; Wang, H.; Chen, Y.; Zhang, L.; Tian, L.; Ni, Z.H.; Jiang, J. *Dalton Trans.***2009**, 9418.

[121] Zhang, D.; Wang, H.; Tian, L.; Ni, Z.H.; Jiang, J.*Cryst. Eng. Comm*, **2009**, *11*, 2447.

[122] Bonadio,F.; Senna,M. C.; Ensling, J.; Sieber, A.; Neels,A.; Stoeckli-Evans,H.; Decurtins, S. *Inorg. Chem.* **2005**, *44*, 969.

[123] Paraschiv,C.; Andruh,M.; JournauxY.; Žak, Z.; Kyritsakasd, N, Ricarde, L. *J. Mater. Chem.* **2006**, *16*, 2660.

[124] Zhang, Y. Z.; Sato. O. *Inorg. Chem.* **2010**, *49*, 1271.

[125] K□nig, E.**;** Madeja, K. *Inorg. Chem.* **1967**, *6*, 48.

[126] Ionkin, A. S.; Marshall, W. J. *Heteroatom Chemistry*, **2002**, *13*, 662.

[127] Posner, G. H.; Whitten, C. E.; Sterling, J. J. *J. Am. Chem. Soc.* **1973**, *13*, 7788.

[128] Gruza,M. M.; Pokropa, A.; Jurczak, J. *Tetrahedron: Asymmetry*. **2005**, *16*, 1939.

[129] Crosby, J.; Stoddart, F.; Sun, X.; Venner, M. R. W. *Synthesis*, **1993**, 141.

[130] Gülich, P.; Garcia, Y.; Goodwin, H. A. *Chem. Soc. Rev.* **2002**, *29*, 419.

[131] (a) Yang, F. L.; Li, B.; Hanajima, T.; Einaga, Y.; Huang, R. B.; Zheng. L. S.; Tao, J. *Dalton. Trans*. **2010**, *39*, 2288. (b) Cheng, H.; Djukic, B.; Jenkins, H. A.; Gorelsky, S. I.; Lemaire. M. T. *Can. J. Chem*. **2010**, *88*, 954.(c) Farhan, K, A.; Beagley, B.; El-Sayrafi, O.; Gott, G. A.; McAuliffe, C. A.*J. Chem. Soc. Dalton Trans.* **1990**, 1243.

[132] Drew, M. G. B.; Othman, H. B. *Acta Cryst.*. **1975**, B31.

[133] Drew, M. G. B.; Othman, H. B. *J. C. S. Dalton*. **1976**, 1394.

[134] Sanchez-Costa, J.; Guionneau, J. F.; Letard, J. *J. Phys. Conf. Series*. **2005**, *21*, 67.

[135] Sheldrick, G.M. *Acta Cryst*. **2008**, *A64*, 112.

[136] Macrae, C. F.; Edgington, P. R.; McCabe, P.; Pidcock, E.; Shields, G. P.; Taylor, R.; Towler, M.; van de Streek, J. *J. Appl. Cryst.*, **39**, 2006, 453.

[137] Rzepecki, P.; Molt, O.; Zadmard, k.; Wehner, M.; Schrader, T. *Synthesis.* **2003**, 1815.

[138] A. Jouaiti, M. W. Hosseini, N. Kyritsakas, *Chem. Commun*. **2002**, *7*, 38.

APPENDIX

Crystallographic parameters

Table 2.5 Crystal data and structure refinement parameters for compounds (2.7), (2.8) and (2.17).

	(2.7)	(2.8)	(2.17)
Empirical formula	$C_{42}H_{44}N_{10}O_6$	$C_{25.50}H_{39.50}N_{8.50}O_5$	$C_{168}H_{208}Cl_{16}Cu_8N_{56}O_{16}$
Formula weight	784.87	545.16	4343.42
Temperature	150(2) K	100(2) K	150(2) K
Wavelength	0.71073 A	0.71073 A	MoKα, 0.71073 Å
Crystal system, space group	Tricilnic, $P\bar{1}$	Orthorhombic, P n a 21	triclinic, $P\bar{1}$
Unit cell dimensions	a = 13.263(3) Å, α = 10.838(10)° b = 13.425(3) Å, β = 92.555(11)° c = 13.458(3) Å, γ = 116.251(10)°	a = 17.4186(11) Å, α= 90° b = 32.397(2) Å, β = 90° c = 10.5410(7) Å, γ = 90°	a = 21.5918(15) Å, α = 83.750(4)° b = 24.0051(17) Å, β = 85.664(4)° c = 27.3864(19) Å, γ = 69.107(3)°
Cell volume	1949.5(7) $Å^3$	5948.5(7) $Å^3$	13172.2(16) $Å^3$
Z	2	8	2
Calculated density	1.337 Mg/m^3	1.217 Mg/m^3	1.095 g/cm^3
Absorption coefficient μ	0.092 mm^{-1}	0.087 mm^{-1}	0.850 mm^{-1}
F(000)	828	2336	4480
Crystal colour and size	yellow, 0.4 x 0.10 x 0.08 mm	pale yellow, 0.5 x 0.5 x 0.45 mm	blue, 0.70 × 0.40 × 0.10 mm^3
θ range for data collection	1.91 to 22.50°	1.72 to 23.85°	2.4 to 24.8°
Limiting indices	h –14 to 14, k –14 to 14, l –14 to 12	h –19 to 19, k –36 to 34, l –11 to 11	h –25 to 23, k –27 to 27, l –31 to 31
Reflections collected / unique	16826 / 4946 [R(int) = 0.0614]	122953 / 9096 [R(int) = 0.0681]	175202/42801 [R(int) = 0.0475)
Completeness to θ = 22.50	96.8 %	99.6 %	94.6 %
Absorption correction	Semi-empirical from equivalents	Semi-empirical from equivalents	semi-empirical from equivalents
Max. and min. transmission	0.7454 and 0.5525	0.7456 and 0.6778	0.590 and 0.920
Refinement method	Full-matrix least-squares on F^2	Full-matrix least-squares on F^2	Full-matrix least-squares on F^2
Data / restraints / parameters	4946 / 16 / 371	9096 / 22 / 690	42801 / 12042 / 2739
Goodness-of-fit on F^2	1.518	1.220	1.128
Final R indices [I>2sigma(I)]	R1 = 0.1280, wR2 = 0.3672	R1 = 0.0899, wR2 = 0.2498	R1 = 0.0749, wR2 = 0.2084
R indices (all data)	R1 = 0.1759, wR2 = 0.4087	R1 = 0.0940, wR2 = 0.2530	R1 = 0.1050, wR2 = 0.2277
Largest diff. peak and hole	1.082 and -0.651 e $Å^{-3}$	1.091 and -0.532 e.A^{-3}	2.45 and –1.25 e $Å^{-3}$

Table 4.9. Crystal data and structure refinement parameters for compounds (4.12) and (4.13).

	(4.12)	(4.12)	(4.13)
Empirical formula	C_{66} H_{74} Fe_2 N_{12} O_5	C_{66} H_{74} Fe_2 N_{12} O_5	C_{29} H_{29} Fe N_5 O_2 S_2
Formula weight	1227.07	1227.07	599.54
Temperature	250(2) K	100(2) K	200(2) K
Wavelength	0.71073 A	0.71073 A	0.71073 A
Crystal system, space group	Monoclinic, P2(1)	Monoclinic, $P2_1$	Triclinic, P1
Unit cell dimensions	a = 14.3466(19) Å, α = 90° b = 10.7143(12) Å, β = 100.2(4)° c = 21.144(3) Å, γ = 90°	a = 14.1310(16) Å, α = 90° b = 10.5819(10) Å, β = 99.233(4)° c = 20.876(2) Å, γ = 90°	a = 9.3391(6) Å, α = 76.312(2)° b = 10.4521(7) Å, β = 75.165(2)° c = 17.9526(11) Å, γ = 69.756(2)°
Cell volume	3198.8(7) $Å^3$	3081.2(6) A^3	1568.04(17) A^3
Z	2	2	2
Calculated density	1.274 Mg/m^3	1.323 Mg/m^3	1.270 Mg/m^3
Absorption coefficient μ	0.512 mm^{-1}	0.531 mm^{-1}	0.646 mm^{-1}
F(000)	1292	1292	624
Crystal colour and size	dark blue, 0.44 x 0.09 x 0.07 mm	dark blue, 0.33 x 0.065 x 0.02 mm	dark blue, 0.2 x 0.06 x 0.05 mm
θ range for data collection	1.88 to 26.45°	0.99 to 28.26°.	2.10 to 20.00°
Limiting indices	h -17to17, k -13 to 13, l -26 to 26	h -16 to18, k -13 to 13, l -24 to 27	h -8 to 8, k -10 to10, l -17 to 17
Reflections collected / unique	37579 / 12591 [R(int) = 0.0572]	23943 / 13021 [R(int) = 0.0564]	13332 / 5102 [R(int) = 0.0447]
Completeness to θ = 22.50	98.7 %	94.2 %	97.2 %
Absorption correction	Semi-empirical from equivalents	Semi-empirical from equivalents	Semi-empirical from equivalents
Max. and min. transmission	0.7454 and 0.6514	0.7457 and 0.6361	0.7454 and 0.6627
Refinement method	Full-matrix least-squares on F^2	Full-matrix least-squares on F^2	Full-matrix least-squares on F^2
Data / restraints / parameters	12591 / 15 / 773	13021 / 6 / 774	5102 / 23 / 289
Goodness-of-fit on F^2	1.102	1.044	1.111
Final R indices [I>2sigma(I)]	R1 = 0.0775, wR2 = 0.1588	R1 = 0.0783, wR2 = 0.1718	R1 = 0.0906, wR2 = 0.2177
R indices (all data)	R1 = 0.1138, wR2 = 0.1790	R1 = 0.1480, wR2 = 0.2170	R1 = 0.0983, wR2 = 0.2226
Absolute structure parameter	0.16(2)	0.08(3)	0.25(5)
Largest diff. peak and hole	0.986 and -0.507 e. $Å^{-3}$	1.457 and -0.839 e.A^{-3}	0.724 and -0.491 e.A^{-3}